The University Of Sheffield.

Department Of Mechanical Engineering

Bearing Surface Optimisation on Hydrodynamic Lubrication Film with Vibration-Assisted Machining and Ultrasound Reflectometry

Hiroyuki Suzuki

March 2016

Supervisor: Professor Robert S Dwyer-Joyce

Thesis submitted for the degree of Doctor of Philosophy

Abstract

The collapse of full-film hydrodynamic lubrication in a journal bearing often leads to a significant failure of the whole machine. In order to delay such full-film lubrication collapse, surface optimisation by implementing bespoke surface texture has spurred industrial interest. This thesis aims to optimise the journal bearing surface for an automotive transmission, addressing the deficiency of understanding of the effects of bespoke surface texture on hydrodynamic lubricant film formation under real operation by developing an accurate, inexpensive and fast texturing technique to create bespoke surface textures and a non-invasive technique to measure the film thickness.

A novel variant of non-resonant vibration-assisted machining was developed using an off-the-shelf piezoelectric actuator to create bespoke surface textures. Surface textures consisting of a repeating radial striation pattern of sine waves were reproducibly generated on the face of the disc work piece (an aluminium alloy AlSi1MgMn and a low-alloyed steel 16MnCr5) in a conventional milling machine when the frequency of the superposed vibration was in phase with the rotational speed of the work piece. The developed device was successfully implemented on shaft work pieces (alloyed steels C40 and SCM420H) in a conventional turning machine also.

A journal bearing test platform, which represents operational conditions of an automotive transmission, was developed incorporating a non-invasive ultrasound reflection technique. On the test platform, film thickness measurement was examined under operational conditions in steady-state. The measured film thickness and the attitude angle on the plain journal bearing (ϕ98 mm of the diameter with 0.255 of L/D) agreed well with theoretical curves deduced by a classical Reynolds equation with the short-bearing approximation.

Film thickness measurements on two textured journal bearings (a rough-meshed by a conventional milling and a fine-meshed by the vibration-assisted machining device) were performed on the journal bearing test platform. The load capacity ratio ζ, i.e. a ratio of the load capacity experimentally measured on the textured bearing and on the un-textured bearing, were 0.40 to 0.59 in the rough-meshed bearing and 1.12 to 1.27 in the fine-meshed bearing. Despite several differences in the geometrical model and test conditions between the present experimental work and the literature CFD works compared, the load capacity ratios were quantitatively similar.

Acknowledgements

First and foremost I wish to thank my supervisor Prof. Rob Dwyer-Joyce for his guidance over this project. His enthusiasm and profound knowledge in tribology has greatly enriched my project. I also wish to express my gratitude to Dr. Matt Marshall for his valuable support and advices.

I am grateful to Hino Motors, Ltd for providing the primary funding for this project as well as offering the invaluable opportunity to pursue the PhD. In that respect, my sincere thanks go to Mr. Shin Endo, Mr. Kouji Shouyama, Mr. Youichirou Okazaki, Mr. Junichi Kato, Dr. Masatoshi Yoshizaki, Mr. Isao Oosako, Mr. Katsunobu Takeda, Mr. Toshiyuki Maruyama, Mr. Hiroshi Chida, Mr. Ichiro Kamikura, Mr. Ryo Ichikawa, Mr. Takuma kitazume, and Mr. Ken Okuyama for their support and patience throughout.

I would also like to express my gratitude to Taiho Kogyo Tribology Research Foundation (TTRF) for providing the funding for a part of this project.

I owe my gratitude to Mr. Dave Butcher for his continuous support and helpful attitude, without whom this project would not have been successfully completed.

I wish to express my gratitude to Prof. Haizuka and Dr. Ito for their guidance and invaluable advices for the decision toward this study.

I thank my fellow researchers at the Leonardo Triblogy Centre and the Department of Mechanical Engineering, who shared the excellent and entertaining time over the last four years. Special thanks go to Dr. Nicola Fois, Dr. Jack Naumann, Mr. Giuseppe Tronci, Mr. Luke Buckley-Johnstone, Mr. Michele Schirru, Dr. Tom Howard, Dr. Steve Lewis, Dr. Wenqu Chen, Dr. Oliver Burke, Dr. Daniel Wise, Ms. Elena Marensi, Dr. Rob Thornton, Dr. Tom Anthistle, Mr. Tom Bruce, Dr. Juanjuan Zhu, Dr. Robin Mills, Mr. Mike Watson, Mr. Ben White and Mr. Mike Mesaritis.

Finally, I would like to thank my parents and brothers. This doctoral study would have remained unachieved were it not for their encouragement.

Contents

List of Figures

List of Tables

Nomenclature

A	Area of chip	m^2
A	Amplitude of sound wave	m
A	Signal amplitude from the layer of interest	volt
A_{ref}	Signal amplitude from the reference boundary	volt
B	Slider length in x coordinate	m
B	Bulk modulus	Pa
c	Speed of sound wave	$m\ s^{-1}$
$c_{1,2,3}$	Phase velocity of sound wave of medium 1, 2 and 3	$m\ s^{-1}$
c_a	Phase velocity of sound wave of air	$m\ s^{-1}$
c_m	Phase velocity of sound wave in two phase mixture of mediums	$m\ s^{-1}$
c_o	Phase velocity of sound wave of the oil	$m\ s^{-1}$
c_r	Clearance of journal bearing in radii	m
c_s	Phase velocity of sound wave of the shaft and bush steel	$m\ s^{-1}$
C	Integration constant	dimensionless
d_g	Groove depth	m
D	Nominal diameter of journal bearing	m
e	Eccentricity of journal bearing	m
E	Young's modulus	Pa
f	Frequency of sound wave	Hz
f	Vibration frequency of the piezoelectric actuator	Hz
f_{half}	Halfway frequency between the resonant frequencies	Hz
f_{res}	Resonant frequency	Hz
F_f	Feed force of cutting	N
F_n	Normal force of cutting	N

F_{t}	Tangential force of cutting	N
F_{pull}	Pull force of piezoelectric actuator	N
F_{push}	Push force of piezoelectric actuator	N
F'_{pull}	Pull force capacity of piezoelectric actuator	N
F'_{push}	Push force capacity of piezoelectric actuator	N
$\mathbf{g}$	External force	N
h	Fluid film thickness (height)	m
h'	Fluid film thickness on the groove	m
h_{ave}	Averaged fluid film thickness	m
h_{c}	Annular clearance of the shaft and the bush	m
h_{max}	Maximum fluid film thickness	m
h_{min}	Minimum fluid film thickness	m
h_{nom}	Nominal fluid film thickness	m
K_{s}	Specific cutting force	Pa
L	Slider length (width) in y coordinate	m
m	Mode number of the resonant frequency	dimensionless
m	Mass of piezoelectric element	kg
m_{eff}	Effective mass	kg
M	Mass driven by piezoelectric actuator	kg
p	Pressure	Pa
P_{in}	Pressure at inlet port	Pa
q_{x}	Fluid flow rate per unit length in x coordinate of the slider	$\mathrm{m}^2\ \mathrm{s}^{-1}$
q_{y}	Fluid flow rate per unit length in y coordinate of the slider	$\mathrm{m}^2\ \mathrm{s}^{-1}$
Q	Supplied oil flow rate	$\mathrm{m}^3\ \mathrm{s}^{-1}$
r_{b}	Radius of the bush	m
r_{s}	Radius of the shaft	m
R	Reflection coefficient	dimensionless
$R_{1,2}$	Reflection coefficient of medium 1 and 2	dimensionless
R^2	Coefficient of determination	dimensionless

R_a	Roughness average	m
Re	Reynolds number	dimensionless
R_{half}	Reflection coefficient at f_{half}	dimensionless
R_{ref}	Reflection coefficient from the reference boundary	dimensionless
R_{res}	Reflection coefficient at the resonant frequency	dimensionless
S_r	Reciprocal of Sommerfeld number	dimensionless
t	Time	s
t	Time of flight	s
t_0	Initial depth of cut	m
t_d	Depth of cut	m
T	Material thickness	m
$T_{1,2,3}$	Transmission coefficient of medium 1, 2 and 3	dimensionless
T	Temperature	°C
T_o	Temperature of the oil	°C
u	Displacement field of sound wave	m
u	Velocity of fluid in x coordinate of the slider	m s^{-1}
u_{fpr}	Feed per revolution	m
u_f	Feed speed	m s^{-1}
$\mathbf{u}$	Velocity vector	m s^{-1}
U	Velocity of the slider surfaces in x coordinate	m s^{-1}
v	Velocity of fluid in y coordinate of the slider	m s^{-1}
V	Volume of fluid	m^3
V	Velocity of the slider surfaces in y coordinate	m s^{-1}
V_e	Operating voltage of piezoelectric element	volt
V_m	Mean voltage commanded to voltage source	volt
w	Velocity of fluid in z coordinate of the slider	m s^{-1}
w_g	Groove width	m
W	Load	N
W	Velocity of the slider surfaces in z coordinate	m s^{-1}

W'	Load	N
$W_{1,2}$	Load components	N
x	Coordinate in direction of sound propagation in a three-layer system in Chapter 2	m
x	Coordinate in sliding direction of slider in Chapter 2 and 5	m
x	Coordinate in tangential direction of disc work piece in Chapter 3	m
x	Coordinate in tangential direction of shaft work piece in Chapter 5	m
y	Coordinate in width direction of slider in Chapter 2 and 5	m
y	Coordinate in radial direction of disc work piece in Chapter 3	m
y	Coordinate in axial direction of shaft work piece in Chapter 5	m
z	Coordinate in film thickness direction of slider in Chapter 2 and 5	m
z	Coordinate in vibration direction of piezoelectric actuator in Chapter 3 and 5	m
z_0	Initial position of cutter tip in z coordinate	m
z_c	Dynamic position of cutter tip in z coordinate	m
Z	Acoustic impedance	Pa s m^{-3}
$Z_{1,2,3}$	Acoustic impedance of medium 1, 2 and 3	Pa s m^{-3}
Z_s	Acoustic impedance of the shaft and bush steel	Pa s m^{-3}
β	Attitude angle	degree
δ	Peak to peak amplitude of surface texture	m
Δ	Sommerfeld number	dimensionless
ΔL	Displacement of piezoelectric element	m
$\Delta L'$	Displacement capacity of piezoelectric actuator	m
ΔL_r	Displacement range of piezoelectric element	m
ΔL_{rm}	Displacement range of piezoelectric element measured by the strain gauge	m
ΔL_{rt}	Displacement range of cutter tip	m
ΔV	Voltage range commanded to voltage source	m
ΔV_e	Operating voltage range of piezoelectric element	volt
ε	Eccentricity ratio of journal bearing	dimensionless
ζ	Load capacity ratio to the measured value in the plain journal bearing	dimensionless
ζ'	Load capacity ratio to the value with the short-bearing approximation	dimensionless

η	Ratio of vibration frequency and rotation speed of spindle	dimensionless
η	Dynamic viscosity	Pa s
θ	Angle from the maximum film thickness	degree
κ	Stiffness of the fluid layer per unit area	Pa m^{-1}
$\bar{\kappa}$	Mean stiffness of the fluid layer per unit area on the textured surface	Pa m^{-1}
κ_a	Stiffness of piezoelectric actuator	N m^{-1}
κ_e	Stiffness of piezoelectric element	N m^{-1}
κ_{sp}	Stiffness of preload spring	N m^{-1}
λ	Wavelength of sound wave	m
λ	Lambda ratio	dimensionless
λ_g	Groove wavelength	m
λ_t	Tangential wavelength of texture	m
ν	Poisson's ratio	dimensionless
ν	Kinematic viscosity	m^2 s^{-1}
ν_o	Kinematic viscosity of the oil	m^2 s^{-1}
ρ	Density	kg m^{-3}
ρ_a	Density of air	kg m^{-3}
ρ_o	Density of oil	kg m^{-3}
ρ_s	Density of the shaft and bush steel	kg m^{-3}
σ	Stress field of sound wave	Pa
τ	Shear stress	Pa
ϕ	Air volume fraction	dimensionless
ϕ	Signal phase from the layer of interest	rad
ϕ_{ref}	Signal phase from the reference boundary	rad
Φ_R	Phase of the reflection coefficient	rad
φ	Angular coordinate	degree
ω	Rotation speed of spindle	rad s^{-1}
ω	Angular frequency of sound wave	rad s^{-1}

Chapter 1

Introduction

1.1 Statement of the Problem

Studies of hydrodynamic lubricant film have been a keystone in tribology for the past two centuries. The collapse of such full-film formation (e.g. Figure 1.1) often leads to a significant failure of the whole machine, thus it has been intensively investigated both experimentally and theoretically. Journal bearings, which are typically operated under a full-film hydrodynamic lubrication regime, have been widely used in automotive transmissions due to their reliability and economic viability. In the past decades, the increased requirements for transmission reliability along with stringent legislations controlling vehicle emissions have increased the severity of the tribological environment of the journal bearings.

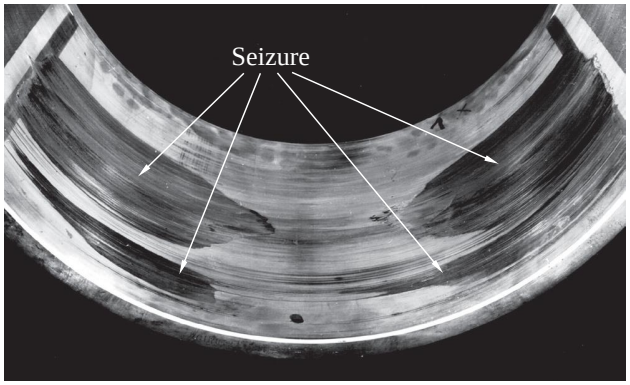

Figure 1.1: Seizure on a journal bearing surface due to lubricant film collapse (Koring, 2013).

With such background, surface optimisation by implementing bespoke surface textures to enhance lubricant film formation has spurred industrial interest. The effect of such bespoke surface

texture as a method of enhancing film formation delaying the film collapses has been experimentally recognised in parallel sliders (e.g. Hamilton et al. (1966); Salama (1950)) and a non-parallel slider (e.g. Glavatskih et al. (2005)). However, there exists several technical challenges to implement the bespoke surface textures into industrial journal bearings.

Firstly, the existing manufacturing techniques for creating bespoke surface textures are costly. Although there exists several techniques to create such bespoke surface textures into tribological interfaces, all of which are post-process techniques after the finish cut is performed, therefore most of the techniques are economically viable in limited industrial applications.

Secondly, there are no in-situ film thickness measurement technique and its test platform which allows a non-invasive accurate assessment for the effect of bespoke surface texture under operational condition. The conventional techniques available to date for film thickness measurement, such as optical or electrical techniques, were only applicable under laboratory conditions because of the inherent limitations of the apparatus arrangement and physical penetration to the parts involved in the film formation.

Thirdly, the effect of such bespoke surface texture on journal bearing has not been fully understood under real operational conditions. In-depth understanding as to the magnitude, mechanism, and influential factors of the effect on the lubricant film formation are insufficient.

1.2 Aim and Objectives

The aim of this thesis was to tribologically optimise a journal bearing surface for an automotive transmission, addressing the deficiency of in-depth understanding of the effects of the bespoke surface texture on hydrodynamic lubricant film formation under real operational situation by developing an accurate, inexpensive and fast texturing technique to create bespoke surface textures and a non-invasive technique to measure the film thickness.

The following objectives were pursued in order to accomplish the aim of this thesis:

- Objective 1: Design and implement a novel variant of non-resonant vibration-assisted machining device to create bespoke surface textures to the face of a disc work piece in a conventional milling machine and a journal bearing shell in a conventional turning machine.

- Objective 2: Develop a journal bearing test platform with the ultrasound reflection technique which allow the examination of the film thickness with no physical penetration to the

parts involved in film formation under operational condition of an automotive transmission.

- Objective 3: Examine a film thickness measurement on two journal bearings with bespoke surface textures in the developed journal bearing test platform to validate a hypothesis obtained through a literature review on the effects of the bespoke surface texture.

1.3 Thesis Layout

This thesis is divided into the following chapters:

- Chapter 1 describes the introduction of the thesis including the statement of problem, the research aim and objectives, and the thesis layout.

- Chapter 2 outlines the background to hydrodynamic lubrication and ultrasound reflectometry.

- Chapter 3 presents the design and implementation of a non-resonant vibration-assisted machining device to create bespoke surface textures. This technique will be implemented on the journal bearing test pieces investigated in Chapter 5.

- Chapter 4 shows the development of a journal bearing test platform which represents operational condition of an automotive transmission. A film thickness measurement on the plain journal bearing was examined using an ultrasonic reflection technique.

- Chapter 5 investigates the effect of bespoke surface textures on hydrodynamic lubricant film formation. One of the bespoke surface textures is created by the developed texturing device in Chapter 3, and the lubricant film thickness on the textured bearings are measured on the platform developed in Chapter 4.

- Chapter 6 summarises the concluding remarks for achievements against project aim and objectives and suggests the directions for the future study.

Chapter 2

Hydrodynamic Lubrication and Ultrasound Reflectometry

In this chapter, the background to hydrodynamic lubrication and ultrasound reflectometry are presented. The first part of this chapter gives a brief introduction to hydrodynamic lubrication theory development. The basic equations to describe hydrodynamic lubrication with several key assumptions and approximations for practical use of engineering applications are followed. The latter part of this chapter presents ultrasound reflectometry with a basic introduction to ultrasound and acoustic behaviour in a three-layer system to deduce an embedded thin layer thickness. The measurable limits of the techniques for the layer thickness are also presented.

2.1 Hydrodynamic Lubrication

2.1.1 Appreciation and development of hydrodynamic lubrication

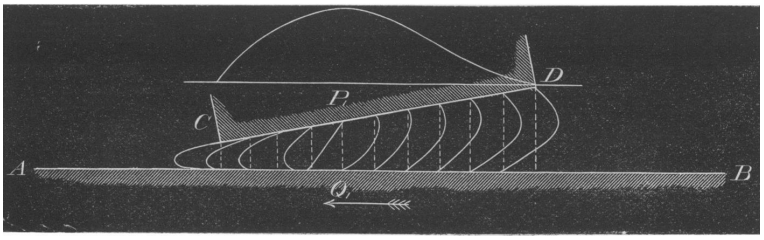

Figure 2.1: Schematic of two surfaces tilted to each other with relative motion (Reynolds, 1886).

In hydrodynamic lubrication a viscous fluid film carries an applied load physically separating two sliding surfaces. Engineering applications such as thrust bearings or journal bearings are

mainly designed to be operated in steady-state of this lubrication regime, where friction and wear rate is very low. There are two conditions, as presented in Figure 2.1, in order that the hydrodynamic pressure occurs; firstly two surfaces must have relative motion with sufficient velocity, and secondly the surfaces must be tilted to each other (except parallel stepped surface). The mechanism of hydrodynamic lubrication was firstly appreciated then experimentally investigated by an engineer, Beauchamp Tower. In 1883 he reported his experimental finding as (Tower, 1883):

> "A very interesting discovery was made when the oilbath experiments were on the point of completion. The experiments being carried on were those on mineral oil; and the bearing having seized with 625 lb/sq in, the brass was taken out and examined, and the experiment repeated. While the brass was out, the opportunity was taken to drill a 1/2-inch hole for an ordinary lubricator through the cast iron cap and the brass. On the machine being put together again and started with the oil in the bath, oil was observed to rise in the hole which had been drilled for the lubricator. The oil flowing over the top of the cap made a mess, and an attempt was made to plug up the hole, first with a cork and then with a wooden plug. When the machine was started the plug was slowly forced out by the oil in a way which showed that it was acted on by a considerable pressure. A pressure gauge was screwed into the hole, and on the machine being started the pressure, as indicated by the gauge, gradually rose to above 200 lb./sq in. The gauge was only graduated up to 200 lb and the pointer went beyond the highest graduation. The mean load on the horizontal section of the journal was only 100 lb/sq in. This experiment showed conclusively that the brass was actually floating on a film of oil, subject to a pressure due to the load. The pressure in the middle of the brass was thus more than double the mean pressure. No doubt if there had been a number of pressure gauges connected to the various parts of the brass, they would have shown that the pressure was highest in the middle, and diminished to nothing towards the edges of the brass."

This experimental discovery by Tower was then theoretically analysed by Osborne Reynolds. He, in his classic paper of 1886 published in the Proceeding of the Royal Society (Reynolds, 1886), derived an equation for hydrodynamic lubrication from Navier-Stokes equations and con-

firmed that the derived equation, known as Reynolds equation, agreed well with the Tower's experimental result. Though the Reynolds equation is a simplified form of the complex Navier-Stokes equations, the Reynolds equation can be easily derived by another procedure considering the equilibrium of an element of fluid and the continuity of flow principle, which will be discussed in the following section.

2.1.2 Reynolds equation

The Reynolds equation can be derived considering the equilibrium of an element of fluid and the continuity of flow principle with eight assumptions (assumption I to VIII), further mathematical processes are involved in conditions where these assumptions are invalid (Cameron, 1966; Stachowiak and Batchelor, 2005). The assumptions are following:

- Assumption I: Body forces are neglected. Outside field of force such as gravitational or magnetic forces does not act on the fluid significantly; however, which may be invalid in cases with conductive fluid (magneto hydrodynamics).

- Assumption II: Pressure is constant across the film thickness. This assumption is normally true as the film thickness is generally very thin (an order of a few μm to 30 μm), but some exceptional cases.

- Assumption III: No slip is present at the boundaries, which means that the velocity in a boundary is same as velocity of the oil layer adjacent to the boundary. This is considered to be generally valid.

- Assumption IV: Lubricant is a Newtonian fluid.

- Assumption V: Lubricant flow is laminar. This is generally valid except a few engineering applications e.g. very large bearing with high surface velocity where the flow might not be in laminar.

- Assumption VI: Fluid inertia is neglected. In some conditions the inertia effect could become prominent and should be taken into account for more elaborate analyses.

- Assumption VII: Fluid density is constant across the film. Crude assumption neglecting the thermal effect over the film.

- Assumption VIII: Fluid viscosity is constant across the film. Crude assumption neglecting the thermal effect over the film.

2.1.2.1 Equilibrium of an element of fluid

Consider an element of fluid in a slider subject to shear stresses τ and pressures p with sides of length dx, dy and dz as shown in Figure 2.2. For equilibrium the forces acting on the top and side faces must balance each other (for simplicity consider the balance in x direction only here) as follows:

$$pdydz + \left(\tau_{xz} + \frac{\partial \tau_{xz}}{\partial z} dz\right) dxdy = \left(p + \frac{\partial p}{\partial x} dx\right) dydz + \tau_{xz} dxdy, \tag{2.1}$$

which then becomes after simplifying with an assumption that $dxdydz \neq 0$ as:

$$\frac{\partial \tau_{xz}}{\partial z} = \frac{\partial p}{\partial x}. \tag{2.2}$$

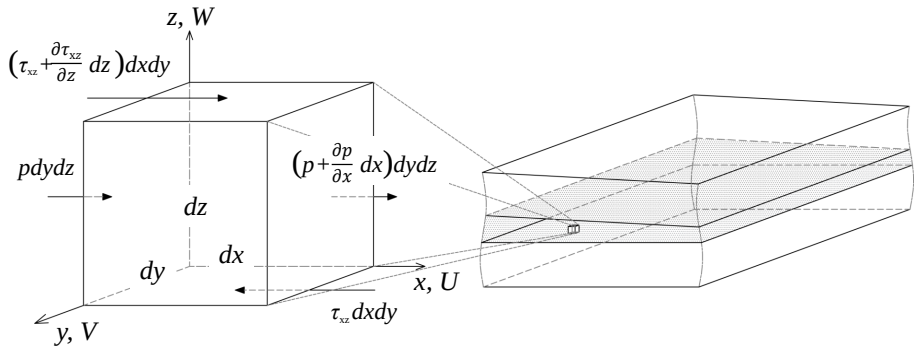

Figure 2.2: Equilibrium of an element of fluid and pressure and stress acting in x direction only.

In the same way for the equilibrium in y direction as:

$$\frac{\partial \tau_{yz}}{\partial z} = \frac{\partial p}{\partial y}. \tag{2.3}$$

As the pressure is constant across the film by the assumption II so:

$$\frac{\partial p}{\partial z} = 0. \tag{2.4}$$

Remembering that the shear stress can be expressed with shear rate and dynamic viscosity η as:

$$\tau_{xz} = \eta \frac{\partial u}{\partial z}, \tag{2.5}$$

$$\tau_{yz} = \eta \frac{\partial v}{\partial z}, \tag{2.6}$$

where u is the velocity in the x direction, v the velocity in the y direction. Substituting Equation (2.5) into Equation (2.2) the equilibrium equation in the x direction becomes:

$$\frac{\partial p}{\partial x} = \frac{\partial}{\partial z}\left(\eta \frac{\partial u}{\partial z}\right), \tag{2.7}$$

which can be simply integrated as the viscosity is constant through the film from the assumption VIII:

$$\frac{\partial p}{\partial x}\frac{z^2}{2} + C_1 z + C_2 = \eta u. \tag{2.8}$$

Since the boundary conditions can be given from the assumption III that no slips are present at the boundaries as:

$$u = U_2 \quad at \quad z = 0, \tag{2.9}$$

$$u = U_1 \quad at \quad z = h, \tag{2.10}$$

where U_1 and U_2 corresponds to velocities of the moving surfaces respectively, h the fluid height in z direction, the constants of Equation (2.8) C_1 and C_2 are:

$$C_1 = (U_1 - U_2)\frac{\eta}{h} - \frac{\partial p}{\partial x}\frac{h}{2}, \tag{2.11}$$

$$C_2 = \eta U_2. \tag{2.12}$$

With substituting these into Equation (2.8) and rearranging, the velocity u in x direction yields:

$$u = \left(\frac{z^2 - zh}{2\eta}\right)\frac{\partial p}{\partial x} + (U_1 - U_2)\frac{z}{h} + U_2. \tag{2.13}$$

The velocity in y direction is given in a similar manner as:

$$v = \left(\frac{z^2 - zh}{2\eta}\right)\frac{\partial p}{\partial y} + (V_1 - V_2)\frac{z}{h} + V_2. \tag{2.14}$$

2.1.2.2 Continuity of flow

Consider the continuity of flow under steady-state in a column with a height h, as shown in Figure 2.3, the mass of an element of fluid in-flowing into the column and out-flowing from the column must be equal considering mass conservation principle. It was assumed that the density is constant through the film (assumption VII), therefore the volume inflow and outflow rate must equal too as shown in the following equation:

$$q_{\mathrm{x}}dy + d_{\mathrm{y}}dx + w_0 dxdy = \left(q_{\mathrm{x}} + \frac{\partial q_{\mathrm{x}}}{\partial x}dx\right)dy + \left(q_{\mathrm{y}} + \frac{\partial q_{\mathrm{y}}}{\partial y}dy\right)dx + w_{\mathrm{h}}dxdy, \tag{2.15}$$

where q_{x} and q_{y} are the flow rates per unit width or length, w_0 and w_{h} are the velocities moving up in the z direction at the top and the bottom faces, respectively. With a simplification that $dxdy \neq 0$ (i.e. the area is not zero), the equation is presented by:

$$\frac{\partial q_{\mathrm{x}}}{\partial x} + \frac{\partial q_{\mathrm{y}}}{\partial y} + (w_{\mathrm{h}} - w_0) = 0. \tag{2.16}$$

The flow rates q_{x} and q_{y} can be expressed integrating the velocities u and v over the film thickness h as:

$$q_{\mathrm{x}} = \int_0^h u dz = -\frac{h^3}{12\eta}\frac{\partial p}{\partial x} + (U_1 + U_2)\frac{h}{2}, \tag{2.17}$$

$$q_{\mathrm{y}} = \int_0^h v dz = -\frac{h^3}{12\eta}\frac{\partial p}{\partial y} + (V_1 + V_2)\frac{h}{2}. \tag{2.18}$$

Substituting these flow rate equations into Equation (2.16) with assumptions that $U \neq f(x)$ and $V \neq f(y)$:

$$\frac{\partial}{\partial x}\left(\frac{h^3}{\eta}\frac{\partial p}{\partial x}\right) + \frac{\partial}{\partial y}\left(\frac{h^3}{\eta}\frac{\partial p}{\partial y}\right) = 6\left(U\frac{dh}{dx} + V\frac{dh}{dy}\right) + 12(w_{\mathrm{h}} - w_0), \tag{2.19}$$

which is the full Reynolds equation in three dimensions ($U \equiv U_1 + U_2$ and $V \equiv V_1 + V_2$).

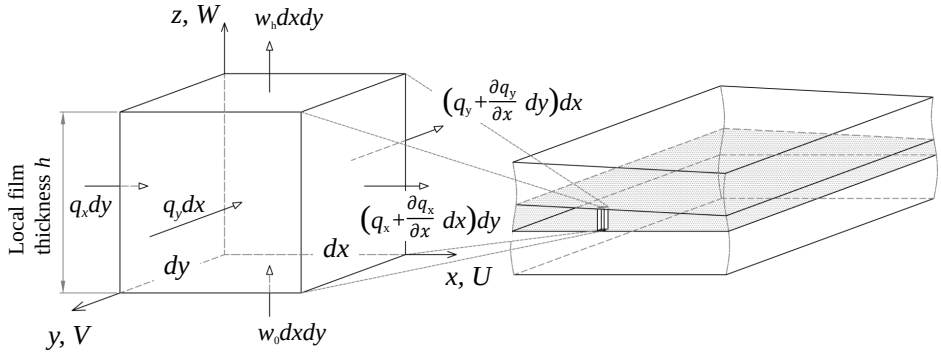

Figure 2.3: Continuity of flow in a column.

2.1.2.3 Approximations for practical engineering applications

The three-dimensional full Reynolds equation (Equation (2.19)) is complex in form and hard to solve directly. In order to use this equation for practical engineering applications, some approximations can be made for convenience in the suitable cases.

Unidirectional velocity approximation. Unidirectional velocity approximation is to consider that one of the surface velocities is neglected, for example in general use of journal bearing, the velocity in the axial direction is negligibly small compared to the velocity in the rotational direction, i.e. $V = 0$. With this approximation, the full Reynolds equation can be simplified down to:

$$\frac{\partial}{\partial x}\left(\frac{h^3}{\eta}\frac{\partial p}{\partial x}\right) + \frac{\partial}{\partial y}\left(\frac{h^3}{\eta}\frac{\partial p}{\partial y}\right) = 6U\frac{dh}{dx} + 12(w_h - w_0). \tag{2.20}$$

No vertical flow approximation. No vertical flow approximation is to consider that the vertical flow across the steady film thickness is not present i.e. $w_h - w_0 = 0$. This approximation is valid unless the surface roughness or bespoke surface texture on the shaft are of similar magnitude to the expected film thickness, or the shaft vibrates in the film thickness direction due to profile inaccuracy or shaft misalignment. With this approximation, Equation (2.20) can be further simplified to:

$$\frac{\partial}{\partial x}\left(\frac{h^3}{\eta}\frac{\partial p}{\partial x}\right) + \frac{\partial}{\partial y}\left(\frac{h^3}{\eta}\frac{\partial p}{\partial y}\right) = 6U\frac{dh}{dx}. \tag{2.21}$$

Iso-viscous approximation. Iso-viscous approximation is to consider that the fluid viscosity is constant throughout the film neglecting the temperature variation i.e. $\eta =$ constant. This approximation allows to rearrange the equation (2.21) as:

$$\frac{\partial}{\partial x}\left(h^3\frac{\partial p}{\partial x}\right)+\frac{\partial}{\partial y}\left(h^3\frac{\partial p}{\partial y}\right)=6U\eta\frac{dh}{dx}, \tag{2.22}$$

which is the Reynolds equation form commonly quoted in the literature. It cannot be directly integrated, further approximations are needed. Two approximations based on the bearing geometry will be discussed in the following sections.

Infinitely long bearing approximation. The first geometrical approximation is so-called infinitely long bearing or simply long bearing approximation. Assuming that width of the bearing i.e. the length along the y axis is infinitely long, in which case it can be approximated that the pressure gradient in the y direction is negligibly small compared to the pressure gradient in the x direction. This approach to reduce the two-dimensional equation down to one-dimensional form was first solved by Reynolds in 1884 and Sommerfeld in 1904. By neglecting the term containing $\partial p/\partial y$, Equation (2.22) can be arranged as follows:

$$\frac{\partial}{\partial x}\left(h^3\frac{\partial p}{\partial x}\right)=6U\eta\frac{dh}{dx}, \tag{2.23}$$

integrating in x gives:

$$h^3\frac{dp}{dx}=6U\eta h+C. \tag{2.24}$$

In order to get the constant C in this equation, a boundary condition is necessary. It can be assumed that the pressure becomes a maximum value at a point in the x direction, where the pressure gradient in the x direction is zero, i.e. $dp/dx=0$ at a film thickness, h'. This boundary condition can be summarised as:

$$\frac{dp}{dx}=0 \quad \text{at} \quad h=h', \tag{2.25}$$

substituting this into Equation (2.24) and rearranging yields:

$$\frac{dp}{dx} = 6U\eta\frac{h-h'}{h^3}, \tag{2.26}$$

integrating this equation then the pressure can be expressed as:

$$p = 6U\eta\left(\int_0^x \frac{1}{h^2}dx - h'\int_0^x \frac{1}{h^3}dx + C\right). \tag{2.27}$$

Short (narrow) bearing approximation. The second geometrical approximation is the so-called short or narrow bearing approximation. Assuming that the length along the y axis, L, is sufficiently shorter than the length in the x direction, B, the pressure gradient along the x direction could be seen to be very much smaller than that along the y direction, namely $\partial p/\partial x \ll \partial p/\partial y$. This approach was first proposed by Michell (1929) and extensively developed by Dubois and Ocvirk (1953). With this approximation, the two-dimensional form of Reynolds equation (Equation (2.22)) can be simplified down neglecting the term with $\partial p/\partial x$ as:

$$\frac{\partial}{\partial y}\left(h^3\frac{\partial p}{\partial y}\right) = 6U\eta\frac{dh}{dx}. \tag{2.28}$$

As the film thickness is not function of y, the equation can be easily integrated as:

$$p = \frac{6U\eta}{h^3}\frac{dh}{dx}\frac{y^2}{2} + C_1 y + C_2, \tag{2.29}$$

where C_1 and C_2 are integration constants. This equation can be rearranged with boundary conditions that $p = 0$ at $y = \pm L/2$ and $dp/dy = 0$ at $y = 0$ as:

$$p = \frac{3U\eta}{h^3}\frac{dh}{dx}\left(y^2 - \frac{L^2}{4}\right). \tag{2.30}$$

The applicability of the infinitely long bearing approximation has been usually accepted that $L/B > 3$, and that of the short-bearing approximation when $L/B < 1/3$ (Stachowiak and Batchelor, 2005). In between the ratios (i.e. $1/3 < L/B < 3$) another approach should be applied to solve the equation.

2.1.2.4 Short-bearing approximation in journal bearing

In practical analysis of the hydrodynamic lubrication with the simplified Reynolds equation in a journal bearing, the bearing geometry should be defined before substituting them into the Reynolds equation. Figure 2.4 shows a schematic of load and film thickness in the journal bearing. Since the ratio of width L and nominal diameter D, that is, $L/D = 25/98$ in the journal bearing used in the present study, the short-bearing approximation can be used in good accuracy as $L/D < 1/3$ (Stachowiak and Batchelor, 2005). The coordinate x, y, and z is set for the journal bearing as shown in Figure 2.4. The x coordinate is the tangential direction of the journal bearing, the y coordinate is the axial direction of the journal bearing, and the z coordinate is the radial direction of the journal bearing, respectively.

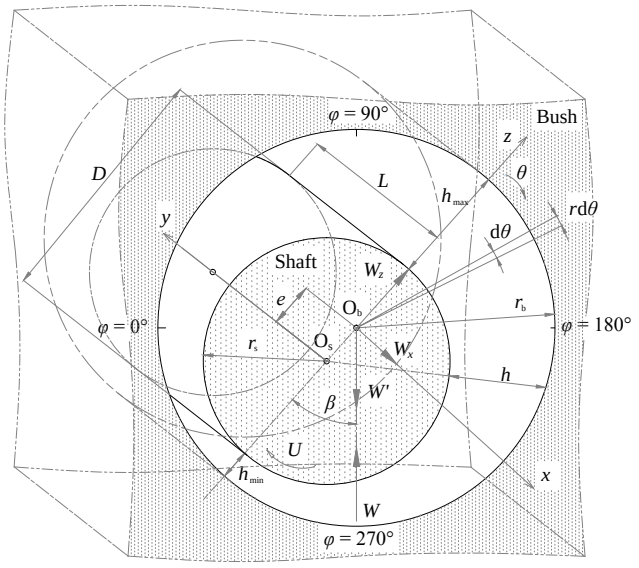

Figure 2.4: Schematic of load and film thickness on the journal bearing.

As summarised in Figure 2.4, the film thickness is geometrically described that:

$$h = c_{\mathrm{r}}(1 + \varepsilon\cos\theta), \tag{2.31}$$

where θ is the angle from the maximum film thickness (where $x = r\theta$), c_{r} the clearance of the journal bearing in radii (i.e. $r_{\mathrm{b}} - r_{\mathrm{s}}$), and ε the ratio of eccentricity to the clearance c_{r}, that is, expressed as e/c_{r}. It is assumed for the moderately or heavily loaded bearings that the pressure from $\theta = \pi$ to $\theta = 2\pi$ carries the negligibly small load (i.e. the Half-Sommerfeld condition).

Thus, the two load components, $W_{x,z}$ are deduced by double integrals of the pressure distribution in y and θ coordinates, and its resultant load, W', which support the applied load, W, are given.

$$W_x = \int_0^{\pi} \int_{-\frac{L}{2}}^{\frac{L}{2}} pr\sin\theta \mathrm{d}\theta \mathrm{d}y, \tag{2.32}$$

$$W_z = \int_0^{\pi} \int_{-\frac{L}{2}}^{\frac{L}{2}} pr\cos\theta \mathrm{d}\theta \mathrm{d}y, \tag{2.33}$$

$$W' = \sqrt{W_x^2 + W_z^2}, \tag{2.34}$$

$$W' + W = 0. \tag{2.35}$$

By arranging Equation (2.30) and (2.31) with the resultant load, a relation with ε and Sommerfeld number, Δ, which is a variable containing the conditions and journal bearing geometries, is obtained as:

$$\Delta\left(\frac{D}{L}\right)^2 = \frac{\pi\varepsilon}{(1-\varepsilon^2)^2}(0.62\varepsilon^2+1)^{0.5}, \tag{2.36}$$

$$\Delta \equiv \frac{W'}{LU\eta}\left(\frac{c_\mathrm{r}}{r}\right)^2, \tag{2.37}$$

$$S_\mathrm{r} \equiv \frac{1}{\Delta} \equiv \frac{LU\eta}{W'}\left(\frac{r}{c_\mathrm{r}}\right)^2, \tag{2.38}$$

where S_r is a reciprocal of Sommerfeld number. As presented in Equation (2.36), given the designed bearing geometries and the test conditions to be applied, the theoretical film thickness distribution can be deduced for each L/D ratios.

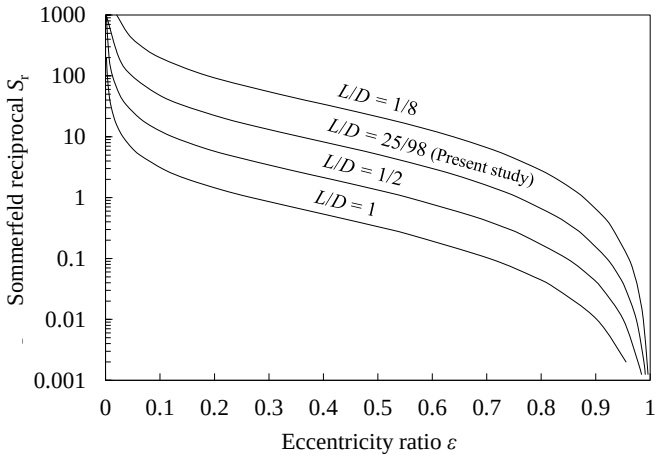

Figure 2.5: Eccentricity ratio ε and Sommerfeld reciprocal S_r with various L/D with the short-bearing approximation.

Figure 2.5 presents the curves deduced with the short-bearing approximation in eccentricity ratio over Sommerfeld reciprocal S_{r} with various ratios including the ratio $L/D = 25/98$ used in the present study. The angle between the line of centres and the applied load line known as attitude angle, β, is expressed as follows:

$$\tan\beta = -\frac{W_x}{W_z} = \frac{\pi}{4}\frac{(1-\varepsilon^2)^{0.5}}{\varepsilon}. \tag{2.39}$$

2.2 Ultrasound Reflectometry

In this section, the background of ultrasound and film thickness measurement using ultrasound are presented. The basic principles of ultrasound and acoustic properties are firstly presented, then the theory to deduce thickness of embedded thin layer by ultrasonic reflection.

2.2.1 Introduction

In nature several mammals such as bats, moles, whales and dolphins are ultrasound users for their communication and navigation etc (Figure 2.6). Techniques using ultrasound has contributed greatly in very wide range of industrial applications not only due to its non-invasive nature but as a versatile, mobile, reliable, cost effective and instantaneous means. In medicine, marine, material, optics, physics as well as mechanical fields the techniques have been successfully implemented. These techniques can be seen often in our daily life such as; optical lenses cleaning, fetal medical scanning or sound navigation ranging for marine applications.

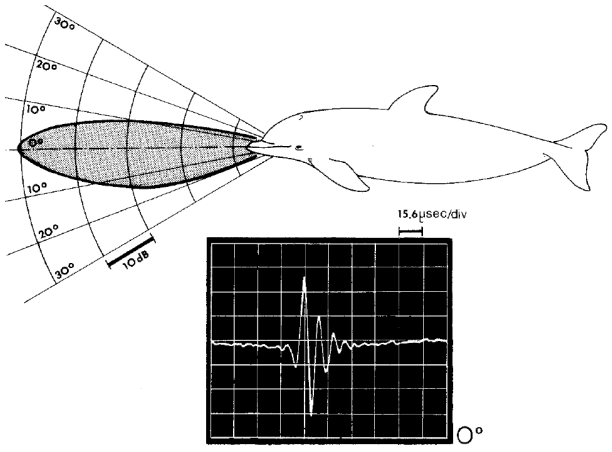

Figure 2.6: A directivity diagram of the sonar fields of the bottle-nosed dolphin (Tursiops truncatus) with a dominant frequency of 100 kHz (Pilleri, 1983).

In mechanical/tribological engineering context, flaw/defect detection (Lowe et al., 1998; Tattersall, 1973), wear measurement (Birring and Kwun, 1989; Lee et al., 2011), contact pressure mapping (Marshall et al., 2006a,b), lubricant film failure (Zhang et al., 2006), load monitoring (Chen et al., 2015), viscosity measurement (Kasolang and Dwyer-Joyce, 2008b; Schirru and Dwyer-Joyce, 2015) as well as film thickness measurement (Drinkwater et al., 2009; Dwyer-Joyce et al., 2003, 2004; Kasolang and Dwyer-Joyce, 2008a; Mills et al., 2012, 2015; Reddyhoff et al., 2005; Tsukahara et al., 1989) have been studied and implemented.

2.2.2 Basic principles of ultrasound

2.2.2.1 Ultrasonic sound waves

Ultrasound is a wave that propagates through a host medium at frequencies beyond the range audible to human i.e. above 20 kHz (although others suggest values above 18 kHz (Blitz, 1971)). Figure 2.7 represents an elastic body model with particles connected with a series of elastic springs, through which the sound wave propagates. The particles in a host medium are vibrated by elastic forces when stresses are caused by an oscillatory external forces.

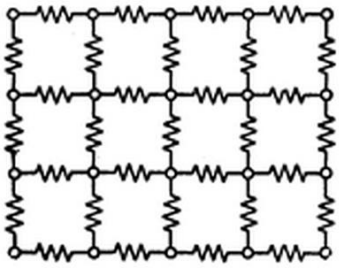

Figure 2.7: Model of an elastic body with particles connected with a series of springs (Krautkrämer and Krautkrämer, 1969).

A longitudinal wave (also known as pressure/compression wave), as used in this study, vibrates in a host medium along the direction of wave motion (Figure 2.8), while a transverse wave propagates through a medium at right angles to the direction of the motion of sound. The relation between the speed of sound c, frequency of the wave f and wavelength λ can be defined as follows:

$$c = f\lambda. \tag{2.40}$$

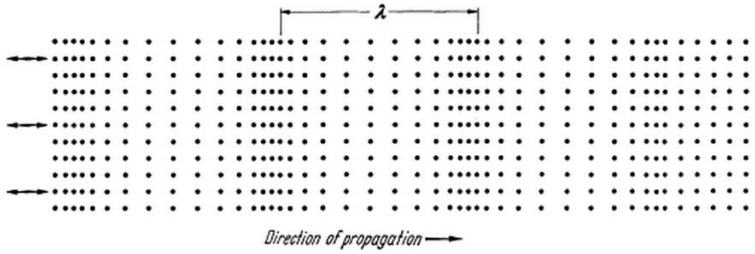

Figure 2.8: Schematic of a longitudinal sound wave (Krautkrämer and Krautkrämer, 1969).

2.2.2.2 Speed of sound

Speed of sound is the speed at which a wave travels through a medium. The speed varies with the medium through which the wave propagates and is dependent on the elastic modulus i.e. the Young's modulus E for a solid and the bulk modulus B for a liquid body. In a solid with assumptions that the solid is homogeneous and isotropic, the bulk longitudinal speed of sound (longitudinal velocity) is expressed as (Krautkrämer and Krautkrämer, 1969):

$$c = \sqrt{\frac{E}{\rho}\left(\frac{1-\nu}{(1+\nu)(1-2\nu)}\right)}, \tag{2.41}$$

where E is the Young's modulus, ρ the density, and ν the Poisson's ratio. Similarly in a liquid:

$$c = \sqrt{\frac{B}{\rho}}, \tag{2.42}$$

where B is the bulk modulus and ρ the density. The longitudinal velocity in several engineering materials are summarised in Table 2.1.

2.2.2.3 Acoustic impedance

Acoustic impedance, typically denoted as Z, is a acoustic resistance to the passage of sound wave in a host medium. The acoustic impedance is a product of the density, ρ and the sound velocity, c, as:

$$Z = \rho c. \tag{2.43}$$

The proportion of reflection and transmission of the sound wave is related to the acoustic impedance mismatch between the materials in a boundary. When the sound wave strikes a bound-

ary with the higher acoustic mismatch, the higher proportion of the sound wave is reflected back, and vice versa. The proportion of the incident wave reflected back on a boundary between medium 1 and medium 2 is given by the equation as:

$$R = \frac{Z_1 - Z_2}{Z_1 + Z_2}, \tag{2.44}$$

where the subscripts refer to the media. The acoustic impedance in several engineering materials are summarised in Table 2.1. Generally the acoustic impedances of liquid are one-order lower than those of metal.

Table 2.1: Summary of acoustic properties (Olympus Corporation, 2006).

Materials	Longitudinal velocity m/s	Acoustic impedance kg/(m^{2}s) $\times 10^6$
Water (20 °C)	1480	1.48
Motor oil (SAE 20 or 30)	1740	1.51
Acrylic resin	2730	3.22
Aluminum	6320	17.06
Copper	4660	41.61
Iron	5900	45.43
Lead	2160	24.49
Steel, 4340	5850	45.63
Titanium, Ti 150A	6100	27.69

2.2.2.4 Attenuation

Attenuation of the sound wave propagating through a medium occurs mainly due to two factors, absorption and scattering. When the wave travels through a medium, the wave vibrates the constituent particles and is subject to resistive frictional forces. In order to overcome these frictional forces, some of the wave energy is converted to heat. This principle of the wave energy reduction is typically called absorption. Another principle which weakens the wave energy is scattering. The wave scattering is caused by inhomegeneities, such as inclusions, flaws, or voids, in the host medium. These inhomegeneities create boundaries between the bulk materials. When the wave encounters such boundaries in the materials, the wave is partially reflected as well as being refracted. The absorption is reduced by emitting higher pressure wave, whereas it is not case in the scattering issue. However, such scattering could be an issue in limited applications as the quality of engineering materials in terms of the inhomegeneities have been improved.

2.2.3 Principle to determine film thickness by ultrasonic wave reflection

There exist ultrasound reflection techniques to determine the lubricant film thickness depending on the film thickness range to be measured. Figure 2.9 shows an ultrasonic wave propagating through in a lubricated area on a journal bearing, which is a three-layer system consisting of Medium 1 (shaft) - Medium 2 (oil) - Medium 3 (bush). As the sections and their curvature of the medium 1 (bush) and 3 (shaft) on the journal bearing used in this study are large, they can be modelled as a parallel layer seperating two half-space medium. If the thickness of the embedded layer is sufficiently thick when compared to the wavelength, the reflections R_1 and R_2 are discrete in time domain. By measuring the time of flight of the reflections R_1 and R_2, the layer thickness can be determined if the speed of sound through the layer is known. Typically, the measurable range of this technique is limited in the thickness greater than 50 μm since it is hard to distinguish discrete reflections in a very thin layer (Dwyer-Joyce et al., 2003).

There are two alternatives to determine the thickness of the embedded layer using the responses of the sound wave from the three-layered system. Firstly, if the wavelength and the film thickness are similar, the wave interaction with the layer is controlled by its resonant behaviour. Secondly, if the wavelength is much greater than the layer thickness, then the response is governed by the layer stiffness. The detail will be presented in the following section.

2.2.3.1 Reflection coefficient from an embedded layer

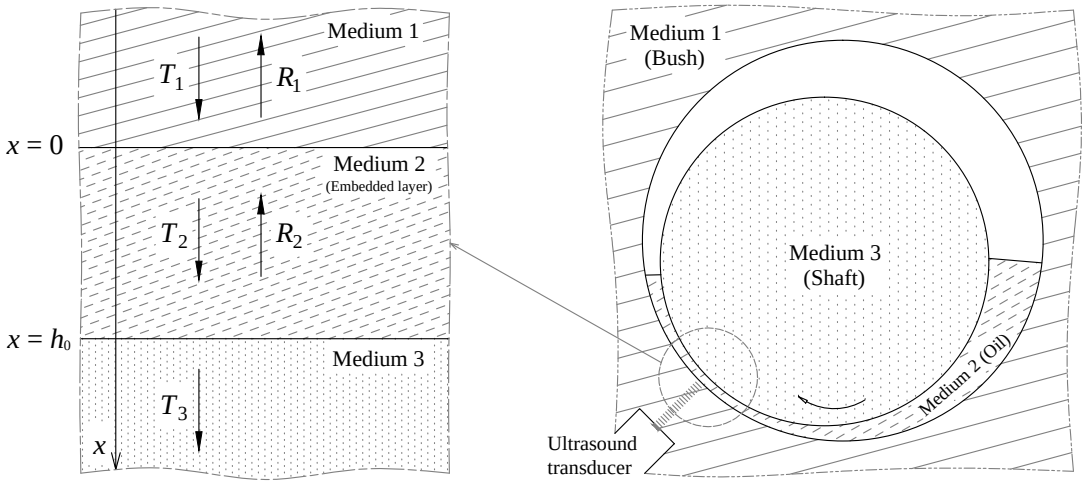

Figure 2.9: Schematic of an ultrasonic wave propagating through a three-layer system (medium 1, 2 (embedded layer with thickness of h_0), and 3) and its coordinate in a journal bearing.

The behaviour of a longitudinal plane wave propagating through an embedded layer (of thickness h_0) separating two half-space medium in the direction perpendicular to the layer (shaft-oil-bush on a journal bearing) was analytically studied by Krautkrämer and Krautkrämer (1969) in a condition where the displacement and the stress are continuous at the boundaries. This is known as continuum model.

The displacement field may be described by the sum of the two waves i.e. a transmitted wave and a reflected wave in each medium as waves of amplitudes T_1 and R_1 in medium 1, waves of amplitudes T_2 and R_2 in medium 2, and only a transmitted wave of amplitude T_3 in medium 3, respectively. A longitudinal plane wave travelling along the x coordinate can be presented with a simplification that the wave propagates without attenuation as:

$$u(x,t) = A\mathrm{e}^{\mathrm{i}\omega(t-x/c)}, \tag{2.45}$$

where u is the displacement field in the x direction, A the amplitude, ω the angular frequency, c the phase velocity of the wave. Omitting the term $\mathrm{e}^{\mathrm{i}\omega t}$ from Equation (2.45) for simplicity, the displacement field in each medium can be expressed by:

$$u_1(x) = T_1\mathrm{e}^{-\mathrm{i}\omega x/c_1} + R_1\mathrm{e}^{\mathrm{i}\omega x/c_1}, \tag{2.46}$$

$$u_2(x) = T_2\mathrm{e}^{-\mathrm{i}\omega x/c_2} + R_2\mathrm{e}^{\mathrm{i}\omega x/c_2}, \tag{2.47}$$

$$u_3(x) = T_1\mathrm{e}^{-\mathrm{i}\omega x/c_3}. \tag{2.48}$$

Then the stress fields can be expressed, differentiating the displacements with respect to x, that is:

$$\sigma_1(x) = -\mathrm{i}\omega Z_1(T_1\mathrm{e}^{-\mathrm{i}\omega x/c_1} - R_1\mathrm{e}^{\mathrm{i}\omega x/c_1}), \tag{2.49}$$

$$\sigma_2(x) = -\mathrm{i}\omega Z_2(T_2\mathrm{e}^{-\mathrm{i}\omega x/c_2} - R_2\mathrm{e}^{\mathrm{i}\omega x/c_2}), \tag{2.50}$$

$$\sigma_3(x) = -\mathrm{i}\omega Z_3 T_3\mathrm{e}^{-\mathrm{i}\omega x/c_3}, \tag{2.51}$$

where Z is the acoustic impedance of the medium (a product of density, ρ, and phase velocity, c, i.e. $Z = \rho c$). With the aforementioned boundary condition where the displacement and stress

fields are ideally continuous in space, the following relationships are given at the boundaries of the embedded layer as:

$$u_1(0) = u_2(0), \tag{2.52}$$

$$u_2(h_0) = u_3(h_0), \tag{2.53}$$

$$\sigma_1(0) = \sigma_2(0), \tag{2.54}$$

$$\sigma_2(h_0) = \sigma_3(h_0). \tag{2.55}$$

By combining these equations and setting the amplitude T_1 of the incident wave to unity, the exact analytical solution for the reflection coefficient (R_1 or simply R) is obtained for a three-layered system, that is:

$$R = \frac{e^{-i\omega h_0/c_2}(Z_1+Z_2)(Z_2-Z_3) - e^{i\omega h_0/c_2}(Z_2-Z_1)(Z_2+Z_3)}{e^{-i\omega h_0/c_2}(Z_2-Z_1)(Z_3-Z_2) + e^{i\omega h_0/c_2}(Z_2+Z_1)(Z_2+Z_3)}. \tag{2.56}$$

Figure 2.10 shows an amplitude curve of normal incidence longitudinal reflection coefficient from a steel/35 μm thick oil/steel system. The curve of $|R|$ was obtained by solving Equation (2.56) with the acoustic properties used in this study. The resonant and stiffness-governed region were presented in the figure, which will be discussed in detail in the next sections.

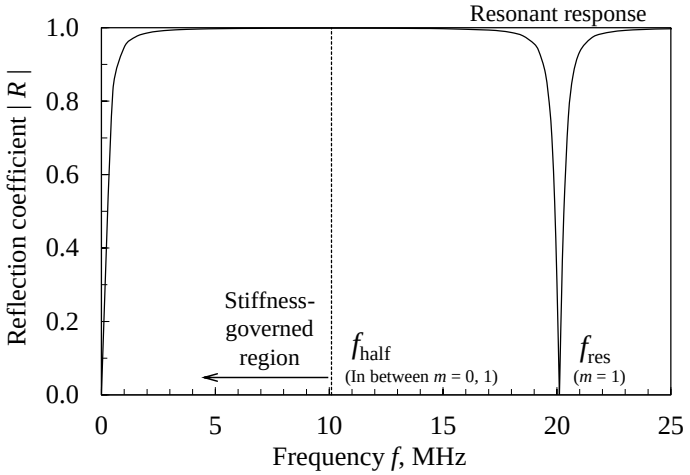

Figure 2.10: Amplitude curve of normal incidence longitudinal reflection coefficient from a steel/35 μm thick oil/steel system.

Resonant response. As described earlier if the wavelength and the layer thickness are similar, the wave interaction with the three-layered system is controlled by its resonant behaviour. When the incident wave drives the system at the resonance frequency of the layer, the reflection coefficient R_{res} at its resonant frequency f_{res} is given (Pialucha and Cawley, 1994):

$$R_{\text{res}} = \frac{Z_1 - Z_3}{Z_1 + Z_3}. \tag{2.57}$$

As can be seen in the equation, the reflection coefficient at the resonant frequency is only determined by the acoustic impedances of the medium 1 and 3, being independent from the properties of the embedded later. The reflection coefficient at the frequencies halfway between the resonant frequency i.e. at $f = f_{\text{half}}$, can be expressed as:

$$R_{\text{half}} = \frac{Z_1 Z_3 - Z_2^2}{Z_1 Z_3 + Z_2^2}. \tag{2.58}$$

The resonant frequency f_{res} of the mth mode can be expressed in terms of the layer thickness h_0 and the phase velocity through the layer c_2 as:

$$f_{\text{res}} = \frac{c_2 m}{2h_0}, \tag{2.59}$$

where m is the mode number of the resonant frequency. The frequency halfway between the mth and (m + 1)th resonance frequencies of the layer can be expressed as:

$$f_{\text{half}} = \frac{c_2}{2h_0}\left(m + \frac{1}{2}\right). \tag{2.60}$$

Figure 2.11 shows an example case on the amplitudes of the reflection coefficients from a water/oxide (100 μm thick) /water system and a water/oxide (100 μm thick) /epoxy system (Pialucha and Cawley, 1994). As can be seen in the figure, the coefficient reaches local minima at the resonance frequencies of the layer (0.0 MHz, 52.0 MHz, and 104.0 MHz) in both the system but at different magnitudes of the amplitudes. Both the curves reaches shallow maxima at the halfway between the resonance frequencies of the layer (26.0 MHz and 78.0 MHz). Table 2.2 summarises the resonance response in a steel/oil/steel system which was used in this study. The

acoustic properties used in this calculation are presented in Table 4.6 for the oil and Table 4.3 for the steel (bush and shaft). As can be seen in Table 2.2, the thinner layer thickness corresponds the higher resonant frequency.

Dwyer-Joyce et al. (2003) examined a liquid wedge experiment using two different wide-band transducers for a range of film thickness and the results are presented in Figure 2.12. As seen in Figure 2.12(b) mimima of the amplitudes are observed, then the film thicknesses can be readily determined by Equation (2.59). However, as the authors discussed, the measurable lowest film thickness is limited to above 10 μm by the frequency of the ultrasound transducers since the highest frequency available is practically below 40 MHz to 60 MHz due to signal attenuation through the bearing materials. Therefore, another approach is required to measure the range below 10 μm of film thickness, which will be presented in the following section.

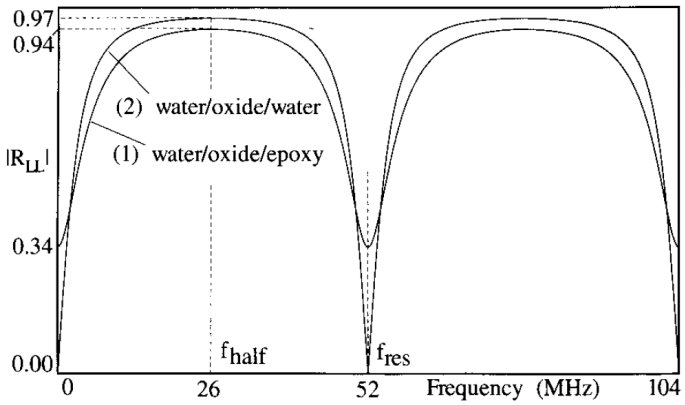

Figure 2.11: Amplitudes of normal incidence longitudinal reflection coefficients from a water/100 μm thick oxide/water system and a water/100 μm thick oxide/epoxy system (Pialucha and Cawley, 1994).

Table 2.2: Amplitudes of the reflection coefficient at f_{res} and f_{half} in a steel/oil/steel system with the layer thickness variation.

Layer thickness	Resonant frequency ($m = 1$)	Frequency halfway (between $m = 0$, 1)	Reflection coefficient	
h_0 μm	f_{res} MHz	f_{half} MHz	R_{res}	R_{half}
10	70.4	35.2	0	0.9986
20	35.2	17.6	0	0.9986
35	20.1	10.1	0	0.9986
100	7.0	3.5	0	0.9986
200	3.5	1.8	0	0.9986
1000	0.7	0.4	0	0.9986

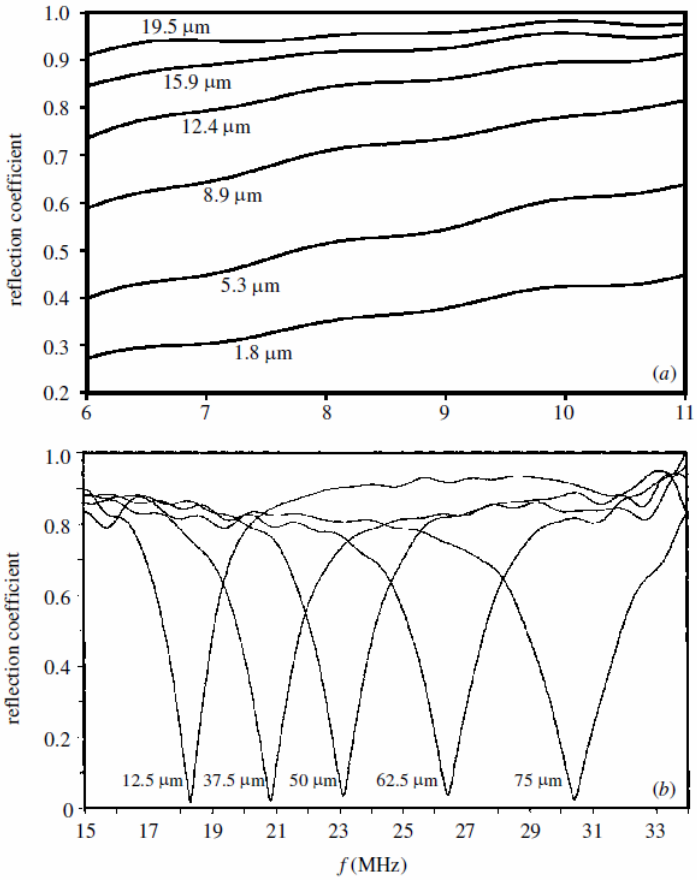

Figure 2.12: Measured reflection coefficient spectra for a range of film thicknesses using (a) a 10 MHz and (b) a 25 MHz centre-frequency transducer (Dwyer-Joyce et al., 2003).

Stiffness-governed response. The reflection responce at this region below the halfway of the fisrt resonance f_{half} is known as stiffness-governed region since the deflection of the mass purely depends on the applied load and the spring stiffness. The wave responses in the stiffness-governed region, which is also called spring model developed by Schoenberg (1980); Tattersall (1973), can be introduced by simplifying Equation (2.56) for convenience of use.

In typical tribological interfaces in engineering components, the acoustic impedance of the embedded layer (which is usually liquid) is generally lower than the surrounding media (which are usually metal) and the layer thickness is thinner than the wavelength of the longitudinal wave. Rewriting the exponential term as a Taylor expansion, Equation (2.56) can be rearranged as:

$$R = \frac{2Z_2(Z_1 - Z_3) + 2\gamma(Z_1Z_3 - {Z_2}^2) + \gamma^2 Z_2(Z_1 - Z_3) + \gamma^3(Z_1Z_3 - {Z_2}^2)/3 + \cdots}{2Z_2(Z_1 + Z_3) + 2\gamma(Z_1Z_3 + {Z_2}^2) + \gamma^2 Z_2(Z_1 + Z_3) + \gamma^3(Z_1Z_3 + {Z_2}^2)/3 + \cdots}, \tag{2.61}$$

where

$$\gamma = \frac{i\omega h_0}{c_2}. \tag{2.62}$$

Since $\omega h_0/c_2 \to 0$ in the aforementioned tribological interfaces, Equation (2.61) can be arranged neglecting γ^2 and above:

$$R = \frac{Z_2(Z_1 - Z_3) + \gamma(Z_1 Z_3 - {Z_2}^2)}{Z_2(Z_1 + Z_3) + \gamma(Z_1 Z_3 + {Z_2}^2)}, \tag{2.63}$$

and when the acoustic impedance of the layer is lower than the surrounding media (i.e. $Z_1 Z_3 \gg {Z_2}^2$), then Equation (2.63) becomes:

$$R = \frac{Z_1 - Z_3 + i\omega h_0 (Z_1 Z_3)/(Z_2 c_2)}{Z_1 + Z_3 + i\omega h_0 (Z_1 Z_3)/(Z_2 c_2)}. \tag{2.64}$$

At the tribological interfaces in hydrodynamic lubrication regime which this study focuses, the medium 1 and 3 is separated by an oil layer. The stiffness of the oil layer, κ, expressed per unit area, is given by the rate of pressure change, P, and the layer thickness change as:

$$\kappa = \frac{dP}{dh}. \tag{2.65}$$

The bulk modulus, B, of the oil can be described by change in volume, V, along the change in pressure as:

$$B = -\frac{dP}{dV/V}. \tag{2.66}$$

Since the thickness of the oil layer is generally much smaller than the area of which the sound wave interacts (i.e. $dV/V = dh/h$), Equation (2.66) can be written as:

$$B = -\frac{dP}{dh/h}. \tag{2.67}$$

The bulk modulus can be written with respect to its properties, density and speed of sound,

that is:

$$B = \rho c^2. \tag{2.68}$$

Combining Equation (2.65), (2.67), and (2.68) gives the stiffness of the layer in terms of its acoustic properties as follows:

$$\kappa = \frac{\rho c^2}{h}. \tag{2.69}$$

Arranging Equation (2.64) to (2.69) gives:

$$R = \frac{Z_1 - Z_3 + \mathrm{i}\omega(Z_1 Z_3/\kappa)}{Z_1 + Z_3 + \mathrm{i}\omega(Z_1 Z_3/\kappa)}, \tag{2.70}$$

which shows that the wave reflection with interaction of the wave and the very thin oil layer in tribological interface is governed by the spring stiffness of the layer. In order to deduce the film thickness using Equation (2.70), two independent methods, i.e. magnitude and phase shift method has been examined by Reddyhoff et al. (2005). With a rearrangement for the real and imaginary component, Equation (2.70) becomes:

$$R = \frac{{Z_1}^2 - {Z_3}^2 + {Z_1}^2{Z_3}^2(\omega/\kappa)^2}{(Z_1 + Z_3)^2 + {Z_1}^2{Z_3}^2(\omega/\kappa)^2} + \mathrm{i}\left[\frac{2Z_1{Z_3}^2(\omega/\kappa)}{(Z_1 + Z_3)^2 + {Z_1}^2{Z_3}^2(\omega/\kappa)^2}\right]. \tag{2.71}$$

Since the reflection coefficient R is arranged in a polar form, R is given by:

$$R = \mid R \mid \cos\Phi_{\mathrm{R}} + \mathrm{i} \mid R \mid \sin\Phi_{\mathrm{R}}, \tag{2.72}$$

where $\mid R \mid$ is the magnitude and Φ_{R} the phase of the reflection coefficient. The $\mid R \mid$ and Φ_{R} of Equation (2.70) are respectively given as:

$$\mid R \mid = \sqrt{\frac{(\omega Z_1 Z_3)^2 + \kappa^2(Z_1 - Z_3)^2}{(\omega Z_1 Z_3)^2 + \kappa^2(Z_1 + Z_3)^2}}, \tag{2.73}$$

$$\Phi_{\mathrm{R}} = \arctan\left[\frac{2\omega Z_1{Z_3}^2/\kappa}{(Z_1 - Z_3) + \omega^2(Z_1 Z_3/\kappa)^2}\right]. \tag{2.74}$$

A graphical representation of those equations in the complex plane is shown with three variations of Z_1 and Z_3 (same material and dissimilar materials) in Figure 2.13.

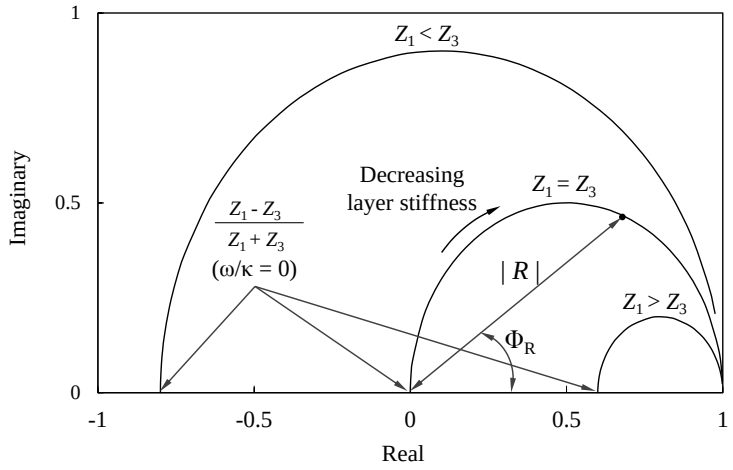

Figure 2.13: Graphical representation of reflection coefficient R in complex plane: calculated at 5 MHz in f and from 1 nm to 100 μm in the layer thickness.

Since the $\mid R \mid$ and Φ_R are experimentally measured (the detail will be presented in Chapter 4), the film thickness (h_0 or simply h) can be deduced as:

$$h = \frac{\rho_2 {c_2}^2}{\omega Z_1 Z_3} \sqrt{\frac{\mid R \mid^2 (Z_1+Z_3)^2 - (Z_1-Z_3)^2}{1 - \mid R \mid^2}}, \tag{2.75}$$

$$h = \frac{\rho_2 {c_2}^2 \tan\Phi_R ({Z_1}^2 - {Z_3}^2)}{\omega Z_1 {Z_3}^2 \pm \sqrt{(\omega Z_1 {Z_3}^2)^2 - \tan^2\Phi_R ({Z_1}^2 - {Z_3}^2)(\omega Z_1 Z_3)^2}}. \tag{2.76}$$

If the acoustic impedances Z_1 and Z_3 are equal, and Equation (2.75) is equated to Equation (2.76), a simple relation is obtained:

$$\mid R \mid = \cos\Phi_R. \tag{2.77}$$

In this study, the magnitude approach was exclusively used as Reddyhoff et al. (2005) proved that both the methods were equally accurate and favourably agree with theoretical value (Figure 2.14). The authors found that both the methods were equally temperature sensitive, by which an apparent rise/fall in the film thickness occurred. This temperature influence over the measurement will be discussed in Chapter 4. Equation (2.75) is further arranged as $Z_1 = Z_3$ (i.e. acoustic

impedance of the shaft and the bush) in this study, that is:

$$h = \frac{2\rho_2 c_2^2}{\omega Z_s} \sqrt{\frac{|R|^2}{1-|R|^2}}, \tag{2.78}$$

where Z_s is the acoustic impedance of the journal bearing steel (both the shaft and the bush, that is, $Z_s = Z_1 = Z_3$).

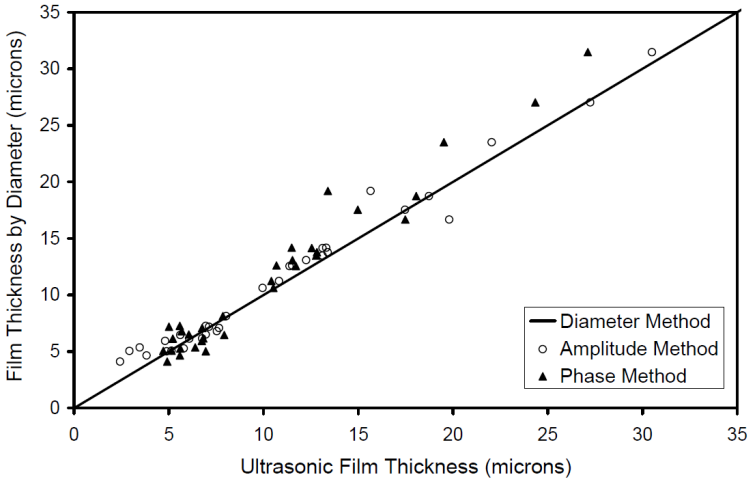

Figure 2.14: Comparison of amplitude and phase methods of film thickness measurement with thickness determined optically from the diameter of the spread oil spot (Reddyhoff et al., 2005).

2.2.3.2 Measurable range of layer thickness

The principles of the three methods, i.e. time of flight, resonance and spring model, to measure the layer thickness in a three-layered system have been described in the previous section. The measurable ranges of the methods are restricted by several factors, and the limits of the operations are summarised by Dwyer-Joyce et al. (2003), as shown in Figure 2.15.

- For the time of flight method, the layer thickness should be sufficiently thick so that the reflected pluses can be discrete in time domain, and the layer thickness must be greater than the ultrasound wavelength. This method is also limited by the attenuating losses when the wave travels through the materials. In case of engineering steels, below 40 to 60 MHz of the sound frequencies are only feasible for this method, resulting in 40 μm as its lower limit of measurement.

- For the resonance method, the lower limit of the measurement is determined by the wave

attenuations through the materials as well as the time of flight method. By pulsing waves 40 to 60 MHz frequencies, the lowest film thickness approximately 10 μm can be measured.

- For the spring model method, the upper limit is considered to be $R = 0.9$ from their measurement experiences as the curve plotted in Figure 2.15. In similar ultrasonic measurements, the authors found that less than $R = 0.95$ in a journal bearing (Dwyer-Joyce et al., 2004), $R = 0.98$ in a compression ring-cylinder interface (Mills et al., 2015) can give satisfactory accurate results. The lowest limit, that is, the smallest possible value of R is dependent on the signal-to-noise ratio. Although it will depend on the measurement situations, the author set a conservative estimation for the possible lowest limit as $R = 0.1$. As long as a steel/oil/steel system is separated by two smooth surfaces, 0.1 of the reflection coefficient would allow to measure a film thickness of 2 nm.

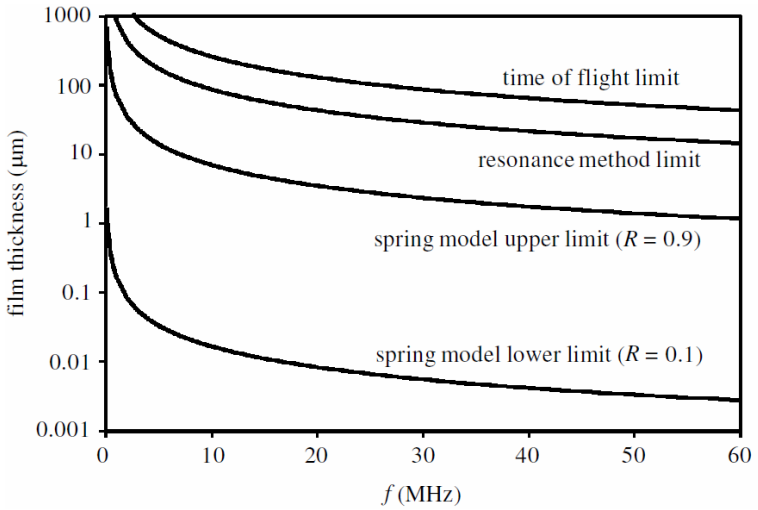

Figure 2.15: Limits of operation for film-thickness measurement by ultrasonic means (Dwyer-Joyce et al., 2003).

2.3 Conclusions

In this chapter the background to hydrodynamic lubrication and ultrasound reflectometry are presented. The following conclusions are drawn as follows.

In the section of hydrodynamic lubrication:

- A historical development and a basic of the hydrodynamic lubrication theory was presented. Reynolds equation was derived from the equilibrium of an element of fluid and the conti-

nuity of flow principle with eight assumptions.

- Further simplifications to Reynolds equation were made with several approximations for a practical use of the equation. The short-bearing approximation was found to be suitable to analyse the journal bearing of $L/D = 25/98$ focused on the present study.

In the section of ultrasound reflectometry:

- A basics of ultrasound regarding ultrasonic sound wave, speed of sound, acoustic impedance and attenuation was presented as well as a brief summary of the applications where techniques using ultrasound were implemented.

- The principle of ultrasound reflection to determine the embedded layer thickness on the three-layered system was presented. The measurable thickness range of the three measurement approaches, i.e. time of flight, resonant response and spring model, was discussed.

Through the literature review, it was found that the ultrasound reflection technique is practically very useful due to its non-invasive nature to measure lubricant film thickness for hydrodynamic journal bearings. In particular, the amplitude method of the spring model was found to be suitable for the film thickness range expected for the present study. Film thickness measurement using the spring model will be experimentally examined in Chapter 4 in a transmission plain journal bearing where all the assumptions and approximations of Reynolds equation mentioned in this chapter are satisfactorily valid. While some of the assumptions and approximations are not valid for textured bearings, which will be discussed in Chapter 5.

Chapter 3

Development of a Non-Resonant Vibration-Assisted Machining Device to Create Bespoke Surface Textures

In this chapter, the development of a non-resonant vibration-assisted machining device to create bespoke surface texture using an off-the-shelf piezoelectric actuator is presented. Firstly the conventional techniques to create such textures are summarised and their advantages and limitations are discussed as a literature review. The design and feasibility of the device is then discussed. Finally the machining test results implementing the developed device to a disc work piece in a conventional milling machine are presented.

3.1 Literature Review

In terms of tribological performance, the effect of bespoke surface texture has been recognised in many industrial applications (an example in automotive applications, fired-engine cylinder liner textured by honing), the detail of the literature regarding the effect of the bespoke surface texture will be given in Chapter 5. There are several techniques available to fabricate such surface textures and may be divided into three categories: (i) overlaying techniques, (ii) deforming techniques, and (iii) subtractive techniques. As a method of the subtractive techniques, literature works of vibration-assisted machining techniques are extensively summarised to define the research gap and to discuss the potential improvement of the system, which motivates the development of a

novel non-resonant vibration-assisted machining device presented in the next section.

3.1.1 Overlaying techniques

Overlaying techniques provide an additional layer on the substrate such as; chemical vapour deposition (Schade et al., 2006), physical vapour deposition (Lugscheider et al., 2003), electro deposition (Ruprecht et al., 1997), inkjet printing (Lejeune et al., 2009), or laser micro cladding methods (Otero et al., 2012). Of which techniques, the chemical vapour deposition (CVD) technique, which has been widely implemented in tribological applications, is briefly described in the following section.

3.1.1.1 Chemical vapour deposition

Chemical vapour deposition is a coating process which involves the chemical reactions of gaseous reactants generating a stable solid layer on the substrate surface. The formation of the layer occurs in an activated environment of heat, light or plasma. Figure 3.1 (left) shows an equipment for SiC coating.

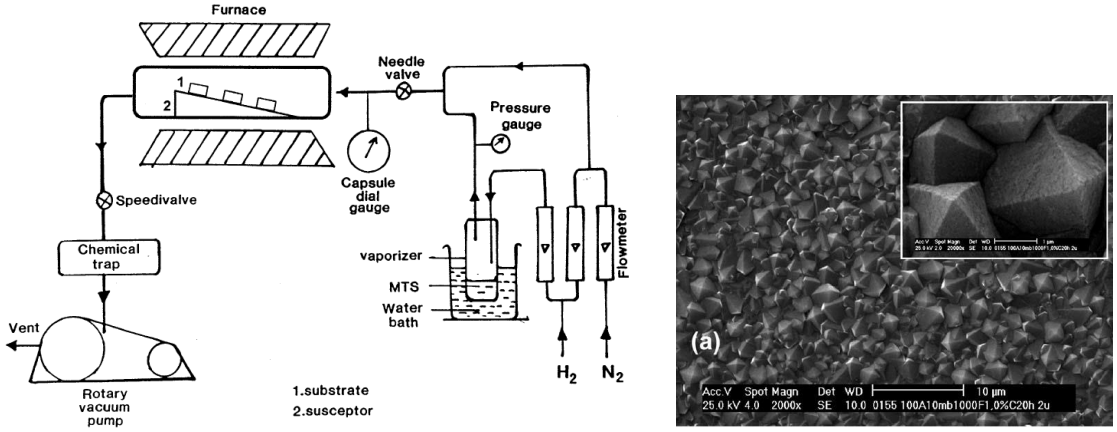

Figure 3.1: (Left) a schematic diagram of a typical laboratory CVD equipment for the deposition of SiC coatings (Choy, 2003) and (right) coated surface by chemical vapour deposition technique (Schade et al., 2006).

The diamond based coating by the CVD technique has been intensively investigated because of the good wear resistance. The Figure 3.1 (right) shows the formed CVD diamond layer on substrate surface. This deposition process took 20 to 30 hours to achieve the 4 to 10 μm in thickness of the layer. Distinctive texture with a series of pockets can be seen in the distance of a few μm between the crystal grains.

Advantage of the technique. The distinctive advantage of this process is that the crystal structure and the coat layer thickness can be easily controlled, and because the gaseous form acts on the heated substrate, the layer can be formed uniformly, as far as size of the reaction chamber is allowed, even on complex shaped components with wide range of chemical precursors. The controllable range of coat thickness is from nm to a few μm. Although the coated layer itself can have distinctive characterises in its texture, the range of texture geometry available can be further extended with suitable masking process.

Limitation of the technique. The main disadvantage of this technique is that the coating process is performed after the substrate profile is fixed, which requires additional manufacturing cost and even more expensive overall cost is inevitably needed when the aforementioned masking process is applied. Size of the work pieces is limited by the size of reaction chamber and generally the increased size of work piece requires more expensive reaction chamber. The bond strength of the coating and strength of coated layer itself to wear or imposed stress in operational condition are one of the concern, which could limit the possible coating.

3.1.2 Deforming techniques

Deforming techniques which create plastic deformations on the substrate such as; shot peening (Zhang and Lindemann, 2005) or fine particle bombardment methods (Yoshizaki, 2008). Yet little literature works have been examined exclusively focusing the tribological effect of the textures generated this deforming techniques, Yoshizaki (2008) pointed out that the generated microhollow by the fine particle bombardment method could have worked beneficially for improved tooth surface strength.

3.1.2.1 Shot peening

Shot peening is a process where the surface is impacted with round solid particles which are thrown at a high velocity by an eternal force such as compressed air or centrifugal force by impeller. The shot hammers the surface, which creates a series of small dents on the surface when plastic deformation occurs. This technique has been implemented into numerous engineering applications mainly aiming to improve the fatigue strength. The improvement of the fatigue can be contributed down to residual compressive stress on surface induced by the impact when the thrown pieces are hit. The researches have been carried out to improve the bending fatigue strength (Aida

and Oda, 1966), surface fatigue strength (Townsend, 1992) in gears. Rolling element bearings have also been investigated to improve their static and cyclic strength (Pfeiffer and Frey, 2006) as presented in Figure 3.2 (left).

Advantage of the technique. Since this technique has been widely used and matured in industrial applications, it is comparatively easy to choose an optimum apparatus from various options with competitive cost. The conditions of shot peening, e.g. velocity, material, size or hardness of particle, or exposed duration to the shot are controllable to obtain desired depth of the dimple to some extent. Generally the residual compressive stress induced by this technique works beneficially in tribological contact where tensile stress caused by the operation influences harmfully the substrate fatigue or static strength.

Limitation of the technique. As the shot particles are randomly hit on the substrate surface, the shape of the dimples randomly varies to some extent sample by sample. It was reported in a work with magnesium alloy samples that roughness increase and severe defects such as overlaps and micro cracks occurred in some conditions of the peening (Zhang and Lindemann, 2005) as presented in Figure 3.2 (right). It is a post-process technique, so that increased overall manufacturing time and cost is inevitable.

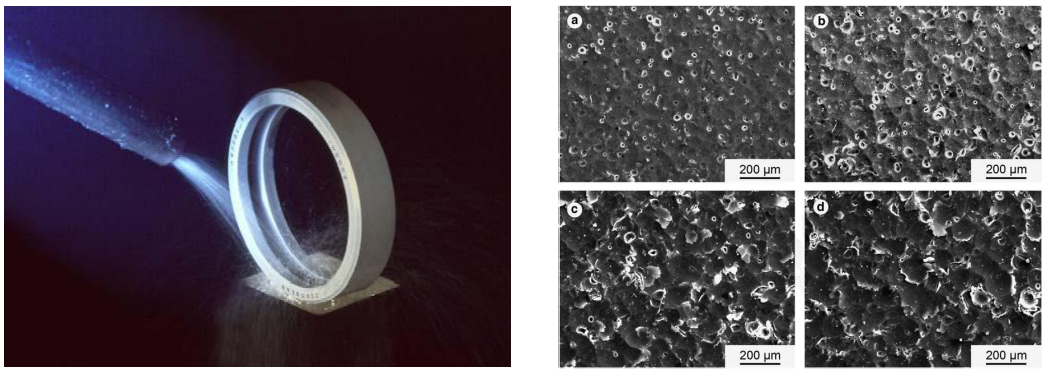

Figure 3.2: (Left) a bearing ring shot-peened (Pfeiffer and Frey, 2006) and (right) deformed surface by shot peening (Zhang and Lindemann, 2005).

3.1.3 Subtractive techniques

Subtractive techniques which form recesses or depressions removing out the material on the substrate such as; traditional machining (Malburg et al., 1993), photolithography and reactive ion

etching (Waits et al., 2005), electrical discharge (Ho and Newman, 2003), ion beam (Sprang et al., 1995), or laser based methods (Ryk et al., 2002). From these subtractive techniques, photolithography and reactive ion etching technique and laser based methods, as well as vibration-assisted machining technique, are summarised in the following sections.

3.1.3.1 Photolithography and reactive ion etching

Photolithography and reactive ion etching technique is a well established micro fabrication method in semiconductor industry and in principle a combination of two independent techniques to create the texture on surface; process of pattern transfer using a photosensitive material and process of a sort of dry etching, reactive ion etching (RIE). The pattern transfer can be achieved by inducing a physical property change to the photosensitive material by exposing the material selectively to a radiation source. In the next step, the unmasked area of substrate material is removed chemically and physically by sputtering ions which is generated by striking a plasma into a gas typically in a low-pressure chamber. An example of the procedure with cross sectional samples and a fabricated sample are shown in Figure 3.3. Advantages and disadvantage over this technique can be summarised as follows.

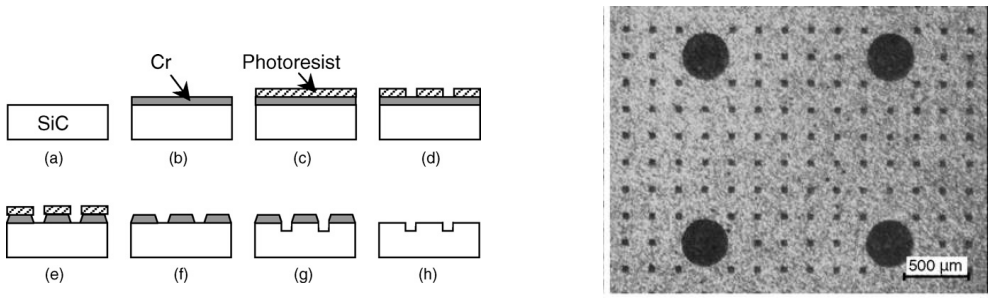

Figure 3.3: (Left) procedure of a photolithography and reactive ion etching process (Wang et al., 2006), and (right) generated dimples by the technique (Wang et al., 2006).

Advantage of the technique. The advantages includes that this technique is well developed in industry, which could provide competitive cost in terms of the equipment purchase. Various shapes of the texture on complex substrate profile are available to fabricate as far as the masking process can be implemented. Mechanical deformation, stress or burr is not generated by this process. Majority of engineering metals, such as steel, aluminium, copper, titanium, silver, gold including alloyed metals can be fabricated.

Limitation of the technique. While the disadvantages of this technique is that the procedure needs to be implemented after the finish-cut is performed. Such post-process is generally costly in industrial production process due to the overall manufacturing time. However a less time-consuming process, termed as maskless chemical etching method, has been investigated by Costa and Hutchings (2009), by which a single mask tool is applied for successive texturing of multiple work pieces (Figure 3.4). In their study, the method was implemented on carbon steel samples with process times ranging from 20 seconds to 120 seconds which is short enough in an industrial context.

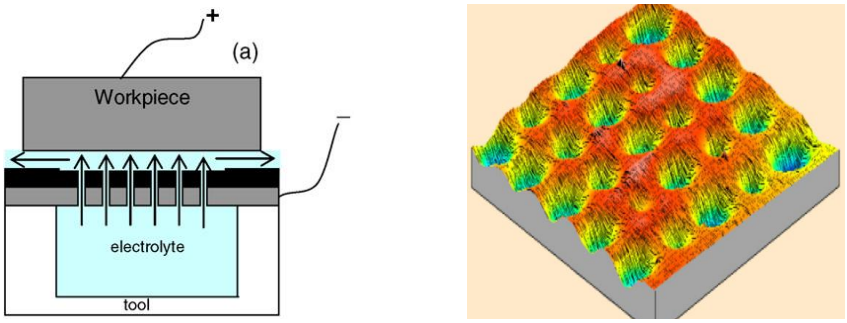

Figure 3.4: (Left) arrangement of work piece in the maskless chemical etching method (Costa and Hutchings, 2009), and (right) generated dimples by the method (Parreira et al., 2012).

3.1.3.2 Laser based methods

The laser has been of significant importance in variety of industrial fields. The highly concentrated energy form which imposes melting and vaporising to work piece material is used for welding, cutting, drilling process as well as micro modification on substrate surface. There exists various type of laser available such as excimer lasers, ion lasers, metallic vapour lasers, solid state lasers, semiconductor lasers, or molecular lasers, which is respectively chosen for requirements of the applications (Dahotre, 1998). A schematic of Nd:YAG laser beam cutting system and a dimpled sample generated by the technique is shown in Figure 3.5.

Advantage of the technique. The advantages of this technique could be summarised as following. This technique can be used on various types of industrial materials such as steel, titanium, nickel, cast iron, copper-based alloys, steel alloys, silicon nitride, silicon carbide or polymers (Coblas et al., 2015). The removal rate and area of the substrates can be flexibly changed by controlling the beam projection, power, wavelength and duration exposed to the substrate sur-

face. Various shapes of texture are available by using a patterned mask to selectively expose the substrate to the beam.

Limitation of the technique. The laser technique inherently imposes its energy to the textured area of the substrate, which mechanically and thermally affects the substrate material property in the textured area and its vicinity. Crack generation and hardness decrease around the created pores were identified on a study with SiC samples (Wang et al., 2001). Generation of bulges or burrs with a hight of a few μm in the edges of the dimples have been also reported (Amanov et al., 2013), because of which an additional process such as lapping or polishing to remove them should be treated after the texturing process. As it is a post-process technique, overall manufacturing time and cost is inevitably expensive. The cost can be even more expensive when the aforementioned patterned mask is used to create unique shape of the texture.

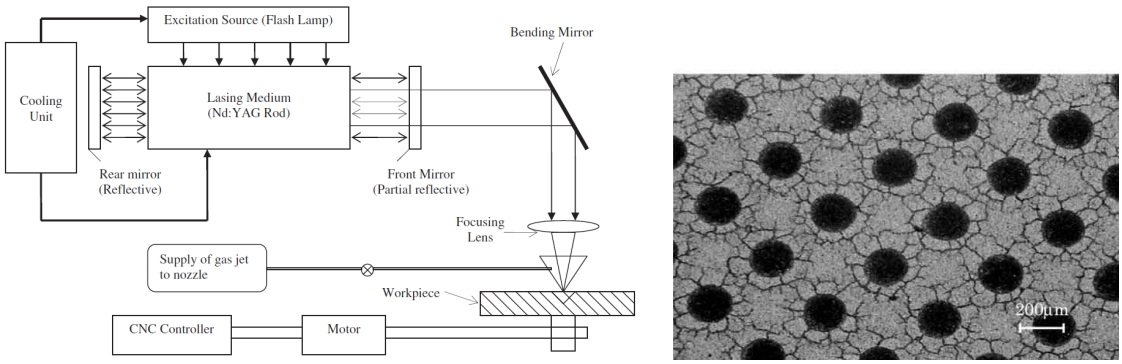

Figure 3.5: (Left) schematic of Nd:YAG laser beam cutting system (Dubey and Yadava, 2008), (right) generated dimples by laser texturing technique (Wang et al., 2001).

3.1.3.3 Vibration-assisted machining

All of the above techniques are finishing processes applied after the initial machining and therefore are only economically viable in limited applications. Vibration-assisted machining involves the superposition of controlled vibrations onto traditional machining processes such as turning or milling. These machining techniques can be categorised into two by the means of vibration generation (Brehl and Dow, 2008); (i) resonant technique where a sonotrode (also called horn or concentrator) vibrates at its natural frequency transferring and amplifying a given vibration from a vibration source (usually by magnetostrictive or piezoelectric transducer), or (ii) non-resonant technique where a piezoelectric material vibrates below its first natural frequency

driven by an amplified dynamic voltage.

Resonant technique. The resonant techniques have been implemented mainly for improved surface profile or roughness, burr suppression, cutting force reduction, or longer cutting tool life (Dambon et al., 2007; Jin and Murakawa, 2001; Moriwaki and Shamoto, 1991, 1995; Shamoto and Moriwaki, 1999). However, there exists a limitation in the resonant technique that the operating vibration parameters, frequency and displacement, are inherently fixed in a given design, by which the machining conditions available can be limited.

Non-resonant technique. Non-resonant techniques have been examined for the purposes as mentioned in the resonant technique (Negishi, 2003; Overcash and Cuttino, 2003) as well as for creating bespoke surface textures (Greco et al., 2009). The beneficial points of the non-resonant technique are the controllability of vibration parameters in a given design, and good displacement uniformity and resolution.

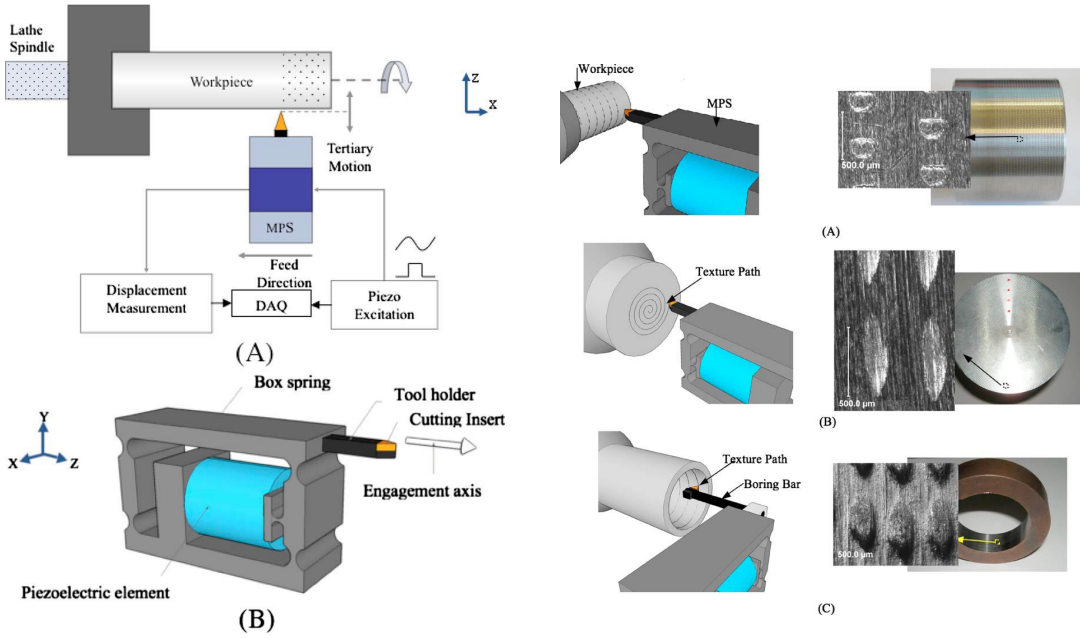

Figure 3.6: (Left) vibro-mechanical machining arrangement (Greco et al., 2009), and (right) the generated textures by the technique in various machining arrangements (Greco et al., 2009).

Greco et al. (2009) investigated the potential of a non-resonant vibration-assisted machining technique (termed Vibromechanical texturing) to create bespoke surfaces for tribological interfaces. A piezoelectric-actuated tool and positioning stage (developed by Hong and Ehmann

(1995)) were used to superpose controlled vibrations on to a cutting tool normal to the work piece surface as shown in Figure 3.6. The intermittent engagement of the cutter to the surface created dimples in aluminium and hardened steel work pieces; however, the errors between the desired profiles and the profiles generated were large, particularly in the hardened steel work piece. The authors concluded that the inaccuracy was attributed to elastic restoration of the material and deflection of the positioning stage, which are inherently present in the chosen arrangement. A further issue arose from burr generations in the diverging edge of the generated dimples, which required an additional removal process. It is presumed that the burrs were generated due to the intermittent engagement of the cutting tool.

3.1.4 Summary

The texturing works mentioned in the previous section is briefly summarised in Table 3.1 with 3-levels score rating (Good: 3, Average: 2, Poor: 1) in three main categories i.e. production cost, texture generation, and work piece limitation. There are pros and cons in the present texturing techniques; however, all of the texturing techniques presented above, except the vibration-assisted machining, are finishing processes applied after the initial machining and therefore could be only economically viable in limited applications. Non-resonant vibration-assisted machining technique seems to be a promising method in terms of manufacturing cost since the texture can be generated when the finish cut is performed with comparatively quick fabrication cycles. Although there are several beneficial points in this technique, it was found that there are a couple of issues to create bespoke surface textures accurately in the present vibration-assisted machining techniques, so that the corresponding score rating in Table 3.1 are low.

Table 3.1: Summary of the texturing techniques. Score rating Good: 3, Average: 2, Poor: 1.

Techniques	Production cost		Texture generation		Work piece limitation	
	Apparatus	Overall production time	Accuracy achievable	Controll-ability	Material	Size
Chemical vapour deposition	2	1	3	3	3	$1 \sim 2$
Shot peening	3	$1 \sim 2$	1	2	3	3
Photolithography and reactive ion etching	2	1	3	3	3	3
Laser based	1	$1 \sim 2$	3	3	2	3
Vibration-assisted machining	2	3	1	$1 \sim 2$	$2 \sim 3$	3

In the next section, a novel device design is proposed to superimpose controlled vibrations

on to a cutting tool normal to the work piece surface using an off-the-shelf piezoelectric actuator in order to minimise the aforementioned issues of elastic deflection and burr generation. The mechanical assembly is designed to achieve high axial mechanical stiffness so that elastic deflection as a consequence of the cutting process is limited. The constructed device is validated experimentally using disc work pieces in a conventional milling machine.

3.2 Development of a Non-Resonant Vibration-Assisted Machining Device

In summary, there exists several design parameters to be considered to achieve the feasible design of the non-resonant vibration-assisted machining device in the desired operation range. Hydrodynamic oil films are generally formed in the thickness range from a few μm to 30 μm, thus the displacement range of the actuator needs to be of that order. The actuator needs to have suitable force capacities to drive the cutting tool with forces by the cutting process. Then, an electrically suitable amplifier should be selected to excite the selected actuator. In the mechanical arrangement, the mass driven by the actuator is a critical parameter as the mass would determine the resonant frequency and dynamic force in the dynamic operation. As well as the high axial mechanical stiffness of the assembly to avoid the undesired elastic deflection, a protective measure is necessary such that the piezoelectric element of the actuator is not exposed to the shear or twist forces which would be generated by the cutting process.

3.2.1 Piezoelectric actuator and amplifier selection

3.2.1.1 Piezoelectric actuator

A piezoelectric (lead zirconate titanate (PZT)) actuator (P-212.40 from Physik Instrumente (PI) GmbH & Co) with a displacement and a force capacity was selected as summarised in Table 3.2. The push force of piezoelectric actuator, F_{push}, is generated by the piezoelectric element by its piezoelectric effect, interacting with a preload spring installed on the top of the piezoelectric element. The piezoelectric actuator can generate a maximum push force when displacement of piezoelectric actuator, ΔL, is zero, and can travel a maximum displacement with zero force generation in an applied operating voltage of piezoelectric element, V_{e}, as summarised in Figure 3.7. Maximum push force of the actuator, i.e. push force capacity of piezoelectric actuator, F'_{push}, is generated with zero displacement when maximum operating voltage, 1000 V is applied. The

pull force of the piezoelectric actuator, F_{pull}, is generated by the preload spring and its capacity, F'_{pull}, is set at 300 N. Inherently the piezoelectric element is not able to generate the negative force (pull force) as the piezoelectric element, especially the electrode layer, is very vulnerable to tensile stress. The stiffness of the piezoelectric actuator, κ_{a}, is 33.3 N/μm, determined by interaction of the stiffness of the piezoelectric element and the stiffness of the preload spring. κ_{a} is not a mechanical stiffness of the piezoelectric actuator, as it is the ratio of the push force generation and its according displacement range of the piezoelectric element, ΔL_{r}, with an operating voltage by its piezoelectric effect (or simply $F'_{\text{push}}/\Delta L'$).

Table 3.2: Specification of actuator, P-212.40 of PI (Physik Instrumente GmbH and Co P-212).

Operating voltage V_{e}	V	0 to 1000
Displacement capacity $\Delta L'$	μm	60
Push force capacity F'_{push}	N	2000
Pull force capacity F'_{pull}	N	300
Capacitance	nF	180
Stiffness κ_{a}	N/μm	33.3
Mass of piezoelectric element m	grams	35
Operating temperature	°C	-40 to +80

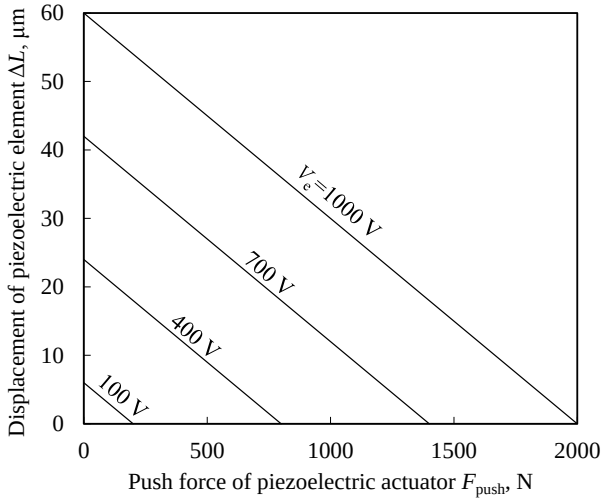

Figure 3.7: F_{push} and ΔL variation with the operating voltage of P-212.40 (Physik Instrumente GmbH and Co P-212).

3.2.1.2 Amplifier

An amplifier which suited the excitation of this actuator was chosen. The amplifier selected (E-481 from Physik Instrumente (PI) GmbH & Co) is a high-power amplifier designed specifically

for dynamic operation of high-capacitance PZT actuators. The output voltage is from 0 V to 1100 V with a voltage gain of 100. The main specification is summarised in Table 3.3. The selected actuator (P-212.40) with E-481 can be driven in either open-loop or closed-loop operation. In this study open-loop was used as the operation required a faster response than closed-loop can achieve, in particular, in test conditions with a high required frequency range. Figure presents the electrical operating limits of E-481 for sinusoidal vibrations in three piezoelectric actuators (180 nF (P-212.40), 800 nF, and 4000 nF in the capacitance) in vibration frequency, f, over the operating voltage range of the piezoelectric element, ΔV_{e}.

Table 3.3: Specification of amplifier, E-481 of PI (Physik Instrumente GmbH and Co E-481).

Voltage gain		100
Output voltage	V	0 to 1100
Output current average	mA	>600
Output current peak	mA	2000
Output power average	VA	630
Output power peak	VA	2000

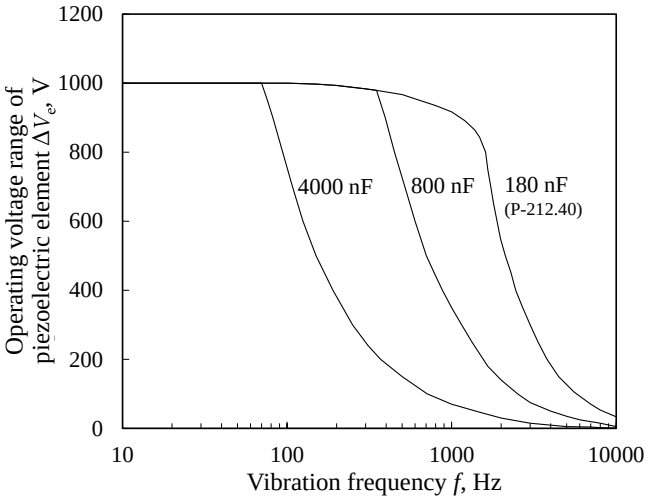

Figure 3.8: Electrical operating limits of E-481 for sinusoidal vibrations with the capacitances of piezoelectric actuator (Physik Instrumente GmbH and Co E-481).

3.2.2 Mechanical arrangement

In this study the constructed device is arranged in a conventional milling machine for the simplicity of the arrangement. The disc work piece (an aluminium alloy AlSi1MgMn and a low-alloyed steel 16MnCr5) is set in the milling machine spindle and the mechanical assembly on the milling machine stage to turn the face of the work piece. The work piece represents the

counterpart of a tilting pad thrust bearing used in a production gas turbine engine, as summarised in Table 3.4.

3.2.2.1 Mechanical assembly

Figure 3.9 shows the mechanical arrangement of the device developed for this study. The height of the assembly is 199 mm from the base plate to the cutter insert tip and the outer diameter of the housing is ϕ80 mm. The selected actuator is rigidly bolted against a conventional cutting tool. The vibration is transmitted through the cutter (cutter insert and cutter shank) normal to the face of the work piece. The cutter and the actuator are secured in the housing and the base plate which is bolted on the milling machine stage. The cutter feeds in the radial direction with respect to the work piece, with its vertical position also controlled and set at the start of a machining test. A roller bearing guides the vibration and supports the bending force acting on the cutter insert, and the pin supports the twisting force from the cutting process, so that the shear stress is not transmitted to the piezoelectric element that makes up the actuator.

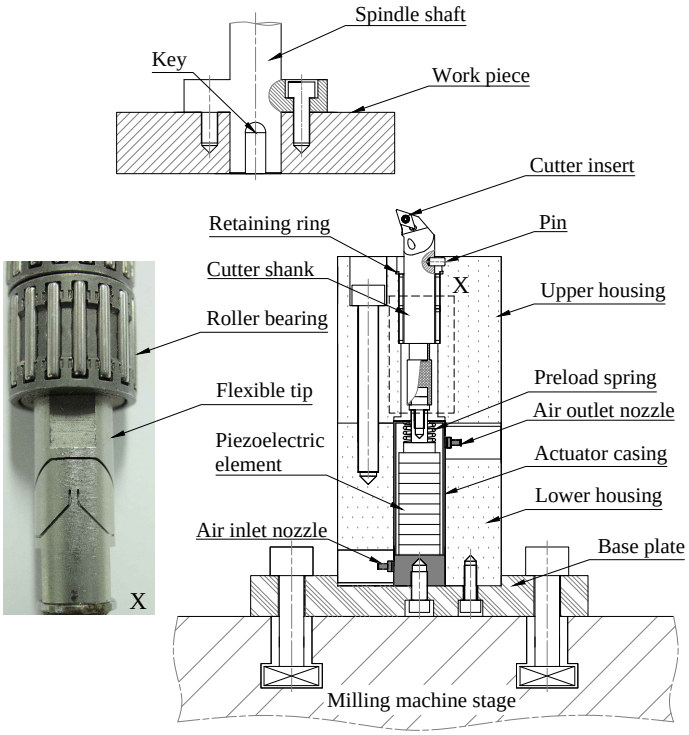

Figure 3.9: Mechanical arrangement.

The flexible tip (P-176.60 from Physik Instrumente (PI) GmbH & Co) set between the cutter shank and the actuator is flexible mainly to the bending direction due to the notches arranged on

the surface. This flexible tip further reduces the stress on the piezoelectric element induced by the bending force acting on the cutter insert, and the bending force which might occur through misalignment between the actuator and the cutter shank when assembled. Specific cutting forces, K_s, including a safety factor (SF) of 3.0 were selected as summarised in Table 3.4 (Sandvik Coromant Ltd, 2012).

Table 3.4: Specifications of work pieces.

Work piece symbol		A1 to A7	S1 to S6
Material		AlSi1MgMn	16MnCr5
Machined diameter	mm	84 to 136	84 to 136
Vickers hardness	MPa	1216	2491
Specific cutting force K_s	MPa	2100 incl. SF	5100 incl. SF

3.2.2.2 Cutter shank and insert

The cutter shank (CoroTurn 107 from Sandvik Coromant) and the cutter insert (DCET 07 02 01-UM 1125 from Sandvik Coromant) were selected on the basis of mass and cutter insert edge radius. The shank and insert masses are critical because this mass contributes to the dynamic force of vibration which limits the operation range. The smallest edge radius of the cutter insert available was chosen to generate the surface textures with good geometrical resolution. The main specifications of the selected shank and the cutter insert are summarised in Figure 3.10.

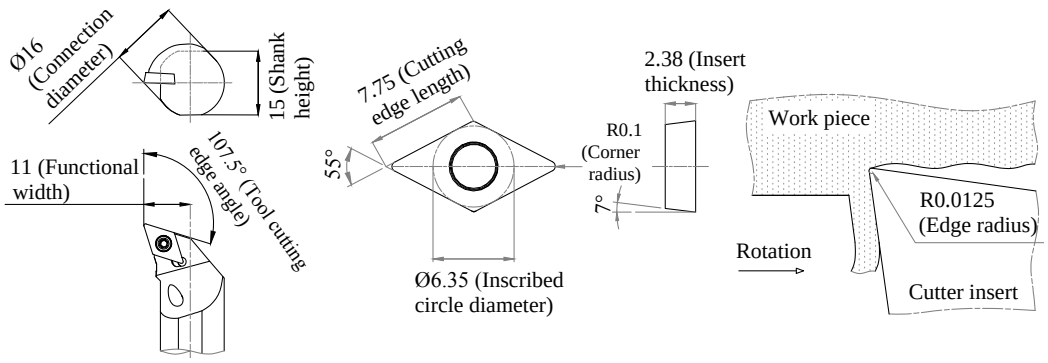

Figure 3.10: Specifications of cutter shank, CoroTurn 107 A16R-SDQCR 07, and cutter insert, DCET 07 02 01-UM 1125, from Sandvik Coromant (Sandvik Coromant Ltd, 2012).

3.2.3 Electrical control and air cooling arrangement

The piezoelectric element is excited by a voltage source unit (NI-USB-9263 from National Instruments) amplified by the amplifier (E-481). The displacement signal of the piezoelectric

element via a strain gauge (strain gauge (a)) and the operating voltage of piezoelectric element are monitored by a voltage monitor unit (NI-USB-6008 from National Instruments) as shown in Figure 3.11.

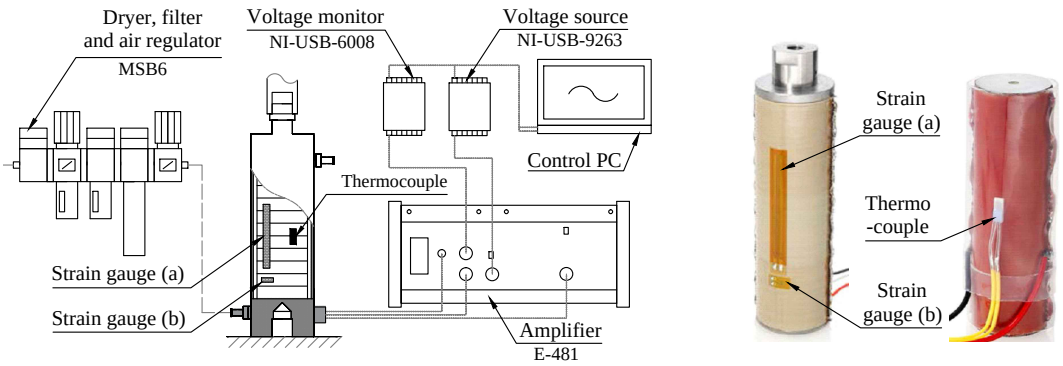

Figure 3.11: Electrical control and air cooling arrangement.

An apparent strain caused by a resistance change of the strain gauge (a) over the temperature change of the piezoelectric element is compensated using a Wheatstone bridge circuit with another strain gauge (strain gauge (b)) which is also placed on the piezoelectric element. The parameters of the vibration are commanded by a control PC. The possible vibration wave forms include sine wave, triangle wave, square wave, and saw tooth wave. In this study the sine wave was exclusively used to obtain tribologically optimised surfaces. The heat that the piezoelectric element generates in dynamic operation is dissipated by compressed air which is controlled down to 0.5 bar through a dryer, filter and air regulator (MSB6 from Festo). The temperature of the piezoelectric element is monitored through a thermocouple placed on the piezoelectric element with a fail-safe set should the temperature exceed 80 °C, which is the operating limit of the piezoelectric element.

3.2.4 Operating regimes

In a dynamic operation where the cutter vibrates perpendicular to the work piece at a given frequency and displacement, the mass-spring system of the developed assembly interacts with friction forces incurred by the contacts (e.g. between the roller bearings and the cutter shank or the pin and the housing slot), and cutting resistance i.e. the cutting force of the work piece. In respect of the feasibility of a dynamic operation the friction forces are considered to be negligibly small. The piezoelectric element generating the pushing force and the preload spring generating the pulling force are considered to be a spring element of the system. The coordinate x, y, and z

is set as shown in Figure 3.12. The x coordinate is the tangential direction of the disc work piece, the y coordinate is the radial direction of the disc work piece, and the z coordinate is the vibration direction, i.e. the axial direction of the cutter shank, respectively.

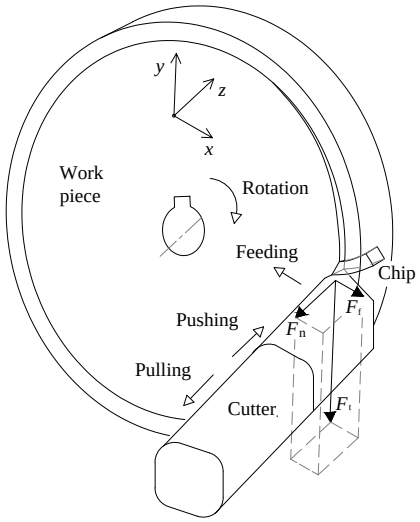

Figure 3.12: Schematic of the motion of the cutter and work piece, and forces acting on the cutter.

3.2.4.1 Cutting force

The cutting force is a force generated from the contact between the cutter insert and the work piece. It is assumed that the cutting of the spinning work piece with a feeding cutter can be approximated as a three-dimensional turning operation of infinite work piece diameter. Since the cutter engages with the work piece continuously along the sinusoidal displacement, the cutting could be considered as a conventional cutting engagement with a varying depth of cut. Therefore, the generated cutting force acting on the cutter can be divided into three components; tangential force of cutting, F_t, feed force of cutting, F_f, and normal force of cutting, F_n, as shown in Figure 3.12. The cutting force varies with operational conditions such as cutting speed, feed speed, depth of cut, interfacial friction, and material properties (Groover, 2011). Although it is difficult to deduce these force components accurately, a suitable simplification (The Japan Society of Mechanical Engineers, 2012) is that the ratio of each component remains constant for all operating conditions as:

$$F_t = K_s A, \tag{3.1}$$

$$F_t : F_n : F_f \approx 10 : 3 : 1, \tag{3.2}$$

where K_s is the specific cutting force (a force per unit area), and A is the area of the chip. A can be expressed as follows:

$$A = u_{fpr} t_d, \tag{3.3}$$

where u_{fpr} is feed per revolution and t_d is the depth of cut. u_{fpr} is given as:

$$u_{fpr} = \frac{u_f}{\omega}, \tag{3.4}$$

where u_f is the feed speed of milling machine stage and ω is the rotation speed of spindle (work piece). As mentioned in the section describing the mechanical arrangement, only the normal force of cutting interacts with the vibration since the tangential force and feed force of cutting are decoupled by the roller bearing. F_n can be rearranged with Equations (3.1) to (3.4) as:

$$F_n = -\frac{3}{10}\frac{u_f}{\omega} K_s t_d, \tag{3.5}$$

where t_d is a function of time, t, and varies with sinusoidal displacement, so it can be expressed as:

$$t_d(t) = \frac{\Delta L_{rt}}{2} \sin 2\pi f t + t_0, \tag{3.6}$$

where t_0 is initial depth of cut before the vibration is commanded and ΔL_{rt} is displacement range of cutter tip as seen in Figure 3.13.

It is assumed that ΔL_{rt} and the measured displacement range of the piezoelectric element, ΔL_{rm}, are approximately equal as the cutter and piezoelectric element is rigidly bolted and the elastic deformation of the cutter during cutting is negligibly small in the conducted conditions. Therefore Equations (3.5) and (3.6) can be rearranged as:

$$F_n(t) = -\frac{3}{10}\frac{u_f}{\omega} K_s \left[t_0 + \frac{\Delta L_{rm}}{2} \sin 2\pi f t \right]. \tag{3.7}$$

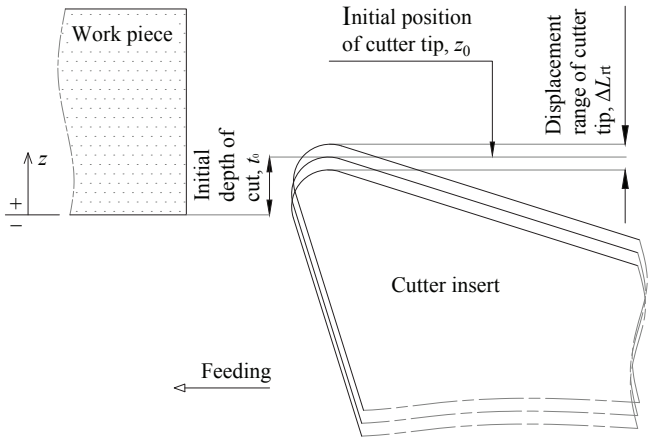

Figure 3.13: Schematic of the cutting parameters.

3.2.4.2 Operation limits of vibration with cutting

With an approximation that the damping element in this mass-spring system is negligibly small, the motion of a dynamic operation in steady state can be described by:

$$m_{\text{eff}}\ddot{z}_{\text{c}}(t) + (\kappa_{\text{sp}} + \kappa_{\text{e}})z_{\text{c}}(t) = F_{\text{n}}(t), \tag{3.8}$$

where z_{c} is the dynamic position of cutter tip in the z coordinate, κ_{sp} is the stiffness of the preload spring, κ_{e} is the stiffness of the piezoelectric element, m_{eff} is effective mass of the moving parts. The effect of the gravitational acceleration could be neglected in the dynamics. m_{eff} is given as (Physik Instrumente GmbH and Co, 2009):

$$m_{\text{eff}} \approx \frac{m}{3} + M, \tag{3.9}$$

where m is the mass of the piezoelectric element and M is the mass driven by the piezoelectric actuator as summarised in Figure 3.14. The preload spring is assumed to be of negligible mass. For a sinusoidal vibration, z_{c} is given by:

$$z_{\text{c}}(t) = \frac{\Delta L_{\text{rm}}}{2}\sin 2\pi f t + z_0, \tag{3.10}$$

where z_0 is initial position of cutter tip in z coordinate. The acceleration of this sinusoidal vibration is that:

$$\ddot{z}_c(t) = -2\pi^2 f^2 \Delta L_{rm} \sin 2\pi f t. \tag{3.11}$$

Graphical representation in the time domain of Equation (3.8) at two conditions, **a** and **b** is presented in Figure 3.15. The parameters of the conditions are summarised in Table 3.5. The condition **a** represents a feasible operation and the condition **b** an unfeasible one. At both conditions it is noted that $m_{eff}\ddot{z}_c$ are predominantely greater than F_n and $m_{eff}\ddot{z}_c$ yields greatest to the negative direction (point **A** and **B**) at the positive peak of z_c.

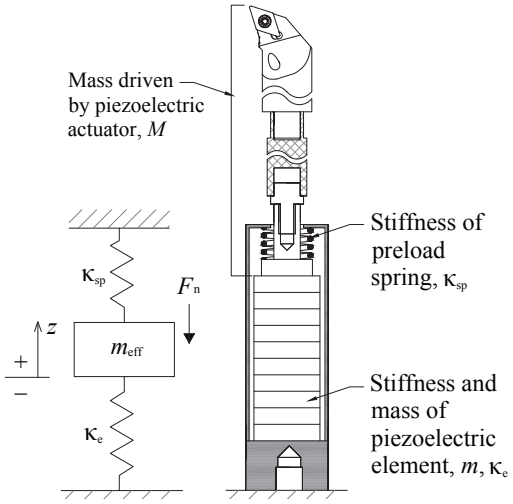

Figure 3.14: Schematic of force interactions between normal force of cutting and the actuator.

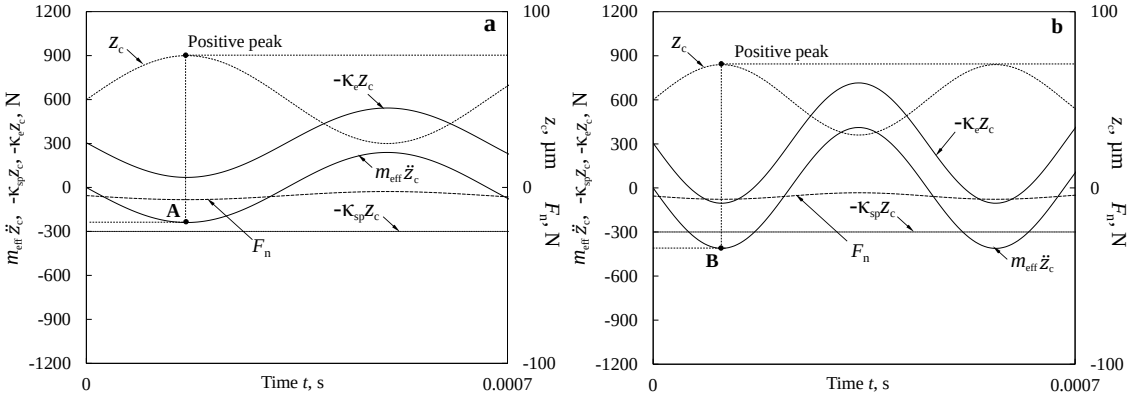

(a) At the condition **a**

(b) At the condition **b**

Figure 3.15: Graphical representation of Equation (3.8).

Table 3.5: Parameters for the feasibility calculations.

Symbol	Specific cutting force	Effective mass	Rotation speed of spindle	Feed speed	Initial depth of cut	Displacement range of piezo-electric element	Vibration frequency	Wave form
	K_s	m_{eff}	ω	u_f	t_0	ΔL_r	f	
	MPa	grams	rpm	mm/s	μm	μm	Hz	
a	5100	108	500	0.5	50	50	1500	Sine
b	5100	108	500	0.5	50	40	2200	Sine
c	5100	108	500	0.5	50	10 to 60	0 to 5000	Sine

Figure 3.16 shows $m_{eff}\ddot{z}_c$ at the conditions **a** and **b** with the force characteristics of the selected actuator over ΔL. At the condition **a**, $m_{eff}\ddot{z}_c$ does not exceed either the F_{push} line (at $V_e = 1000$ V) or the F_{pull} line. In contrast at the point **B** of the condition **b**, $m_{eff}\ddot{z}_c$ exceeds the F_{pull} line while it does not exceed the F_{push} line (at $V_e = 1000$ V) at the other end of the displacement. This is attributed to the force characteristics of the selected actuator where F_{pull} is smaller than the usable F_{push} while $V_e > 150$ V.

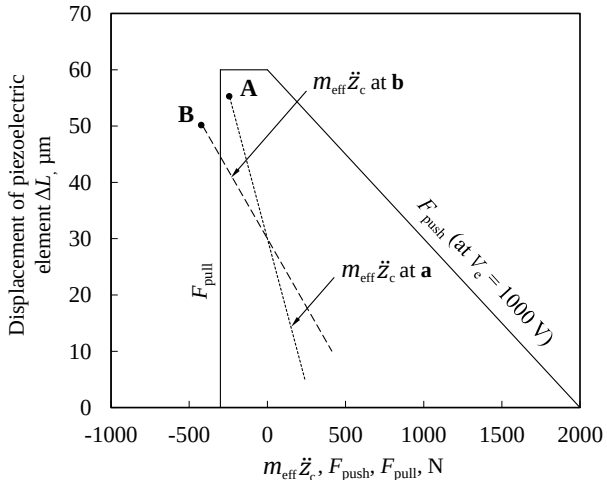

Figure 3.16: Deduced $m_{eff}\ddot{z}_c$ at the condition **a** and **b** with the force characteristics of the selected actuator.

It is noted that $\kappa_{sp}z_c$ is almost constant at a value of 300 N within the travel range of the piezoelectric element due to its small value of κ_{sp}. Therefore, as far as a suitable operating voltage is applied to the piezoelectric element, the operation limits of vibration would be determined by the dynamics at the positive peak of z_c by substituting 300 N to $\kappa_{sp}z_c$ and 0 N to $\kappa_e z_c$ in Equation

(3.8), that is:

$$m_{\text{eff}}\ddot{z}_{\text{c}}(t) - F_{\text{n}}(t) \geq -300. \tag{3.12}$$

The operation would be feasible while Equation (3.12) is satisfied within the range of the electrical operating limit of the amplifier and the range below the first resonant frequency of the mass-spring system. The first resonant frequency, f_{res}, is given as (Physik Instrumente GmbH and Co, 2009):

$$f_{\text{res}} = \frac{1}{2\pi}\sqrt{\frac{\kappa_{\text{a}}}{m_{\text{eff}}}}, \tag{3.13}$$

where κ_{a} is stiffness of the selected actuator. In the constructed mass-spring system, f_{res} was determined as 2.8 kHz by Equation (3.13). In order to investigate the limit of the pull force, a calculation for determining the feasible range of operation considering Equation (3.7) and (3.12) was carried out at the condition **c** as presented in Table 3.5. As summarised in Figure 3.17 two boundaries by the pull force limitation and the resonant frequency are shown. It is noted that this feasibility discussion can not be applied to machining tests with hard materials or with a deeper depth of cut where F_{n} would be much greater, for which case the dynamics might be limited by $\kappa_{\text{e}} z_{\text{c}}$ rather than $\kappa_{\text{sp}} z_{\text{c}}$.

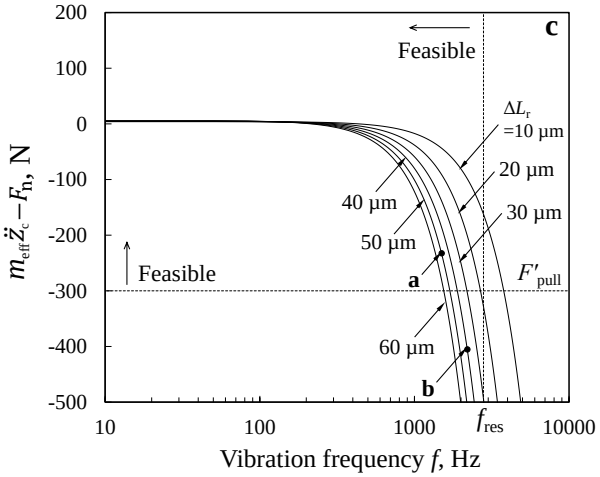

Figure 3.17: Feasible range of operation deduced at the condition **c**.

3.2.4.3 Preliminary actuation tests

Prior to the machining tests, actuation tests were carried out without engagement of the work piece to validate the design. The system is controlled by setting; mean voltage, V_{m} (from 0 V to 10 V), voltage range, ΔV (from 0 V to 10 V), vibration frequency, f, and wave form (sinusoidal in this study). A LabVIEW interface was written to enter these parameters. Figure 3.18 shows the voltage range, ΔV, compared with the displacement of the piezoelectric element as measured by the strain gauge, ΔL_{rm}, in one of the conducted tests.

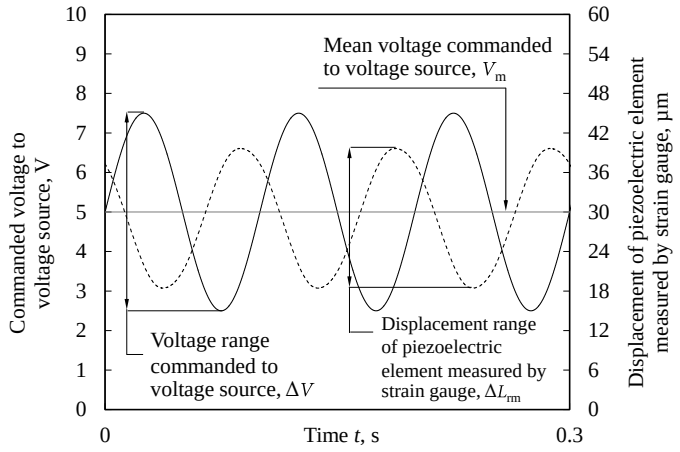

Figure 3.18: Displacement of piezoelectric element measured by the strain gauge and the commanded voltage in a 10 Hz open-loop operation without engagement to work piece.

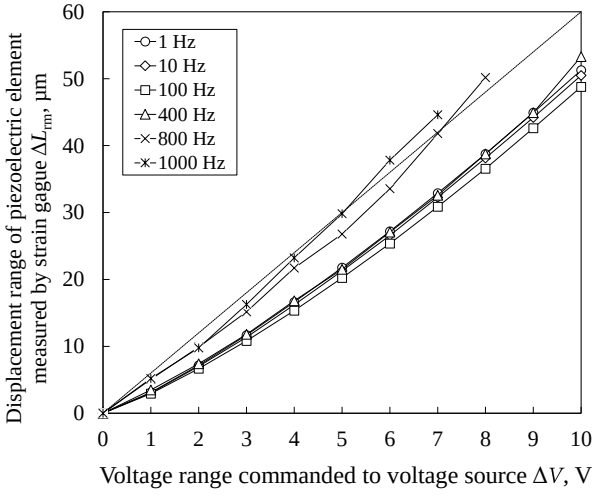

Figure 3.19: Summary of ΔL_{rm} with various operating frequencies at $V_{\mathrm{m}} = 5$ V without engagement to work piece.

The actuation tests were examined at six vibration frequencies, 1, 10, 100, 400, 800 and 1000

Hz, in the commanded voltage range, from 0 V to 10 V with the mean voltage 5 V. The results are summarized in Figure 3.19. Overall the system was actuated well with good repeatability of displacements in all the test conditions with a phase shift between the driving voltage and the observed displacement. The measured displacement, ΔL_{rm}, yielded greater when a higher vibration frequency was commanded in a commanded voltage range, ΔV, e.g. the measured displacement was 25.4 μm at 400 Hz, 33.6 μm at 800 Hz, and 37.8 μm at 1000 Hz when the voltage range was commanded at 6 V. It is presumed that these measured displacement increased because the vibration frequency approached the first resonant frequency. The conditions with the large voltage ranges in 800 Hz and 1000 Hz were not tested as the operation became marginally unstable.

3.3 Experiment

3.3.1 Machining and surface measurement procedure

The machining tests were examined at thirteen test conditions on the face of the disc work pieces with no cutting fluid. Table 3.6 shows the machining parameters and the commanded vibration parameters.

Table 3.6: Machining test conditions.

Work piece symbol	Rotation speed of spindle ω rpm	Feed speed u_{f} mm/s	Initial depth of cut t_0 μm	Voltage range ΔV V	Mean voltage V_{m} V	Vibration frequency f Hz	Wave form
A1	200	0.5	50	0	5	N/A	N/A
A2	200	0.5	50	2	5	400	Sine
A3	200	0.5	50	4	5	400	Sine
A4	200	0.5	50	6	5	400	Sine
A5	200	0.5	50	4	5	800	Sine
A6	200	0.5	50	4	5	1000	Sine
A7	200	0.5	50	2	5	401	Sine
S1	500	0.5	50	0	5	N/A	N/A
S2	500	0.5	50	2	5	400	Sine
S3	500	0.5	50	4	5	400	Sine
S4	500	0.5	50	6	5	400	Sine
S5	500	0.5	50	4	5	800	Sine
S6	500	0.5	50	4	5	1000	Sine

The machining parameters, ω, u_{f}, and t_0 were chosen on the basis of surface finish. The vibration parameter ΔV was chosen on the basis of the order of hydrodynamic lubricant film

thickness (from a few μm to 30 μm generally) and then f was set within the stably operable range confirmed in the preliminary actuation tests. The ratios of f and ω were selected so that the textures were meshed roughly and finely. The effect of such geometrical features to the oil film formation will be discussed in Chapter 5. In order to suppress the burr generation, the depth of cut was set so that the machining is continuously engaged to the work piece surface. Each work piece took 52 s to machine from the outer diameter of ϕ136 mm to the inner diameter of ϕ84 mm. These machining parameters and the commanded vibration parameters were not changed once set at start of a machining test until completed. Figure 3.20 schematically shows the generated surface features machined with vibration. Each of the work pieces was initially machined without vibration (i.e. conditions A1 and S1 for aluminium and steel, respectively).

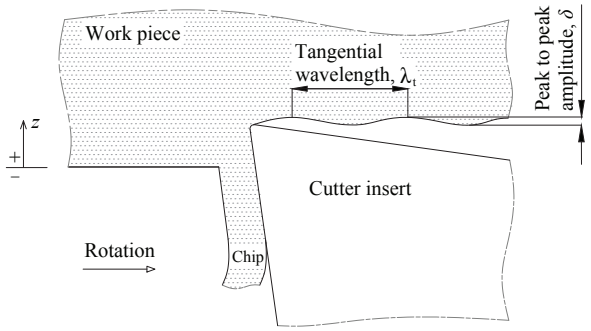

Figure 3.20: Schematic of generated surface features with a vibration-assisted machining.

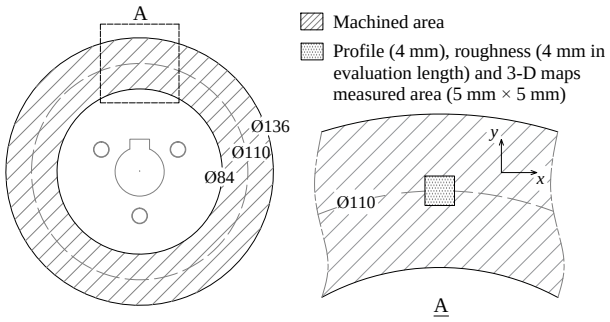

Figure 3.21: Schematic of the area selected for surface measurement using a stylus profilometer and a 3-D optical scanner.

After the machining tests, surface measurements were conducted at a diametrical location of 110 mm. Surface profile (length of 4 mm in x and y direction with tilt compensation) and surface roughness, R_a, (evaluation length of 4 mm in the x direction with tilt compensation) were

measured using a stylus profilometer (SV-602 Series 178 from Mitutoyo) and 3-D maps (area of 5 mm $\times$ 5 mm) were measured using a 3-D optical scanner (Contour GT from Bruker) as summarised in Figure 3.21.

3.3.2 Results and discussions

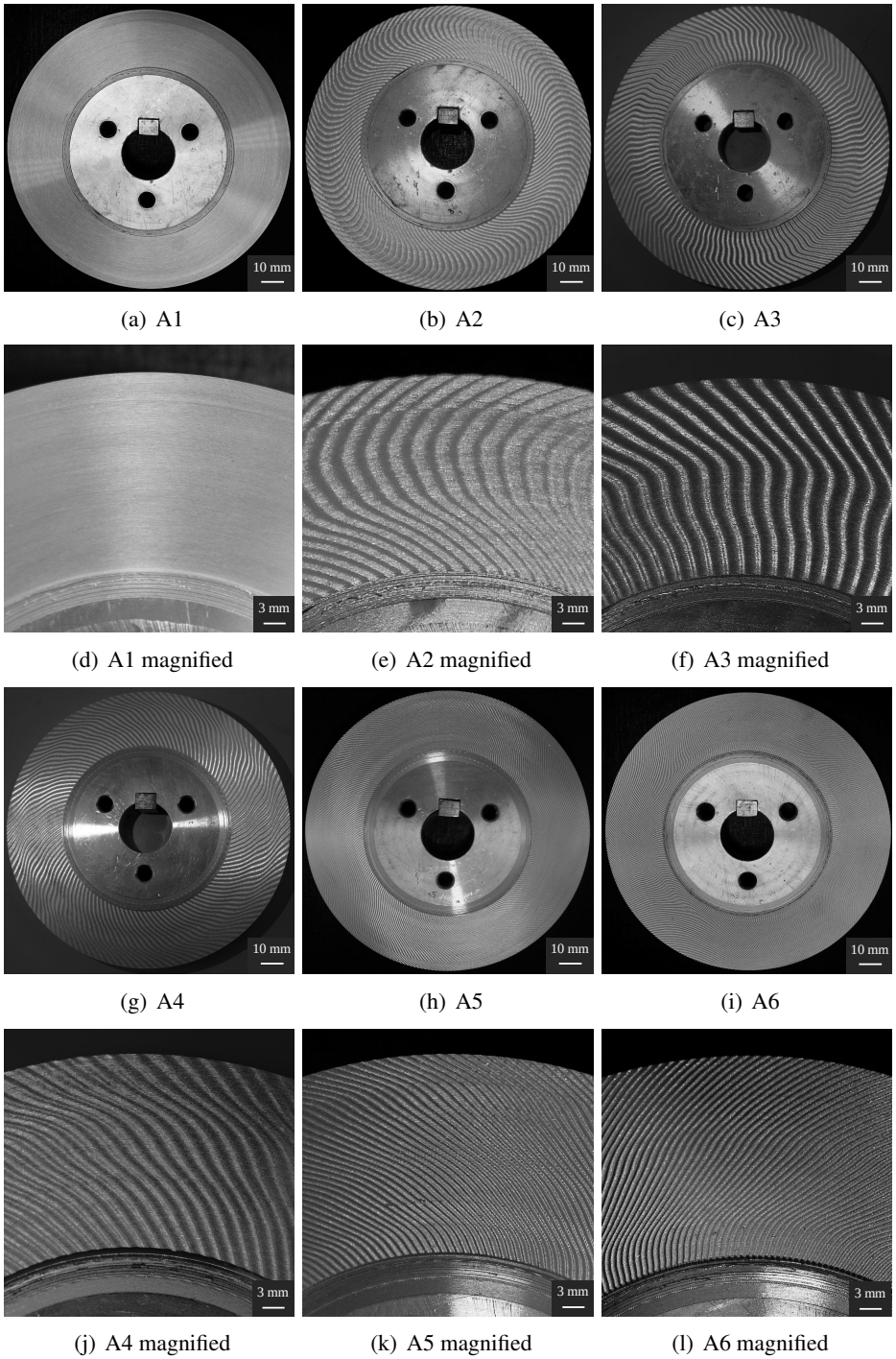

(a) A1 (b) A2 (c) A3

(d) A1 magnified (e) A2 magnified (f) A3 magnified

(g) A4 (h) A5 (i) A6

(j) A4 magnified (k) A5 magnified (l) A6 magnified

Figure 3.22: Generated textures in work pieces of A1 to A6.

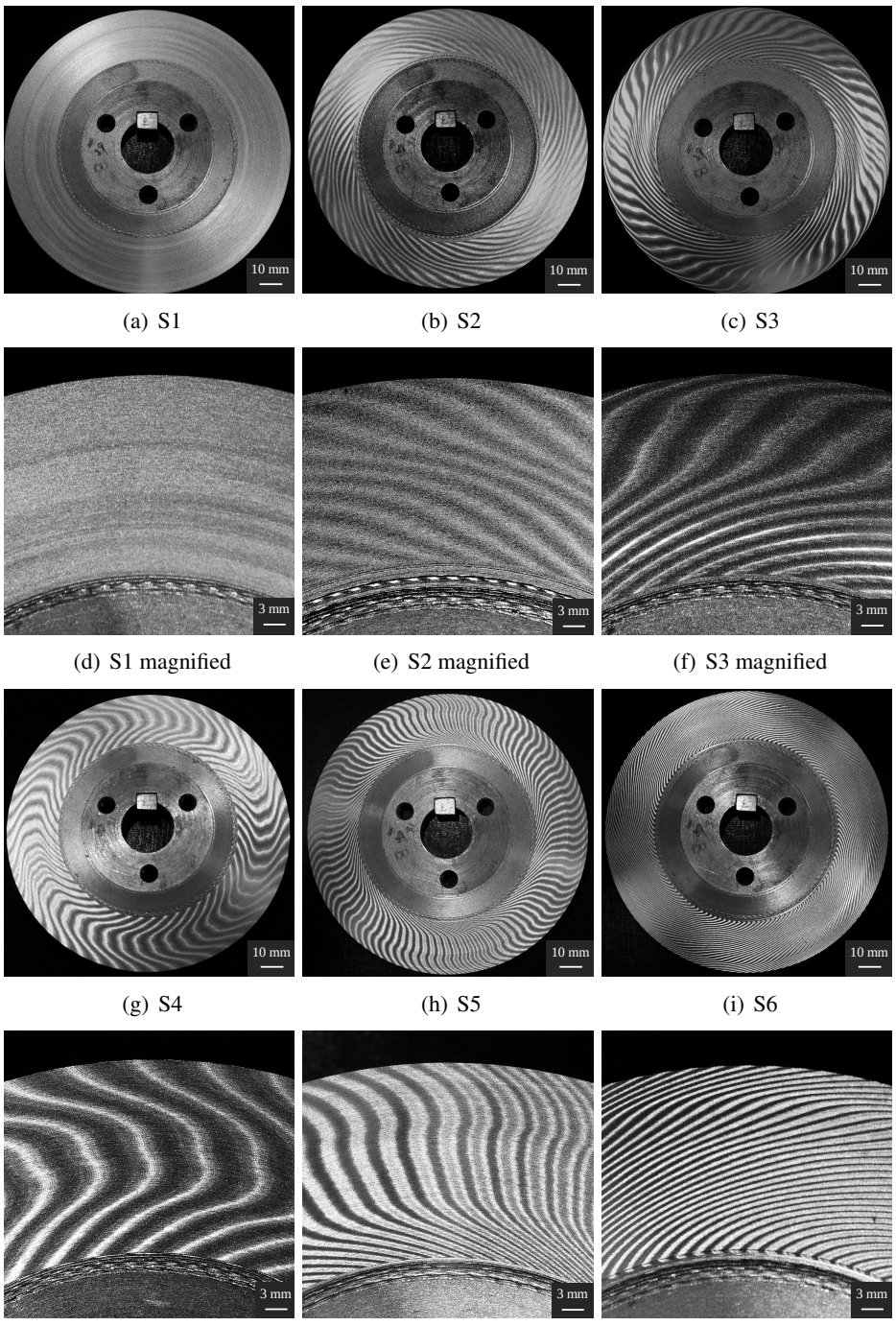

(a) S1 (b) S2 (c) S3

(d) S1 magnified (e) S2 magnified (f) S3 magnified

(g) S4 (h) S5 (i) S6

(j) S4 magnified (k) S5 magnified (l) S6 magnified

Figure 3.23: Generated textures in work pieces of S1 to S6.

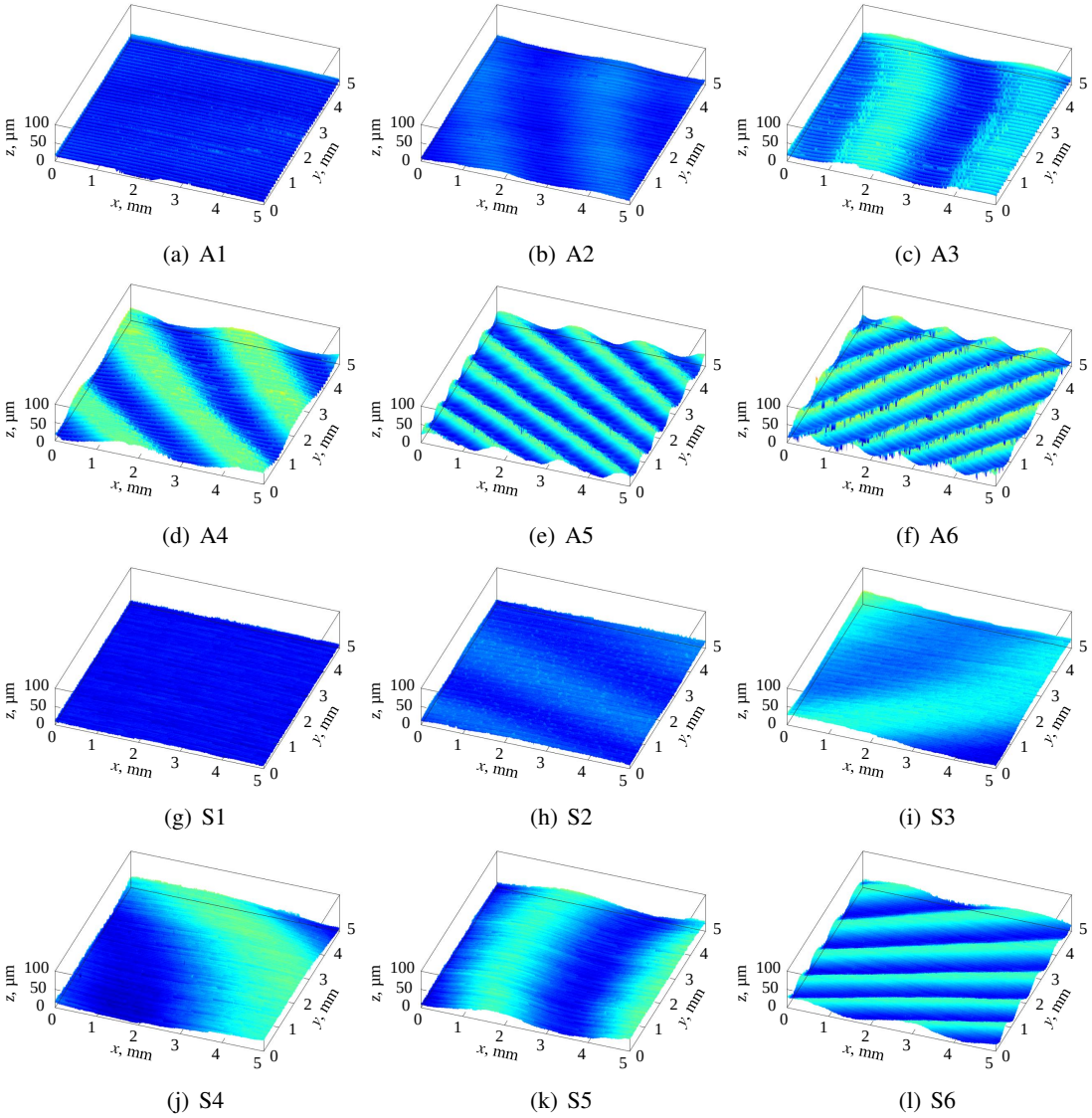

(a) A1 (b) A2 (c) A3

(d) A4 (e) A5 (f) A6

(g) S1 (h) S2 (i) S3

(j) S4 (k) S5 (l) S6

Figure 3.24: 3-D maps measured by 3-D optical scanner in work pieces of A1 to A6 and S1 to S6.

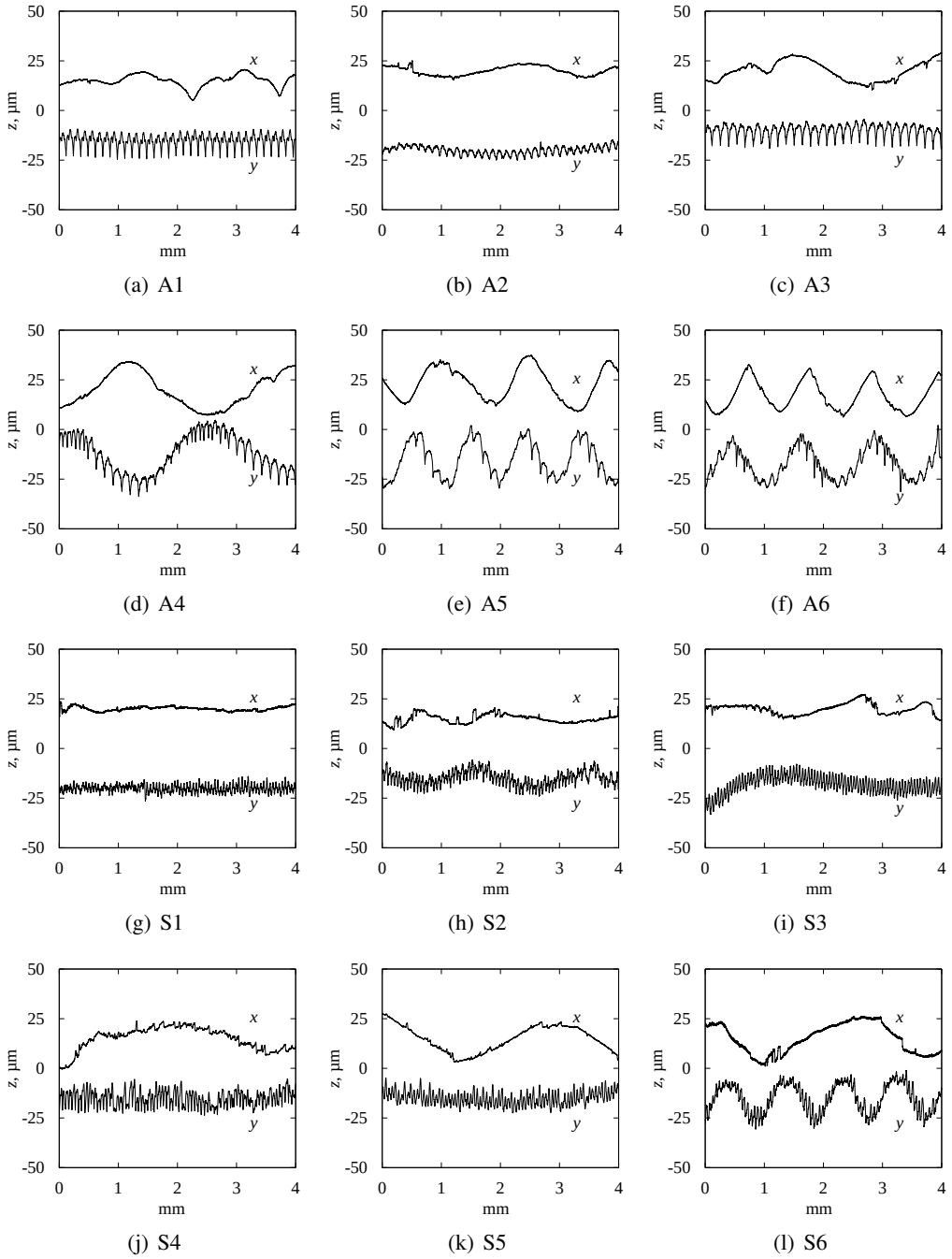

(a) A1 (b) A2 (c) A3

(d) A4 (e) A5 (f) A6

(g) S1 (h) S2 (i) S3

(j) S4 (k) S5 (l) S6

Figure 3.25: Surface profiles measured by stylus profilometer in work pieces of A1 to A6 and S1 to S6.

The photographs of the machined surfaces are presented in Figure 3.22 and Figure 3.23, 3-D maps in Figure 3.24, and surface profiles in Figure 3.25. The tests without vibration, work pieces A1 and S1, demonstrated that smooth surfaces were generated, confirming the stability of the developed device. Overall the vibrations superposed satisfactorily well on the work pieces, and

waves of an undulating radial striation pattern were generated on the surfaces of the work pieces A2 to A6 and S2 to S6. The burrs in the diverging area seen on Greco's work (Greco et al., 2009) were not generated. This was achieved by the continuous engagement of the cutting tool to the work piece surfaces. The sine waves generated through the machining process had peak to peak amplitudes, δ, varying from a few μm to 25 μm, and the tangential wavelengths, λ_t, varying from approximately 1 mm to 8 mm.

3.3.2.1 Generated peak to peak amplitude on surface

Figure 3.26 presents the generated peak to peak amplitude of surface texture over the displacement of the piezoelectric element measured by the strain gauge in the machined surfaces with vibration. The values of δ plotted in the graph were read from the obtained 3-D maps.

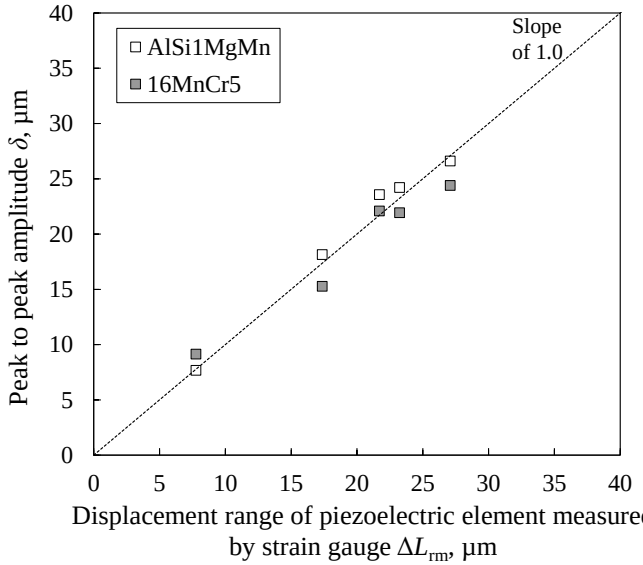

Figure 3.26: Summary of ΔL_{rm} and δ in work piece of A2 to A6 and S2 to S6.

Approximately 8 μm (A2 and S2) to 25 μm (A4 and S4) of the peak to peak amplitude were generated on the surfaces. The generated peak to peak amplitude of surface texture showed good agreement with the superposed displacement overall. It is assumed that the amplitudes of the surface textures were accurately generated due to the high axial stiffness of the mechanical components (i.e. cutter insert, cutter shank, and flexible tip) between the work piece and piezoelectric element, so that little deflection occurred. The coefficient of determination, R^2, yielded 0.948 with the samples of δ and the predicted line with slope of 1.0.

3.3.2.2 Surface roughness

The roughness average, R_a, was measured after machining using a stylus profilometer in the tangential direction. For the work pieces without vibration, A1 and S1, an evaluation length of 4 mm with a cut-off length of 0.8 mm was used as R_a was expected less than 2.0 μm (ISO 4288:1996, 1996). R_a of 1.2 μm in the AlSi1MgMn and 0.5 μm in the 16MnCr5 were obtained, which confirmed the stability of the constructed assembly. For the other work pieces, where waviness was intentionally created (A2 to A6 and S2 to S6), the waviness was removed for the roughness assessment. 1st to 20th order polynomial lines were fitted to the surface profiles, and the deviation of the measured profiles from the fitted lines integrated across the evaluation length (4 mm). Figure 3.27 shows an example of this process, where 1st, 4th, and 7th order polynomial lines are fitted to a measured profile.

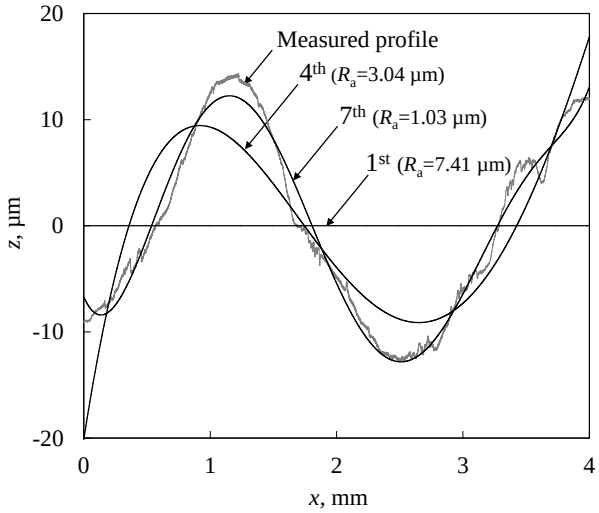

Figure 3.27: Measured surface profile of work piece A4 with the 1st, 4th, and 7th order polynomial lines.

As shown in Figure 3.28, the obtained R_a values were summarised and compared with the work pieces without vibration (A1 and S1) for each material investigated. As shown, as the order of the fitted polynomial was increased for a given roughness profile, the calculated average surface roughness values converged. In all cases, it was found that the value after convergence was less than 1.0 μm, indicating a similar level of performance in all of the machining operations once the surface waviness had been removed.

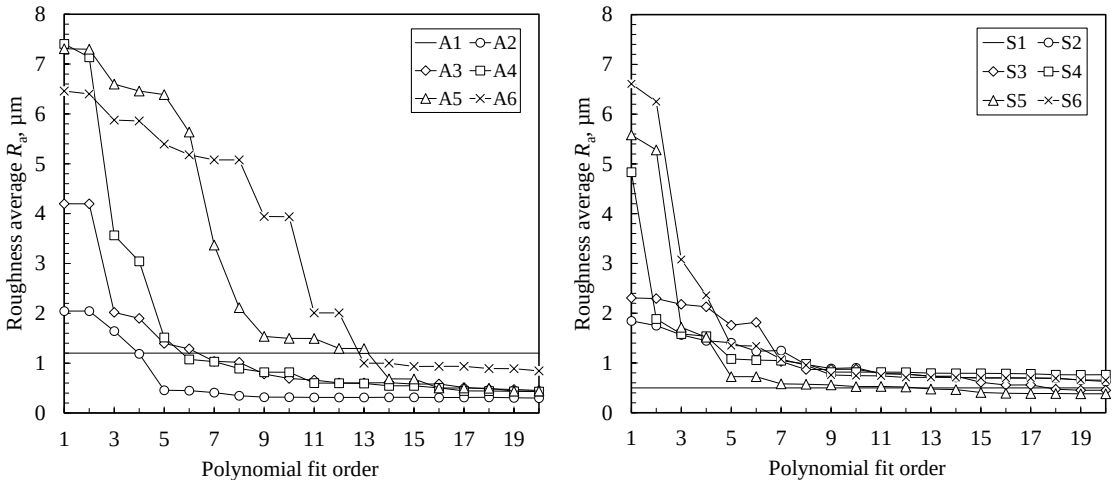

(a) AlSi1MgMn (b) 16MnCr5

Figure 3.28: Summary of roughness average in 1st to 20th polynomial fit order.

The data showed that R_a of the underlying surface, once the intentional surface waviness has been removed, is little changed by the use of vibration-assisted cutting over the settled order, although it was expected that the roughnesses could be improved by the vibration superposition as seen in a resonant technique by Moriwaki and Shamoto (1991). This could be because of the superposed vibration direction and the way of cutting tool engagement. In the study by Moriwaki and Shamoto (1991), the linear vibration was superposed on to the cutter in the cutting direction and the cutter engaged with the work piece intermittently in ultrasonic frequency range (40 kHz). While in this study the vibration was superposed normal to the face of the work piece and the cutter engaged with the work piece continuously along the sinusoidal displacement, which could have acted as the conventional cutting engagement.

3.3.2.3 Phase shift

The turned surface on the disc has the form of a helical spiral. In the vibration-assisted machining process described in this paper, long range waviness is superimposed on top of this topography. As shown in Figure 3.29 (left), when the rotational speed of the work piece is in phase with the vibration frequency of the actuator, the developed surface texture will be in phase between coincident cutter paths as the tool moves radially inwards, resulting in visible radial striations on the surface. Conversely if the process is out of phase, an interference pattern occurs (Figure 3.29 (right)). This is summarised in Equation (3.14), where η represents the phase shift,

and f and ω the vibration frequency and spindle rotation speed respectively. Where η is an integer, the system is said to be in phase.

$$\eta = \frac{60f}{\omega}. \tag{3.14}$$

This effect was further explored in test piece A7 (Figure 3.30), which was machined with a phase shift deliberately introduced (f = 401 Hz and ω = 200 rpm as presented in Table 3.6).

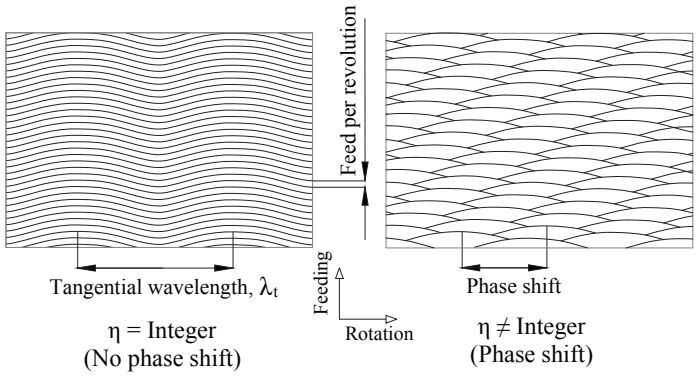

Figure 3.29: Schematic of textures with a phase shift and with no phase shift.

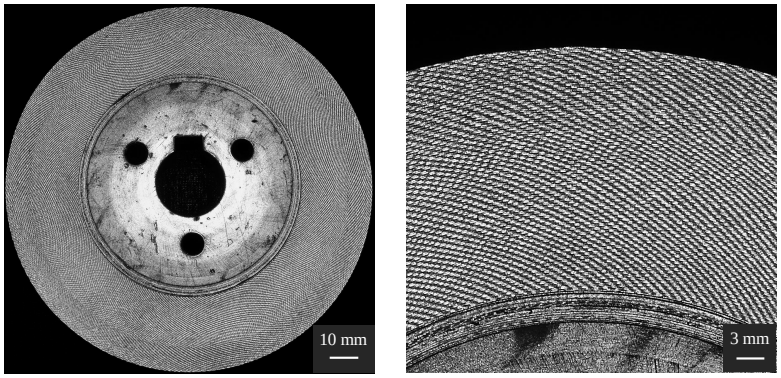

(a) A7 (b) A7 magnified

Figure 3.30: Generated surface texture with a phase shift in work piece of A7.

As shown in Figure 3.31, the surface profile of this specimen was subsequently measured, and the previously described interference pattern was evident. However, as shown in Figure 3.22 and 3.23, undulating radial patterns were also visible on work pieces A2 to A6 and S2 to S6, which were produced with the system nominally in phase. These samples were markedly different in appearance to A7, and the phase appeared subject to low frequency variations. Further

investigation of the test set-up indicated that this was due to a varying speed output from the spindle, as it did not have a feedback controller. This was confirmed in subsequent research work into the application of the technique, where a journal bearing shell was machined on a CNC turning machine with the device (Figure 5.12 in Chapter 5). The turning machine used in this case had an accurate speed controller on the spindle, and phase shifts were not evident on the machined specimen (Figure 5.13 in Chapter 5). The detail for the machining on the turning arrangement will be presented in Chapter 5.

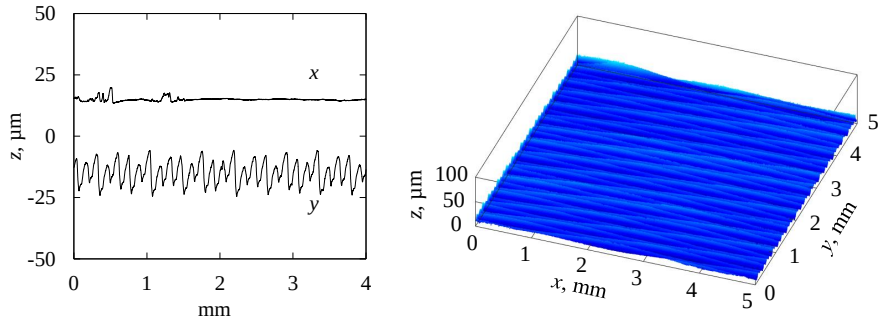

(a) Surface profile (b) 3-D map

Figure 3.31: Surface profile and 3-D map of generated surface texture with a phase shift in work piece of A7.

3.4 Conclusions

A novel variant of non-resonant vibration-assisted machining technique has been investigated to create bespoke surface textures in a conventional milling machine. The following conclusions are drawn from this chapter:

- A non-resonant vibration-assisted machining device has been constructed using an off-the-shelf piezoelectric actuator, its control system, and a conventional cutting tool. The geometry of the constructed mechanical assembly was compact, 199 mm in height and ϕ80 mm in outer diameter. The assembly required a small space to set up in the milling machine and could be easily arranged on other machining platforms, e.g. in a turning machine with a simple adapter.

- The feasible operational range with interaction of the cutting force was discussed with a focus of pull force limitation of the preload spring. In high frequency operation range the dynamic force was predominantly greater than the cutting force which was approximated

as a conventional cutting process with a varying depth of cut.

- The machining process with the developed device took 52 s to create the bespoke surface textures on the face of a disc work piece. The vibration commanded on the work pieces corresponded well to the textures generated on the surfaces with regards to frequency and amplitude of the wave forms with no burr generation. This was achieved by the limitation of the elastic deflection effect of the developed mechanical assembly due to the high axial stiffness and the continuous engagement of the cutting tool to the work piece surface. Surface textures consisting of a repeating radial striation pattern of sine waves were reproducibly generated when the frequency of the superposed vibration was in phase with the rotational speed of the work piece. The generated sine wave were controllable from approximately 1 mm to 8 mm in the wavelength and from a few μm to 25 μm in the peak to peak amplitudes which would reasonably cover the range of hydrodynamic lubricant film thickness.

- The work pieces were also machined without vibration, and smooth surfaces with a roughness average in tangential direction, R_a of 1.2 μm in the AlSi1MgMn and 0.5 μm in the 16MnCr5 were obtained, confirming the stability of the test rig developed. Once the waviness of the surface profile was filtered out, R_a of work pieces generated with vibration were almost as smooth as those without vibration.

- A machining test where a phase shift was deliberately introduced between the vibration frequency and the spindle rotation speed was examined. The result was that the radial striation patterns seen on the work pieces in which the system was nominally in phase were not created, instead an interference pattern occurred.

In Chapter 5, a bespoke surface texture will be created on an automotive transmission journal bearing using the developed device. Then effect of the bespoke surface texture on hydrodynamic lubricant film formation will be experimentally investigated using an ultrasonic film thickness measurement technique.

Chapter 4

Development of a Journal Bearing Test Platform to Determine Hydrodynamic Film Thickness with Ultrasound Reflectometry

In this chapter, the development of a journal bearing test platform to measure hydrodynamic film thickness in an automotive transmission journal bearing using an ultrasound reflection technique is presented. Firstly, early experimental investigations for the film thickness determination are discussed and summarised for the literature review. Then, the design and specifications of the test platform constructed is explained as well as the ultrasound apparatus used, finally the obtained experimental result in the test platform are discussed.

4.1 Literature Review

In this section, the literature works regarding the oil film thickness measurement are summarised, exclusively those conducted experimentally on journal bearing application in hydrodynamic lubrication regime. The literature works are discussed mainly focusing on the measurement techniques which the authors implemented on three measurement categories, i.e. mechanical, electrical and ultrasonic techniques which was employed in this study. The advantages and disadvantages of the techniques will be discussed.

4.1.1 Experimental works on film thickness measurement in journal bearing

Significant efforts have been directed toward measuring oil film thickness in journal bearing experimentally to date and various techniques to quantify the lubricant film thickness has been implemented. In general these measurement techniques could be fall into three categories: (i) mechanical methods (Dubois and Ocvirk, 1953) where relative displacement between shaft and bush are mechanically measured using mechanical dial indicator, (ii) electrical methods where electrical variations of, e.g. capacitance (Spearot and Murphy, 1988), resistance (Spearot and Murphy, 1988), or inductance (Dyer and Reason, 1976; Read and Flack, 1987; Tonnesen and Hansen, 1981) are measured to convert them to the film thickness, or (iii) ultrasonic methods, as the principle were presented in Chapter 2, where the response of an ultrasonic wave to a lubricant film layer is used to determine the film thickness (Dwyer-Joyce et al., 2003; Kasolang and Dwyer-Joyce, 2008a). The experimental works are briefly summarised by measuring techniques and presented chronologically in Table 4.1. In the following sections, the features of the measuring techniques and the measurement results are briefly presented.

Table 4.1: Summary of the literature works on film thickness measurement of journal bearing.

Authors (year)	Diameter D, mm	Width diameter ratio L/D	Technique
Dubois and Ocvirk (1953)	34.93	2.0, 1.0, 0.5, 0.25	Mechanical
Dyer and Reason (1976)	25.4	1.0, 0.75	Inductive
Tonnesen and Hansen (1981)	100	0.55	Inductive
Read and Flack (1987)	70	1.0	Inductive
Spearot and Murphy (1988)	58	0.344	Capacitive and resistive
Dwyer-Joyce et al. (2003)	75	0.5	Ultrasonic
Present work (2016)	98	0.255	Ultrasonic

4.1.1.1 Mechanical technique

Back in the 1950's an intensive experimental work, which experimentally validated the analytical approach of short-bearing approximation, was conducted by Dubois and Ocvirk (1953) using a mechanical technique. The vertical and horizontal displacements of the test shaft were measured by the four dial indicators (laboratory grade with 0.0001-inch (≈ 2.54 μm) divisions) which was set at the coordinate positions of each end of the test shaft, as shown in Figure 4.1. These tests were performed for each length-diameter ratio L/D of 0.25, 0.5, 1.0, 2.0 at combinations of the rotational speed (500, 1,000, 2,000, 2,500, 4,000, 5,000, and 6,000 rpm), the inlet oil pressure (40 and 100 pounds per square inch ($\approx$ 0.28 and 0.69 MPa respectively)), the maxi-

mum load on projected area 900 pounds per square inch ($\approx$ 6.2 MPa) and the maximum oil film temperature 161 °F ($\approx$ 72 °C).

The principle results were in useful agreement with theoretical analysis with short-bearing approximation in the low L/D range, 0.25, 0.5, 1.0; however, the result was not satisfactory in 2.0. These apparatus could only be arranged in laboratory environment with tailored components due to spacial limitation. In terms of reading accuracy, as the authors pointed out, the deflection of the test shaft by the applied load which could appear in the gauge readings have to be compensated from the film thickness value. It is noted that thermal deformation of the rig and the measurement equipment could be superposed on the reading, particularly if the related components consists of the materials of different thermal expansion coefficients.

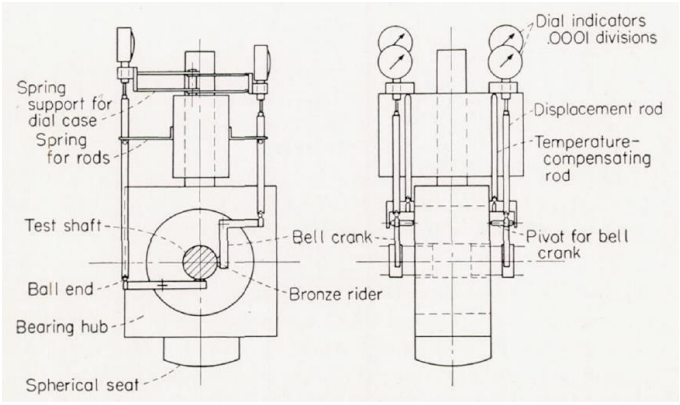

Figure 4.1: Schematic of mechanical technique (Dubois and Ocvirk, 1953).

4.1.1.2 Electrical technique

Inductive method. An experimental investigation of lubricant film thickness was examined on a ϕ100 mm diameter cylindrical journal bearing having a L/D of 0.55 by Tonnesen and Hansen (1981) using an electrical inductive method. The measurements were performed at 400 to 8000 rpm with the loads from zero to 9000 N in steady-state. The inductive probes were arranged in the test shaft in two planes each located 18.5 mm from the bearing mid-plane, as presented in Figure 4.2.

The results of eccentricity over attitude angle showed a consistent deviation from the theoretical locus. One drawback of this technique is the invasive nature for the probe installation. The probes need to be filled with non-magnetic material, an epoxy was used in their study. The cavity filled with the epoxy was approximately twice the diameter of the probe and one diameter deep.

The finish of the epoxy face could cause geometrical change with respect to the shaft surface, which could influence the film formation. Though the authors took a precautionary measure to cancel out the effect of thermal expansion (thermal coefficient of the epoxy is approximately 5 times that of steel) for an operating temperature 70 °C, at the rest of the operating temperature another calibration is required.

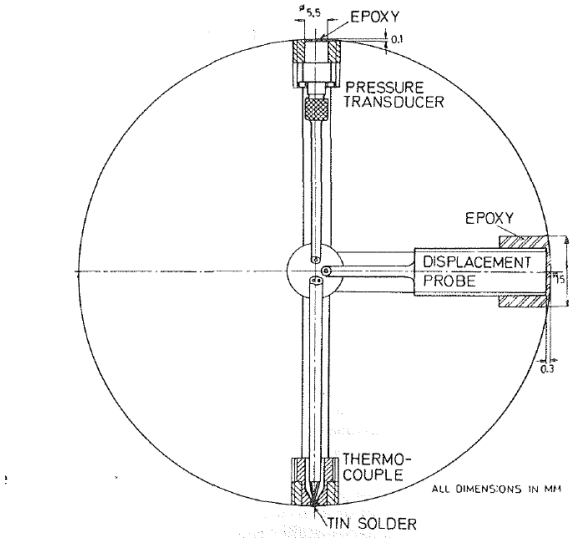

Figure 4.2: Schematic of inductive technique (Tonnesen and Hansen, 1981).

Capacitive and resistive method. Spearot and Murphy (1988) demonstrated an experimental work for film thickness measurement in a four-cylinder 2.5 L engine bearing. The authors compared the results obtained by two means - a capacitive method which assumed the film as a simple electric capacitor, and a resistive method which assumed the film as a simple electric resistance. The bearing was $\phi 58$ mm in diameter with 0.344 of L/D, respectively. One of the key procedures for the technique is to insulate the bearing electrically, as presented in Figure 4.3. In their study the insulation modification was achieved using a 0.127 mm plastic film separating the bearing from the rest of the block. The trials were examined at two different engine speed (1600 and 2500 rpm) and two loads that represents 50 percent throttle at each engine speed (72 and 91 Nm) with three oil sump temperatures (100, 120, and 140 °C).

Although fair agreement was found between the results measured by the two method qualitatively, the agreement to the absolute film thickness was poor. The authors concluded that the poor agreement and data scatter were attributed to the sensitivity of the parameters, oil conductivity for

the resistive method, and dielectric constant for the capacitive method, which were used to deduce the film thickness. It is also noted that the reading by the capacitive method is significantly affected by the presence of cavitation.

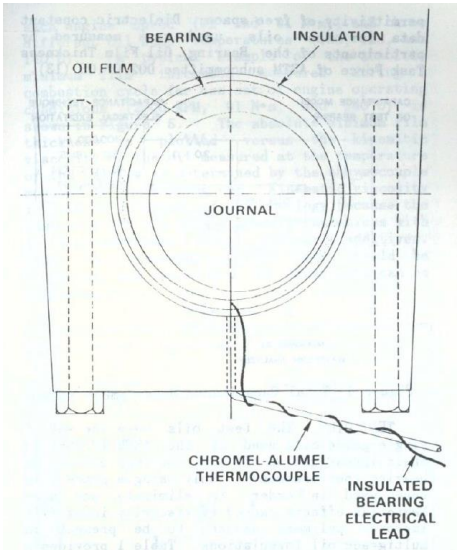

Figure 4.3: Schematic of capacitive technique (Spearot and Murphy, 1988).

4.1.1.3 Ultrasonic technique

Ultrasonic investigation with the aforementioned spring model for hydrodynamic oil film was performed by Dwyer-Joyce et al. (2003) on a cylindrical journal bearing. The main bearing profile was ϕ75 mm in diameter with 0.5 of L/D, and 25 μm of the radial clearance. A 1.1 MHz planar transducer was spring-loaded onto the surface of the bush with a water based couplant. The ultrasonic wave was pulsed and received by the transducer. Measurements recorded for Sommerfeld numbers in the range from 0.06 to 1 and films in the range from 4 to 20 μm showed repeatable and reasonable agreement with predictions based on classic Reynolds equation (Figure 4.5). The measurement limit was also suggested in terms of the reflection coefficient. The authors discussed on the two points which can be improved to profile the oil film more accurately.

Firstly, the spatial resolution can be improved if a smaller transducer element is used or the wave can be focused by arranging a lens to the element. Secondly, measurements in their work could only be recorded at a single place at the same time, by which the operator needs to take several measurement relocating the transducer in the circumferential direction.

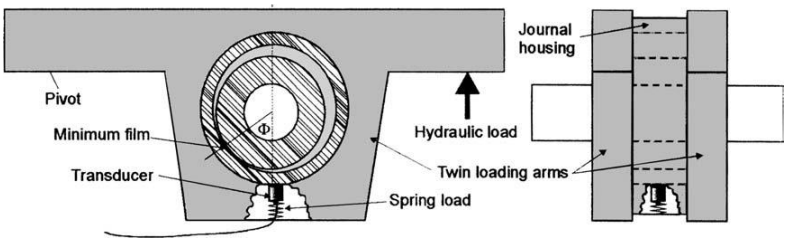

Figure 4.4: Schematic of ultrasonic technique (Dwyer-Joyce et al., 2003).

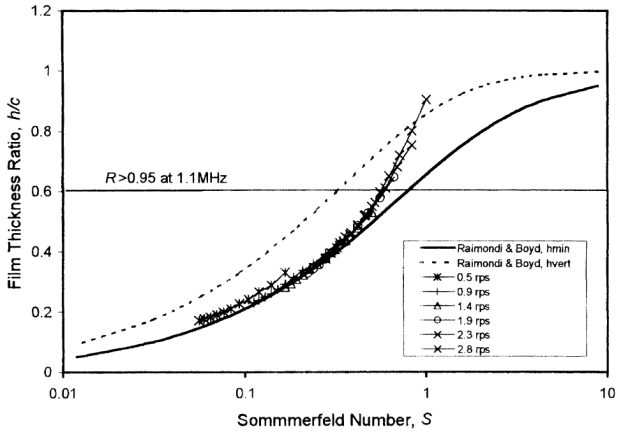

Figure 4.5: Film thickness measurements re-plotted on axes of Sommerfeld number against film thickness ratio. The predictions are shown. The horizontal line shows the limit of validity of the experiment (as R>0.95) (Dwyer-Joyce et al., 2003).

4.1.1.4 Summary

As has been discussed in this section, there exists pros and cons in each measuring technique to measure the oil film in journal bearing. Among all the applicable methods, the ultrasonic technique can be the most suitable and beneficial method for the objective of the present study. The aforementioned two issues in the ultrasonic technique are spatial resolution and the number of locations to capture the data in one trial. In this study, the spatial resolution will be improved by employing a smaller size of transducer element, and the latter issue will be solved by arranging a multi-channel capturing system, which has been successfully developed and implemented on a piston-cylinder application studied by Mills et al. (2012). The detail will be presented on the following section.

4.2 Construction of Journal Bearing Test Platform

In this section, the test platform for the oil film thickness measurement is presented. The platform was exclusively constructed for this study in order to represent the operational condition

of an automotive transmission journal bearing, such as relative rotational speed, load, viscosity/temperature/flow rate of oil. Firstly a general introduction regarding automotive transmission is briefly presented as well as detail of the operating conditions. Then the mechanical, lubricant feed, and electrical arrangement of the constructed test platform are presented followed by the ultrasonic apparatus and data acquisition arrangements.

4.2.1 Transmission for commercial vehicle

Transmission in automotive applications has been broadly used to provide optimum speed and torque for the driving conditions. Manual and semi-automatic transmissions are commonly used in commercial vehicles such as trucks or buses, yet automatic transmission or continuously variable transmission (CVT) are rarely used in such applications. The speed and torque are generated by a power source, mainly diesel engines, and transferred through the clutch, transmission, propeller shaft, final gear, axles shafts and tyres to drive the vehicle.

Figure 4.6: A 11 ton plus Gross Vehicle Weight truck.

4.2.1.1 Mechanical characteristics

The transmission focused on this study (presented in Figure 4.7) is incorporated with a 10,000 cc class diesel engine (L6, 2,200 Nm, 530 PS) in a 11 ton plus Gross Vehicle Weight both in truck (Figure 4.6) and bus. 12 gear ratios are made by three main-gear couples and two sub-gear couples (front and rear) in the transmission, although the number of gear couples corresponds with the number of gear ratios in typical layout of the transmission. The speed and torque from the engine are transmitted through the input shaft, then goes down to the counter shaft. The counter shaft drives the main shaft through the selected gear, then the final torque and speed conversion

is determined on the rear sub-gear couples (planetary gear system). For the transmission with manual selection system, the driver selects the gears manually by controlling the mechanical link which links the shifter knob and a shifting unit on the transmission. Whilst in the transmission with automated selection system, the driver selects the gears on the shifter knob, then the shifter knob sends electric signals to control a gear actuation unit in order to select the gear. The gears and the shafts are supported by needle bearings, taper roller bearings or journal bearings (shaft bearings). One of the front sub-gear couples, i.e. the input shaft and the bush (gear) composes of the journal bearing focused in this study, as shown in Figure 4.8.

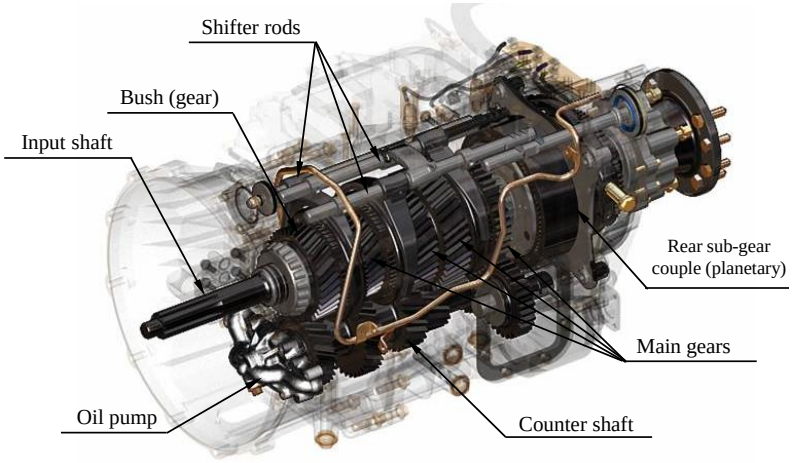

Figure 4.7: An illustration of the production 12-speed automotive transmission.

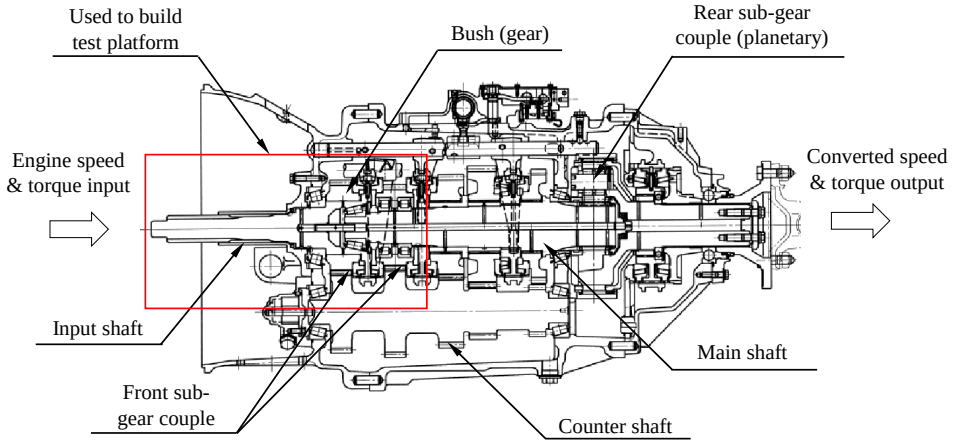

Figure 4.8: A cross-sectional view of the transmission.

4.2.1.2 Lubricants

The transmission is composed of several machine elements such as gear, synchroniser, seal, rolling bearing or journal bearing. Though both liquid and solid lubricants are used in the each

elements, a mineral oil based gear oil of GL-5 in the API service category is exclusively used for the journal bearing. The temperature of the gear oil varies from -30 °C to 130 °C during the vehicle operation, although the most frequently used range is roughly from 60 °C to 80 °C. The gear oil to the journal bearing is supplied by two means - splashing reserved oil and force feed system. The oil is splashed from the oil reserved in the bottom of the transmission casing by the rotating gear teeth aligned in the counter shaft. The amount of oil dragged into the load carrying area of journal bearing could be limited by this means.

The force feed system, which is the main source to supply oil to the bore of the bush, pumps the oil sucking the oil reserved in the transmission casing by a trochoid pump installed in the housing. The oil flow rate proportionally varies with the speed of the counter shaft since the pump is mechanically coupled with the counter shaft. The pumped oil flows through the clutch housing, oil filter, input shaft cover then the bore of the bush. Although most of the wear particles, debris or other contaminants are designed to be trapped by the filter, very fine particles smaller than the filter mesh can become circulated in the oil flow.

4.2.1.3 Relative rotational speed in journal bearing

One of the unique operational condition to which the journal bearing is exposed is comparatively low rotational speed, where it is difficult to generate an oil film. The shaft and bush (gear in this transmission) of the journal bearing has a relative rotation when the gear is not selected. Since the bush (gear) is driven by the counter shaft (as presented in Figure 4.8) when the gear is not selected, the shaft and the bush (gear) rotates at different speeds independently, therefore relative speed. Table 4.2 shows the relative speeds that the journal bearing yields in each input speed from the engine, from the idling speed to the maximum speed. The relative speed of the shaft and bush (gear) ranges from 61 rpm to 267 rpm within the engine capacity with this transmission's gear ratio. In the low engine speed where the engine can generate roughly its maximum torque, the relative speed is only 122 rpm. The experiments will follow these speed profiles, which will be presented in the following section in detail.

Table 4.2: Relative speed of the journal bearing with the engine speed variation.

Engine speed		Idling	Low	Middle	High	Max
Input shaft speed	rpm	500	1000	1500	2000	2200
Bush (gear) speed	rpm	561	1122	1682	2243	2467
Relative speed in journal bearing	**rpm**	**61**	**122**	**182**	**243**	**267**

4.2.2 Mechanical, lubricant feed and electrical arrangement

4.2.2.1 Mechanical arrangement

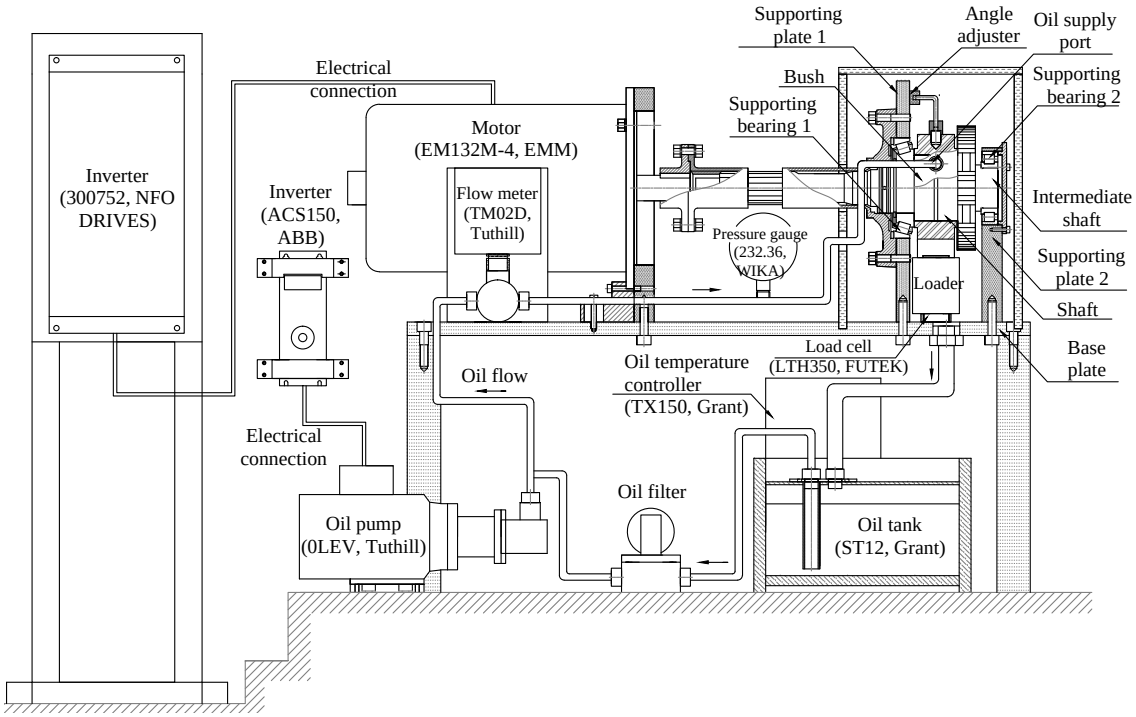

Figure 4.9: Overview of the journal bearing test platform.

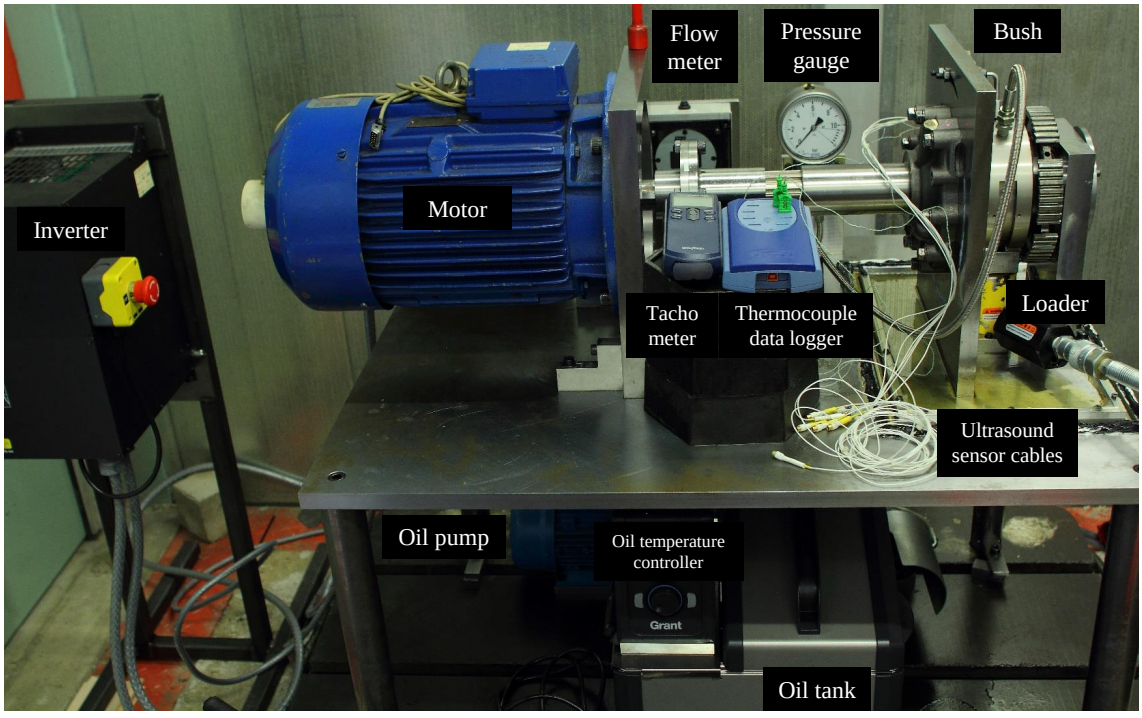

Figure 4.10: Photo of the journal bearing test platform.

The test platform is constructed using the journal bearing and the corresponding components of the production 12-speed automotive transmission as presented in Figure 4.8, Figure 4.9 and Figure 4.10. The shaft is secured by a taper roller bearing (supporting bearing 1) and another taper roller bearing which is connected to an intermediate shaft with a roller bearing (supporting bearing 2). The shaft is driven by an AC motor via the spline of the shaft. As the spline of the shaft and the coupling of the motor is a loose-fit both radially and circumferentially, undesirable stresses on the motor which could be caused by the misalignment between the motor and the shaft can be minimised. The supporting bearing 1 and 2 are mounted in the supporting plate 1 and 2 which is respectively bolted on the base plate. The angle adjuster connecting the supporting plate 1 and the bush is used to determine the angular position of the bush, that is, the angular position of the ultrasonic transducers held on the bush. The bush is stationary while the shaft is spun and the load is applied to the journal bearing by a hydraulic loader perpendicular through the bush.

Journal bearing. Figure 4.12 and Table 4.3 summarises the main dimensions of the journal bearing. The photos of bush bore and shaft are presented in Figure 4.11. The journals of the bush and shaft are ground-finished after the heat treatment, carburising and quenching. The journal bearing is split into two journal parts (front and rear journal) by the shaft and bush grooves (5 mm and 15 mm in width respectively), being 25 mm in nominal width, L, respectively. Because of the chamfered and the rounded edge of the shaft and bush, the actual load carrying width are slightly shorter than the nominal width.

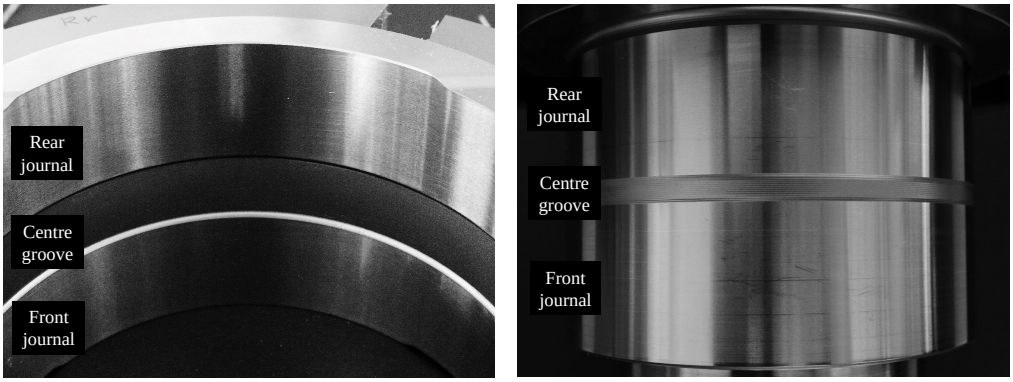

(a) Bush bore (b) Shaft

Figure 4.11: Photos of the bush bore and shaft.

The detail is presented in the sction of X1 in Figure 4.12. The two holes of $\phi 3$ mm are

arranged on the groove centre of the shaft. The radial clearance, c_r, is 35 μm with ϕ98 mm of nominal diameter, D, being 0.255 in the ratio of nominal diameter and nominal width, L/D. The slot holding the ultrasound transducers are located 120° from the angle adjuster anticlockwise and the adjacent slots are 30° away, respectively. The oil supply port of BSPT 1/4" is located 30° from the angle adjuster clockwise on the bush.

Table 4.3: Dimensions and property of the journal bearing.

Component		Shaft	Bush
Material		SCM420H	
Heat treatment		Carburising and quenching	
Nominal diameter D	mm	98	
Nominal width L (Fr and Rr respectively)	mm	30	25
Width diameter ratio L/D		0.255	
Radial clearance c_r	μm	35	
Roughness average R_a			
Tangential	μm	0.060	0.056
Axial	μm	0.123	0.110
Density ρ_s	kg/m^3	7850*	
Speed of sound c_s	m/s	5803	

∗ Smithells (1992)

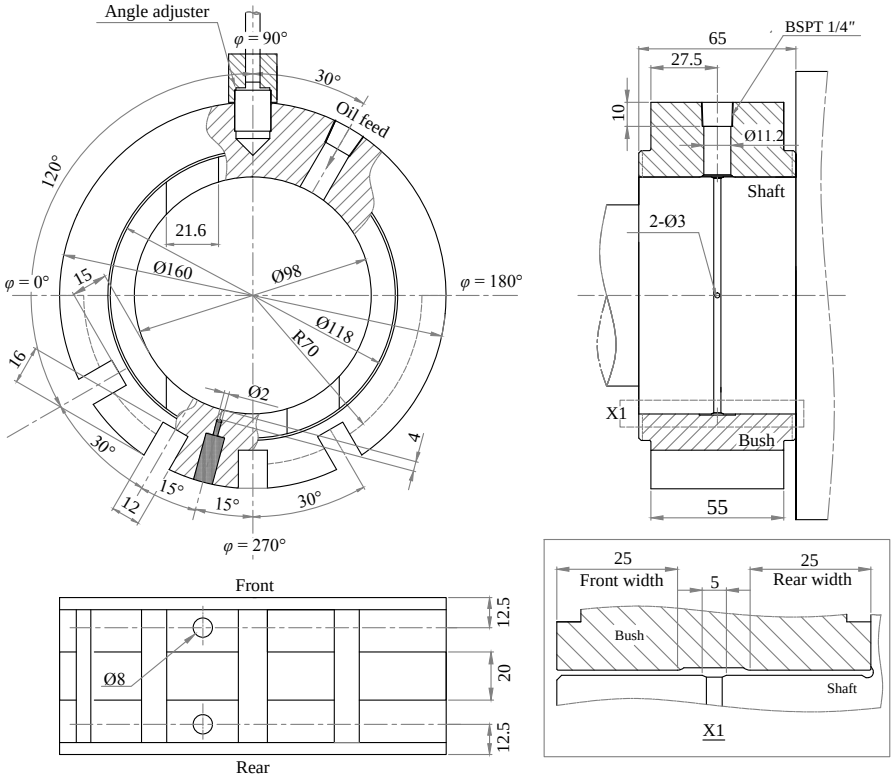

Figure 4.12: Dimensions of the bush and shaft.

The density and speed of sound used for the film thickness determination are presented in Table 4.3. The roughness profile and the roughness average R_a in axial and tangential direction were measured in the journal of the bush and the shaft as summarised in Figure 4.13.

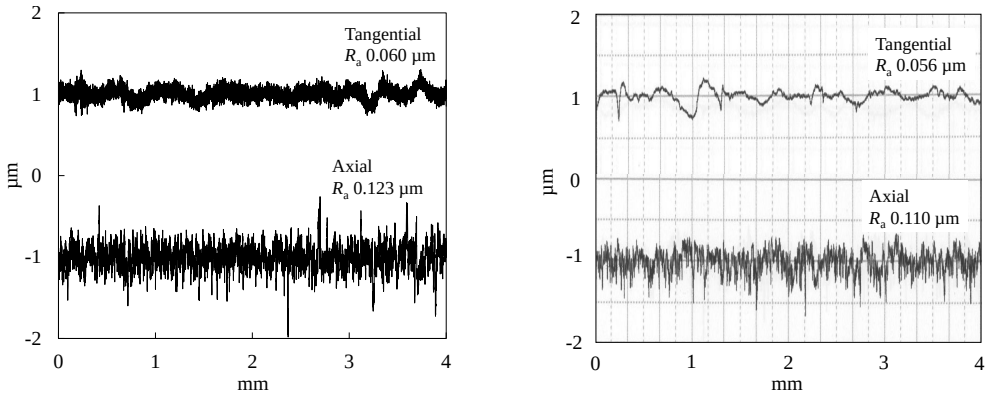

(a) Shaft journal (b) Bush journal

Figure 4.13: Measured roughness on the shaft and bush journal.

4.2.2.2 Lubricant Feed and Electrical Arrangement

Lubricant feed arrangement. The lubricant feed arrangement was designed to circulate the oil at a controlled temperature and flow rate as presented in Figure 4.9 and Table 4.4.

Table 4.4: Summary of lubricant feed arrangement.

Oil temperature controller (TX150) and bath (ST12) from Grant		
Operating temperature range	°C	5 to 150
Heater power (230 V)	kW	1.9
Bath capacity	L	12
Oil pump (0LEV) from Tuthill		
Pumphead		Internal gear pump
Rated power of coupled motor	kW	0.12
Flow rate	L/min	6.8 at 1800 rpm
Operating viscosity range	cSt	1 to 1078
Maximum operating temperature	°C	246
Maximum operating pressure	MPa	3.45
Flow meter (TM02D) from Tuthill		
Flow range	L/min	0.1 to 1.1
Accuracy	%	±0.25
Maximum operating pressure	MPa	10.3
Operating temperature range	°C	-40 to 150

The operable maximum temperature of the feed system is 150 °C. The oil pump (0LEV from Tuthill) circulates the oil stored in the oil tank (TX150 and ST12 from Grant) where the oil temperature is controlled from the room temperature to 150 °C. The operating viscosity range of

the pump is from 1 cSt to 1078 cSt which represents a 16 °C to 344 °C temperature range of the oil (GELCO5090) used in this study. The oil filter which is actually used in the transmission was arranged in between the oil tank and the pump to remove debris or wear particles. The volumatic flow rate and the pressure of the oil flow were measured by using a flow meter (TM02D from Tuthill) and a pressure gauge (232.36 from WIKA). The oil was pumped through the oil supply port (BSPT 1/4") on the bush into the load carrying area.

Electrical arrangement. The electrical arrangement was designed to drive the shaft and to run the oil pump as presented in Figure 4.9 and Table 4.5. The 3-phase main AC motor (EM132M-4 from EMM) controlled by the inverter (300752 from NFO DRIVES) drives the shaft. The motor was selected based on the available torque and speed in order to represent the operating conditions of the transmission. The NFO DRIVES inverter which has been successfully used in an ultrasound measurement in the University of Sheffield was selected because of its low background noise emission during operation. The oil pump was driven by another inverter (ACS150 from ABB) to meet the flow requirement as described above.

Table 4.5: Summary of electrical arrangement.

Motor (EM132M-4) from EMM		
Rated power	kW	7.5
Rated speed	rpm	1752
Nominal torque	Nm	44.8
Maximum torque / Nominal torque	Nm	2.3
Supply voltage		3-phase 230 V
Inverter (300752) from NFO DRIVES		
Rated power	kW	7.5
Output frequency range	Hz	0 to 150
Output voltage wave form		sine
Supply voltage		3-phase 230 V
Inverter for pump motor (ACS150) from ABB		
Rated power	kW	0.37
Supply voltage		3-phase 230 V

4.2.3 Ultrasonic Instrumentation and Acquisition Arrangement

A lead zirconate titanate (PZT) longitudinal ultrasonic transducer (from MEGGIT) of rectangular shape with 5 MHz centre frequency was chosen with consideration in the limitations of the measurable film thickness range (as shown later in Figure 4.19). The area on the interface where the emitted ultrasonic wave interacts is approximately equal to the size of the transducer (5 mm $\times$ 2 mm) as shown in Figure 4.14. Six bare transducers (UTF1 to UTR3 as presented in Figure 4.15

and Figure 4.16) that is pre-tailored in its shape are placed down on the bottom surface of the slot so that the emitted wave strikes normal to the oil layer (radial direction of the bush and shaft). The shorter side of the transducer (i.e. the side of 2 mm) is arranged in the circumferential direction of the bearing so that the oil film profile in the circumferential direction can be measured with good resolution. The distance from the bottom surface of the slots to the oil layer are set at 15 mm, therefore 30 mm for the round trip. A high-temperature strain gauge adhesive (M-Bond 610 from Micro Measurements) which has an upper operational temperature limit at 230 °C was used to glue those transducers. Shielded coaxial cables were soldered on the electrode (screen printed silver) using lead-free iron plus flux (Powerflow Flux from FRY) in order to prevent the temperature from exceeding the curie point at which the depolarisation occurs. The bare elements and cables were protected from physical, heat, or chemical aggression by using a high-temperature resistant silicon gasket.

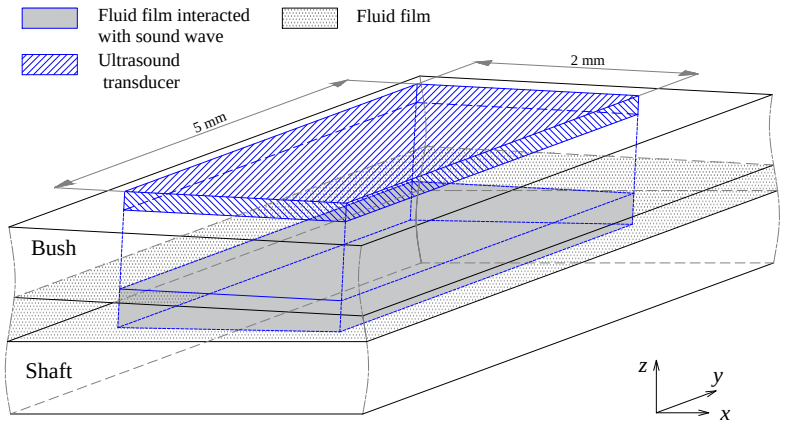

Figure 4.14: Schematic of ultrasound transducers and sound wave interaction with fluid film.

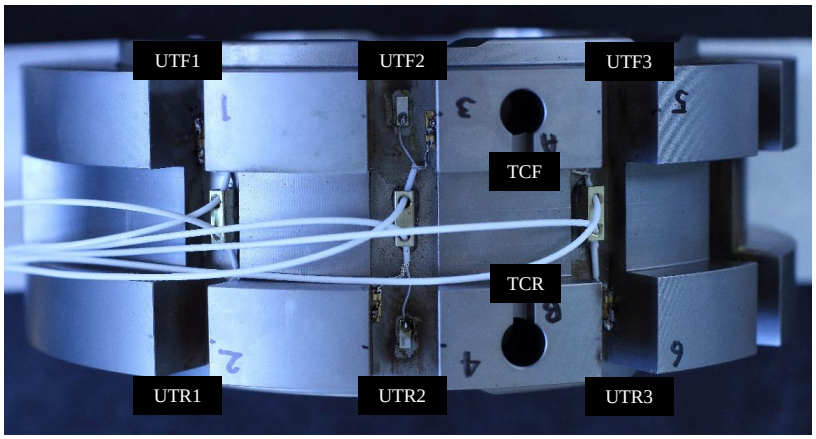

Figure 4.15: Installed ultrasound transducers and thermo couples on the bush.

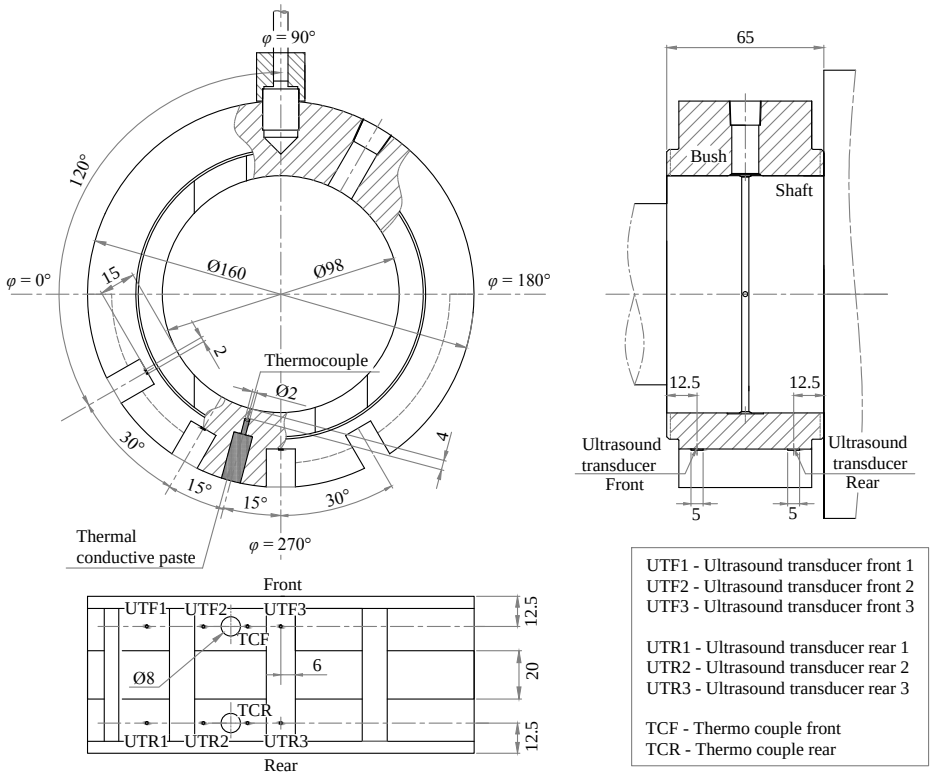

Figure 4.16: Installed ultrasound transducers and thermo couples on the bush.

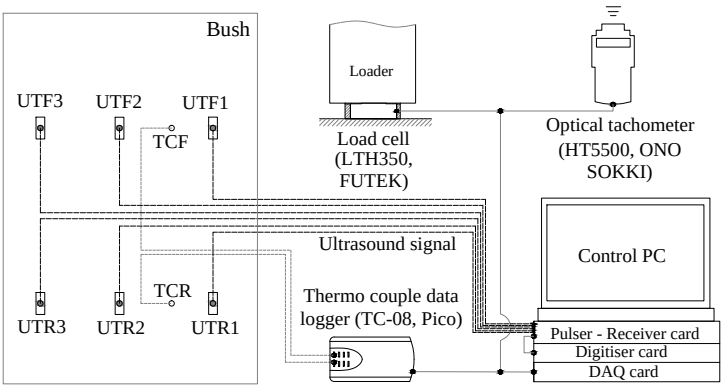

Figure 4.17: Ultrasonic and data acquisition arrangement.

As presented in Figure 4.17 and Figure 4.18, a pulser-receiver card fitted in a control PC was used to excite the piezoelectric transducer and receive the reflected pulses from the interface. A top-hat shape excitation voltage of 100 ns duration was applied to the transducer. The repetition rates are controllable upto 80 k pulses per second which are divided by active channels, i.e. 10 k pulses per second per channel with eight active channels. The reflected signal received was then digitised by the digitiser card at 100 M samples per second with 12 bit resolution and recorded on

the hard disc drive for a post-process analysis. This series of process, i.e. pulsing, receiving and digitisation can be performed in the single and comparatively compact kit.

Two type k thermocouples (TCF and TCR as presented in Figure 4.15) are mounted on sub-surface of the load carrying area to monitor the temperature. The two holes of $\phi 8$ mm with two smaller holes of $\phi 2$ mm for the thermocouple instrumentation are arranged between the slots holding the ultrasound elements. The distance from the spot of the thermocouple and the bush bore surface was set at 4 mm and the space around the spot was filled by using a high thermal conductivity paste (OMEGATHERM 201 from OMEGA). The paste is suitable for continuous use up to 200 °C. Load applied to the bush by a hydraulic loader was monitored by a load cell mounted beneath the loader and rotational speed of shaft was monitored by an optical tachometer. Those parameters, temperature, rotation speed, and load are monitored during the test runs with a DAQ card on the control PC.

Figure 4.18: Ultrasonic and data acquisition apparatus.

4.3 Experimental Investigations

In this section, the experimental results on film thickness measurement are presented. Prior to the result the experimental procedure of the film thickness determination is explained in the first part of this section followed by two preliminary tests: a measurement of speed of sound with oil temperature variation and a validation measurement in static condition comparing with the known annular clearance of the journal bearing. The measurement results obtained under five test conditions are then discussed as well as the cavitation in the diverging section of the bearing and the thermal drift of wave signal with the operating temperature variation.

4.3.1 Film thickness determination procedure

As presented in the previous chapter, the present work used the amplitude method of ultrasonic reflection using the spring model to determine the film thickness. Figure 4.19 shows the magnitude of reflection coefficient curves in frequency domain with variation of film thickness predicted by using Equation (2.75) with the oil and journal bearing properties (Table 4.3 and Table 4.6). The -6 dB bandwidth of the ultrasound sensor of 5 MHz centre frequency (used in this study) in which the amplitude dropped to -6 dB of its peak value was also presented in the figure. The bandwidth is approximately from 4.5 MHz to 6.5 MHz.

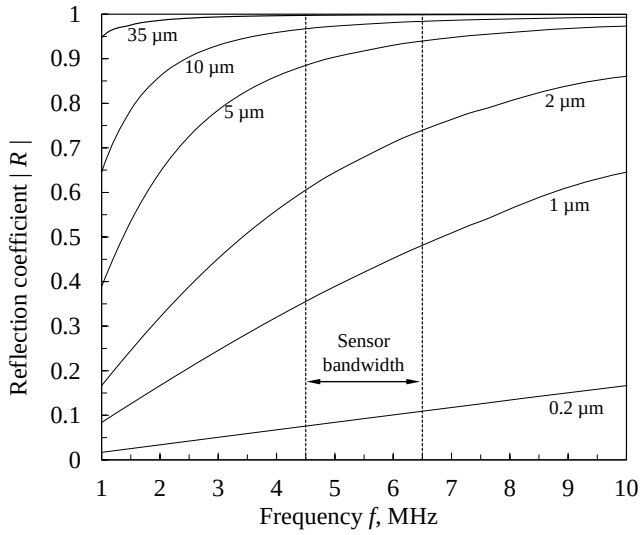

Figure 4.19: Reflection coefficient curves with the various oil film thickness at steel (bush) - lubricant (GELCO5090) - steel (shaft) interface at 80 °C oil temperature.

4.3.1.1 Reference signal

The lubricant film thickness is determined by using Equation (2.75) with the measured magnitude of reflection coefficient and the acoustic properties of the oil and the journal bearing. In theory the $|R|$ is the ratio of the amplitude of the incident wave signal and the reflected wave signal from an interface of interest. Since it is difficult to measure the amplitude of the incident wave signal itself, the amplitude of "reference signal" is practically used to deduce the reflection coefficient. The amplitude of the reference signal can be approximated by several approaches, which will be discussed in the following section.

Steel-air interface. The proportion of sound wave reflection in the boundary of a two-layer system is determined by the acoustic impedances of the layers as shown in Equation (2.44). If the acoustic impedances are sufficiently dissimilar e.g. steel/air interface, almost all the incident wave bounces back. Therefore the reflected signal can be practically used as reference signal. The reflection coefficient $\mid R(f) \mid$ is then expressed as:

$$\mid R(f) \mid = \frac{A(f)}{A_{\text{ref}}(f)} \mid R_{\text{ref}} \mid, \tag{4.1}$$

where $A(f)$ is the signal amplitude from the layer of interest, $A_{\text{ref}}(f)$ the amplitude of the reference signal, $\mid R_{\text{ref}} \mid$ the reflection coefficient from the reference boundary. The reflection coefficient $\mid R_{\text{ref}} \mid$ in the steel/air interface is very close to unity (= 0.99982) regardless the wave frequency as shown in Equation (2.44). Therefore Equation (4.1) can be simplified for convenience as:

$$\mid R \mid = \frac{A}{A_{\text{ref}}}. \tag{4.2}$$

In some mechanical elements it would be easy to capture the reference signal in such steel/air boundary (e.g. ball bearings or roller bearings when the rolling elements are absent in the interface) during the test. While in the journal bearing where the annular clearance between the shaft and bush is filled with lubricant once the bearing is assembled (i.e. steel/oil/steel interface), it is hard to capture the reference signal from such steel/air interface. The simplest approach could be to record the reference signal before the journal bearing is assembled. This approach could be limited in cases that the transducer is not subject to significant temperature change.

Since the energy output from the piezoelectric material is subject to the temperature variation and the attenuation in the bonding layer also vary with temperature, the thermal drifts on both the signal amplitude and the phase correspondingly occurs. This thermal effect could be calibrated by measuring the reference signal changes along the temperature variation such as recording them in a temperature controlled chamber. However, one of the inevitable issues of this calibration approach is that it is technically very difficult to represent perfectly the same thermal conditions in the chamber with those in the real measurement situations. Because the heat source (usually the

ambient temperature change in such chambers whereas mainly frictional heat in the real measurement situation) and eventual thermal distribution over and around the transducers are different in such chambers with the real measurement arrangement, the thermal behaviour to the signal amplitude might not be the same between them.

In order to minimise such thermal distribution effect, the reference signal with temperature variation can be recorded after a test run when the journal bearing disassembled but still warm. This approach was implemented by Kasolang and Dwyer-Joyce (2008a) and the obtained calibration curve over the temperature is shown in Figure 4.20. Although the amplitude decreased consistently as temperature increased in their study, the prediction curve obtained could be only applicable to the transducer specifically. Additionally it is technically difficult and unsafe to disassemble the bearing at the higher operating temperature.

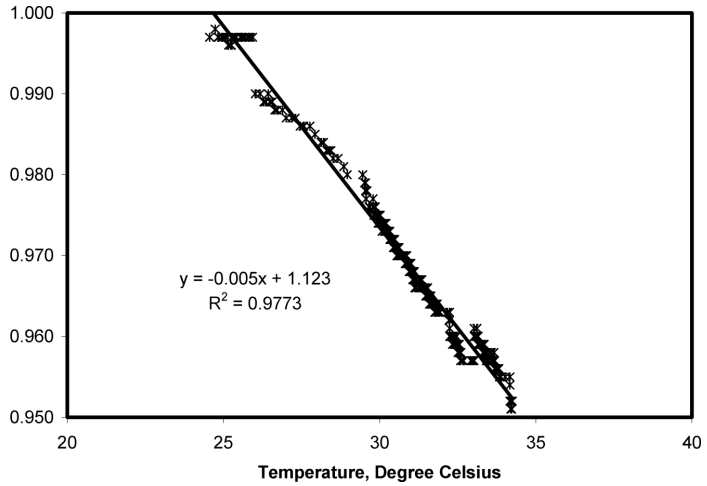

Figure 4.20: Variation in the ultrasonic reflection coefficient as the sensor temperature changes (Kasolang and Dwyer-Joyce, 2008a).

Amplitude and phase measurement. There is an approach to deduce the reference signal by measuring simultaneously the signal amplitude and phase, which was proposed by Reddyhoff et al. (2005). As detailed above, the amplitude of the reflection coefficient is given by Equation (4.2), similarly the phase Φ_R of the reflection coefficient is given by the phase of the wave reflected from a film of interest ϕ and the phase of the completely reflected wave ϕ_{ref} as:

$$\Phi_R = \phi - \phi_{ref}. \tag{4.3}$$

Equation (4.2) and Equation (4.3) can be substituted into Equation (2.77) gives:

$$A = A_{\text{ref}} \cos(\phi - \phi_{\text{ref}}). \tag{4.4}$$

In order to deduce A_{ref} and ϕ_{ref} (i.e. constants in the reference signal), the amplitude A and phase ϕ are measured simultaneously as the oil film thickness varies. The data pairs are plotted and a least mean square curve is fitted to give the two constants A_{ref} and ϕ_{ref} at a given frequency, as shown in Figure 4.21. The measured and the deduced reference values showed excellent agreement in their study. One of the beneficial points of this approach is that this can be performed with the journal bearing assembled filled with oil. However, this approach is also influenced by the temperature sensitivity on the piezoelectric transducer and the bonding layer. Since the thermal drift appears on both the amplitude and phase, the curve would vary in each thermal conditions.

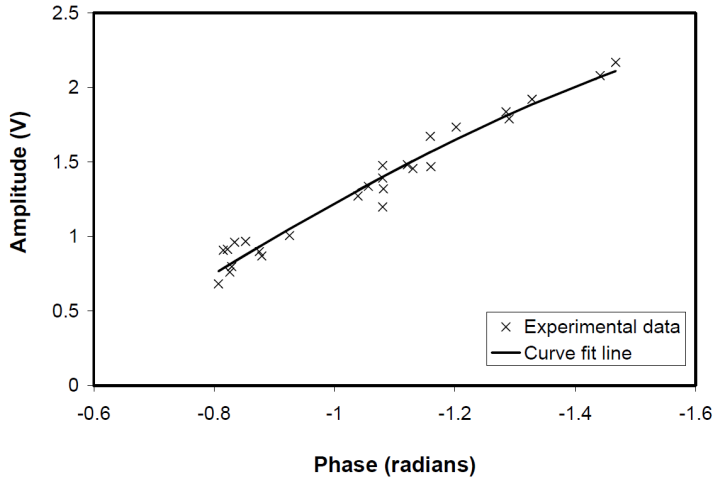

Figure 4.21: Plot of amplitude against phase at the centre frequency of the wave reflected from the oil film, with LMS curve-fit line (Reddyhoff et al., 2005).

Steel/thick oil layer/steel interface. Another approach can be also conducted with the bearing assembled and filled with oil. The reference signal is captured in a thick annular clearance filled with oil (i.e. steel/thick oil layer/steel interface) where the reflection coefficient is close to unity. Such thick film in the journal bearing of present study can be created to spin the shaft in conditions of very high Sommerfeld reciprocal S_r (e.g. when very low load applied), where the shaft spins almost concentrically against its bush. This results in the annular gap being almost same as the radial clearance (35 μm in the journal bearing in this study) regardless the angular positions. Within the bandwidth of the selected transducer (approximately from 4.5 MHz to 6.5 MHz), the

reflection coefficients are very close to unity with the 35 μm thick oil layer, being 0.9967 at 4.5 MHz and 0.9981 at 6.5 MHz, respectively (presented as a curve labelled as 35 μm in Figure 4.19). If the reference signal measurements are performed just before the measurement in the interface of interest, the thermal drift of the signal can be minimised.

Similar to Equation (4.1) the reflection coefficient in this approach can be given as:

$$| R(f) | = \frac{A(f)}{A_{\text{ref}}(f)} | R_{\text{ref}}(f) |, \tag{4.5}$$

where $A(f)$ is the signal amplitude from the layer of interest, $A_{\text{ref}}(f)$ the amplitude of the reference signal, $| R_{\text{ref}}(f) |$ the reflection coefficient from the reference interface. When $| R_{\text{ref}}(f) |$ is close to unity then it can be neglected for ease of the use. It is obvious that if $| R_{\text{ref}}(f) |$ is not close to unity in the usable frequency range of a selected sensor at a thick film available in a selected bearing profile, $| R_{\text{ref}}(f) |$ should remain in the equation. In this study, steel/ thick oil layer/steel approach was exclusively used for the reference signal, neglecting $| R_{\text{ref}}(f) |$ term in Equation (4.5).

4.3.1.2 Signal processing

The first step to determine the film thickness is to measurement the reference signal using the aforementioned approach and to measure the measurement signal in a layer of interest.

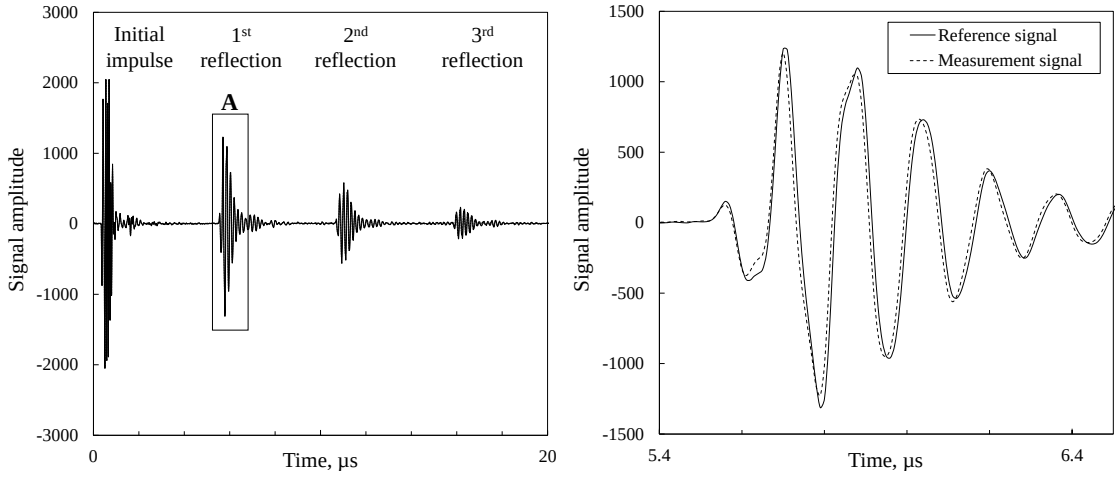

(a) Reflected reference and measurement signals

(b) Signals at the window **A**

Figure 4.22: Reflected reference and measurement ultrasound signal in time domain.

Figure 4.22(a) shows a wave signal data over time domain measured in a test condition per-

formed in this study. The sound wave generated by the initial impulse travels through the medium, reflected back from the interfaces and then received by the transducer. Figure 4.22(b) shows the reference and the measurement reflections overlay at the 1st reflection as sampled with the window **A**. Both the signals sampled are then converted to the frequency domain (Figure 4.23) via a fast Fourier transform (FFT).

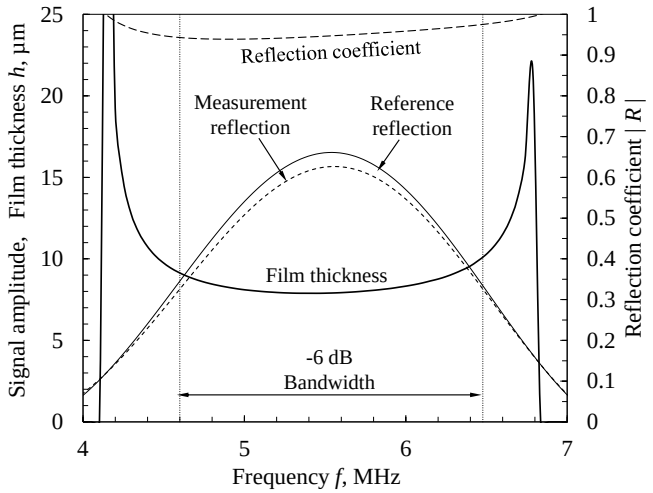

Figure 4.23: Reflected ultrasound amplitude, reflection coefficient $|R|$, and deduced film thickness h in frequency domain.

Figure 4.23 summarises four curves in frequency domain, that is, the reference reflection, measurement reflection, reflection coefficient obtained by Equation (4.5), and film thickness curve deduced by Equation (2.75), as well as the -6 dB bandwidth of the sensor. As seen in the figure, the deduced film thickness is satisfactorily consistent within the bandwidth as supposed to be in the theory. The median value of the deduced film thickness within the bandwidth was plotted for the analysis in the following experimental section.

4.3.2 Preliminary measurements

Prior to the film thickness measurements in the operational conditions, two preliminary tests were conducted. Firstly the speed of sound of the oil was measured with temperature variation using a small oil-filled chamber. Then an oil film thickness test was also performed using the test platform in static condition for validation. The results were compared with the known annular clearance between the bush and shaft.

4.3.2.1 Speed of sound measurement of the oil with temperature variation

The speed of sound travelling through the oil used in this study was measured with temperature variation by using a time of flight method in an oil-filled chamber. The method is based on the calculation with material thickness (or depth) and the round trip time of flight through the materials measured by the ultrasound transducer. The equation is simply given as:

$$c = \frac{2T}{t}, \tag{4.6}$$

where c is the speed of sound, T the material thickness and t is the time of flight. The main property of the oil used in this study (GELCO 5090 from Shell) is presented in Table 4.6. The schematic of the oil-filled chamber which is composed of two perspex plates and an aluminium bath is presented in Figure 4.24. The perspex was selected based on the acoustic mismatch between the oil. The transducer glued on the perspex plate emits and receives the wave signal which travels and reflects back from the 1st and 2nd interfaces. The oil temperature was controlled by monitoring the value via an installed thermocouple.

Table 4.6: Lubricant property of GELCO 5090 from Shell (at atmospheric pressure).

API category		GL5
API viscosity rating		90
Kinematic viscosity ν_o at 40 °C	cSt	199.1
Kinematic viscosity ν_o at 100 °C	cSt	18
Density ρ_o	kg/m^3	$-0.614T_o$+904.2*
Speed of sound c_o	m/s	-2.98T_o+1646

∗ ISO 91-1:1992 (1992)

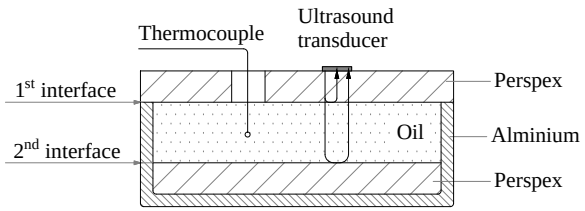

Figure 4.24: Schematic of the oil-filled chamber to measure the speed of sound through the oil with temperature variation.

The measured speed of sound variation over the oil temperature 30 °C to 80 °C is summarised in Figure 4.25 and compared with a line of a motor oil measured in previous work by Mills et al. (2012). The speed of sound decreased almost linearly as the temperature was increased,

which agreed with the result by Mills. The fit 1st polynomial line of the measured speed of sound yielded $c_o = -2.98T_o + 1646$ with 0.975 of R^2 (coefficient of determination) where T_o is the oil temperature in °C. The obtained line was then used for the determination of the film thickness in the following measurement.

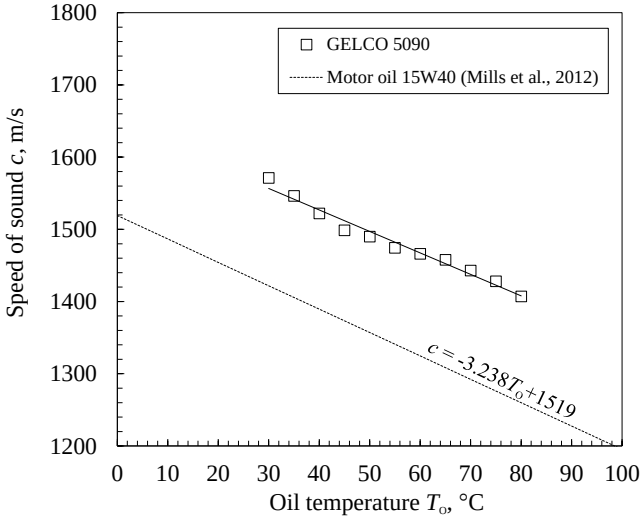

Figure 4.25: Measured speed of sound variation over the oil temperature in comparison with the curve from Mills et al. (2012).

4.3.2.2 Film thickness measurement under static condition

An ultrasonic film thickness measurement with the spring model was examined under static condition in the oil-filled annulus of the constructed journal bearing test platform prior to the film thickness measurement under the operational condition. The film thicknesses were deduced by using the properties of the oil and bearing listed in Table 4.12 and Table 4.24, and reflected ultrasonic signals received by the six transducers positioned on the bush. As shown in Figure 4.26, a load was applied at $\varphi = 270°$ so that the annular clearance becomes zero at $\varphi = 270°$. The film thickness measurements were conducted three times at each angular positions where the geometrical annular clearance were a range of approximately 3 μm to 13 μm, which covers the predicted oil film thickness range in the operational conditions.

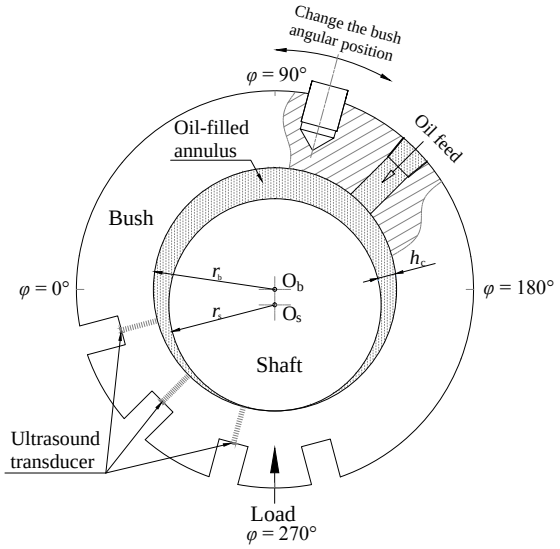

Figure 4.26: Schematic of an oil-filled annulus measured under static condition.

The film thickness measured was then compared with the geometrical annular clearance of the bush and shaft. The geometrical annular clearance curve with the surface roughness neglected, h_c is expressed as (Dwyer-Joyce et al., 2003):

$$h_c = r_b\left[1-\left(\frac{r_b-r_s}{r_b}\right)^2\sin^2(\varphi-90^\circ)\right]^{0.5} - r_s + (r_b-r_s)\cos(\varphi-90^\circ), \tag{4.7}$$

where r_b and r_s are the radii of the shaft and bush, φ the anglular position as shown in Figure 4.26.

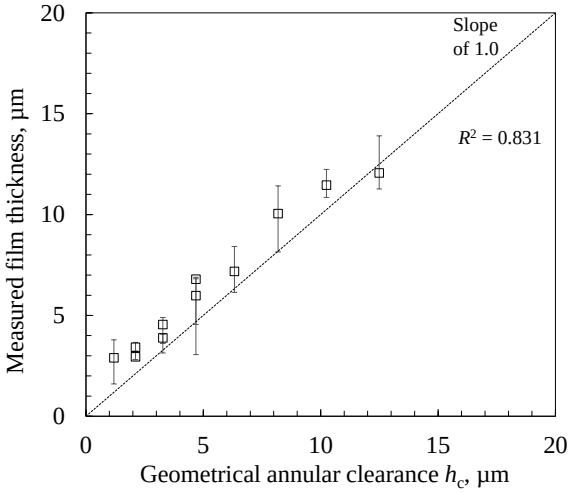

Figure 4.27: Film thickness measured in the static condition and film thickness deduced by the geometrical solution.

The median values of the measured oil film thickness are plotted with the corresponding error

bars as presented in Figure 4.27. As shown, the film thickness measured by ultrasound reflection agreed well with the geometrical solution. The coefficient of determination R^2 to the slope of 1.0 yielded 0.831. By this good agreement the validity of the oil film thickness measurement with the spring model and properties of the oil and bearing on this test platform was confirmed.

4.3.3 Film thickness measurements in operational conditions

4.3.3.1 Test conditions

Following the experimental validation under the static condition, the film thickness measurements were examined under steady state of fixed spinning speeds and a fixed applied load after the temperatures monitored by the thermocouples were saturated. The test conditions (test conditions **a** to **e**) represents the operational conditions of the automotive transmission.

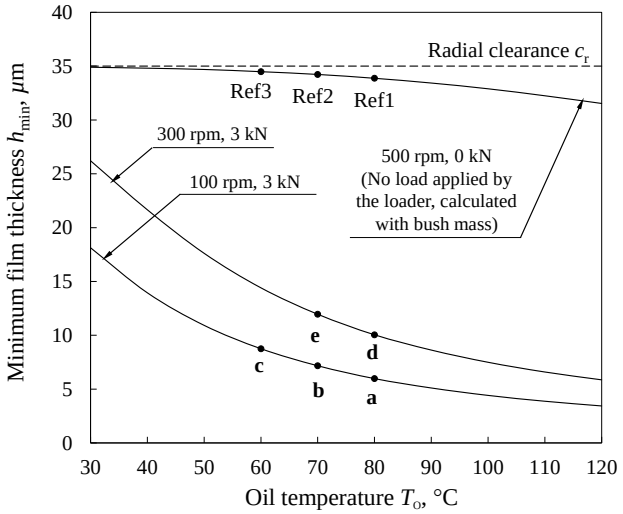

Figure 4.28: Theoretical film thickness deduced by the short-bearing approximation over oil temperature variation.

The reference signal were measured in the corresponding oil temperatures with no applied load just before the measurement signals were captured. In the reference signal measurements, the reflection coefficients were assumed to be close to unity regardless the circumferential position as previously discussed. The theoretical minimum film thicknesses curves obtained with the short-bearing approximation over the oil temperature as well as the plots of the test conditions (shown as **a** to **e**) and the conditions in which the reference signals were sampled (shown as Ref1 to Ref3 calculated with the bush mass 4.8 kg) are summarised in Figure 4.28. The temperatures, 60 °C, 70 °C and 80 °C, at the test run are set using the values read from the thermocouples in subsurface of the bush bore, whose temperatures were also used to deduce the viscosity, density

and speed of sound of the oil for the film thickness determination. During these trials oil was fed into the bearing at a volumatic flow rate of 1.5 L/min, and a load of 3 kN was applied (at $\varphi = 270^{\circ}$), at shaft rotation speeds of 100 rpm and 300 rpm. The pressures monitored in the pressure gauge just before the oil inlet port were confirmed to be 0.04 MPa at 80 °C, 0.06 at 70 °C, and 0.1 MPa at 60 °C in the conducted tests. These externally given pressures were neglected in the theoretical film thickness calculations as those are considered to be sufficiently smaller than pressures hydrodynamically generated.

Table 4.7: Test condition for measurement and reference signals.

Symbol	Rotation speed of shaft ω	Load applied W	Temperature of TCF, TCR T	Supplied oil flow rate Q	Pressure at inlet port P_{in}	Pulse rate per channel
	rpm	kN	°C	L/min	MPa	Hz
a	100	3	80	1.5	0.04	167
b	100	3	70	1.5	0.06	167
c	100	3	60	1.5	0.1	167
d	300	3	80	1.5	0.04	167
e	300	3	70	1.5	0.06	167
Ref1	500	0	80	1.5	0.04	167
Ref2	500	0	70	1.5	0.06	167
Ref3	500	0	60	1.5	0.1	167

Six data sets were captured in a trial from the embedded six transducers. The measurements were conducted three times at each angular position under a test condition. The median value of the three measurement data was plotted as well as the maximum (top error bar) and the minimum (bottom error bar) values. In order to profile the oil film, the bush having the transducers were swept circumferentially by an angular step of 3° by using the angular adjuster. In total roughly 36 to 48 points of data were obtained in a test condition.

4.3.3.2 Experimental results

The film thickness measurements were performed at test condition **a** to **e** and plotted over the angular position φ where the wave was captured. As summarised in Figure 4.29 the measured film thickness and the attitude angle favourably agreed with the theoretical curves deduced by the short-bearing approximation in all the test conditions performed. The error to the median value generally increased as the film thickness increased because the obtained reflection coefficient $\mid R \mid \rightarrow 1$ the film thickness $h \rightarrow \infty$ as presented in Equation (2.78) in Chapter 2. In this measurement, around 15 μm in the film thickness was found to be the measurable upper limit,

corresponding to a reflection coefficient of 0.98 at 4.5 MHz. A similar upper limit 0.98 in the reflection coefficient was confirmed in a previous work by Mills et al. (2012).

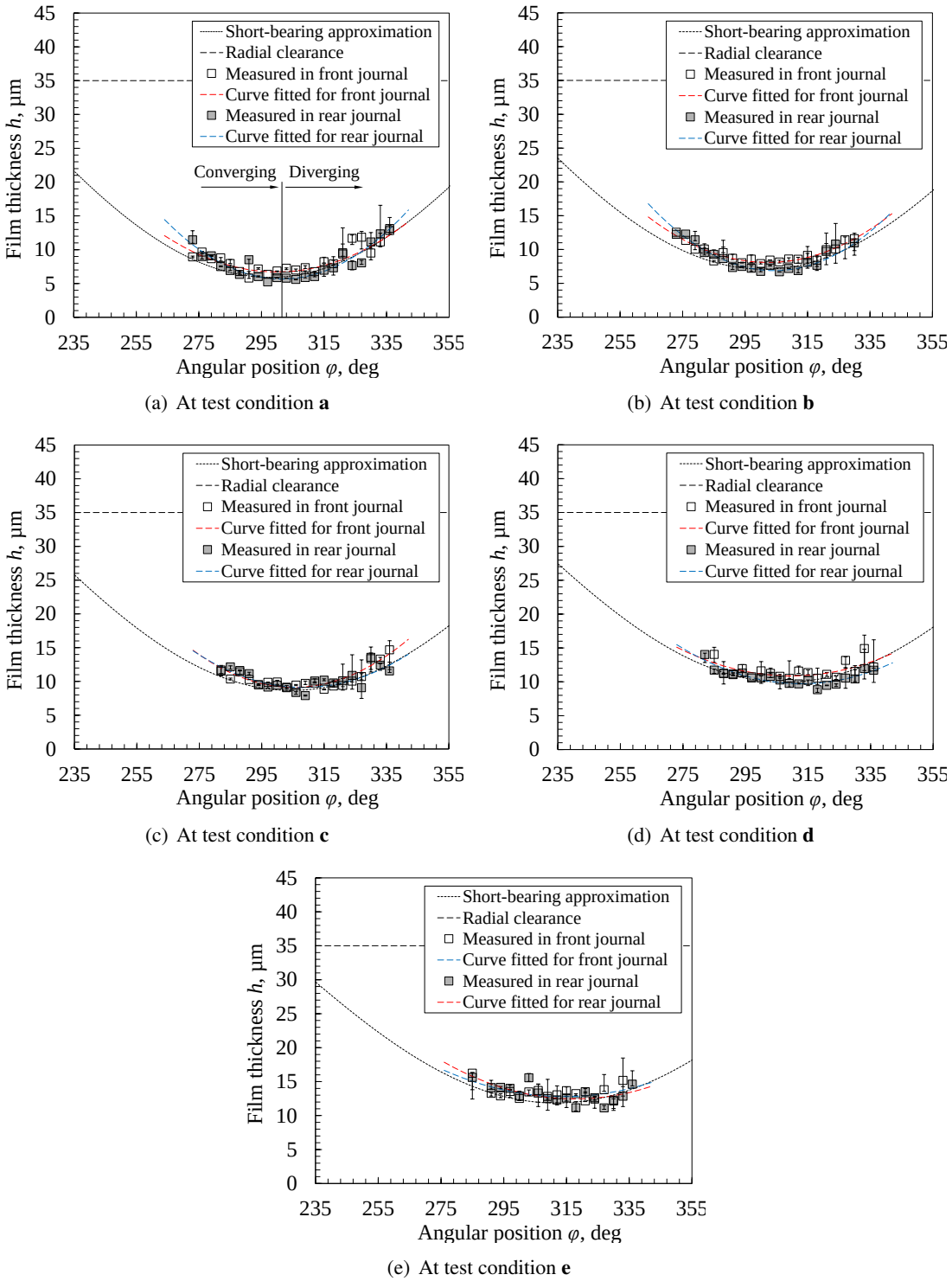

(a) At test condition **a**

(b) At test condition **b**

(c) At test condition **c**

(d) At test condition **d**

(e) At test condition **e**

Figure 4.29: Measured film thickness at the test condition **a** to **e** with the corresponding theoretical curve by the short-bearing approximation.

The measured film thickness in the rear journal yielded slightly thinner than the thickness measured in the front journal at all the test conditions consistently despite the fact that the radial clearance of the front and rear journal was equally measured to be 35 μm. There could exist several factors which could have influenced it. Firstly the bush was probably slightly tilted axially due to the radial clearance. If this is the case, the film thicknesses at one of the bearing edge, perhaps at the rear edge in this case, must have been thinner than those measured at the width centre by the transducers. As well as the tilt, the misalignment of the front and rear journal could have been another factor. Both the factors are obviously present in the real component, which means that, if these two factors works greatly the more unbalanced film thickness may be generated. This could increase the risk that the section at the edge is exposed to asperity contact.

Minimum film thickness and attitude angle. The attitude angle and the minimum film thickness were read by fitting 2nd-order polynomial curves on the obtained data sets in which the film thicknesses with great errors due to cavitation in the diverging section were excluded. The cavitation effect will be discussed in the detail in the following section. The curves were fitted in the front and rear journal data separately, then the minimum film thickness data were summarised over the Sommerfeld reciprocal with the theoretical curve obtained by the short-bearing approximation as presented in Figure 4.30. All the read minimum film thickness agreed well with the theoretical curve in the Sommerfeld reciprocal range from 0.5 to 2.1.

As well as the minimum film thickness, the Lambda ratio, which is a ratio of the film thickness to a combined surface roughness of the two bodies (the surface roughness on the bush and shaft journal) separated by the film, are also plotted as seen in the 2$^{\text{nd}}$ vertical axis in Figure 4.30. This ratio λ is commonly used as an index to identify what the lubrication regime (i.e. hydrodynamic, mix or boundary) a machine is operated roughly, and can be expressed as:

$$\lambda = \frac{h_{\text{min}}}{\sqrt{(R_{\text{a1}})^2 + (R_{\text{a2}})^2}}, \tag{4.8}$$

where h_{min} is the minimum film thickness, R_{a} the roughness average in which the subscript refer to the body 1 and 2. In order to obtain the Lambda ratio, the values of roughness average measured in the tangential coordinate were used, that is, 0.060 μm in the shaft surface, 0.056 μm in the bush surface, respectively. As plotted in Figure 4.30 all the Lambda ratios obtained by the measured

minimum film thickness exceeded 50, meaning that the bearing was likely to have been run within hydrodynamic lubrication regime, although as discussed previously, the Lambda ratio would have been slightly smaller at the rear axial edge of the film.

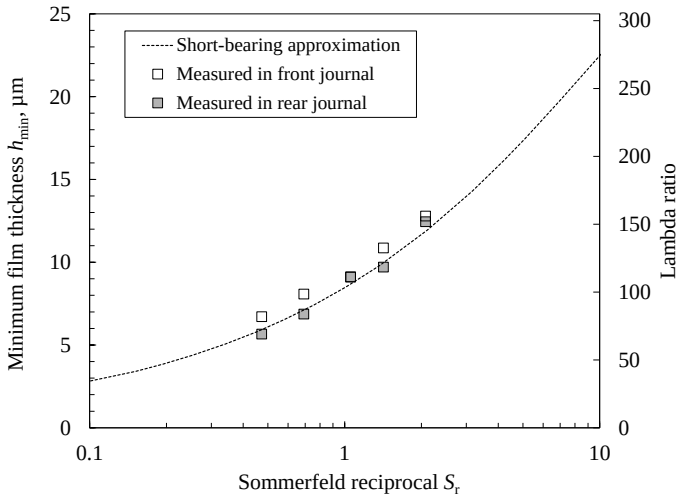

Figure 4.30: Measured minimum film thickness at the test conditions **a** to **e** in Sommerfeld reciprocal domain.

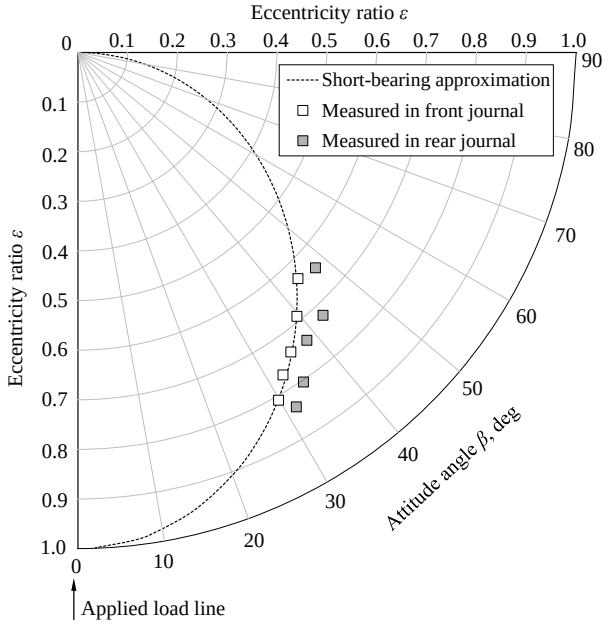

Figure 4.31: Plot of eccentricity ratio against attitude angle for comparison of experimental data at the conditions **a** to **e**.

The Figure 4.31 summarises the measured data with the theoretical curve of the short-bearing approximation in the eccentricity ratio over the attitude angle in a quarter circle. The line where the load was applied is set at 0 deg. It was found that both the eccentricity ratio and attitude angle

deduced agreed satisfactorily well with the theoretical curve.

Cavitation. The effect of cavitation over the film thickness in the diverging area was expected as seen in the previous work (Kasolang and Dwyer-Joyce, 2008a). In the present study the greater errors from the median values were observed at the diverging section of the bearing, which could have been caused by the cavitation.

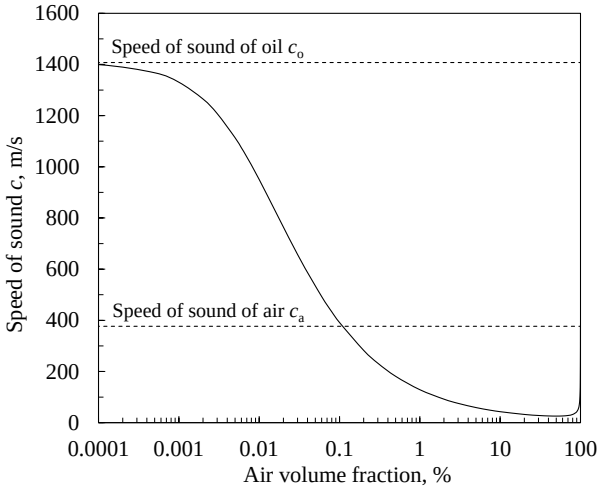

Figure 4.32: Speed of sound in two phase mixture of oil and air.

Typical mineral-based oils contain dissolved air. When the cavitation occurs, the dissolved air appears as a form of bubble and are dispersed in the oil. The large size of the bubbles could scatter and reflect all the sound wave back, and the small bubbles dispersed in the oil reduces the speed of sound significantly, which upset the reflection coefficient. In such a state where a two phase (oil and air) are finely mixed, the speed of sound travelling through can be estimated by an equation as (Urick, 1947):

$$c_{\mathrm{m}} = \frac{1}{\sqrt{\left(\frac{\phi}{\rho_{\mathrm{a}} c_{\mathrm{a}}^2} + \frac{(1-\phi)}{\rho_{\mathrm{o}} c_{\mathrm{o}}^2}\right)\left(\phi\rho_{\mathrm{a}} + (1-\phi)\rho_{\mathrm{o}}\right)}}, \tag{4.9}$$

where c_{m} is the speed of sound in the two phase mixture, ρ the density and ϕ the air volume fraction. The subscripts "a" and "o" refer to air and oil, respectively. Figure 4.32 shows the speed of sound in the two phase mixture of oil and air calculated using Equation (4.9) at 80 °C. As seen in the figure, a small portion of dispersed air can cause a significant reduction in the speed of sound. It is difficult to discuss the accurate cavitation effect over the film thickness quantitatively

due to its technical difficulty to determine the air volume fraction. However, Kasolang and Dwyer-Joyce (2008a) revealed that the onset of cavitation and reformation of the film can be identified by fluctuation and noise in the reflection coefficient readings.

Signal amplitude variation with temperature change. As discussed in Section 4.3.1.1, the thermal drift over the wave signal was observed in the present measurements as seen in the previous works (Kasolang and Dwyer-Joyce, 2008a; Reddyhoff et al., 2005). Figure 4.33 summarises the measured reference amplitudes over the frequency in the six transducers (UTF1 to UTR3) under the test conditions conducted (Ref1 to Ref3).

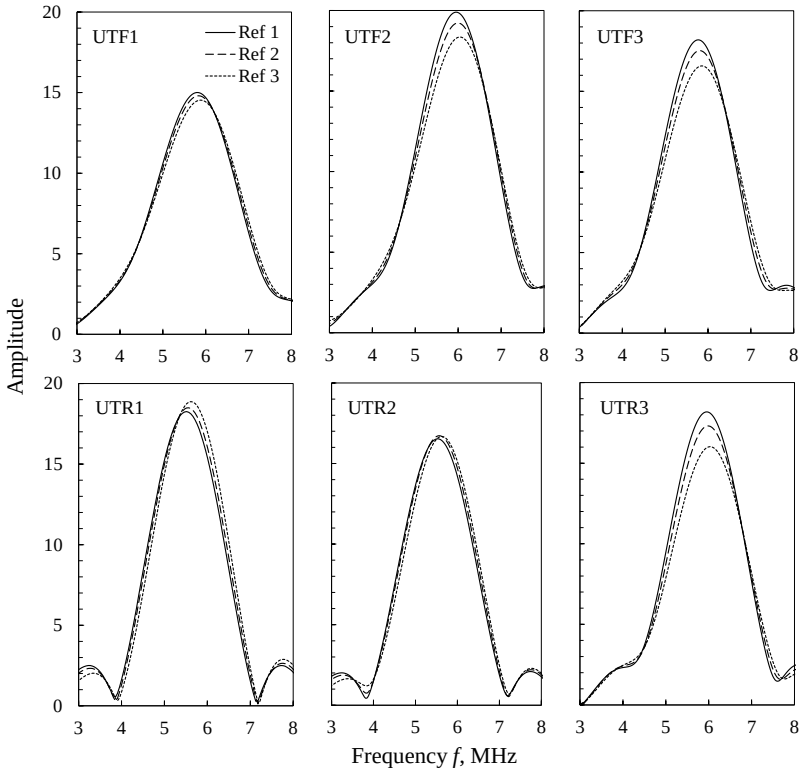

Figure 4.33: Reference signal variations over temperature change in the placed transducers UTF1 to UTR3.

The thermal drift occurred in all the transducers with different magnitudes. For example in the transducer UTR1, the magnitude at its peak decreased by approximately 5 % as the temperature increased as seen from Ref1 (at 60 °C) to Ref3 (at 80 °C), while in the transducer UTR3 the magnitude at the peak increased more significantly by 11 % as the temperature increased. If the Ref1 data and Ref3 data in the UTR3 are used as the reference signal and the measurement signal, the corresponding film thickness is deceptively calculated as 4 μm even though the measurement

signal is captured from a layer where all the wave are supposed to reflect back. As shown here, significance to remove the thermal effect is evident for accurate film thickness measurement. In the film thickness measurements conducted in this chapter the thermal effects were appropriately removed by implementing the approach, the reference signal measurements with steel/thick oil layer/steel and the subsequent measurement on the layer of interest, by which it was possible to measure the film thicknesses accurately.

4.4 Conclusions

The film thickness measurement using an ultrasound reflection technique was examined under operational conditions of an automotive transmission journal bearing in steady-state. The following conclusions are drawn from this chapter:

- The journal bearing test platform which represents operational conditions of the automotive transmission journal bearing was constructed incorporating the ultrasound measuring apparatus.

- The measured film thickness and the attitude angle on the plain journal bearing (ϕ98 mm of the diameter with 0.255 of L/D) under the steady-state conditions agreed well with the theoretical curves deduced by a classical Reynolds equation with the short-bearing approximation. The measured range of the minimum film thickness was approximately from 5 μm to 12 μm at the Sommerfeld reciprocal range from 0.5 to 2.1.

- The significant thermal drift on the reflection amplitude was observed as seen in the previous works. In order to minimise such drift effect on the film thickness measurement, an approach to capture the reference signal was proposed and implemented. Although there is a limitation to use this approach on the applicable range of the film thickness and transducer frequency, this approach could be an useful alternative to minimise the thermal drift on the film thickness measurement on journal bearing especially on measurements under high operational temperature.

- The measured film thickness were marginally thinner in the rear journal than those in the front journal. Which would have been caused by the axial tilt or the misalignment between the journals.

- Judging from the Lambda ratio (exceeded 50 at all the conditions) obtained from the measured minimum film thickness and the combined surface roughness, the journal bearing is run within the hydrodynamic lubrication regime under the steady-state conditions performed in this study.

Chapter 5

Effect of Bespoke Surface Texture on Hydrodynamic Film Thickness and Load Capacity

In this chapter, the effect of bespoke surface texture created on the journal bearing surface is experimentally investigated by measuring film thickness with the ultrasonic reflection technique on the journal bearing test platform constructed in Chapter 4. In the first part of this chapter, the experimental and computational literature works are reviewed regarding the effect. The latter part includes the experimental results obtained on the textured journal bearings and a comparison between the literature works and the present work.

5.1 Literature Review

In respect of tribological performance in many engineering applications, it has been experimentally shown that bespoke surface textures work beneficially by; creating a lubricant reservoir (Lo and Horng, 1999), debris and wear particle trapping and discharge (Pettersson and Jacobson, 2003), and a micro-bearing effect generating additional hydrodynamic pressure (Anno et al., 1969, 1968; Costa and Hutchings, 2007; Etsion et al., 2004; Geiger et al., 1998; Glavatskih et al., 2005; Hamilton et al., 1966; Lu and Khonsari, 2007; Salama, 1950; Wang et al., 2001, 2003) that could prevent the collapse of the full hydrodynamic lubricant film. Table 5.1 summarises the experimental works investigated on the effect of the bespoke surface texture aiming for the

additional hydrodynamic force.

Table 5.1: Summary of the experimental works on the effect of the bespoke surface texture for the additional hydrodynamic force.

Authors (year)	Components	Texturing techniques	Characteristics measured
Salama (1950)	Parallel thrust bearing	Lapping machine	Load capacity, Friction coefficient
Hamilton et al. (1966)	Parallel thrust bearing	Photo-etching	Load capacity
Anno et al. (1968)	Parallel thrust bearing	Photo-engraved	Film thickness, Friction coefficient
Geiger et al. (1998)	Block-on-cylinder	Laser	Film thickness, Friction coefficient
Wang et al. (2003)	Parallel thrust bearing	Laser	Load capacity, Friction coefficient
Etsion et al. (2004)	Parallel thrust bearing	Laser	Load capacity, Friction coefficient
Glavatskih et al. (2005)	Tilting thrust bearing	Conventional Machining	Film thickness, Friction coefficient
Costa and Hutchings (2007)	Block-on-cylinder	Photo-chemical etching	Film thickness

The table is sorted on the examined components, the techniques used for the texture generation and tribological characteristics measured in their studies. The studies have been performed on both the conformal and non-conformal and parallel and non-parallel configurations by measuring the load capacity, friction coefficient and film thickness. Overall, positive results were reported i.e. higher load capacity, lower friction coefficient and thicker film thickness than the corresponding results in the un-textured specimen, although it was also found that some parameters e.g. the depth-diameter ratio of dimple, could impose negative effects.

Figure 5.1 presents an experimental result conducted by Wang et al. (2003) on critical load ratio (a ratio of the critical load where lubrication is transferred from hydrodynamic to mixed between the textured and the un-textured specimen) . As seen in the figure, the critical load measured on the textured specimen yielded significantly greater than those on the un-textured. The critical load was dependent on the depth-diameter ratio of the dimple and the result implies that

optimum ratios in such texture geometries could exist. In the following section, the underlying mechanisms on the additional hydrodynamic force will be discussed.

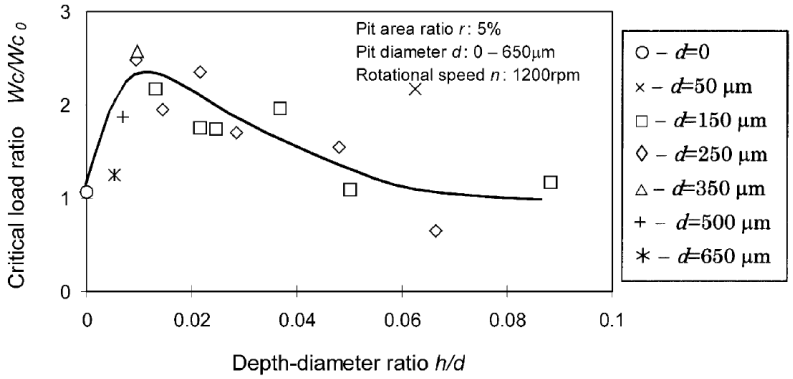

Figure 5.1: The critical load ratio W_c/W_{c_0} versus depth-diameter ratio h/d (Wang et al., 2003).

5.1.1 Mechanism on the additional hydrodynamic force

5.1.1.1 Cavitation effect

According to the classic hydrodynamic theory of lubrication, when the sliding surfaces of a component e.g. thrust bearing or face seal are smooth, fixed and parallel, conditions for steady-state, isothermal and incompressible flow do not allow the generation of a hydrodynamic lubricant film to support an applied load. In general, fixed pad thrust bearings are with parallel faces and the load capacity is usually limited to about 0.345 MPa, while tilting pad thrust bearings where the faces are inclined to the other, the load capacity is about 3.45 MPa (Salama, 1950). However, many experimental works revealed that even thrust bearings with parallel-faces can support the load as great as the tilting thrust bearing. This has been attributed to the various characteristics including macro or micro surface topography such as; surface waviness (Salama, 1950) or protruding micro-asperities (Anno et al., 1969, 1968; Hamilton et al., 1966).

Hamilton et al. (1966) conducted an observation for cavitation on a transparent parallel thrust bearing with micro-asperities as shown in Figure 5.2(a) and they concluded that such cavitation was intimately associated with the additional hydrodynamic force generation. Generally when a flow of incompressible fluid encounters a protruded micro-asperity, the pressure increases in the converging section while it drops in the diverging section (Figure 5.2(b)).

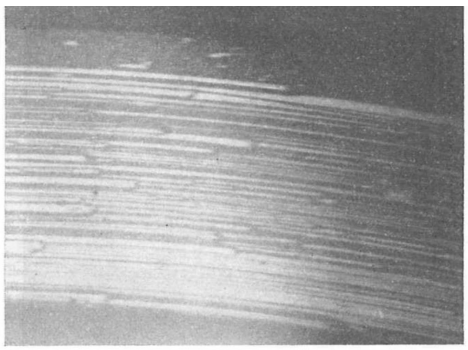

(a) Cavitation streamers in transparent seal. Direction of rotation is right to left. Lubricant: 400 centistoke (130 F) mineral oil; mean seal dia, 3.7 in.; land width, 0.2 in.; speed, 80 fpm; inside sealed pressure, 10 psig; face load, 15 psi (Hamilton et al., 1966)

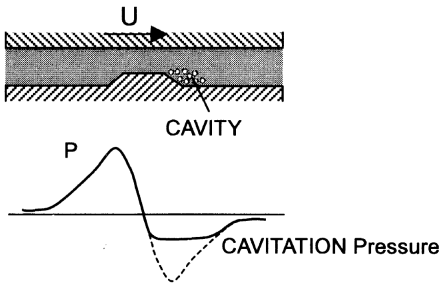

(b) The hydrodynamic effect of idealized micro asperity (Wang et al., 2003).

Figure 5.2: (a) experimental observation for cavitation and (b) schematic of a pressure curve around a micro-asperity on parallel-faces sliders.

When cavitation occurs in the diverging section, the pressure curve is saturated at the vapour cavitation or gaseous cavitation pressure, by which the overall resultant force capacity becomes positive in a section of micro-asperity. This cavitation mechanism explains the additional hydrodynamic capacity mainly on works with parallel sliders, such as Anno et al. (1969, 1968); Etsion et al. (2004); Hamilton et al. (1966); Salama (1950); Wang et al. (2001, 2003). The net pressure gain by cavitation can be predominant on such parallel sliders where no pressure or very low pressure is built due to the very small or no convergence ratio, which was also observed in a simulation work on a linear pad bearing having single closed pocket (Brajdic-Mitidieri et al., 2005).

The simulation work combined with a cavitation model showed that the pressure build-up in the pocket itself on a very low convergence ratio was significantly greater than the pressure that the rest of the section generated as shown in the bottom graph ($K = 0.001$) of Figure 5.3. However, in case of the higher convergence ratio where the positive pressure can develop over the entire section, cavitation does not occur since the pressure in the section entraining into the pocket can not drop to the cavitation pressure, as seen in Figure 5.3. Therefore another mechanism must be present but the cavitation in the non-parallel sliders including journal bearings that the present study focuses on, as the positive effects were experimentally observed on such non-parallel application (Glavatskih et al., 2005).

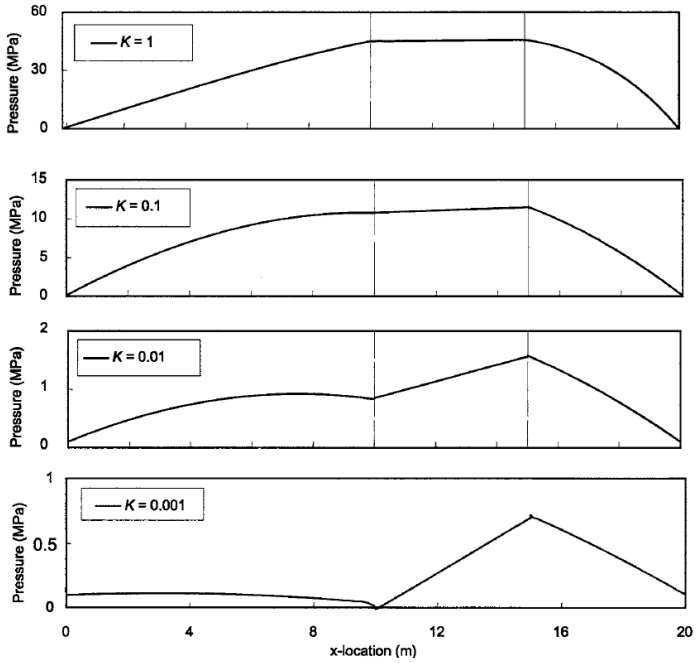

Figure 5.3: Effect of convergence ratio on pressure profiles across bearings with a 20 μm deep pocket. Note different pressure scales in the four plots (Brajdic-Mitidieri et al., 2005).

5.1.1.2 Convective inertia effect

The effect of the roughness or purposely embedded textures on the sliding surfaces to the fluid flow has been theoretically studied by many researchers. One of the keystone in these studies is the magnitude of the characteristic lengths involved in the fluid flow. Figure 5.4 schematically shows the four geometrical lengths on fluid flow of a slider, i.e. macro geometry (e.g. slider width or sliding length), bespoke surface texture (e.g. groove depth or width), film thickness and surface roughness (e.g. roughness amplitude or wavelength). The parameters involved in the flow on the textured slider is graphically presented in Figure 5.5.

As seen in Figure 5.4, the magnitude of the characteristic length in an engineering bearing ranges quite widely, from 10^{-8} m to 10^{0} m. The film thickness is usually an order higher than those of the surface roughness (amplitude or wavelength), thus the important approximation of the classic lubrication theory that the surface is ideally smooth can be reasonably true. However, it should be noted that the bespoke surface texture can be technically generated in very wide magnitude range, that is, lengths comparable to the bearing macro geometry to the surface roughness as long as an appropriate texturing technique is selected (Figure 5.4). If the bespoke surface texture which is of similar magnitude of the expected film thickness is involved in the flow, the

approximation that the surface is ideally smooth is inappropriate to analyse the fluid flow.

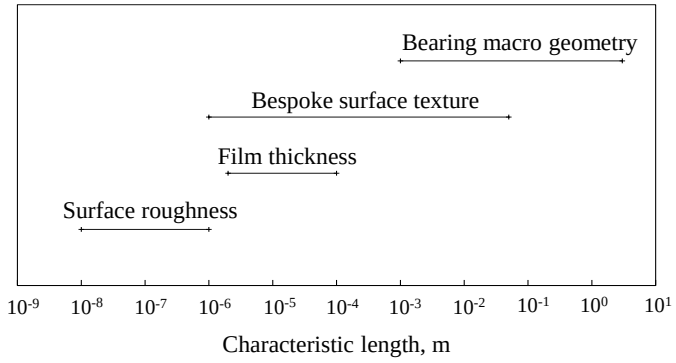

Figure 5.4: Magnitude comparison of characteristic lengths in an engineering bearing.

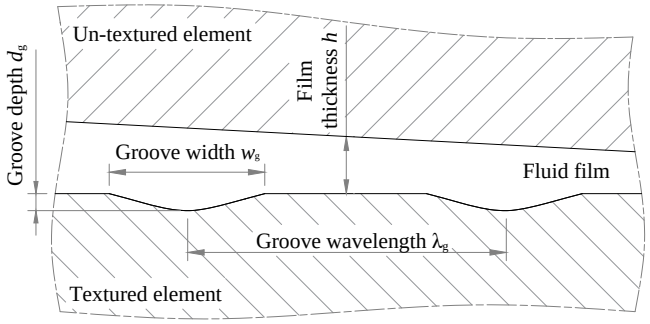

Figure 5.5: Schematic of fluid flow on a slider with bespoke surface texture.

The fluid flow on a rough slider was firstly studied based on the Reynolds assumptions with a stochastic roughness model by Elrod (1979). The author investigated the fluid flow focusing on a ratio of the average film thickness to the roughness wavelength and concluded that when the roughness wavelength (or spacing) is comparable to the film thickness, one of the main assumptions of Reynolds, i.e. the constant pressure across the film thickness (assumption II in Chapter 2), is no longer valid. In order to account the pressure variation across the film, a less simplified model, the Stokes equation or assumption, was studied to deal with the flow (Sun and Chen, 1977). For an incompressible flow of Newtonian fluid in steady-state, the Navier-Stokes and the Stokes equations which is a simplified form of the Navier-Stokes are expressed from the conservation of momentum of a fluid (Versteeg and Malalasekera, 2007):

$$\text{Navier-Stokes:} \quad \underbrace{\nu\nabla^2\mathbf{u}}_{\text{Diffusive term}} \quad \underbrace{-\frac{1}{\rho}\nabla p}_{\text{Pressure term}} \quad \underbrace{+\mathbf{g}}_{\text{Eternal force term}} = \underbrace{(\mathbf{u}\cdot\nabla)\mathbf{u}}_{\text{Convective term}} , \tag{5.1}$$

$$\text{Stokes:} \qquad \underbrace{\nu\nabla^2\mathbf{u}}_{\text{Diffusive term}} \quad \underbrace{-\frac{1}{\rho}\nabla p}_{\text{Pressure term}} \quad \underbrace{+\mathbf{g}}_{\text{Eternal force term}} \quad = \quad 0, \tag{5.2}$$

and the mass of the fluid is conserved as:

$$\nabla \cdot \mathbf{u} \quad = \quad 0, \tag{5.3}$$

where ∇ is the Del operator, ∇^2 the Laplacian operator, $\mathbf{u}$ the velocity vector, ν the kinematic viscosity, p the pressure and $\mathbf{g}$ the external force. The Stokes equation is applicable under a creeping motion where the Reynolds number is very low, $Re \ll 1$, that is, the inertia effect is negligibly small. However, the Reynolds numbers for engineering applications including the journal bearing focused on the present study usually are not $Re \ll 1$ for practical conditions, so that the convective term neglected on the Stokes model from the Navier-Stokes model can not be ignored under such conditions.

In the past decade, due to technical advances in computing power full Navier-Stokes based models have been implemented for theoretical analyses of the fluid behaviour on textured sliders. Table 5.2 summarises the theoretical works on the effect of the bespoke surface texture on the fluid flow with Navier-Stokes model (Arghir et al., 2003; Brajdic-Mitidieri et al., 2005; Cupillard et al., 2008; Dobrica and Fillon, 2009; Huynh, 2005; Li and Chen, 2007; Sahlin et al., 2005). In the table the geometrical parameters (e.g. component model, geometrical ratio between the groove depth and width to film thickness, groove form, and convergence ratio, K, which is expressed as $h_{\max}/h_{\min} - 1$) used in their studies are presented as well as the Reynolds number under which the simulations were run. Note that the data presented in shallow dimples section of Cupillard's work (Cupillard et al., 2008) was not included in Table 5.2 as the data was not sufficient. The overall conclusion drawn from their studies is that the pressure profile or load capacity can not be predicted if the convective term in Navier-Stokes equation is excluded while the following two conditions are satisfied. The first condition is where the film thickness and the bespoke surface textures are of similar magnitude. The second is where the Reynolds numbers are of values in which the practical engineering components are operated. Figure 5.6 shows a simulation result comparing for pressure distribution in a groove obtained with Navier-Stokes and Stokes based

model (Sahlin et al., 2005). As seen in the figures, effect of the convective term becomes more evident i.e. producing a net pressure build-up, as the Reynolds number becomes greater.

Table 5.2: Summary of the theoretical works on the effect of the bespoke surface texture on the fluid flow with Navier-Stokes model.

Authors (year)	Component models	Ratios, groove to film thickness		Groove form	Converge-nce ratio K	Reynolds number Re
		Depth d_g/h	Width w_g/h			
Arghir et al. (2003)	Parallel slider, single groove	2	$1 \sim 4$	Rectangular, sinusoidal, triangular	0	0.1, 1, 10, 100
Brajdic-Mitidieri et al. (2005)	Non-parallel slider, single groove	$3.3 \sim 26.7$	3333	Rectangular	0.001, 0.01, 0.1, 1	0.15
Huynh (2005)	Non-parallel slider, 1∼20 grooves	$0.15 \sim 0.42$	$3.85 \sim 9.62$	Sinusoidal	0.6	21
Sahlin et al. (2005)	Parallel slider, single groove	$0.25 \sim 1.25$	$5 \sim 17$	Circular, spline	0	10, 40, 80, 120, 160
Li and Chen (2007)	Non-parallel slider, 50 grooves	$0.002 \sim 0.4$	0.3	Square	0.56	2
Cupillard et al. (2008)	Journal bearing, 10 grooves	$4.4 \sim 37.1$	$14 \sim 41$	Circular	3.13 and some	23
Dobrica and Fillon (2009)	Parallel sliders, single and 7 grooves	$0.125 \sim 256$	1	Square, rectangular	0	1 ∼512

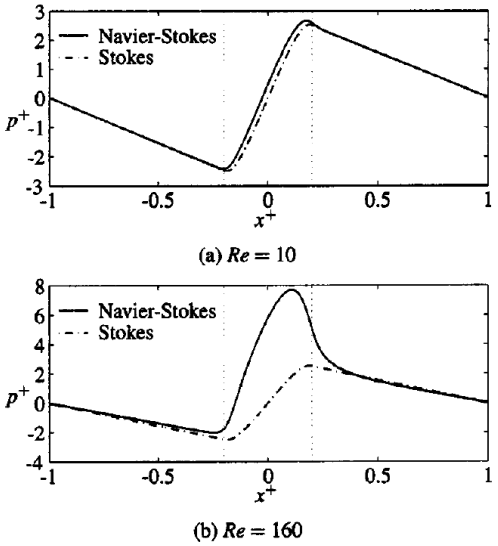

Figure 5.6: Comparison between Navier-Stokes and Stokes solutions for pressure distribution on the upper smooth wall for the cylindrical geometry. $w^+ = 0.2$ and $d^+ = 0.25$ for both plots. The vertical dotted lines represent the groove edges (Sahlin et al., 2005).

Figure 5.7 presents an obtained result comparing a textured surface with the corresponding smooth one in a non-parallel slider investigated by Li and Chen (2007). As seen in the figure, net gain of the load capacity rapidly increases from a point where value of the geometrical ratio, the groove depth to the film thickness β ($= d_g/2h$), exceeds 0.03∼0.04.

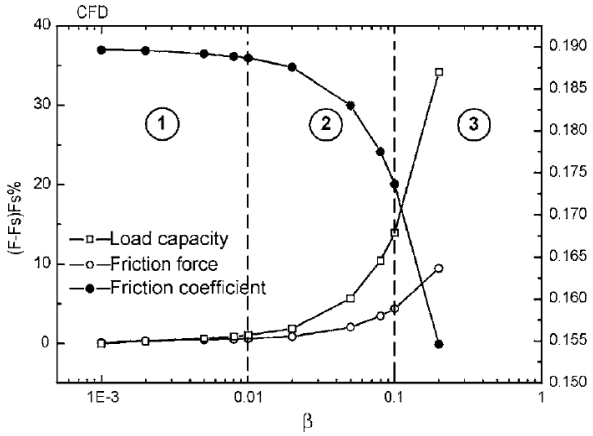

Figure 5.7: Lubrication results acquired by CFD compared to those on smooth surface (Li and Chen, 2007).

Figure 5.8 summarised the predicted effects on the textured non-parallel as compared with the corresponding smooth sliders on the load capacity in a selected Reynolds number with variation of the two geometrical ratios, i.e. the groove depth to the film thickness d_g/h, and the groove width to the film thickness w_g/h in the simulations cited in Table 5.2.

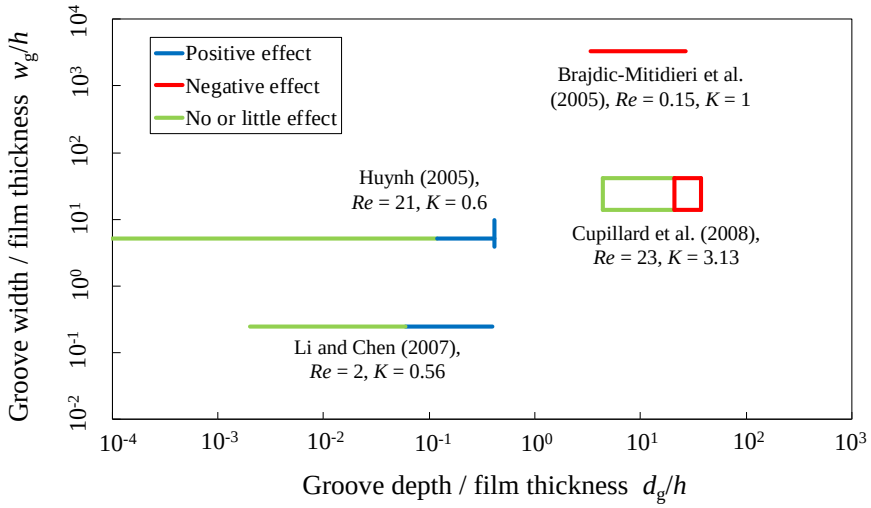

Figure 5.8: Effect of the texture geometries to the load capacity from the CFD based literatures.

The simulations were conducted at several conditions within the range of the drawn lines and

enclosed areas. Note that the values of the film thickness h used to determine the two ratios were the film thickness at the centre position in the sliding coordinate on the non-parallel sliders, and the radial clearance on the journal bearing. For the works where the simulations were performed with various groove locations (e.g. nearby the inlet, the centre or the outlet), a groove location was chosen and the corresponding result was plotted in Figure 5.8.

The effects on the load capacity were divided into three categories i.e. positive, negative or no or little effect from their simulated results. The textured cases where the load capacity became a few percent higher than the corresponding smooth case, are plotted with blue lines as the positive effect. While the textured cases where the load capacity became a few percent lower than the corresponding smooth case, are drawn with red lines as the negative effect. The other cases are shown with green lines as no or little effect. A few percent as thresholds on the load capacity increase and decrease were used here just for a temporary expedient. As shown in the figure, there seems to be a limited range to obtain the positive effect. Only where the aforementioned two conditions are met, the positive effect would appear otherwise the load capacity would be same as the smooth case or even reduced.

This summary map makes sense intuitively since slider models whose grooves are shallow and too finely meshed as those with ideally smooth slider (i.e. left-bottom on the figure), no effect should appear on the load capacity while slider models whose grooves are deep and roughly meshed (i.e. right-top on the figure), which would simply reduce the convergence of the sliders, resulting in the negative effect. As cited in the summary of the experimental investigation (Table 5.1), the work by Glavatskih et al. (2005) where the positive effect was observed also appears to agree with the CFD summary since the geometrical ratios of the tilting pad bearing ($d_g/h \approx 0.11 \sim 0.22$, w_g/h was not given in the paper) would have been of the positive effect range in Figure 5.8. Although these literature works indicates the significance to design such geometrical ratios in the optimum range in order for the additional load capacity, few validation works have been performed experimentally focusing on the influence of the geometrical ratios in the non-parallel application. In the following sections, the film thickness measurement will be conducted on two test journal bearings with distinct bespoke textures which are supposed to represent the geometrical ratios in the blue and red coloured regions in order to verify the summary that the theoretical works lead. The texture which represents the red coloured region will be created using

a conventional milling machine. While the texture which represents the blue coloured region, i.e. the finer-meshed texture will be generated using the vibration-assisted machining device developed in Chapter 3.

5.2 Bespoke Texture Geometry Generated on the Journal Bearing

In this section, the main dimensions of the two bespoke surface textures generated on the journal bearing will be presented as well as the measured surface roughnesses. Of the two textures, texture A represents the red coloured section and texture B does the blue coloured section as shown in Figure 5.8, respectively. These textures are generated on the shaft surfaces. The bearing main geometries, e.g. diameter, width or radial clearance, are set to be same as the journal bearing which have been used for the film thickness measurements in Chapter 4 except the presence of the texture that allows direct comparison of the film thickness measurements with and without texture. One of the important parameters on the shaft, surface roughness on the non-textured area are aimed to be of similar magnitude to that of the plain journal bearing used in Chapter 4 (0.06 μm on the tangential coordinate and 0.123 μm on the axial coordinate) so that only the generated texture effect appears on the hydrodynamic film formation.

5.2.1 Geometry of journal bearing with texture A

Figure 5.9 summarises the main dimensions of the journal bearing shaft with texture A and the photos are presented in Figure 5.10.

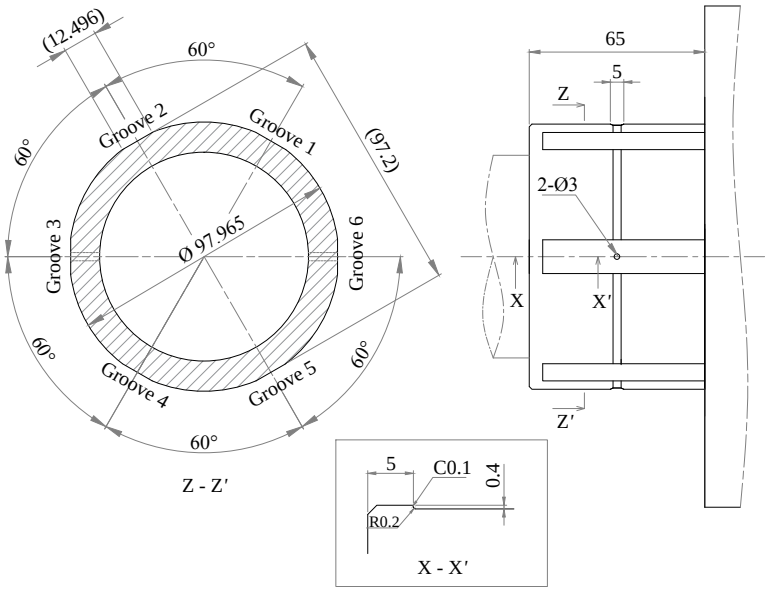

Figure 5.9: Main dimension of shaft with texture A.

The journals of the shaft are ground-finished after the heat treatment (carburising and quenching) which is same as the ground process implemented on the plain bearing used in Chapter 4. As seen in the figures, six axial grooves were machined equally at 60° angularly, being 0.4 mm in the groove depth d_g and 12.496 mm in the groove width w_g. The geometrical ratios, the groove depth to the film thickness d_g/h (or d_g/c_r) and the groove width to the film thickness w_g/h (or w_g/c_r) are 11.4 and 357, respectively. The ratios are plotted later in this chapter in Figure 5.20. The surface roughness was measured by a normal profilometer on the plain surface and on the grooved surface in the axial and the tangential coordinates. As summarised in Figure 5.11, the roughness average on the ground surface is 0.157 μm in tangential coordinate and 0.184 μm in axial coordinate, which are of similar magnitude with those of the plain bearing used in Chapter 4.

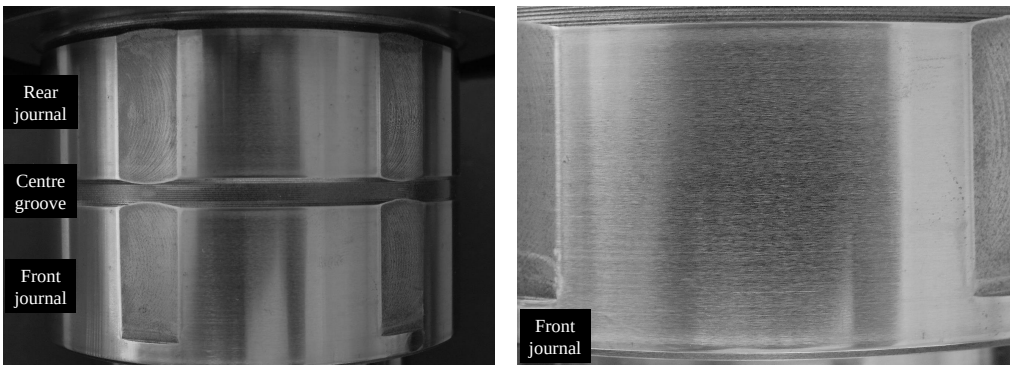

(a) Texture A (b) Texture A magnified

Figure 5.10: Photo of texture A on the shaft.

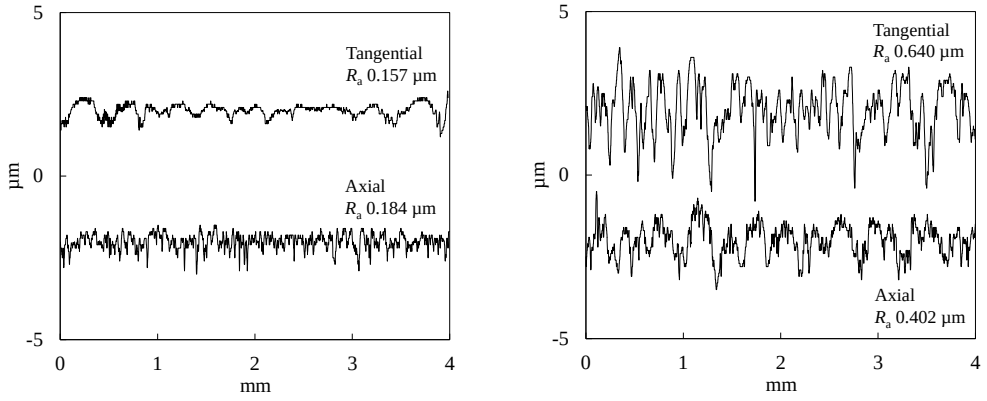

(a) Measured at plain section (b) Measured at groove section

Figure 5.11: Measured roughness on the shaft with texture A.

5.2.2 Geometry of journal bearing with texture B

In this section, the developed vibration-assisted machining technique in Chapter 3 is implemented to generate the texture B on the journal bearing shaft. Prior to the implementation to the journal bearing work piece which can be arranged on the constructed journal bearing test platform, a preliminary machining test is performed on a journal bearing shell element which represents the journal bearing shaft in order to validate the device performance in the turning machine arrangement as shown in Figure 5.12.

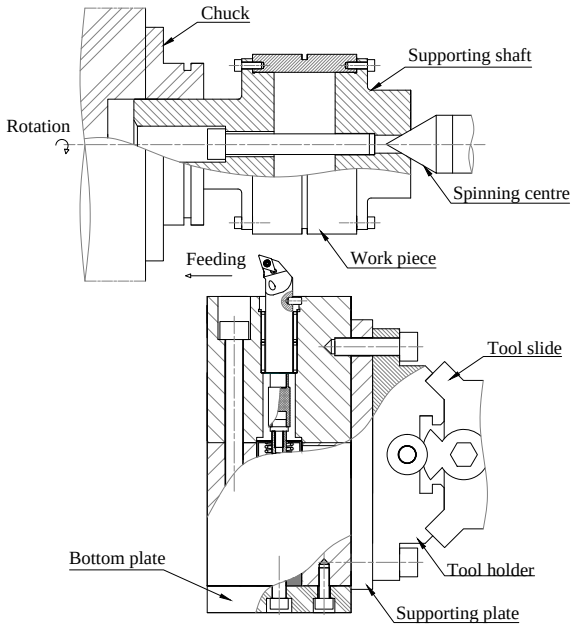

Figure 5.12: Mechanical arrangement in turning machine.

5.2.2.1 Preliminary vibration-assisted machining test on a bearing shell element

The constructed vibration-assisted machining device is set up in a numerically-controlled turning machine (Triumph VS2500 from Colchester Harrison) with a simple adapter. The device body bolted with a tool holder and a supporting plate is positioned vertically along a tool slide of the turning machine. The cutter vibrates normal to the shaft work piece (radial direction) and the device is fed along the axial direction of the shaft work piece. A machining test superposing a sinusoidal vibration in the turning machine arrangement was examined in a mild steel (C40) shell work piece, being ϕ98 mm in outer diameter and 58 mm in width split into two journals by a groove at the centre. The machining test was conducted at; 400 rpm in rotation speed, 0.4 mm/s in feed speed, 50 μm in initial depth of cut, 600 Hz in vibration frequency, and 4 V in voltage range

commanded to voltage source as summarised in Table 5.3. Photographs of the machined surfaces, surface profile (with tilt and round compensation in x, and tilt compensation in y), and 3-D map are presented in Figures 5.13 and 5.14. The x coordinate is the tangential direction of the shaft work piece, the y coordinate is the axial direction of the shaft work piece, and the z coordinate is the vibration direction, i.e. the radial direction of the shaft work piece, respectively.

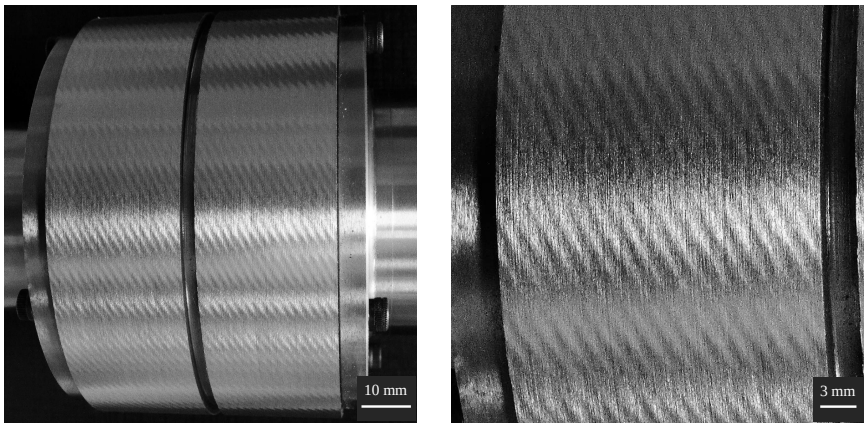

(a) Generated surface texture (b) Ggenerated surface texture magnified

Figure 5.13: Generated surface texture of the shaft work piece in the turning machine arrangement.

The vibration superposed satisfactorily well on the surface and a repeating sinusoidal waves was generated as seen in the disc work pieces. The created pattern was consistent throughout the machined surface without the minor phase shift which was seen in the disc work pieces in Chapter 3. This could be achieved by the stable rotation speed of spindle and the less mechanical clearance of the work piece arrangement.

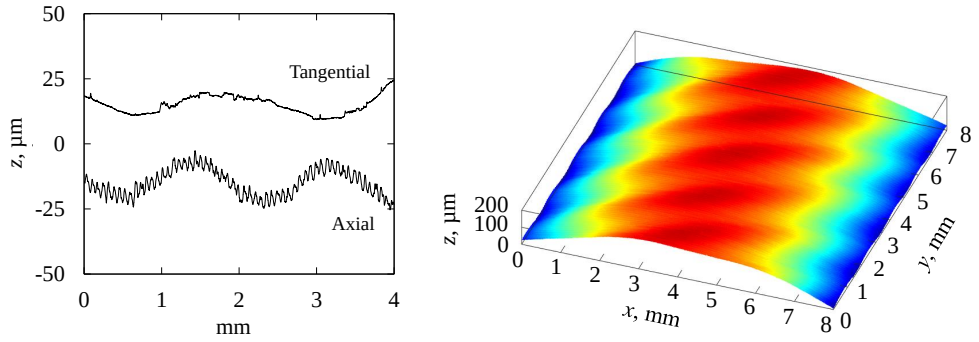

(a) Surface profile of generated surface texture

(b) 3-D map of generated surface texture

Figure 5.14: Surface profile and 3-D map of generated surface texture of the shaft work piece in the turning machine arrangement.

5.2.2.2 Texture generation on journal bearing shaft

Following the successful implementation of the sinusoidal texture on the journal bearing element, a fine-meshed texture (texture B) was machined on the bearing shaft which can be set on the journal bearing test platform as seen in Figure 5.15. The machining test conditions is summarised at Table 5.3.

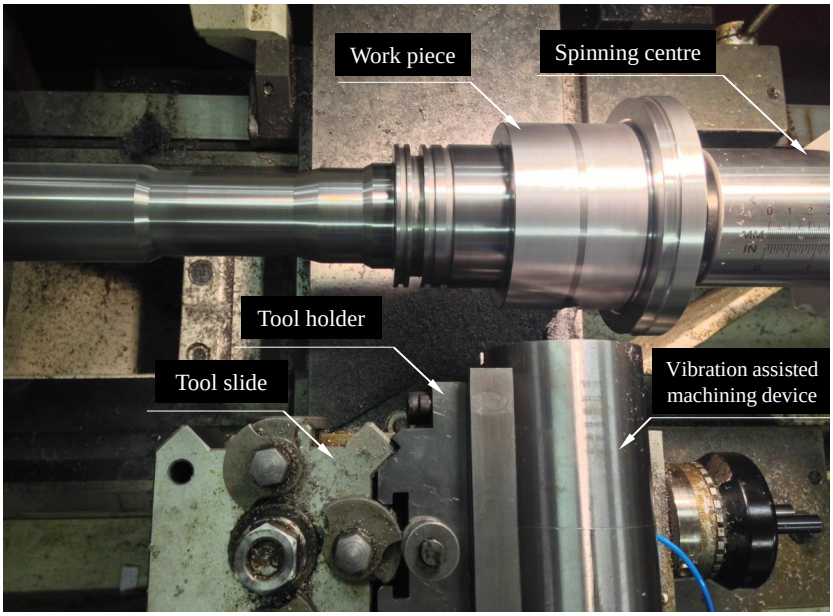

Figure 5.15: Texture generation on the shaft work piece.

Table 5.3: Test conditions on vibration-assisted machinings in turning arrangement.

Work piece symbol	Rotation speed of spindle ω rpm	Feed speed u_f mm/s	Initial depth of cut t_0 μm	Voltage range ΔV V	Mean voltage V_m V	Vibration frequency f Hz	Wave form
Preliminary test	400	0.4	50	4	5	600	Sine
Texture B	160	0.16	0	4	5	800	Sine

The machining with vibration was conducted to generate half-sinusoidal grooves after the finish cut was perform to set the diameter to ϕ97.965 mm. As seen in Figure 5.16, the half-sinusoidal grooves were consistently generated across the surface as designed in Figure 5.17 and Figure 5.18.

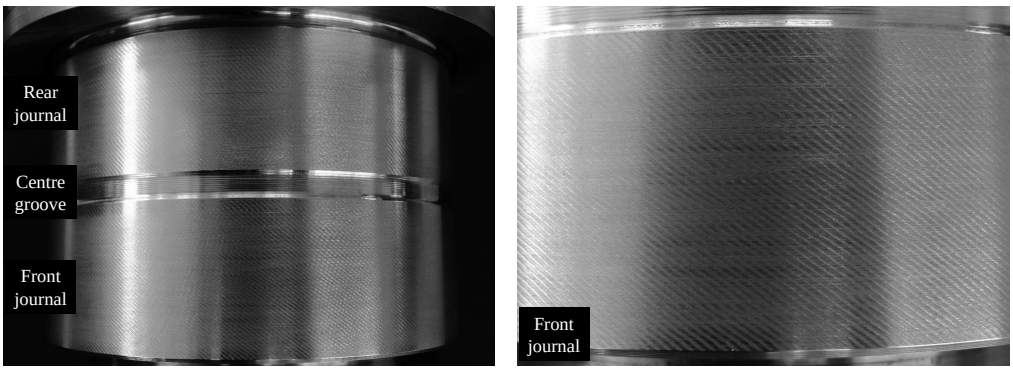

(a) Texture B (b) Texture B magnified

Figure 5.16: Photo of texture B on the shaft.

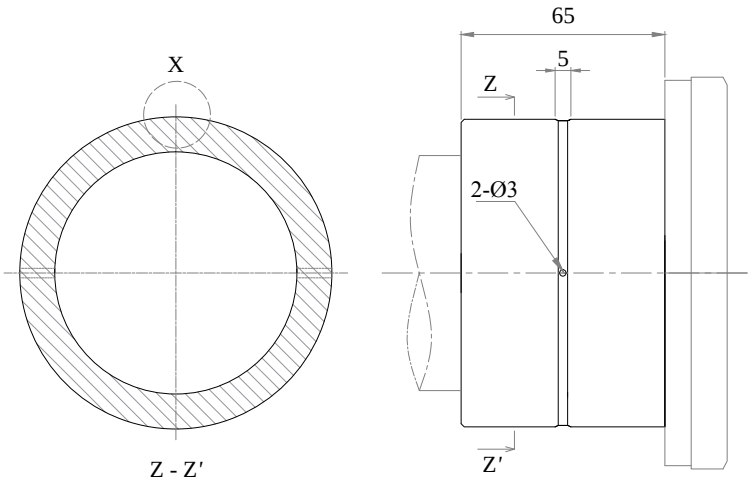

Figure 5.17: Main dimension of the shaft with texture B.

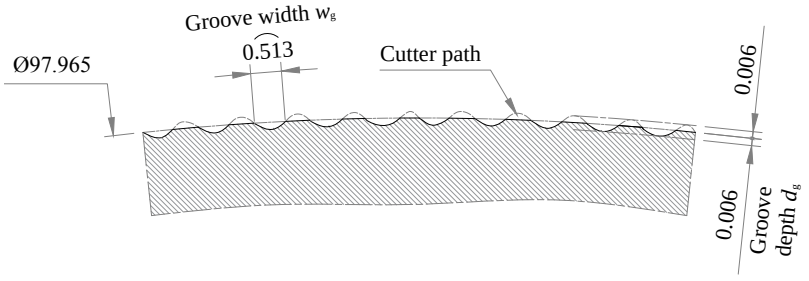

Figure 5.18: Cross-sectional dimension of texture B magnified at X of Figure 5.17.

300 grooves in a cross-section of the shaft were generated with a fixed inclination to the axial coordinate. The individual groove has approximately 6 μm in the groove depth d_g and 0.513 mm in the groove width w_g (length of the arc). The geometrical ratios, the groove depth to the film

thickness d_g/h (or d_g/c_r) and the groove width to the film thickness w_g/h (or w_g/c_r) are 0.2 and 14.7, respectively. The ratios are plotted as texture B in Figure 5.20. After the grooves were created, the shaft diameter i.e. on the ridge of the grooves was slightly polished using an oil stone and lapping stick. The surface roughness after the polishing yielded 0.210 μm tangentially and 0.527 μm axially as presented in Figure 5.19. Only the roughness profiles on the ridge section were taken into the roughness evaluation because the grooves were purposely generated. The obtained roughnesses were of similar magnitude to the other test pieces in tangential coordinate but slightly greater in axial coordinate.

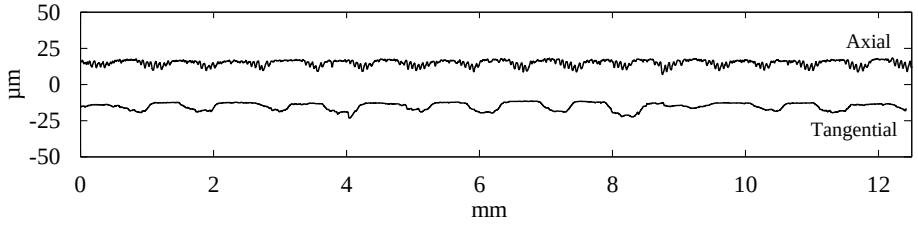

Figure 5.19: Roughness profile of texture B.

Table 5.4 summarises the main dimensions and properties of the three test shafts, i.e. plain which was used in the experiments in Chapter 4, texture A and texture B. In the following section, the film thickness measurements will be conducted using the shafts with texture A and B to discuss the effect of those textures on the film thickness with the reference results obtained on the plain journal bearing in Chapter 4.

Table 5.4: Specifications of the test pieces.

Test pieces		Plain	Texture A	Texture B
Material		SCM420H	SCM420H	SCM420H
Heat treatment		*CQ	*CQ	No treatment
Nominal diameter D	mm	98	98	98
Radial clearance c_r	μm	35	35	35
Roughness average R_a				
Tangential	μm	0.060	0.157	0.210
Axial	μm	0.123	0.184	0.527
Groove depth d_g	μm	0	400	6
Groove depth / film thickness $d_g/h\,(c_r)$		0	11.4	0.2
Groove width w_g	μm	0	12496	513
Groove width / film thickness $w_g/h\,(c_r)$		0	357	14.7

*CQ: Carburising and quenching

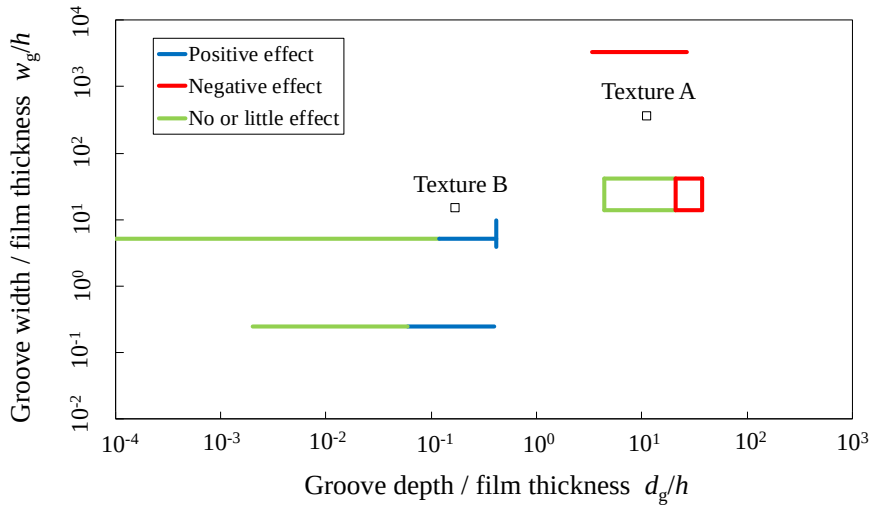

Figure 5.20: Geometrical ratios of texture A and B with the geometries from CFD based literature works.

5.3 Experimental Investigations of Film Thickness Measurements for Textured Bearings

In this section, the film thickness measurements on the journal bearing with texture A and B will be performed on the test platform developed in Chapter 4. The film thickness measured in the plain journal bearing will be compared with the film thickness on the plain section of the texture A, and the film thickness on the ridge of the texture B. Prior to the discussions on the film thickness measurement results, the ultrasound reflection signals are mapped in order to highlight the reflected signal variation due to the geometrical variation when the textured shaft rotates.

5.3.1 Reflected wave signal mapping

For convenience on analysis of the reflected wave signals from the textured surface, two data signal mappings are introduced. The first of the mapping can be obtained by combining the reflection signals (from 1^{st} to n^{th} pulses) in a sampling window over the data measurement duration, as schematically shown in Figure 5.21. This two-dimensional mapping is convenient to find the peak amplitude variation during the measurement.

Secondly the signals can be visualised three-dimensionally by stitching the reflection data (from 1^{st} to n^{th} pulses) in a sampling window over the measurement duration where the colour represents the magnitude of the reflected amplitude as shown in Figure 5.22.

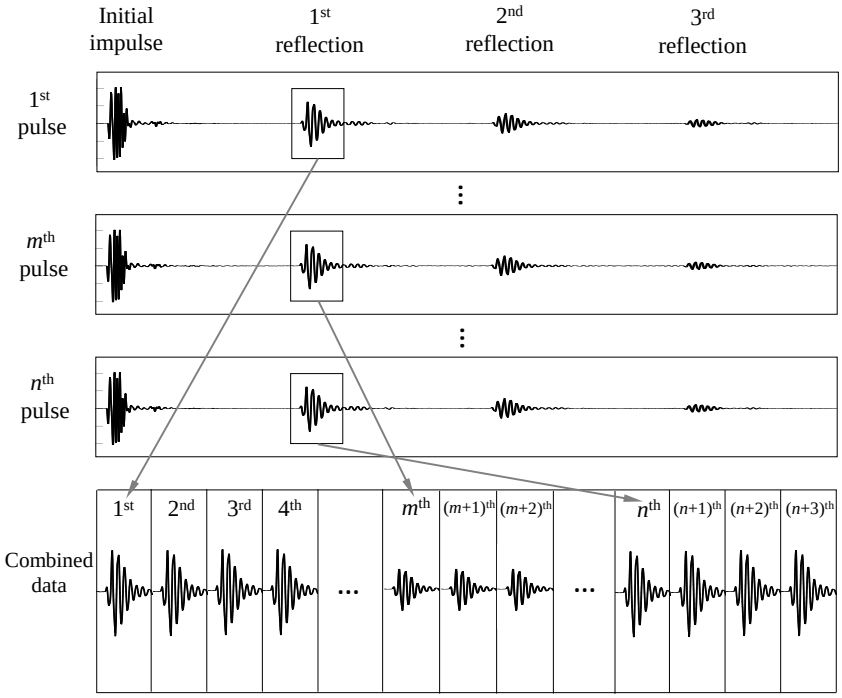

Figure 5.21: Schematic of two-dimensional sound wave map of combined 1st reflections.

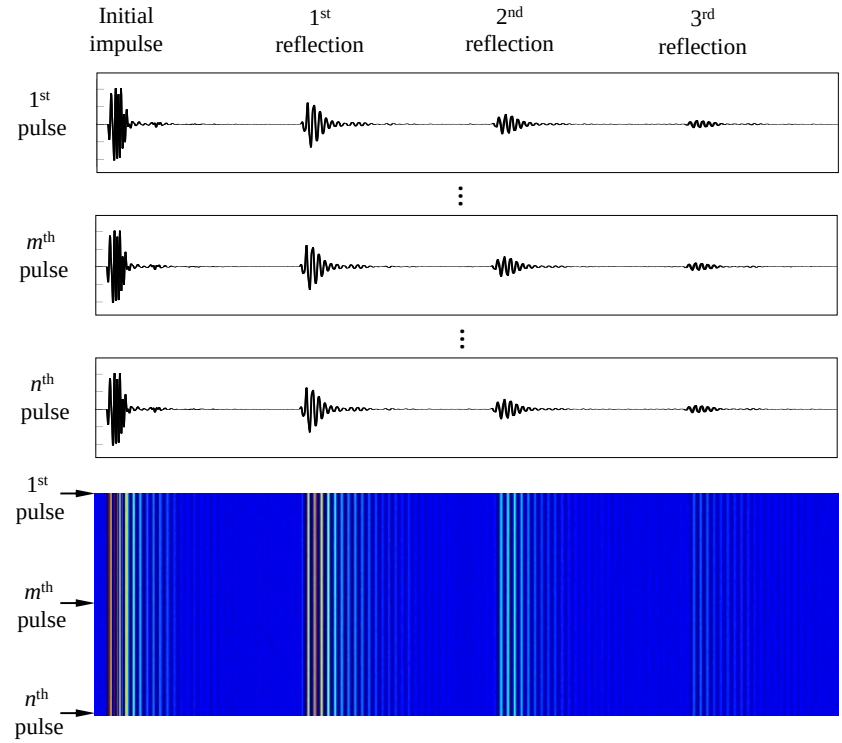

Figure 5.22: Schematic of three-dimensional sound wave map.

This three-dimensionally mapping can be used to see not only the highest amplitude point

but also the wave form variation over the measurement duration. Both the mapping techniques were used for the analysis of the reflection signals from the textured surface to deduce the film thickness, which will be discussed in the following section.

5.3.2 Film thickness measurement on journal bearing with texture A

The film thickness measurements on texture A were examined on steady state of fixed rotational speeds and a fixed applied load after the temperatures monitored by the thermocouples were saturated. The main test procedure is same as mentioned in Section 4.4.3.1. The test conditions for the five measurement signals (**f** to **j**) and the reference signals (Ref4 to Ref6) are summarised in Table 5.5.

Table 5.5: Test conditions for film thickness measurement on journal bearing with texture A.

Symbol	Rotation speed of shaft ω rpm	Load applied W kN	Temperature of TCF, TCR T °C	Oil flow rate Q L/min	Pulse rate per channel Hz
f	100	3	80	1.5	3333
g	100	3	70	1.5	3333
h	100	3	60	1.5	3333
i	300	3	80	1.5	3333
j	300	3	70	1.5	3333
Ref4	500	0	80	1.5	3333
Ref5	500	0	70	1.5	3333
Ref6	500	0	60	1.5	3333

The conditions are same as the conditions conducted in the plain bearing (Table 4.7) but the pulse rate per channel. In order to distinguish the signals that reflected from the plain section and that reflected from the grooved section, a higher pulse rate per channel, 3333 Hz, were set for the six active sensor channels.

5.3.2.1 Mapped reflection signals

Figure 5.23 and Figure 5.24 shows the two-dimensional and three-dimensional wave map obtained at test condition **h** and Ref6, respectively. As seen in these figures, the amplitude of the reflected signals varied responding to geometrical change of the bearing section, from which it can be clearly distinguished if the sound wave was reflected from the plain section or from the grooved section as noted in the figures. Since the size of the ultrasound wave plane interacting with the fluid film (i.e. almost same as the ultrasound transducer size (5 mm $\times$ 2 mm)) was small compared to the size of the plain and textured section, most of the obtained reflected sig-

nals exclusively contained the fluid film information on each plain or grooved section except the section transitioning from the plain section to the grooved section (or vice versa). Reductions of the signal amplitude were observed in the transferring section as seen in Figure 5.23(a). These amplitude reductions could be caused by destructive interference due to the sudden geometrical change. Within the grooved sections the measured amplitudes were almost consistent.

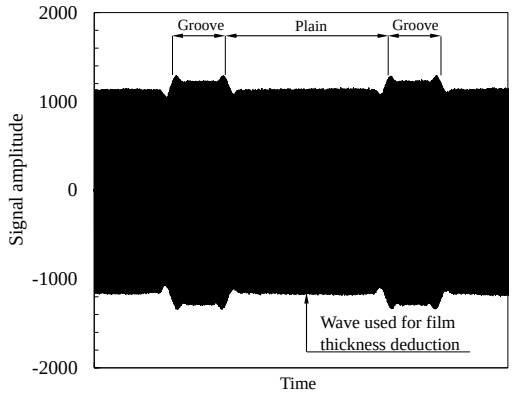

(a) Two-dimensional sound wave map for the 1st reflections

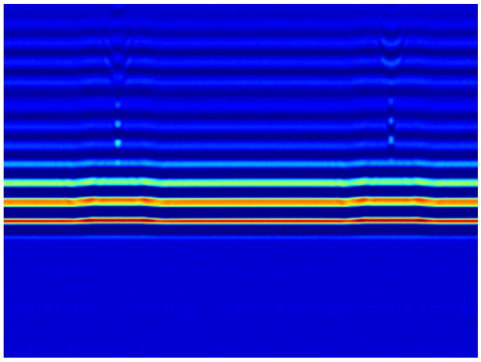

(b) Three-dimensional sound wave map for the 1st reflections

Figure 5.23: Mapped reflection signals at test condition **h**.

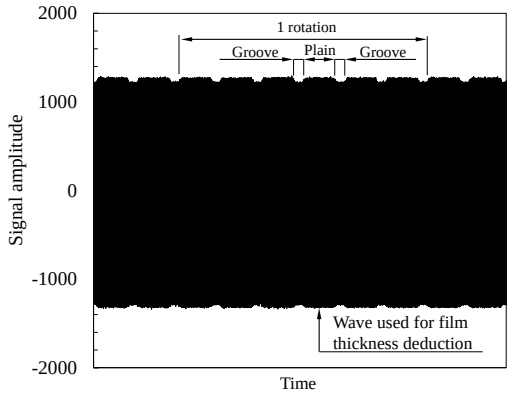

(a) Two-dimensional sound wave map for the 1st reflections

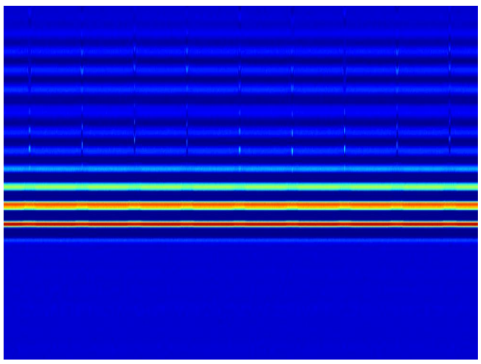

(b) Three-dimensional sound wave map for the 1st reflections

Figure 5.24: Mapped reflection signals at test condition Ref6.

The measured signals with the plain section, as seen both on Figure 5.23 and Figure 5.24, had consistent amplitude, which implies that the shaft in a given test condition was operated stably in a fixed eccentricity ratio with an attitude angle. The reflected signals from the centre of the plain section was selected for the film thickness deduction as noted in Figure 5.23(a) and Figure

5.24(a).

5.3.2.2 Experimental results

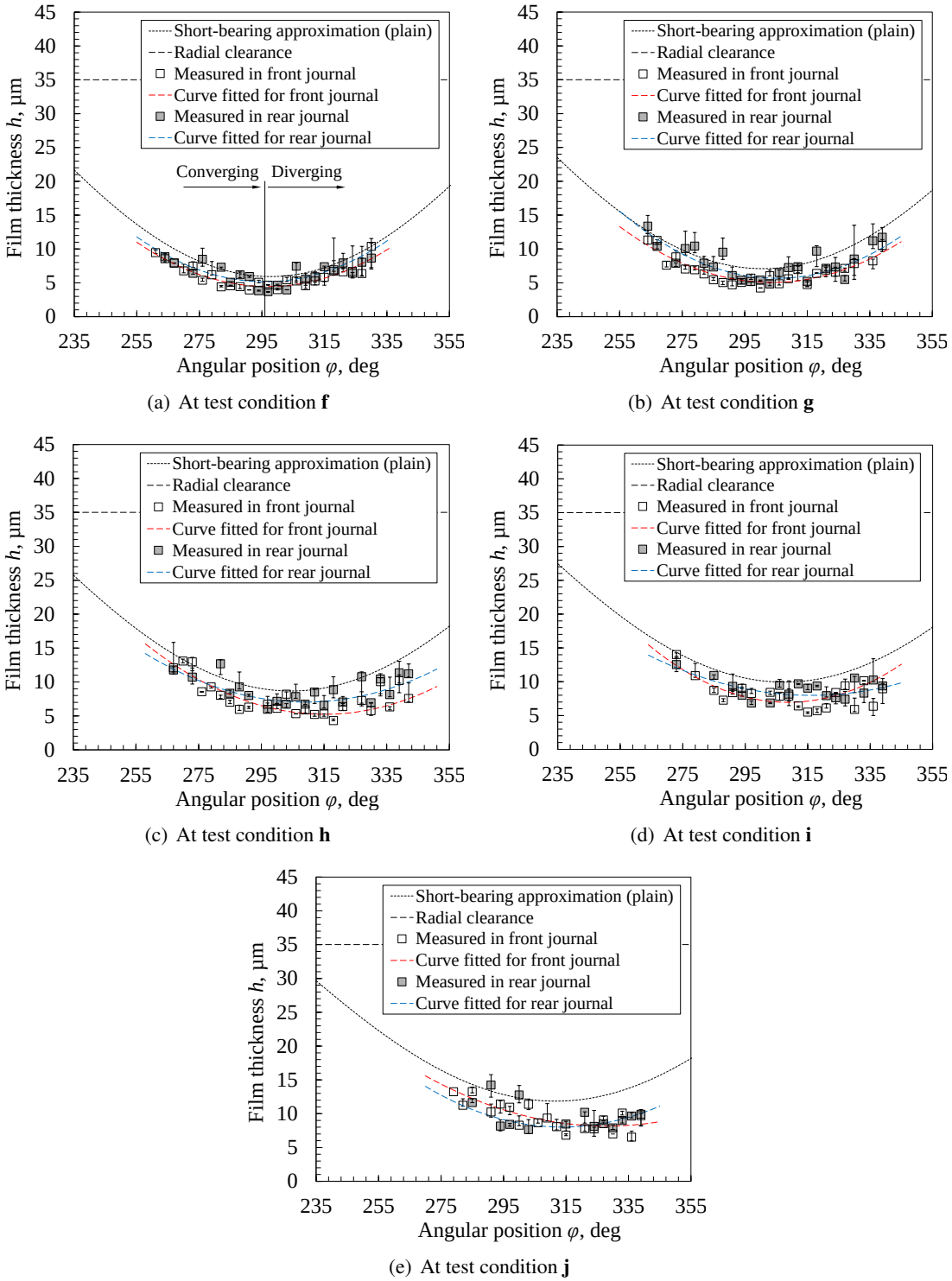

(a) At test condition **f**

(b) At test condition **g**

(c) At test condition **h**

(d) At test condition **i**

(e) At test condition **j**

Figure 5.25: Measured film thickness at the test condition **f** to **j** with the corresponding theoretical curve by the short-bearing approximation in plain bearing configuration.

The film thickness measurements performed at test condition **f** to **j** are plotted over the angular position φ where the wave was captured. As summarised in Figure 5.25 the measured film thickness were thinner than the theoretical values deduced by the short-bearing approximation for all the test conditions performed. The measured film thickness in the front journal yielded slightly thinner than the thickness measured in the rear journal at all the test conditions consistently despite the fact that the radial clearance of the front and rear journal was equally measured to be 35 μm. These results did not correspond with the results as observed in the measurements on the plain journal bearing in Chapter 4 where the measured thickness on the rear journal were thinner than those on the front journal. This could be attributed to that the relative position between the hydraulic loader and the bush was not perfectly repeatable once the test journal bearing was disassembled. Scatters of the measured film thickness were also observed in the diverging area as seen in the Chapter 4, which was assumed to be caused by cavitation. Further discussion over the result will be presented in the following discussion section comparing with the results of the plain journal bearing and journal bearing with texture B.

5.3.3 Film thickness measurement on journal bearing with Texture B

The film thickness measurements on texture B were examined on steady state of fixed rotational speeds and a fixed applied load after the temperatures monitored by the thermocouples were saturated. The main test procedure is same as mentioned in Section 4.4.3.1. The test conditions for the five measurement signals (**k** to **o**) and the reference signals (Ref7) are summarised in Table 5.6.

As discussed in the previous section, the size of the ultrasound wave plane interacting with the fluid film (i.e. almost same as the ultrasound transducer size (5 mm $\times$ 2 mm)) was small enough to the size of the plain and textured section on the journal bearing with texture A, most of the obtained reflected signals exclusively contained the fluid film information either from the plain or the grooved section except the transferring section. However, on the journal bearing with texture B the grooves were rather finely generated that the ultrasound plane wave reflects back from a layer including the fluid film on both the groove and annular clearance (or nominal film thickness) as presented in Figure 5.26. So what is observed from the reflection signals is an "averaged" film thickness over the area with which the sound wave interacts. In order to extract the nominal film thickness out of the "averaged" film thickness for direct comparison with the

other film thickness results obtained on the plain and the texture A, a digitisation process will be implemented and then the feasibility of the process will be experimentally validated in the next section.

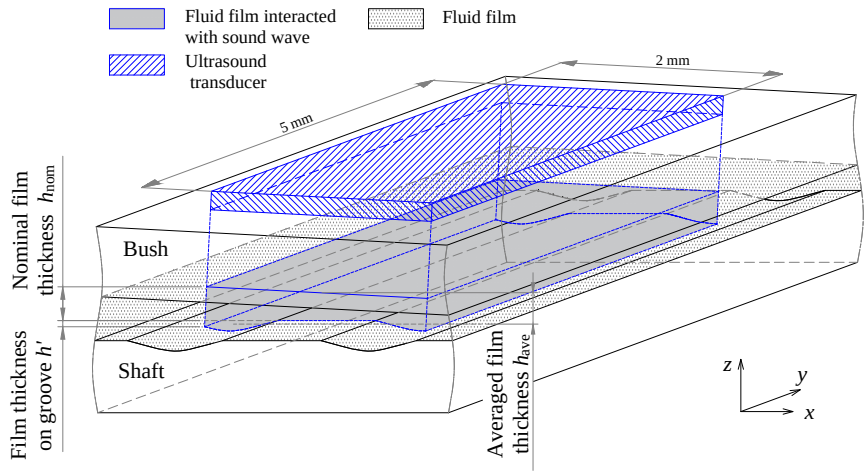

Figure 5.26: Schematic of ultrasound transducer and sound wave interacting the fluid film on the texture B.

Table 5.6: Test conditions for film thickness measurement on journal bearing with texture B.

Symbol	Rotation speed of shaft ω rpm	Load applied W kN	Temperature of TCF, TCR T °C	Oil flow rate Q L/min	Pulse rate per channel Hz
k	80	3	70	1.5	667
l	100	3	70	1.5	667
m	150	3	70	1.5	667
n	200	3	70	1.5	667
o	300	3	70	1.5	667
Ref7	500	0	70	1.5	667

5.3.3.1 Nominal film thickness deduction by fluid film digitisation and its experimental validation

Similar to the relation between stiffness of the layer and its film thickness in the spring-governed region, as expressed in Equation (2.69), stiffness of the layer on a finely textured surface can be expressed as:

$$h_{ave} = \frac{\rho c^2}{\overline{\kappa}}, \tag{5.4}$$

where h_{ave} is the averaged film thickness (shown in Figure 5.26) and $\bar{\kappa}$ the mean stiffness of the layer per unit area. As discussed in the previous section, the film thickness h is a product of the nominal film thickness h_{nom} and the film thickness on the groove h', that is:

$$h = h_{\text{nom}} + h'. \tag{5.5}$$

In order to deduce the mean stiffness of the layer per unit area $\bar{\kappa}$ on the texture B, a geometrical digitisation over the textured area where the wave is interacted was performed. Figure 5.27 shows a digitised projected area of the transducer size (5 mm $\times$ 2 mm) and Figure 5.28 shows the digitised profiles of the axial and tangential cross-sections. The mean stiffness of the layer $\bar{\kappa}$ can be expressed as:

$$\bar{\kappa} = \frac{\rho c^2}{nm} \sum_{i,j} \frac{1}{(h_{\text{nom}} + h'_{i,j})} \quad (1 \leq i \leq n, 1 \leq j \leq m), \tag{5.6}$$

where $h'_{i,j}$ is a film thickness associated with the groove in the digitised array of cells (n cells for the tangential coordinate times m cells for the axial coordinate, 40 $\times$ 100 = 4000 cells in total). As mentioned in the previous section, the texture B is present on the moving surface, i.e. the shaft surface, an area of the texture B interacting with the plan sound wave varies as the shaft rotates. However, the texture B generated was so fine that the variation of the mean stiffness of the layer $\bar{\kappa}$ is marginal regardless of shaft angular position.

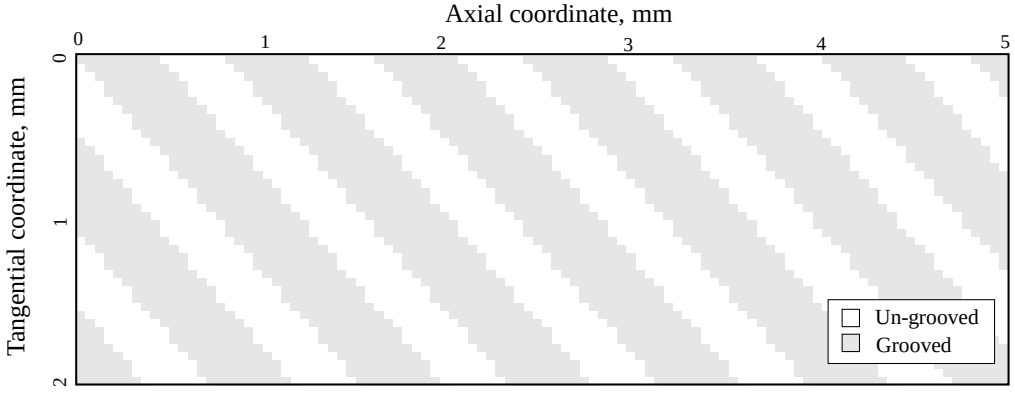

Figure 5.27: Digitised profile of texture B in the size of ultrasound transducer.

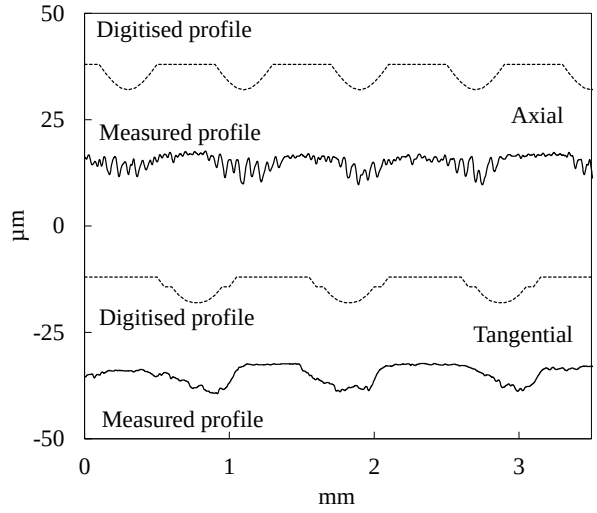

Figure 5.28: Digitised cross-sectional profile of texture B.

By using Equation (5.4) and Equation (5.6) for the digitised profile of texture B, a conversion curve from the averaged film thickness to the nominal film thickenss was obtained as presented in Figure 5.29. A slope of 1.0 which represents the line expected from an ideally smooth surface was plotted for reference also. For an example, as plotted as **X** in the figure, when the average film thickness is measured by the ultrasound reflection as 8.9 μm the nominal film thickness is deduced to be 7.5 μm.

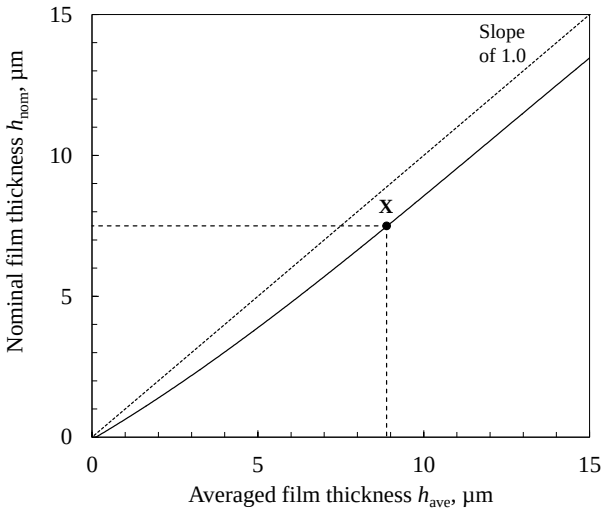

Figure 5.29: Conversion curve from averaged film thickness h_{ave} to nominal film thickness h_{nom}.

Experimental validation under static condition. In order to validate the feasibility of the obtained conversion curve in Figure 5.29, a film thickness measurement for oil-filled annulus of the journal bearing with texture B was conducted in the static condition on the test platform as ex-

amined in Section 4.3.2.2. The validity can be confirmed by comparing values of the geometrical annular clearance with the surface roughness and the generated grooves neglected, and values of the nominal film thickness h_{nom} converted from the measured averaged film thickness h_{ave}. As shown in Figure 4.26, a load was applied at $\varphi = 270^\circ$ so that the annular clearance becomes zero at $\varphi = 270^\circ$ and the film thickness measurements were conducted three times at each angular positions. The geometrical annular clearance with the surface roughness and the generated grooves neglected, h_c, is expressed as presented in Equation (4.7).

The measured averaged film thickness h_{ave} over the geometrical annular clearance is plotted in Figure 5.30(a). As seen in the figure, the measured film thickness, i.e. the averaged film thickness h_{ave} was greater than the geometrical annular clearance, so that the coefficient of the determination to the slope of 1.0 was 0.625, which was not as high as that obtained on the plain bearing in Section 4.3.2.2, R^2 = 0.831. In Figure 5.30(b) the plots of the averaged film thickness were deduced to the nominal film thickness using the conversion curve presented in Figure 5.29. The deduced plots fit better on a slope of 1.0, being R^2 = 0.850, which is comparable to 0.831 on the plain bearing. By this experimental validation, the conversion process can be considered to be feasible for implementation.

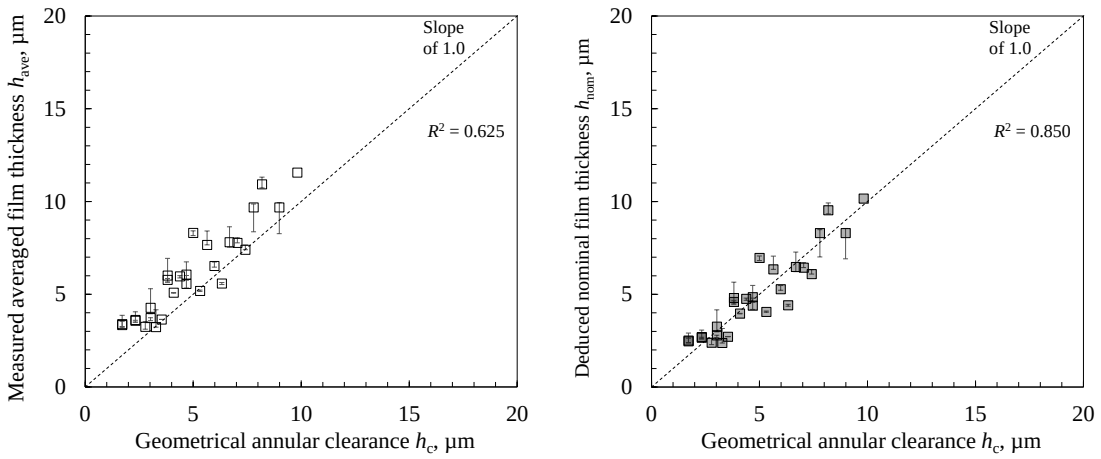

(a) Averaged film thickness over geometrical annular clearance

(b) Deduced nominal film thickness over geometrical annular clearance

Figure 5.30: Experimental results for deduction of the nominal film thickness from the averaged film thickness.

5.3.3.2 Mapped reflection signals

Figure 5.31 and Figure 5.32 shows the two-dimensional and three-dimensional wave map obtained at test condition **k** and Ref7, respectively. As seen in these figures, the amplitude of the reflected signals did not vary over the measurement time, which confirmed the discussion in the previous section regarding the stiffness variation as the shaft rotates.

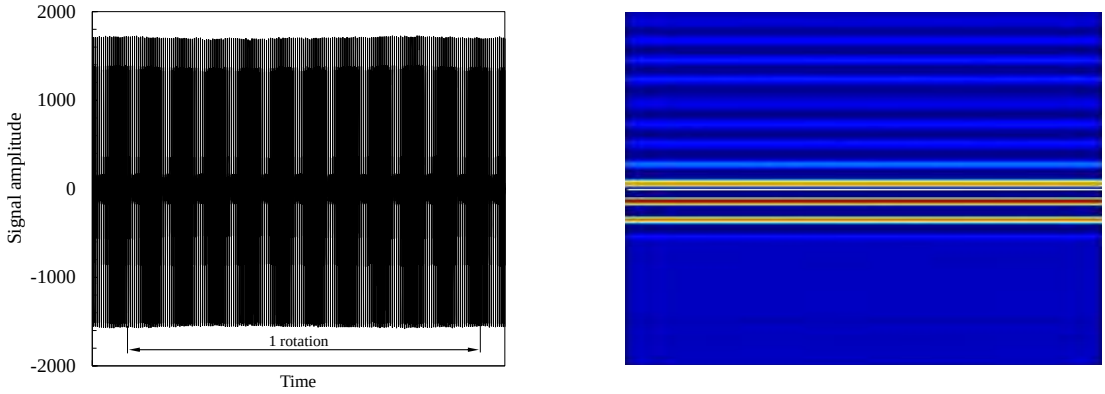

(a) Two-dimensional sound wave map for the 1st reflections

(b) Three-dimensional sound wave map for the 1st reflections

Figure 5.31: Mapped reflection signals at test condition **k**.

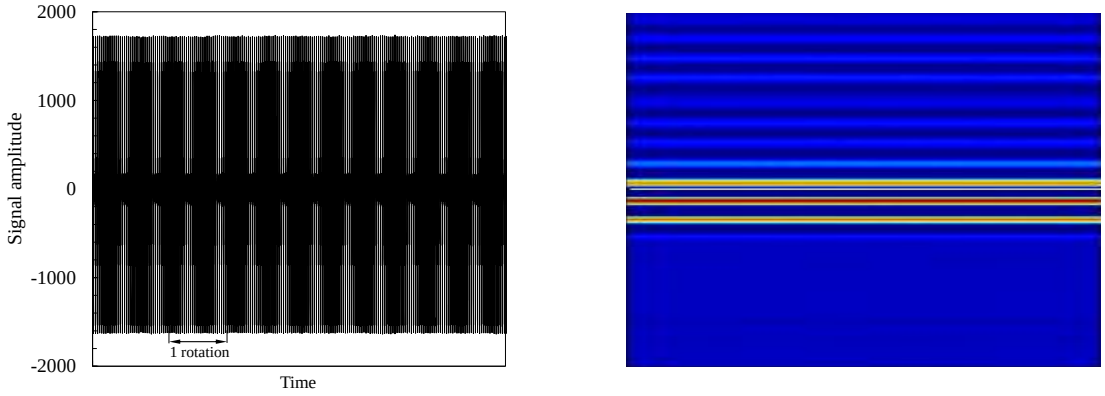

(a) Two-dimensional sound wave map for the 1st reflections

(b) Three-dimensional sound wave map for the 1st reflections

Figure 5.32: Mapped reflection signals at test condition Ref7.

5.3.3.3 Experimental results

The film thickness measurements were performed at test condition **k** to **o** and plotted over the angular position φ where the wave was captured. As summarised in Figure 5.33 the measured film

thickness were thicker than the theoretical curves deduced by the short-bearing approximation in all the test conditions performed.

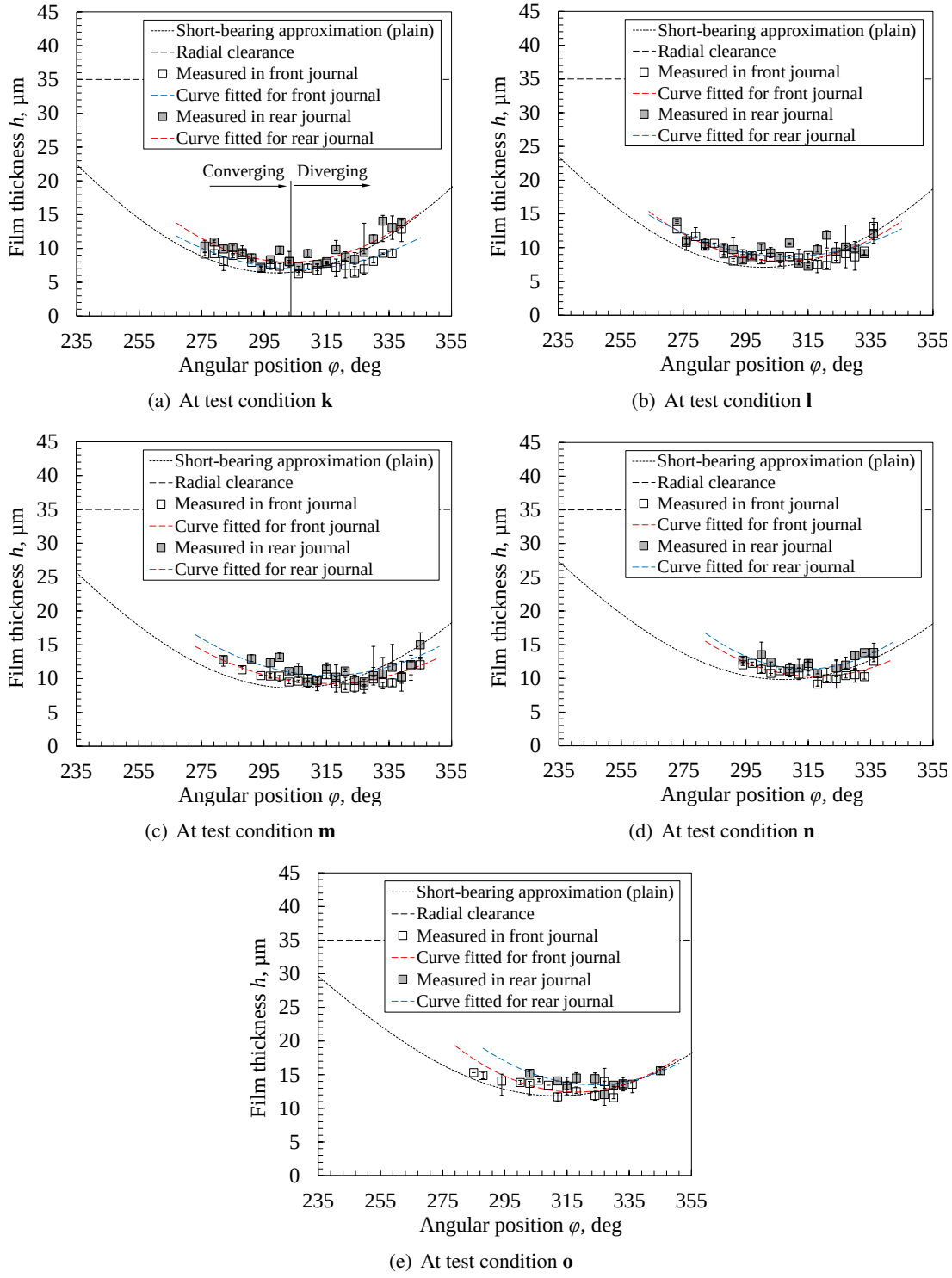

(a) At test condition **k**

(b) At test condition **l**

(c) At test condition **m**

(d) At test condition **n**

(e) At test condition **o**

Figure 5.33: Measured film thickness at the test condition **k** to **o** with the corresponding theoretical curve by the short-bearing approximation in plain bearing configuration.

The measured film thickness in the front journal yielded slightly thinner than the thickness measured in the rear journal at all the test conditions consistently, presumably due to the bush tilt as discussed in the previous sections. Greater errors of the measured film thickness were also observed in the diverging area as seen in the measurements of the plain bearing and bearing with texture A. Further discussion over the result will be presented in the following discussion section comparing with the results obtained from the plain journal bearing and journal bearing with texture B.

5.3.4 Discussion

5.3.4.1 Minimum film thickness

The minimum film thickness and attitude angle were read by fitting 2nd-order polynomial curves on the obtained data in which the film thicknesses with great errors due to cavitation in the diverging section were excluded. The curves were fitted in the front and rear journal data separately, then the minimum film thickness data were summarised over the Sommerfeld reciprocal with the theoretical curve obtained by the short-bearing approximation as presented in Figure 5.34 and the eccentricity ratio and attitude angle in Figure 5.35.

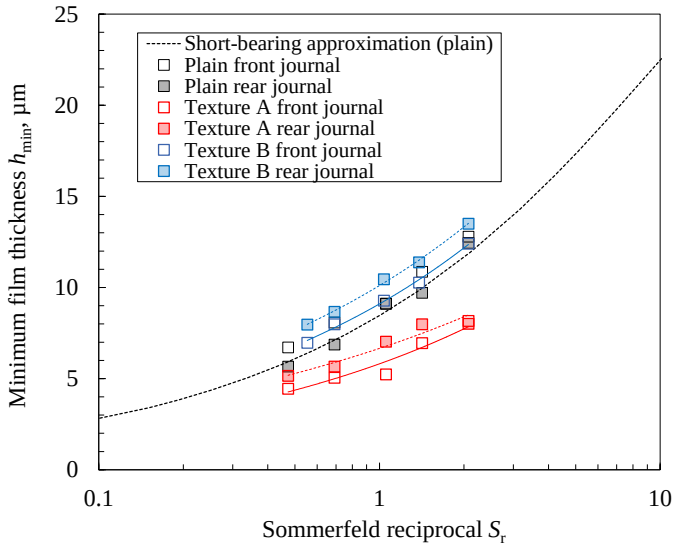

Figure 5.34: Measured minimum film thickness of the plain, texture A and texture B in Sommerfeld reciprocal domain.

Overall the measured minimum film thickness agreed qualitatively with the estimation discussed in the aforementioned literature review in this chapter. The minimum film thickness on the texture A yielded thinner than those of the plain bearing over the Sommerfeld reciprocal range

where the tests were conducted. The minimum film thicknesses to the theoretical thickness decreased by 13 % $\sim$ 40 %. At the test condition **g**, for an example, the measured film thicknesses were reduced by 29 % and 20 % as compared with the theoretical value of the short-bearing approximation, being 5.05 μm and 5.67 μm in the front and the rear journal. Since the geometrical ratios, groove depth and groove width to the radial clearance ($d_g/c_r = 11.4$ and $w_g/c_r = 357$), of the texture A are very high, the convective inertia effect was assumed to be marginal and simply the generated grooves reduced the effective bearing convergence. However, the measured thicknesses would be thick enough to keep the bearing operated under hydrodynamic lubrication regime, as the surface roughness of the plain section of texture A is one-order smaller than the measured film thickness.

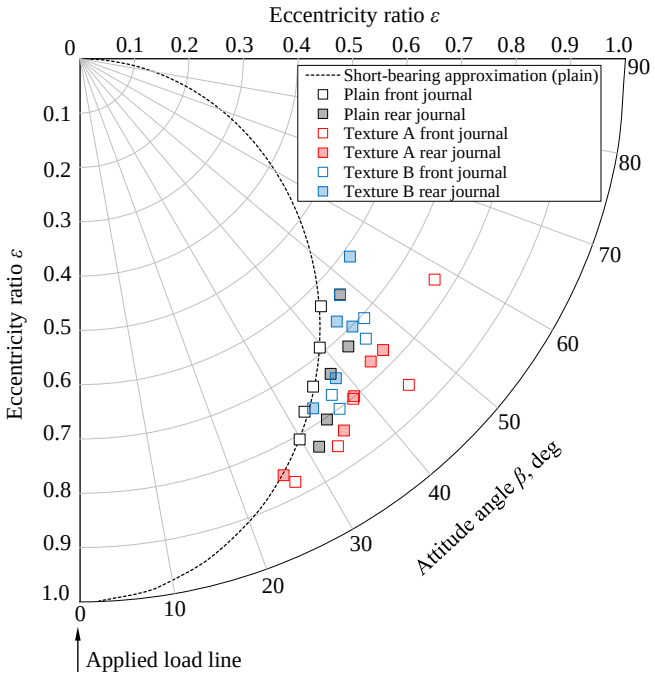

Figure 5.35: Plot of eccentricity ratio against attitude angle of the plain, texture A and texture B.

While the texture B with the fine-meshed grooves was a thicker film across the Sommerfeld reciprocal range, which corresponds qualitatively with the literature CFD works summarised in this chapter. The film thicknesses increased by 4 % $\sim$ 25 % compared with the theoretical counterparts. It is presumed that the aformentioned convective inertia effect appeared positively because the geometrical ratios, groove depth and groove width to the radial clearance ($d_g/c_r = 0.2$ and $w_g/c_r = 14.7$) could have been appropriate, and the Reynolds numbers at the tests were not

sufficiently smaller than 1 ($Re = 0.3 \sim 1.1$). Although such positive effects were observed at all the test conditions when compared to the theoretical values; however, the deduced film thickness at test condition **o** were found to be nearly same when compared with the measured film thickness on the plain bearing. The film thickness measured at test condition **o** were close to the measurable upper limit that the accuracy of the measurement can be questioned.

5.3.4.2 Load capacity

As has been discussed, the relative tilt between the shaft and bush were observed on all the test pieces though the degrees of the tilts were not significant. If such tilt did not occur in an ideal condition, the measured film thickness would have been equal on the front and rear journal and could have yielded a value in between of the front and the rear journal. Therefore, the mean value of the measured minimum film thickness on the front and rear journal was used in order to discuss the load capacity for convenience. As shown in Figure 5.36, the load capacities of the plain, texture A and texture B were deduced by comparing with the corresponding theoretical curve of the short-bearing approximation.

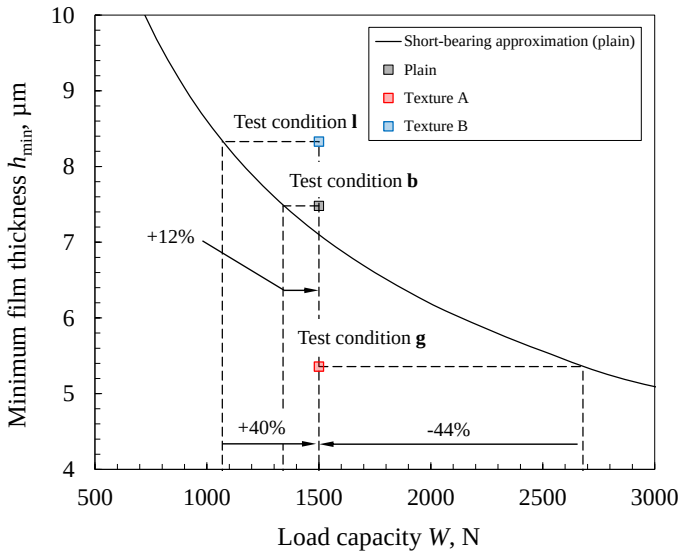

Figure 5.36: Plot of load capacity over film thickness on plain, texture A and texture B at test conditions **b**, **g** and **l** with the theoretical curve.

The deduced load capacity ratio ζ', which is a ratio of the deduced load capacities on the plain, texture A and texture B to theoretical load capacity of the short-bearing approximation, is then summarised over the minimum film thickness in Figure 5.37.

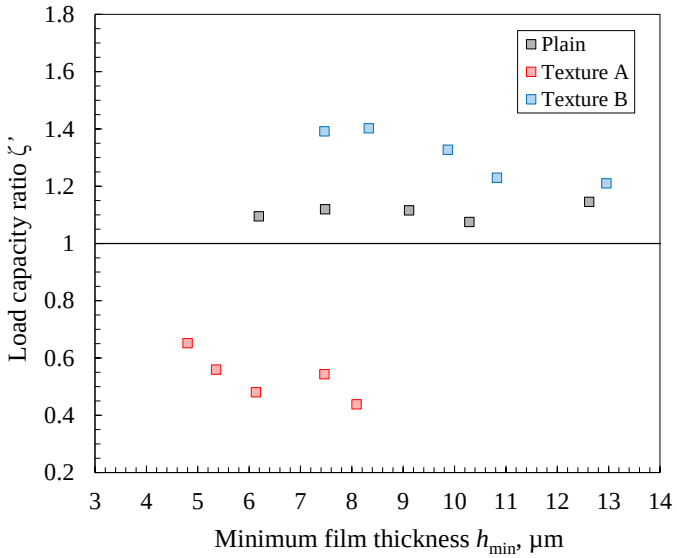

Figure 5.37: Plot of load capacity ratio ζ' over the minimum film thickness on plain journal bearing, texture A and texture B.

The ratios ζ' of the plain journal bearing were 1.09, 1.12, 1.12, 1.08 and 1.15. Except the load capacity ratio at test condition **e**, i.e. $\zeta' = 1.15$ which was deduced in minimum film thickness close to the measurable upper limit, the ratios ζ are almost consistent at its mean value of 1.1. This could be attributed to the limitation of the hydrodynamic lubrication theory with the short-bearing approximation. In order to conduct a direct comparison with the load capacity ratio deduced in the CFD works, the load capacity ratio ζ, a ratio of the load capacities measured on the texture A and texture B to the load capacity measured on the plain, is introduced. For convenience, ζ was deduced by using the ratios ζ' on the textured bearings and the mean ratios ζ' deduced on the plain journal bearing, i.e. $\zeta = \zeta'/1.1$.

Although there are not simulations conducted on the exactly same geometrical model as the present experimental textured test pieces, the quantitative validity of the deduced load capacity ratios ζ could be discussed by comparing with the literature examined on similar Reynolds number *Re* and geometrical ratios to film thickness, d_g/h and w_g/h. From the summarised CFD literature works in Table 5.2, simulation models on non-parallel components are selected, the works by Brajdic-Mitidieri et al. (2005) for comparison with the texture A, Li and Chen (2007) for the texture B as plotted in Figure 5.38. In the figure the sizes of the plotted circles represent the load capacity ratios ζ, where the inner dashed-circles are the lowest ζ and the outer circles are the highest ζ in the conducted measurements. Noted that the result at test condition **o** was excluded

from the figure due to the aforementioned reason. The work conducted by Brajdic-Mitidieri et al. (2005) was simulated with variation of the groove location as the grooves were modelled on the stationary surfaces, several load capacity ratios were obtained at a Reynolds number. As well as the Brajdic-Mitidieri et al. (2005) the dependency of the load capacity in the groove location was also reported on the works by Huynh (2005), Cupillard et al. (2008) and Dobrica and Fillon (2009). Such dependency of the load capacity was not observed in the present work where the textures were generated on the moving surface.

As presented in Figure 5.38, despite the several difference on the geometrical model and test conditions between the theoretical works and the present experimental work, the magnitudes of the load capacity ratios ζ were found to be similar. In the case of texture A the load capacity ratios were measured to be 0.40 to 0.59, while in the corresponding theoretical work the ratios were 0.63 to 0.96 (Brajdic-Mitidieri et al., 2005). In the case of texture B the load capacity ratios were measured to be 1.12 to 1.27, while in the corresponding theoretical work the ratio was 1.15 (Li and Chen, 2007).

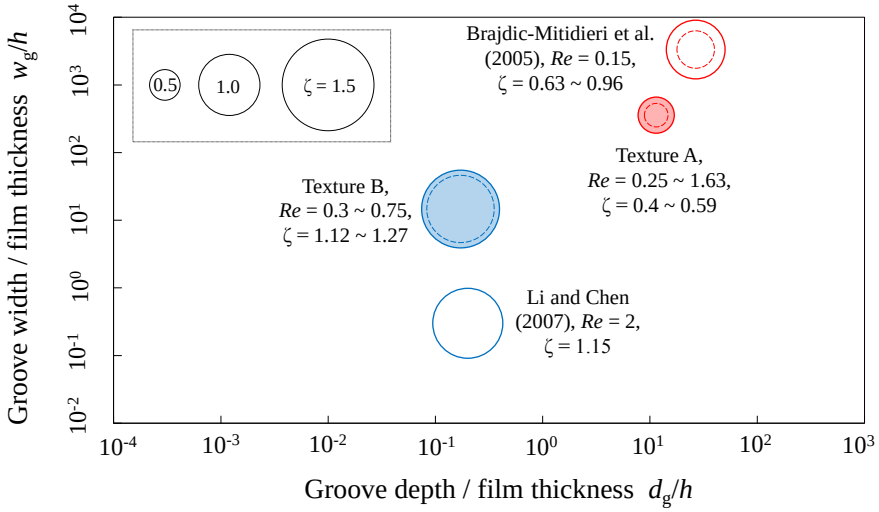

Figure 5.38: Plot of load capacity ratios ζ on the experimental and simulation works over geometrical ratios.

5.4 Conclusions

The film thickness measurements using an ultrasound reflection technique were examined for two journal bearings with bespoke surface texture. The effect of the bespoke surface texture on film thickness was discussed comparing with those deduced by CFD literature works which were

conducted at geometrical configurations similar to those of the present experimental work. The following conclusions are drawn from this chapter:

- The experimental and theoretical literature works conducted on the effect of surface roughness or bespoke surface texture on film thickness or load capacity were reviewed. In a parallel slider where the magnitude of the load capacity is comparatively low, the additional load capacity is explained by asymmetrical pressure in a groove generated by cavitation. While in a non-parallel slider where the load capacity is mainly determined by the geometrical convergence and the cavitation does not occur in a groove, the additional load capacity can be generated by convective inertia within the range where two conditions are met i.e. magnitudes of the film thickness and the bespoke surface textures are of similar magnitude and the Reynolds number is not significantly smaller than 1. The effect on the load capacity was mapped on two geometrical ratios, by which three areas (i.e. positive, negative, or no or little effect) were identified.

- For experimental validation of the effect of bespoke surface texture, two configurations of bespoke surface texture were generated on the journal bearing which was same geometry as the bearing used in Chapter 4. Texture A which represents the hypothetical area as being negative effect was generated by a normal machining. Texture B which represents the hypothetical area as being positive effect was generated by implementing the vibration-assisted machining developed in Chapter 3.

- Film thickness measurements were performed on the journal bearings with texture A and texture B on the journal bearing test platform developed in Chapter 4. The experimental results validated the hypothesis from the reviewed literature works quantitatively. The load capacity ratio ζ, i.e. a ratio of the load capacity experimentally measured on the textured bearing and the load capacity on the plain bearing, were 0.40 to 0.59 in the texture A and 1.12 to 1.27 in the texture B. Despite the several differences in the geometrical model and test conditions between the present experimental work and the literature CFD works compared, the load capacity ratios were quantitatively similar.

Chapter 6

Conclusions

In this chapter, the concluding remarks are summarised on achievements against thesis aim and objectives set in Chapter 1. The key findings are highlighted and recommendations toward the future study are suggested for each objective.

6.1 Objective 1: Development of a Vibration-Assisted Machining

With the aim to create bespoke surface textures in accurate, inexpensive and fast manner, a non-resonant vibration-assisted machining device was developed using an off-the-shelf piezo-electric actuator, its control system, and a conventional cutting tool. The developed device and its machining performance achieved in this study can be assessed in the categories with comparison to the other techniques as shown in Table 6.1.

Table 6.1: Summary of the texturing techniques. Score rating Good: 3, Average: 2, Poor: 1.

Techniques	Production cost		Texture generation		Work piece limitation	
	Apparatus	Overall production time	Accuracy achievable	Controll-ability	Material	Size
Chemical vapour deposition	2	1	3	3	3	$1 \sim 2$
Shot peening	3	$1 \sim 2$	1	2	3	3
Photolithography and reactive ion etching	2	1	3	3	3	3
Laser based	1	$1 \sim 2$	3	3	2	3
Vibration-assisted machining	2	3	1	$1 \sim 2$	$2 \sim 3$	3
Vibration-assisted machining (present study)	**2**	**3**	**3**	**3**	**$2 \sim 3$**	**3**

6.1.1 Production cost

All the main apparatus, the piezoelectric actuator (P-212.40 from PI), the amplifier (E-481 from PI) and the assembly of dryer, filter and air regulator (MSB6 from Festo) employed in the development were available with off-the-shelf. £1,310 for the piezoelectric actuator, £10,849 for the amplifier, £1,050 for the assembly of dryer, filter and air regulator, which is £13,209 in total, were spent on top of the inexpensive components such as the housings, flexible tip, cutting tool, roller bearing or other miscellaneous parts. These prices are the initial cost and do not include the maintenance cost. Additional costs will be needed not only by time-dependent damages e.g. when the cutter insert is worn out or when fatigue failure occurs in the electrode layer of the piezoelectric element by its continuous use, but also by accidental damages e.g. the actuator is subject to an excessive force. Although the wear issue is an area of the future study, the issue related to the accidental damages can be minimised by careful design and operation.

The overall production time consists of two critical times, i.e. time to replace work pieces to another arrangement and processing time to generate the bespoke surface textures. As the developed vibration-assisted machining can be implemented after the finish cut is performed in the same arrangement, the technique does not require the time to change the arrangement. Regarding the processing time, as shown in table 6.2, the face of the disc work pieces were turned in 52 s and the shaft work piece were machined in 125 s in the preliminary test and 313 s in texture B, respectively.

Although the machining time increases as the area to be machined increases and some of the maintenance cost are unknown; however, the overall production cost can be considered to be reasonably good among the techniques cited in Table 6.1.

Table 6.2: Summary of work pieces textured by vibration-assisted machining device.

Work piece symbol		A1 to A7	S1 to S6	Preliminary test	Texture B
Material		AlSi1MgMn	16MnCr5	C40	SCM420H
Machined diameter	mm	84 to 136	84 to 136	98	98
Vickers hardness	MPa	1216	2491	2211	1762
Specific cutting force K_s	MPa	2100 incl. SF	5100 incl. SF	5100 incl. SF	5100 incl. SF
Machining time	s	52	52	125	313
Corresponding chapter		3	3	5	5

6.1.2 Texture generation

The accuracy of the generated textures that this technique achieved, as shown in Figure 3.26 in Chapter 3 for the disc work pieces, was very good both in the aluminium and steel work pieces. As the coefficient determination, $R^2 = 0.948$, in Figure 3.26 indicated, the displacement of the piezoelectric element corresponded well with the generated peak to peak amplitude of the textures.

The generated sine wave in the disc work pieces were controllable from approximately 1 mm to 8 mm in the wavelength and from a few μm to 25 μm in the peak to peak amplitudes in the operation range as predicted in the feasibility study (Figure 3.17). The designed geometry for texture B of the shaft work piece, 0.513 mm in the groove width and 6 μm in the groove depth was successfully generated, which worked beneficially generating additional hydrodynamic pressure as presented in Chapter 5.

6.1.3 Work piece limitation

The geometry of the constructed mechanical assembly was compact, 199 mm in height and ϕ80 mm in outer diameter. The developed device was successfully implemented on a standard milling machine to turn the face of the disc work pieces (ϕ84 mm $\sim$ ϕ136 mm) and on a standard turning machine to turn the shaft work pieces (ϕ98 mm) . The components of the developed device, i.e. the mechanical assembly, amplifier, assembly for the cooling air circulation and the cables (actuator power cable and cooling air), did require a small space, so that they did not limit the work piece size and shape.

As summarised in Table 6.2, the materials machined were an aluminium alloy AlSi1MgMn and steel alloys 16MnCr5, C40 and SCM420H with Vickers hardness of 1216 MPa $\sim$ 2491 MPa. These materials are widely used in real engineering applications. The other materials commonly used in industry, such as titanium alloy, magnesium alloy or cast iron, can be machined with the developed technique with suitable selection of the cutter insert.

6.1.4 Recommendations

Further investigation could be directed toward the implementation of the constructed device in machining with deeper depth of cut on a hardened material where the push force could limit the operation range. As mentioned in the production cost section, wear rate of the cutter insert

is one of the factors to determine the maintenance cycle. The effect of superposition of vibration toward such wear rate is another topic for the future investigation. Although burr generation was not observed both in the disc work pieces and shaft work pieces in the machining conditions conducted in this study, such burr generation may occur in more severe conditions such as machining with greater cutter displacement of higher vibration frequency. It would be useful to define the operation range of no burr generation in the texture design process. Influence on substrate properties which may be induced by the vibration-assisted machining, e.g. crack generation or residual stress, has not been investigated in this study. This investigation will be of importance, in particular, in the case of the textured component operated under very high stress where presence of such crack or residual stress may work negatively. The investigation of contributory factors for the minor phase shift which was evident on the disc work pieces could also be an area for future study.

6.2 Objective 2: Development of a Journal Bearing Test Platform

With the aim to examine lubricant film thickness measurement under real operational situation of an automotive transmission, a journal bearing test platform was developed incorporating an ultrasound reflection technique. This technique allowed the examination of film thickness measurements with no physical penetration of the parts involved in the film formation.

6.2.1 Construction of the journal bearing test platform

A test platform that can represent operational conditions of an automotive transmission journal bearing was constructed incorporating the actual transmission components and the ultrasonic apparatus. Three issues of the ultrasound reflection technique revealed through the literature review i.e. spatial resolution of the ultrasound transducer, the number of locations where the sound wave data can be captured in one trial, and the thermal drift of the ultrasound wave amplitude, were improved in this study.

Firstly, the issue for the spatial resolution was improved by employing small and bare piezoelectric elements of 5 mm $\times$ 2 mm in size. Through the film thickness measurements, it was confirmed that the spatial resolution of the selected element was good to profile circumferentially the film thickness of the selected journal bearing with ϕ98 mm in nominal diameter.

Secondly, the issue for the number of the usable sensor channels in a measurement trial was

solved by arranging a multi-channel capturing system as was successfully developed and implemented on a piston-cylinder application studied by Mills et al. (2012). Six sensors were pulsed successfully in a measurement trial, which helped to reduce the overall measurement time to profile the bearing film thickness. The pulse rate per channel of 167 Hz $\sim$ 3333 Hz was used and was sufficiently fast to capture the reflected signal in the plain and the two textured bearings in the rotational speeds examined in this study.

Lastly, the issue of the significant thermal drift on the sound wave amplitude was minimised by implementing an approach, that is, capturing the reference signal in a steel/thick oil layer/steel interface just before capturing the measurement signal. Through the film thickness measurements, this approach was confirmed to work well under all the temperature conditions (room temperature $\sim$ 80 °C) conducted in this study.

6.2.2 Experimental film thickness measurements on the constructed test platform

On the constructed test platform, the film thickness of a plain bearing in Chapter 4 and two textured bearings (texture A and texture B) in Chapter 5 were successfully measured. The measured film thickness and the attitude angle on the plain journal bearing under the steady-state conditions agreed well with the theoretical curves deduced by a classical Reynolds equation with the short-bearing approximation, which confirmed the accuracy of the constructed test platform and the incorporated ultrasound measuring apparatus.

The measured range of the minimum film thickness on the plain journal bearing was approximately from 5 μm to 12 μm at the Sommerfeld reciprocal range from 0.5 to 2.1. The measured film thickness was marginally thinner in the rear journal than in the front journal. Which would have been caused by the axial tilt or the misalignment between the journals. Judging from the Lambda ratio (exceeded 50 at all the conditions) obtained from the measured minimum film thickness and the combined surface roughness, the journal bearing is run within the hydrodynamic lubrication regime under the steady-state conditions performed in this study.

As well as the film thickness on the plain journal bearing, a rough-meshed bearing (texture A) and a fine-meshed bearing (texture B) were also measured on the test platform. On the journal bearing with texture A, since the size of the ultrasound wave plane interacting with the fluid film (i.e. almost same as the ultrasound transducer size (5 mm $\times$ 2 mm)) was small compared to the size of the plain and textured section, most of the obtained reflected signals exclusively contained

the fluid film information on each plain or grooved section. The pulse rate per channel for the measurement in the bearing with texture A was 3333 Hz, which was fast enough to distinguish the signal whether reflected back from the plain section or the grooved section.

On the journal bearing with texture B, the grooves were rather finely generated that the ultrasound plane wave reflects back from a layer including the fluid film on both the groove and annular clearance (or nominal film thickness). In order to extract the nominal film thickness out of the "averaged" film thickness for direct comparison with the other film thickness results obtained on the plain and the texture A, a digitisation process was implemented and then the feasibility of the process was experimentally validated in a preliminary test.

6.2.3 Recommendations

For future work, assembling the ultrasound transducer in the moving component (i.e. the shaft in the journal bearing) using a slip-ring will further reduce the measurement time to profile the film thickness in journal bearing. This approach was investigated by Kasolang and Dwyer-Joyce (2008a) using a conventional set of slip-rings. The measured film thickness profile in a journal bearing agreed well with classical hydrodynamic lubrication theory. The authors penetrated the steel shaft surface by using a dissimilar material (aluminium) plug for the ultrasound wave transmission. If the transducer with a slip-ring can be arranged inside the shaft by not penetrating the journal surface, accuracy of the film thickness measurement will be further improved.

In the measured film thickness on all the test shafts, the relative tilt between the shaft and bush were observed though the degree of the tilts were not significant. If such tilt did not occur in an ideal condition, the measured film thickness would have been equal on the front and rear journal. In order to accurately deduce the load capacity of a test shaft, such tilt should be marginal and the accuracy will be further improved if the tilt is controllable by an adjuster. This adjuster would allow to conduct the film thickness measurement not only at an ideal (no tilt) condition but also purposely tilt condition which represents an undesirable situation caused by various factors e.g. inaccurate assembling or manufacturing error.

6.3 Objective 3: Examination of Film Thickness Measurement on Two Textured Journal Bearings

With the aim of addressing the deficiency of in-depth understanding as to effect of bespoke surface texture on lubricant film formation under real operational situation, the film thickness measurements in the journal bearing test platform developed in Chapter 4 were conducted on two journal bearings with bespoke surface textures to validate a hypothesis obtained through a literature review for the theoretical studies.

6.3.1 Mechanism of additional hydrodynamic force generation

The experimental and theoretical literature works conducted on the effect of surface roughness or bespoke surface texture on film thickness or load capacity were reviewed and summarised in Table 5.1 and Table 5.2. Through this literature review, it was found that geometrical parameters and operational conditions were involved in hydrodynamic force generation in a complicated manner. With such a complex nature to deal with the hydrodynamic lubrication with bespoke surface texture, this study attempted to identify the most influential parameters on the governing mechanism, separately reviewing works examined on parallel sliders and on non-parallel sliders.

In parallel sliders where the magnitude of the load capacity is comparatively low, the additional load capacity is explained by asymmetrical pressure in a groove generated by cavitation. The net pressure gain by cavitation can be predominant on such parallel sliders since no pressure or very low pressure is built due to the very small or no convergence ratio.

While in non-parallel sliders where the load capacity is mainly determined by the geometrical convergence and cavitation does not occur in a groove, the additional load capacity can be generated by convective inertia within the range where two conditions are met i.e. magnitudes of the film thickness and width and depth of the bespoke surface textures are of similar magnitude and the Reynolds number is not significantly smaller than 1. This hypothetical conclusion could be drawn due to recent technical advances in computational power which enabled to conduct full Navier-Stokes based simulations.

The effect of the bespoke surface texture on the load capacity of non-parallel sliders observed in CFD literature works was mapped for two geometrical ratios (ratio of film thickness to groove width and depth), by which three areas (i.e. positive, negative, or no or little effect) were iden-

tified. This summary map was intuitively understood since slider models whose grooves are shallow and too finely meshed as those with ideally smooth slider, no effect should appear on the load capacity while slider models whose grooves are deep and roughly meshed, which would simply reduce the convergence of the sliders, resulting in the negative effect. Although this summary map did not exclude the effect of the other influential parameters e.g. groove location or groove form, it can be used as a rough design guide.

6.3.2 Experimental investigation

Through reviewing the experimental and theoretical literature works, the effect of the bespoke surface texture on additional load capacity was mapped on the geometrical ratios; however, it was found that little validation work has been experimentally conducted on non-parallel sliding applications including journal bearing thus far focusing on the geometrical ratios and Reynolds number.

In order to experimentally validate the hypothesis obtained from the literature review, two configurations of bespoke surface texture were generated on the journal bearing which was same geometry as the bearing used in Chapter 4. Texture A which represents the hypothetical area as being negative effect was generated by a conventional machining. Texture B which represents the hypothetical area as being positive effect was generated by implementing the vibration-assisted machining developed in Chapter 3.

Film thickness measurements were performed on the journal bearings with texture A and texture B in the journal bearing test platform developed in Chapter 4. The experimental results validated the hypothetical conclusion quantitatively. The load capacity ratio ζ, i.e. a ratio of the load capacity experimentally measured on the textured bearing and the load capacity on the plain bearing, were compared with the corresponding theoretical values. In the case of texture A the load capacity ratios were measured to be 0.40 to 0.59, while in the corresponding theoretical work the ratios were 0.63 to 0.96 (Brajdic-Mitidieri et al., 2005). In the case of texture B the load capacity ratios were measured to be 1.12 to 1.27, while in the corresponding theoretical work the ratio was 1.15 (Li and Chen, 2007). Despite the several differences in the geometrical model and test conditions between the present experimental work and the literature CFD works compared, the load capacity ratios were quantitatively similar.

6.3.3 Recommendations

For future works, further experiments are needed in order to determine the optimum ratio to maximise the load capacity by changing the geometrical ratios (d_g/c_r and w_g/c_r) as well as the cross-sectional form of the groove or groove coverage i.e. ratio of the area grooved and un-grooved etc.

Although dependency of the groove location was reported as an influential parameter on several simulation works where the groove was modelled on the stationary surface, such dependency could not be examined in this study since the textures A and B were generated on the moving surface. It will be an area of further study to investigate such dependency in applications where the groove must be generated on the stationary surface.

In this study, the film thickness measurements were examined on the range of Reynolds number within the operational conditions of the transmission. The sensitivity of the load capacity to the Reynolds number variation can be investigated by largely changing the Reynolds number but the Sommerfeld reciprocals.

In order to experimentally determine the load capacity when the lubrication film collapse, it is necessary to add a measurement unit which can determine a transitional point where the frictional force rapidly increases. An arrangement of the friction measurement unit to determine only the frictional force responsible to the test journal bearing would be needed.

Bibliography

Aida, T. and Oda, S. (1966). Bending fatigue strength of gears. *Bulletin of JSME*, 9(36):793–806.

Amanov, A., Tsuboi, R., Oe, H., and Sasaki, S. (2013). The influence of bulges produced by laser surface texturing on the sliding friction and wear behavior. *Tribology International*, 60:216–223.

Anno, J., Walowit, J., and Allen, C. (1969). Load support and leakage from microasperity-lubricated face seals. *Journal of Tribology*, 91(4):726–731.

Anno, J. N., Walowit, J., and Allen, C. (1968). Microasperity lubrication. *Journal of Tribology*, 90(2):351–355.

Arghir, M., Roucou, N., Helene, M., and Frene, J. (2003). Theoretical analysis of the incompressible laminar flow in a macro-roughness cell. *Journal of Tribology*, 125(2):309–318.

Birring, A. and Kwun, H. (1989). Ultrasonic measurement of wear. *Tribology international*, 22(1):33–37.

Blitz, J. (1971). *Ultrasonics: methods and applications*. Newnes-Butterworth, London.

Brajdic-Mitidieri, P., Gosman, A. D., Ioannides, E., and Spikes, H. A. (2005). CFD analysis of a low friction pocketed pad bearing. *Journal of Tribology*, 127(4):803–812.

Brehl, D. and Dow, T. (2008). Review of vibration-assisted machining. *Precision engineering*, 32(3):153–172.

Cameron, A. (1966). *The Principles of Lubrication*. Longmans Green and Co. Ltd, London.

Chen, W., Mills, R., and Dwyer-Joyce, R. (2015). Direct load monitoring of rolling bearing contacts using ultrasonic time of flight. In *Proc. R. Soc. A*, volume 471, page 20150103. The Royal Society.

Choy, K. (2003). Chemical vapour deposition of coatings. *Progress in materials science*, 48(2):57–170.

Coblas, D. G., Fatu, A., Maoui, A., and Hajjam, M. (2015). Manufacturing textured surfaces: State of art and recent developments. *Proceedings of the Institution of Mechanical Engineers, Part J: Journal of Engineering Tribology*, 229(1):3–29.

Costa, H. and Hutchings, I. (2007). Hydrodynamic lubrication of textured steel surfaces under reciprocating sliding conditions. *Tribology International*, 40(8):1227–1238.

Costa, H. and Hutchings, I. (2009). Development of a maskless electrochemical texturing method. *journal of materials processing technology*, 209(8):3869–3878.

Cupillard, S., Glavatskih, S., and Cervantes, M. (2008). Computational fluid dynamics analysis of a journal bearing with surface texturing. *Proceedings of the Institution of Mechanical Engineers, Part J: Journal of Engineering Tribology*, 222(2):97–107.

Dahotre, N. B. (1998). *Lasers in surface engineering*, volume 1. ASM international, Ohio.

Dambon, O., Klocke, F., Heselhaus, M., Bulla, B., Weber, A., Schug, R., and Bresseler, B. (2007). Vibration-assisted machining research at Fraunhofer IPT–diamond turning and precision grinding. pages 3–10. Proceedings of the Spring Topical Meeting 2007. American Society for Precision Engineering (ASPE).

Dobrica, M. and Fillon, M. (2009). About the validity of Reynolds equation and inertia effects in textured sliders of infinite width. *Proceedings of the Institution of Mechanical Engineers, Part J: Journal of Engineering Tribology*, 223(1):69–78.

Drinkwater, B. W., Zhang, J., Kirk, K. J., Elgoyhen, J., and Dwyer-Joyce, R. S. (2009). Ultrasonic measurement of rolling bearing lubrication using piezoelectric thin films. *Journal of Tribology*, 131(1):011502.

Dubey, A. K. and Yadava, V. (2008). Multi-objective optimization of Nd: YAG laser cutting of nickel-based superalloy sheet using orthogonal array with principal component analysis. *Optics and Lasers in Engineering*, 46(2):124–132.

Dubois, G. and Ocvirk, F. (1953). Analytical derivatioin and experimental evaluation of short-bearing approximation for full journal bearings. *National Advisory Committee for Aeronautics*, (Report 1157).

Dwyer-Joyce, R., Drinkwater, B., and Donohoe, C. (2003). The measurement of lubricant–film thickness using ultrasound. *Proceedings of the Royal Society of London. Series A: Mathematical, Physical and Engineering Sciences*, 459(2032):957–976.

Dwyer-Joyce, R., Harper, P., and Drinkwater, B. (2004). A method for the measurement of hydrodynamic oil films using ultrasonic reflection. *Tribology Letters*, 17(2):337–348.

Dyer, D. and Reason, B. (1976). A study of tensile stresses in a journal-bearing oil film. *Journal of Mechanical Engineering Science*, 18(1):46–52.

Elrod, H. (1979). A general theory for laminar lubrication with Reynolds roughness. *Journal of Tribology*, 101(1):8–14.

Etsion, I., Halperin, G., Brizmer, V., and Kligerman, Y. (2004). Experimental investigation of laser surface textured parallel thrust bearings. *Tribology Letters*, 17(2):295–300.

Geiger, M., Roth, S., and Becker, W. (1998). Influence of laser-produced microstructures on the tribological behaviour of ceramics. *Surface and Coatings Technology*, 100:17–22.

Glavatskih, S., McCarthy, D., and Sherrington, I. (2005). Hydrodynamic performance of a thrust bearing with micropatterned pads. *Tribology transactions*, 48(4):492–498.

Greco, A., Raphaelson, S., Ehmann, K., Wang, Q. J., and Lin, C. (2009). Surface texturing of tribological interfaces using the vibromechanical texturing method. *Journal of manufacturing science and engineering*, 131(6):061005.

Groover, M. (2011). *Principles of modern manufacturing*. John Wiley and Sons, INC, Hoboken, 4th edition.

Hamilton, D., Walowit, J., and Allen, C. (1966). A theory of lubrication by microirregularities. *Journal of Fluids Engineering*, 88(1):177–185.

Ho, K. and Newman, S. (2003). State of the art electrical discharge machining (EDM). *International Journal of Machine Tools and Manufacture*, 43(13):1287–1300.

Hong, M. S. and Ehmann, K. F. (1995). Generation of engineered surfaces by the surface-shaping system. *International Journal of Machine Tools and Manufacture*, 35(9):1269–1290.

Huynh, B. P. (2005). Numerical study of slider bearings with limited corrugation. *Journal of tribology*, 127(3):582–595.

ISO 4288:1996 (1996). Geometrical Product Specifications (GPS) – Surface texture: Profile method – Rules and procedures for the assessment of surface texture.

ISO 91-1:1992 (1992). Petroleum measurement tables – Part 1: Tables based on reference temperatures of 15 degrees C and 60 degrees F.

Jin, M. and Murakawa, M. (2001). Development of a practical ultrasonic vibration cutting tool system. *Journal of materials processing technology*, 113(1):342–347.

Kasolang, S. and Dwyer-Joyce, R. (2008a). Observations of film thickness profile and cavitation around a journal bearing circumference. *Tribology Transactions*, 51(2):231–245.

Kasolang, S. and Dwyer-Joyce, R. (2008b). Viscosity measurement in thin lubricant films using shear ultrasonic reflection. *Proceedings of the Institution of Mechanical Engineers, Part J: Journal of Engineering Tribology*, 222(3):423–429.

Koring, R. (2013). *Changes in Plain Bearing Technology*. SAE International, Warrendale.

Krautkrämer, J. and Krautkrämer, H. (1969). *Ultrasonic testing of materials*. Springer-Verlag, Berlin and New York.

Lee, J.-R., Chong, S. Y., Jeong, H., and Kong, C.-W. (2011). A time-of-flight mapping method for laser ultrasound guided in a pipe and its application to wall thinning visualization. *NDT & E International*, 44(8):680–691.

Lejeune, M., Chartier, T., Dossou-Yovo, C., and Noguera, R. (2009). Ink-jet printing of ceramic micro-pillar arrays. *Journal of the European Ceramic Society*, 29(5):905–911.

Li, J. and Chen, H. (2007). Evaluation on applicability of Reynolds equation for squared transverse roughness compared to CFD. *Journal of Tribology*, 129(4):963–967.

Lo, S.-W. and Horng, T.-C. (1999). Lubricant permeation from micro oil pits under intimate contact condition. *Journal of tribology*, 121(4):633–638.

Lowe, M. J., Alleyne, D. N., and Cawley, P. (1998). Defect detection in pipes using guided waves. *Ultrasonics*, 36(1):147–154.

Lu, X. and Khonsari, M. (2007). An experimental investigation of dimple effect on the stribeck curve of journal bearings. *Tribology Letters*, 27(2):169–176.

Lugscheider, E., Bobzin, K., and Lackner, K. (2003). Investigations of mechanical and tribological properties of CrAlN+ C thin coatings deposited on cutting tools. *Surface and Coatings Technology*, 174:681–686.

Malburg, M. C., Raja, J., and Whitehouse, D. J. (1993). Characterization of surface texture generated by plateau honing process. *CIRP Annals-Manufacturing Technology*, 42(1):637–639.

Marshall, M., Lewis, R., and Dwyer-Joyce, R. (2006a). Characterisation of contact pressure distribution in bolted joints. *Strain*, 42(1):31–43.

Marshall, M., Lewis, R., Dwyer-Joyce, R., Olofsson, U., and Björklund, S. (2006b). Experimental characterization of wheel-rail contact patch evolution. *Journal of tribology*, 128(3):493–504.

Michell, A. (1929). Progress in fluid-film lubrication. *Trans. ASME*, 51(2):153–163.

Mills, R., Avan, E., and Dwyer-Joyce, R. (2012). Piezoelectric sensors to monitor lubricant film thickness at piston–cylinder contacts in a fired engine. *Proceedings of the Institution of Mechanical Engineers, Part J: Journal of Engineering Tribology*.

Mills, R., Vail, J., and Dwyer-Joyce, R. (2015). Ultrasound for the non-invasive measurement of internal combustion engine piston ring oil films. *Proceedings of the Institution of Mechanical Engineers, Part J: Journal of Engineering Tribology*, 229(2):207–215.

Moriwaki, T. and Shamoto, E. (1991). Ultraprecision diamond turning of stainless steel by applying ultrasonic vibration. *CIRP Annals-Manufacturing Technology*, 40(1):559–562.

Moriwaki, T. and Shamoto, E. (1995). Ultrasonic elliptical vibration cutting. *CIRP Annals-Manufacturing Technology*, 44(1):31–34.

Negishi, N. (2003). Elliptical vibration assisted machining with single crystal diamond tools. MS thesis, North Carolina State University.

Olympus Corporation (2006). Ultrasonic Transducers Technical Notes. `https://www.olympus-ims.com/data/File/panametrics/UT-technotes.en.pdf`. Accessed: Sep 2015.

Otero, N., Romero, P., Gonzalez, A., and Scano, A. (2012). Surface texturing with laser micro cladding to improve tribological properties. *JOURNAL OF LASER MICRO NANOENGINEERING*, 7(2):152–157.

Overcash, J. and Cuttino, J. (2003). Development of a tunable ultrasonic vibration-assisted diamond turning instrument. pages 503–506. Proceedings of 18th Annual Meeting. American Society for Precision Engineering (ASPE).

Parreira, J., Gallo, C., and Costa, H. (2012). New advances on maskless electrochemical texturing (MECT) for tribological purposes. *Surface and Coatings Technology*, 212:1–13.

Pettersson, U. and Jacobson, S. (2003). Influence of surface texture on boundary lubricated sliding contacts. *Tribology International*, 36(11):857–864.

Pfeiffer, W. and Frey, T. (2006). Strengthening of ceramics by shot peening. *Journal of the European Ceramic Society*, 26(13):2639–2645.

Physik Instrumente GmbH and Co (2009). *Piezo Nano Positioning Inspirations 2009*. KG product catalogue, Karlsruhe.

Physik Instrumente GmbH and Co E-481. User Manual. http://pi-sales.ws/index.php?id=840. Accessed: Feb 2015.

Physik Instrumente GmbH and Co P-212. User Manual. http://pi-sales.ws/index.php?id=830. Accessed: Feb 2015.

Pialucha, T. and Cawley, P. (1994). The detection of thin embedded layers using normal incidence ultrasound. *Ultrasonics*, 32(6):431–440.

Pilleri, G. (1983). The sonar system of the dolphins. *Endeavour*, 7(2):59–64.

Read, L. and Flack, R. (1987). Temperature, pressure and film thickness measurements for an offset half bearing. *Wear*, 117(2):197–210.

Reddyhoff, T., Kasolang, S., Dwyer-Joyce, R., and Drinkwater, B. (2005). The phase shift of an ultrasonic pulse at an oil layer and determination of film thickness. *Proceedings of the Institution of Mechanical Engineers, Part J: Journal of Engineering Tribology*, 219(6):387–400.

Reynolds, O. (1886). On the theory of lubrication and its application to Mr. Beauchamp Tower's experiments, including an experimental determination of the viscosity of olive oil. *Proceedings of the Royal Society of London*, 40(242-245):191–203.

Ruprecht, R., Benzler, T., Hanemann, T., Müller, K., Konys, J., Piotter, V., Schanz, G., Schmidt, L., Thies, A., Wöllmer, H., et al. (1997). Various replication techniques for manufacturing three-dimensional metal microstructures. *Microsystem technologies*, 4(1):28–31.

Ryk, G., Kligerman, Y., and Etsion, I. (2002). Experimental investigation of laser surface texturing for reciprocating automotive components. *Tribology Transactions*, 45(4):444–449.

Sahlin, F., Glavatskih, S. B., Almqvist, T., and Larsson, R. (2005). Two-dimensional cfd-analysis of micro-patterned surfaces in hydrodynamic lubrication. *Journal of tribology*, 127(1):96–102.

Salama, M. (1950). The effect of macro-roughness on the performance of parallel thrust bearings. *Proceedings of the Institution of Mechanical Engineers*, 163(1):149–161.

Sandvik Coromant Ltd (2012). Turning tools - general turning. http://www.sandvik.coromant.com/sitecollectiondocuments/downloads/global/catalogues/en-gb/turning/turn_a.pdf. Accessed: Feb 2015.

Schade, A., Rosiwal, S. M., and Singer, R. F. (2006). Tribological behaviour of 100 and 111 fibre textured CVD diamond films under dry planar sliding contact. *Diamond and related materials*, 15(10):1682–1688.

Schirru, M. M. and Dwyer-Joyce, R. S. (2015). A model for the reflection of shear ultrasonic waves at a thin liquid film and its application to viscometry in a journal bearing. *Proceedings of the Institution of Mechanical Engineers, Part J: Journal of Engineering Tribology*, page 1350650115610357.

Schoenberg, M. (1980). Elastic wave behavior across linear slip interfaces. *Acoustical Society of America*, 68(5):1516–1521.

Shamoto, E. and Moriwaki, T. (1999). Ultaprecision diamond cutting of hardened steel by applying elliptical vibration cutting. *CIRP Annals-Manufacturing Technology*, 48(1):441–444.

Smithells, C. J. (1992). *Smithells metals reference book. ed. Brandes EA, Brook G, editors*. Butterworth-Heinemann, Oxford, 7th edition.

Spearot, J. A. and Murphy, C. K. (1988). A comparison of the total capacitance and total resistance techniques for measuring the thickness of journal bearing oil films in an operating engine. Technical report, SAE Technical Paper.

Sprang, N., Theirich, D., and Engemann, J. (1995). Plasma and ion beam surface treatment of polyethylene. *Surface and Coatings Technology*, 74:689–695.

Stachowiak, G. and Batchelor, A. W. (2005). *Engineering tribology*. Butterworth-Heinemann, Amsterdam and Boston, 3rd edition.

Sun, D.-C. and Chen, K.-K. (1977). First effects of stokes roughness on hydrodynamic lubrication. *Journal of Tribology*, 99(1):2–9.

Tattersall, H. (1973). The ultrasonic pulse-echo technique as applied to adhesion testing. *Journal of Physics D: Applied Physics*, 6(7):819.

The Japan Society of Mechanical Engineers (2012). *Mechanical Engineer's Concise Handbook :In Japanese*. Maruzen Co, Tokyo, 7th edition.

Tonnesen, J. and Hansen, P. (1981). Some experiments on the steady state characteristics of a cylindrical fluid-film bearing considering thermal effects. *Journal of Tribology*, 103(1):107–114.

Tower, B. (1883). First report on friction experiments. *Proceedings of the institution of mechanical engineers*, 34(1):632–659.

Townsend, D. P. (1992). Improvement in surface fatigue life of hardened gears by high-intensity shot peening. Technical report, DTIC Document.

Tsukahara, Y., Nakaso, N., Kushibiki, J., and Chubachi, N. (1989). An acoustic micrometer and its application to layer thickness measurements. *Ultrasonics, Ferroelectrics, and Frequency Control, IEEE Transactions on*, 36(3):326–331.

Urick, R. (1947). A sound velocity method for determining the compressibility of finely divided substances. *Journal of Applied Physics*, 18(11):983–987.

Versteeg, H. K. and Malalasekera, W. (2007). *An introduction to computational fluid dynamics: the finite volume method*. Pearson Education, Harlow.

Waits, C., Morgan, B., Kastantin, M., and Ghodssi, R. (2005). Microfabrication of 3D silicon MEMS structures using gray-scale lithography and deep reactive ion etching. *Sensors and Actuators A: Physical*, 119(1):245–253.

Wang, X., Adachi, K., Otsuka, K., and Kato, K. (2006). Optimization of the surface texture for silicon carbide sliding in water. *Applied Surface Science*, 253(3):1282–1286.

Wang, X., Kato, K., Adachi, K., and Aizawa, K. (2001). The effect of laser texturing of SiC surface on the critical load for the transition of water lubrication mode from hydrodynamic to mixed. *Tribology International*, 34(10):703–711.

Wang, X., Kato, K., Adachi, K., and Aizawa, K. (2003). Loads carrying capacity map for the surface texture design of SiC thrust bearing sliding in water. *Tribology International*, 36(3):189–197.

Yoshizaki, M. (2008). Improvement in tooth surface strength of carburized transmission gears by fine particle bombarding process. Proceedings of ICSP-10 Tokyo, Japan.

Zhang, J., Drinkwater, B. W., and Dwyer-Joyce, R. S. (2006). Monitoring of lubricant film failure in a ball bearing using ultrasound. *Journal of tribology*, 128(3):612–618.

Zhang, P. and Lindemann, J. (2005). Influence of shot peening on high cycle fatigue properties of the high-strength wrought magnesium alloy AZ80. *Scripta Materialia*, 52(6):485–490.

Appendices

Appendix A

Design drawings

Table A.1: List of design drawings.

Drawing No.	Name	Material	Test rig	Chapter
A001	Spindle shaft	C45 or equivalent	Vibration-assisted machining device	3
A002	Lower housing	C45 or equivalent	Vibration-assisted machining device	3
A003	Upper housing	C45 or equivalent	Vibration-assisted machining device	3
A004	Base plate	C45 or equivalent	Vibration-assisted machining device	3
A005	Disc work piece 1	AlSi1MgMn	Vibration-assisted machining device	3
A006	Disc work piece 2	16MnCr5	Vibration-assisted machining device	3
A007	Supporting plate 1	C45 or equivalent	Journal bearing	4
A008	Supporting plate 2	C45 or equivalent	Journal bearing	4
A009	Angle adjuster	C45 or equivalent	Journal bearing	4
A010	Intermediate shaft	C45 or equivalent	Journal bearing	4
A011	Load cell holder	C45 or equivalent	Journal bearing	4
A012	Bush	SCM420H	Journal bearing	4
A013	Supporting plate	C45 or equivalent	Vibration-assisted machining device	5
A014	Tool holder	C45 or equivalent	Vibration-assisted machining device	5
A015	Supporting shaft 1	C45 or equivalent	Vibration-assisted machining device	5
A016	Supporting shaft 2	C45 or equivalent	Vibration-assisted machining device	5
A017	Shell work piece	C40	Vibration-assisted machining device	5
A018	Bottom plate	C45 or equivalent	Vibration-assisted machining device	5

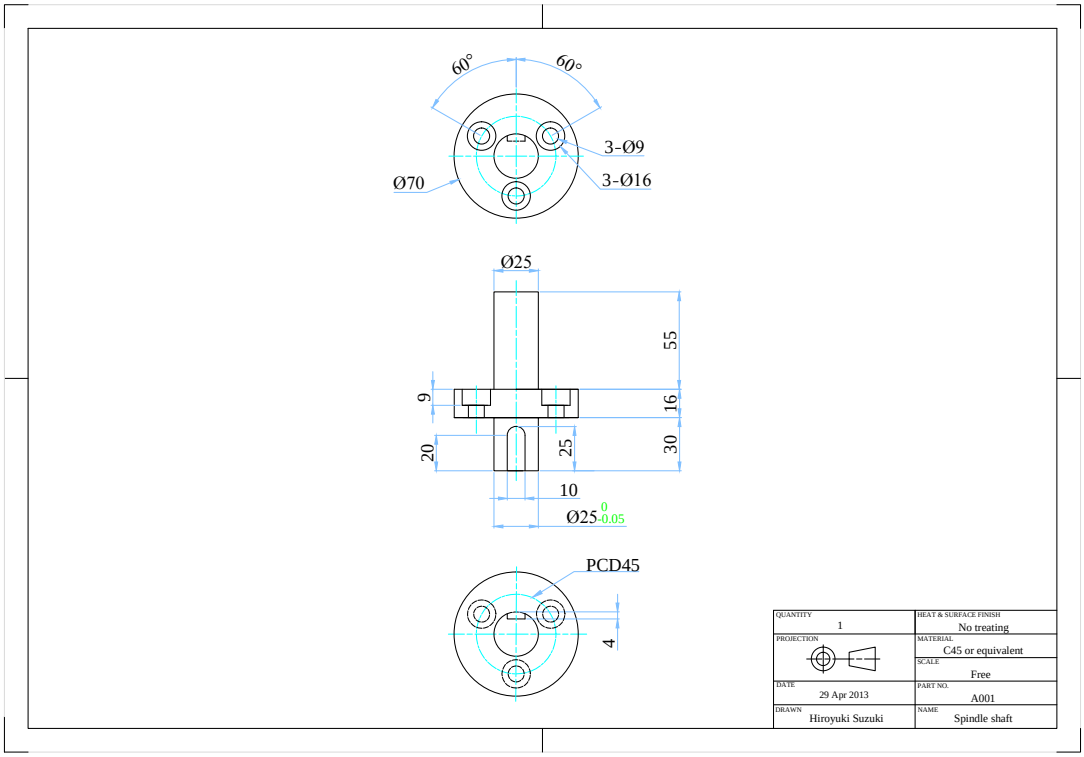

Figure A.1: A001 - Spindle shaft.

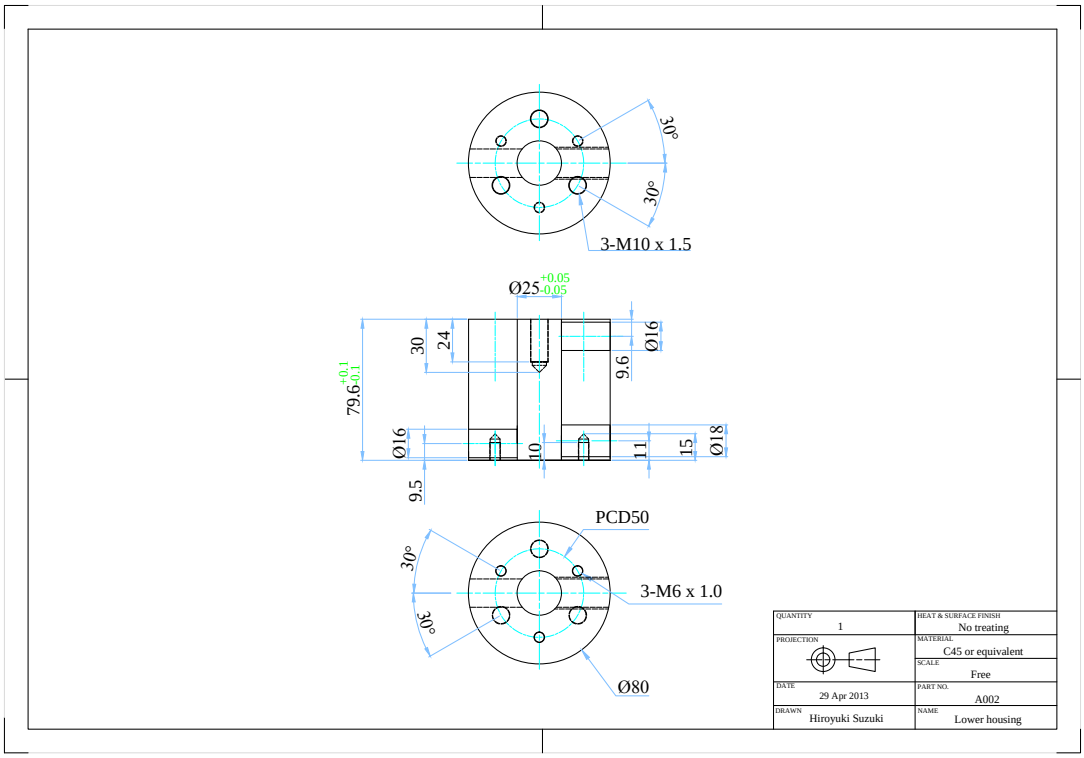

Figure A.2: A002 - Lower housing.

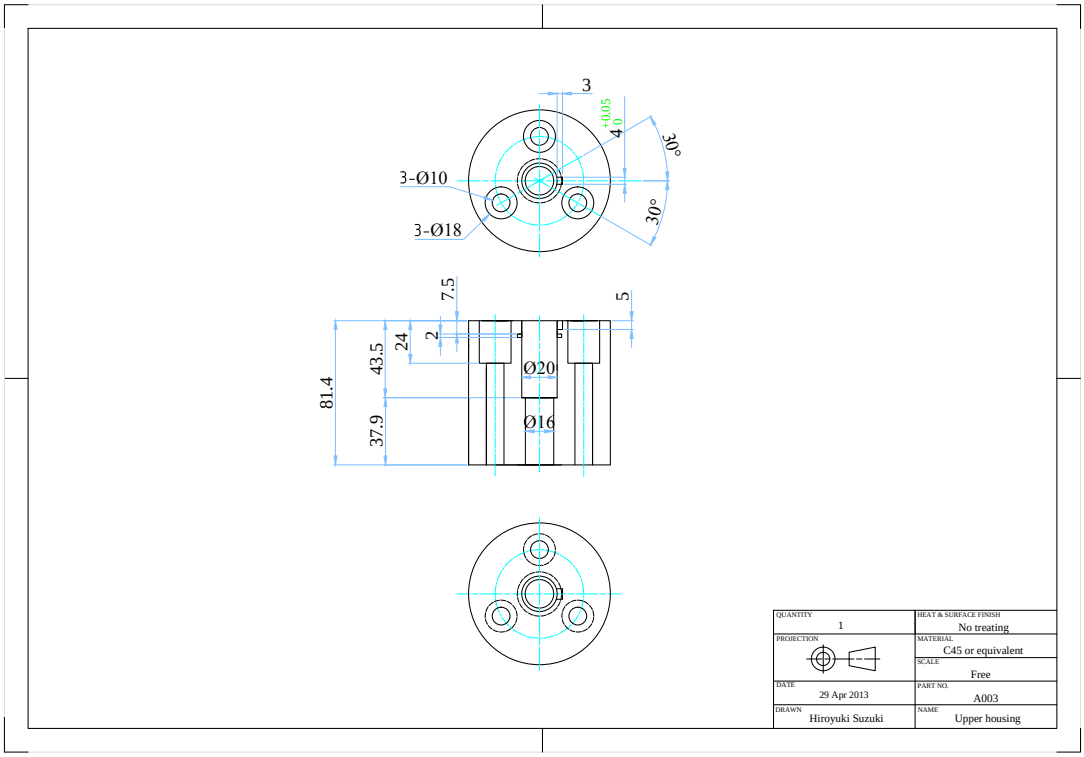

Figure A.3: A003 - Upper housing.

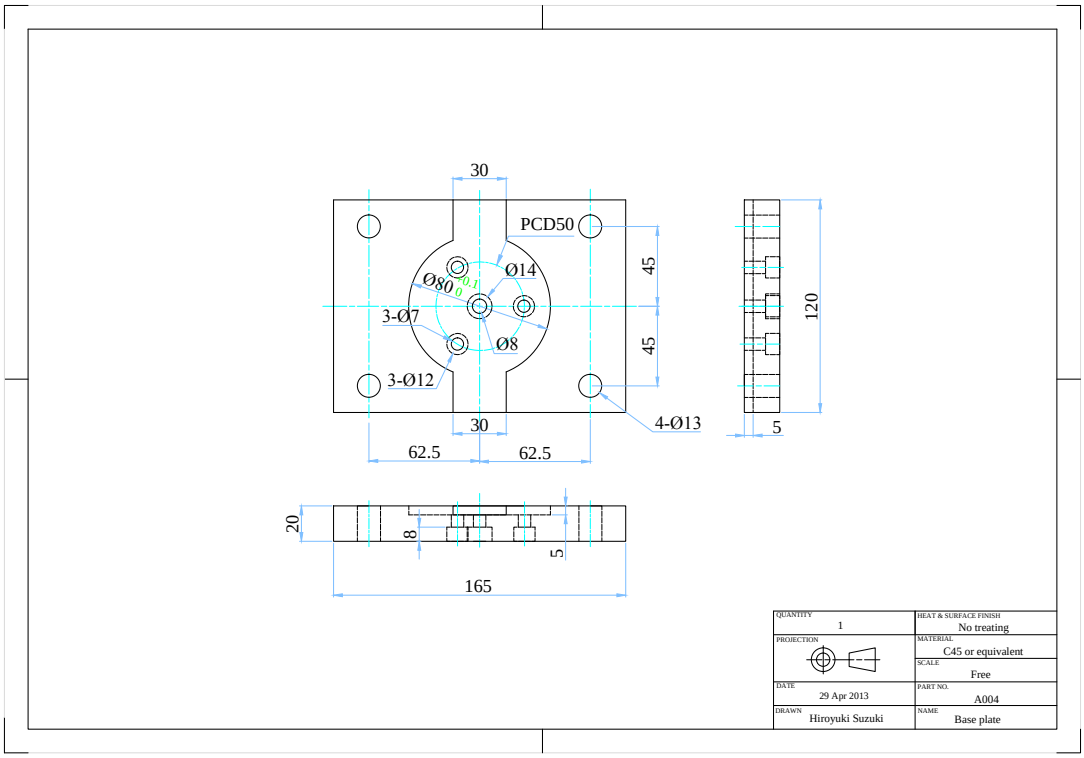

Figure A.4: A004 - Base plate.

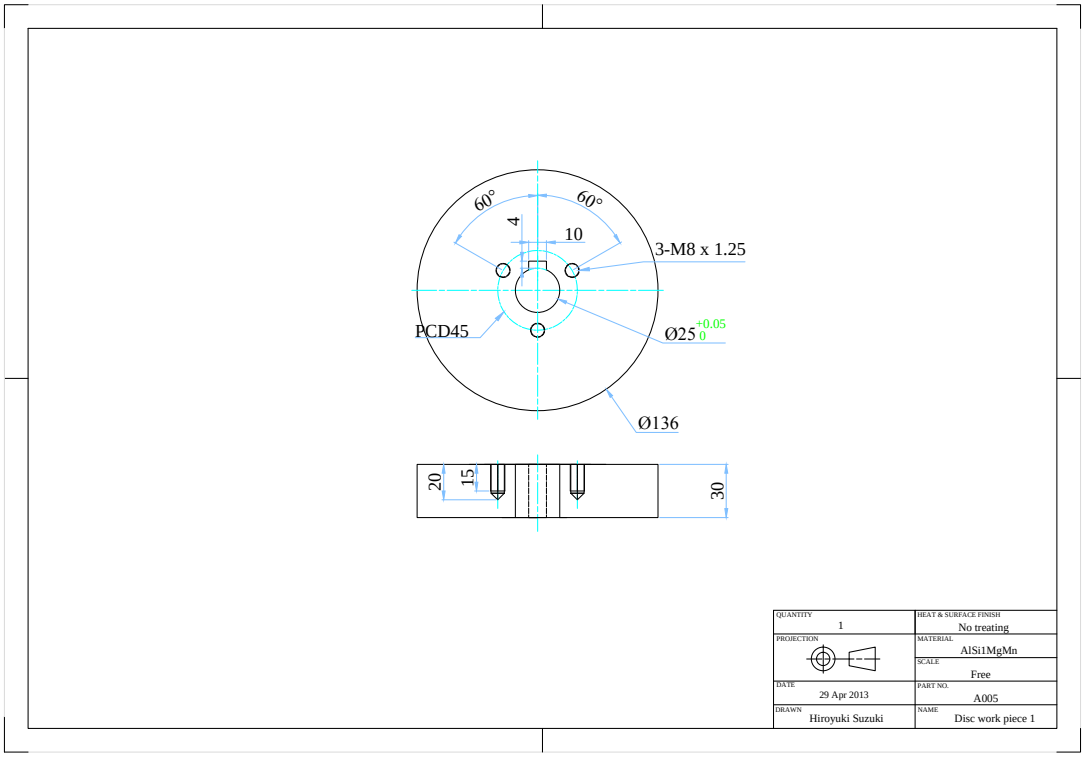

Figure A.5: A005 - Disc work piece.

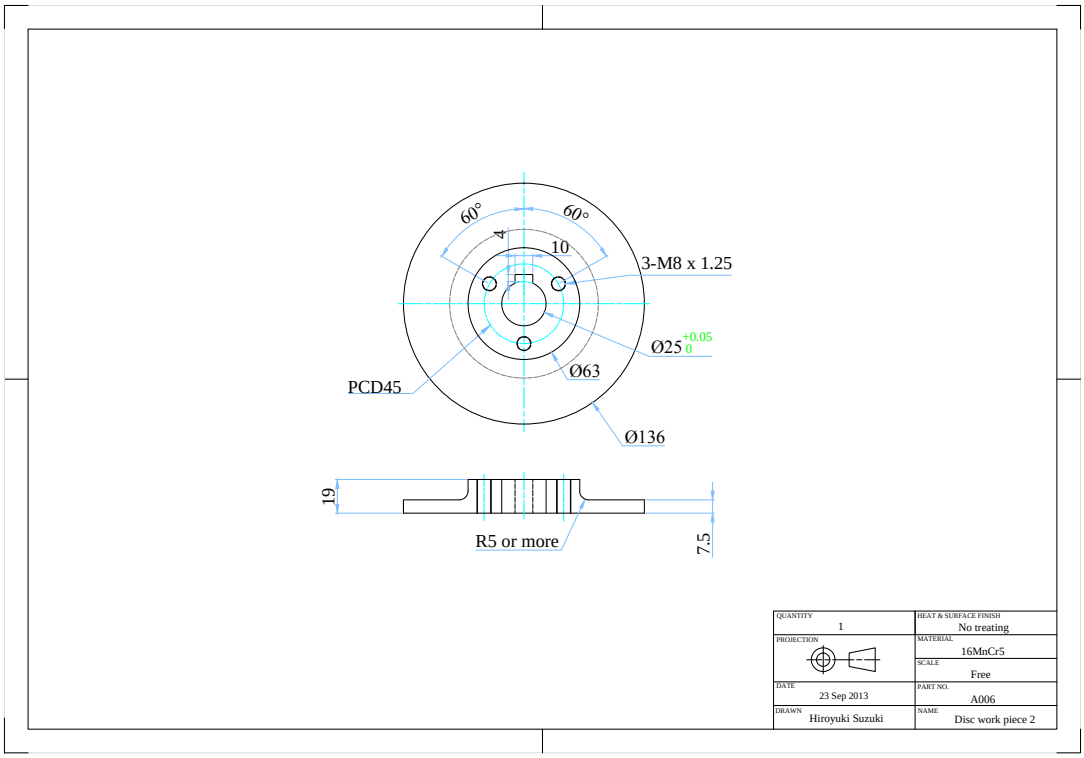

Figure A.6: A006 - Disc work piece.

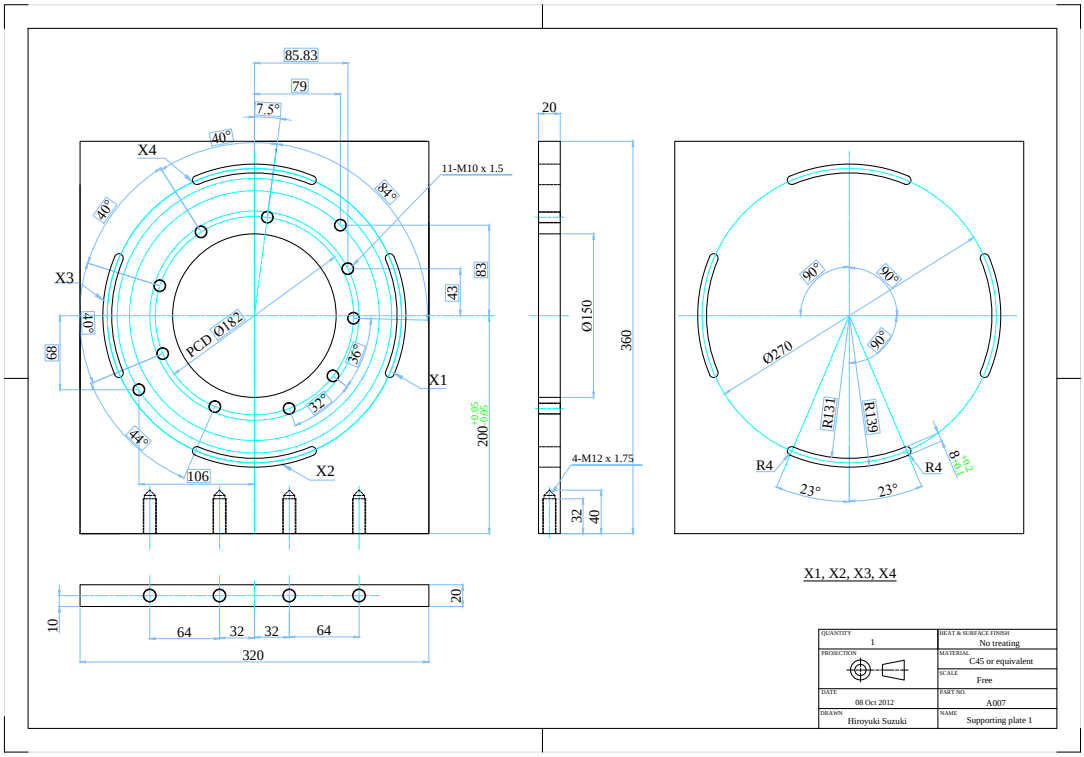

Figure A.7: A007 - Supporting plate 1.

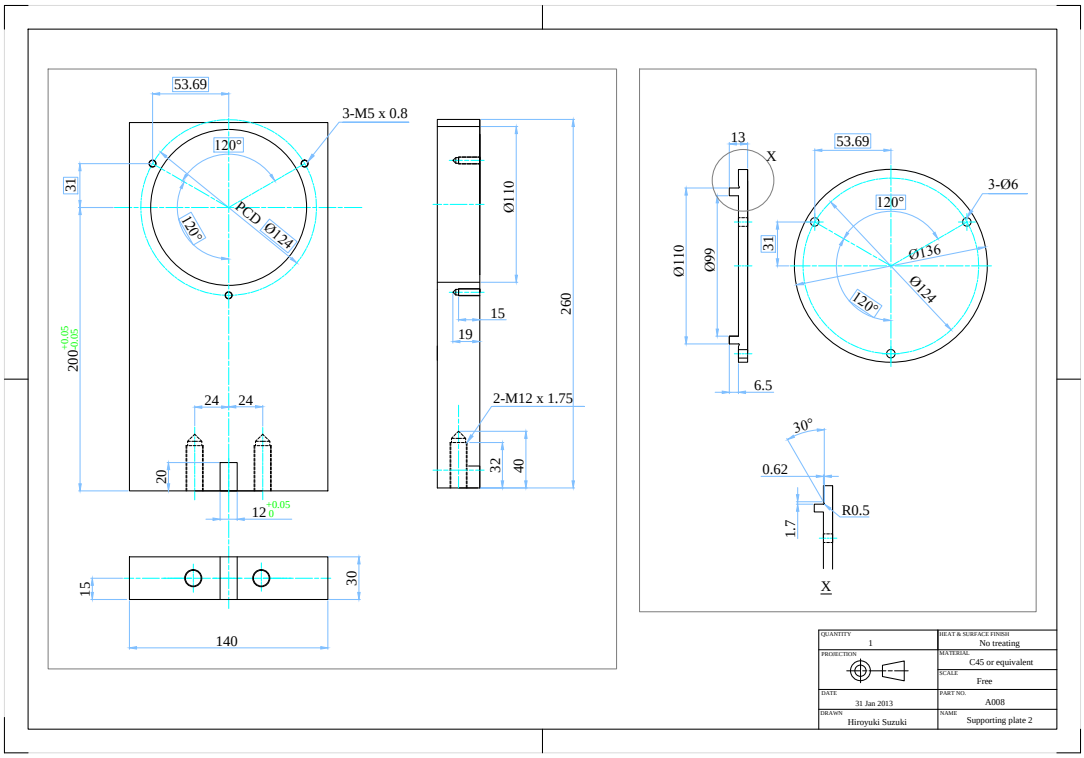

Figure A.8: A008 - Supporting plate 2.

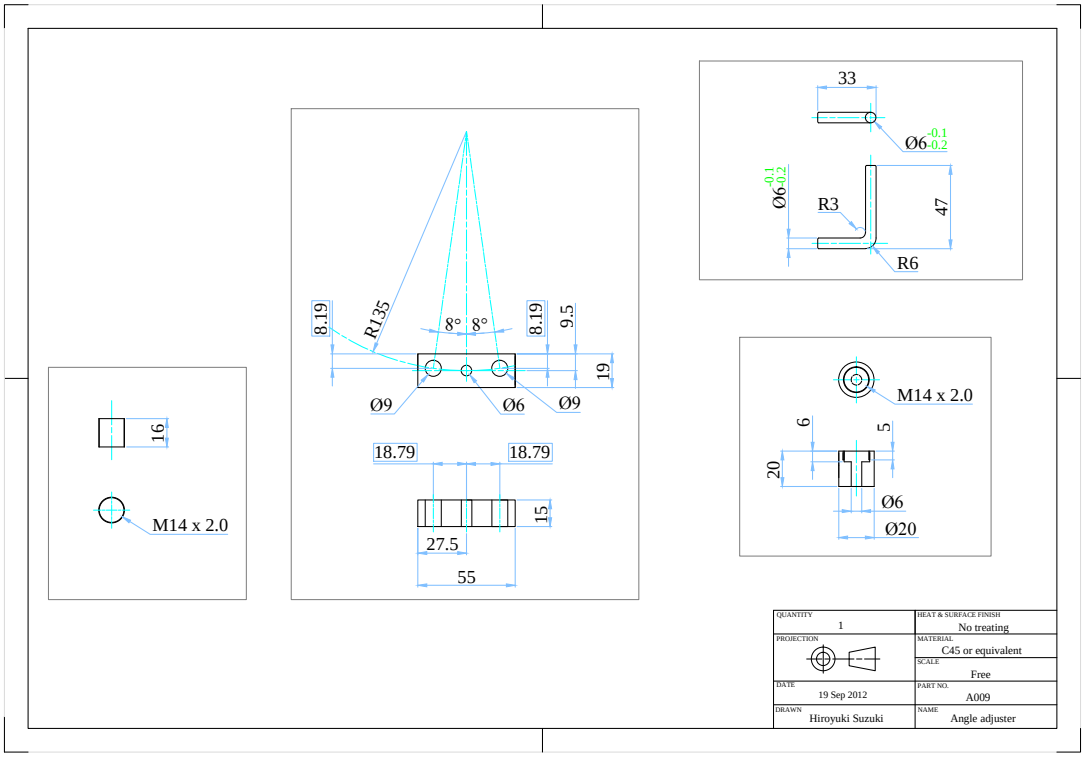

Figure A.9: A009 - Angle adjuster.

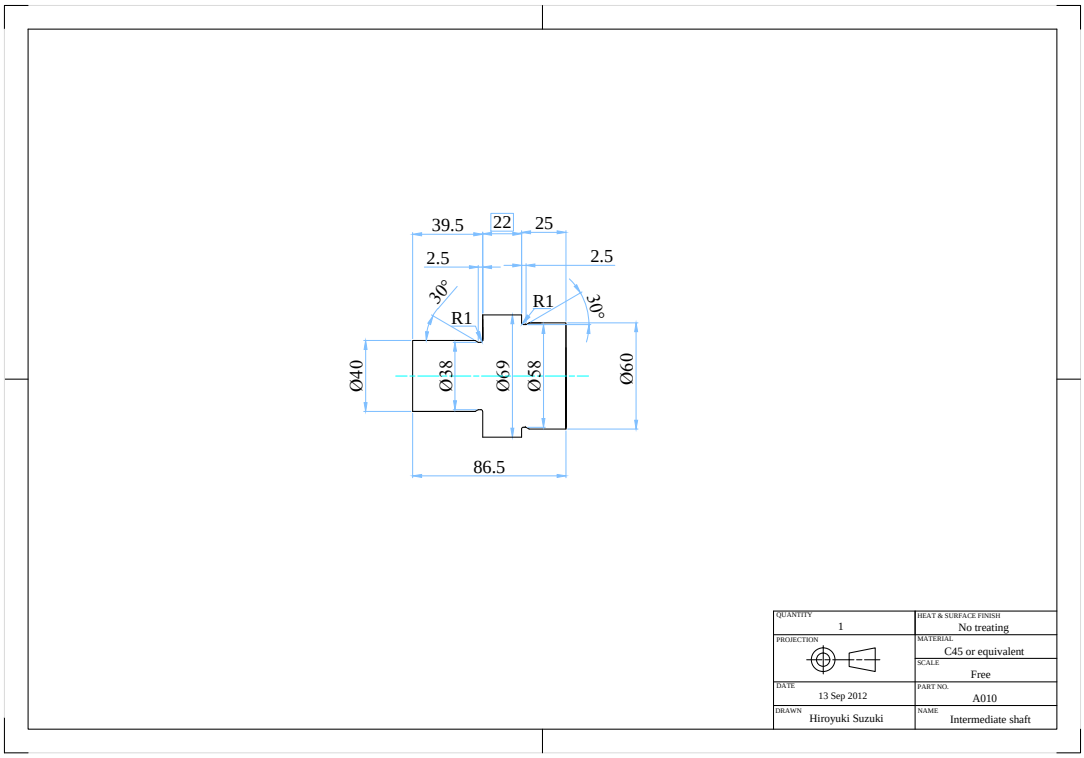

Figure A.10: A010 - Intermediate shaft.

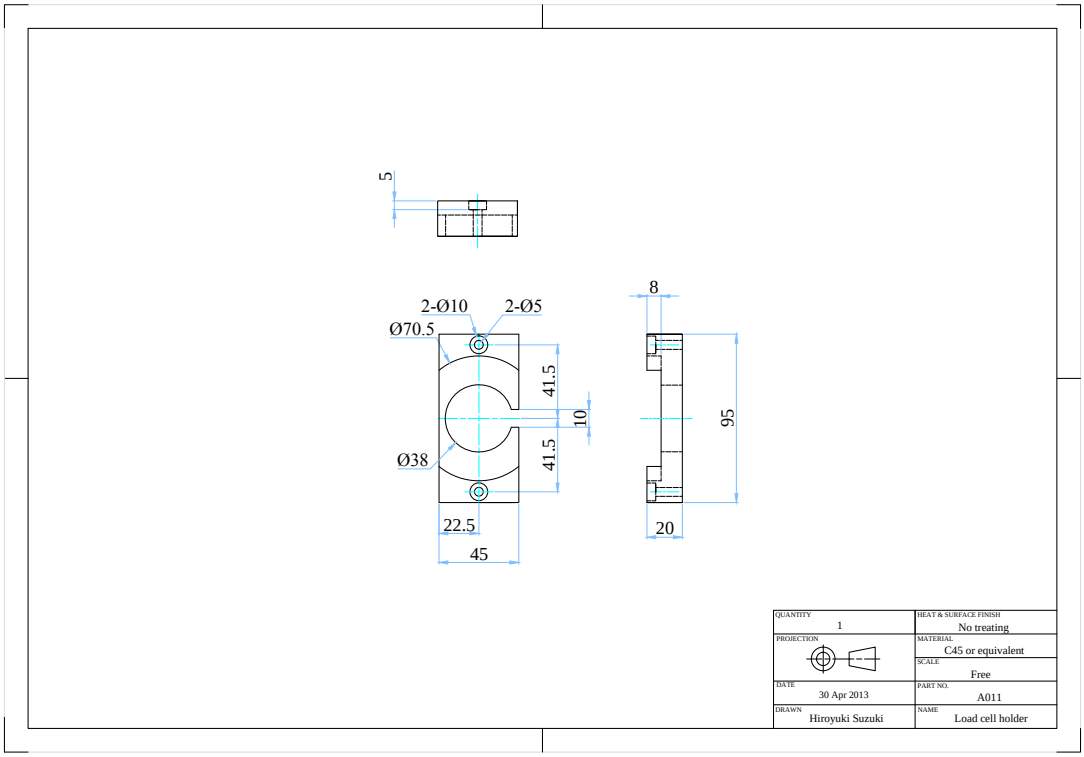

Figure A.11: A011 - Load cell holder.

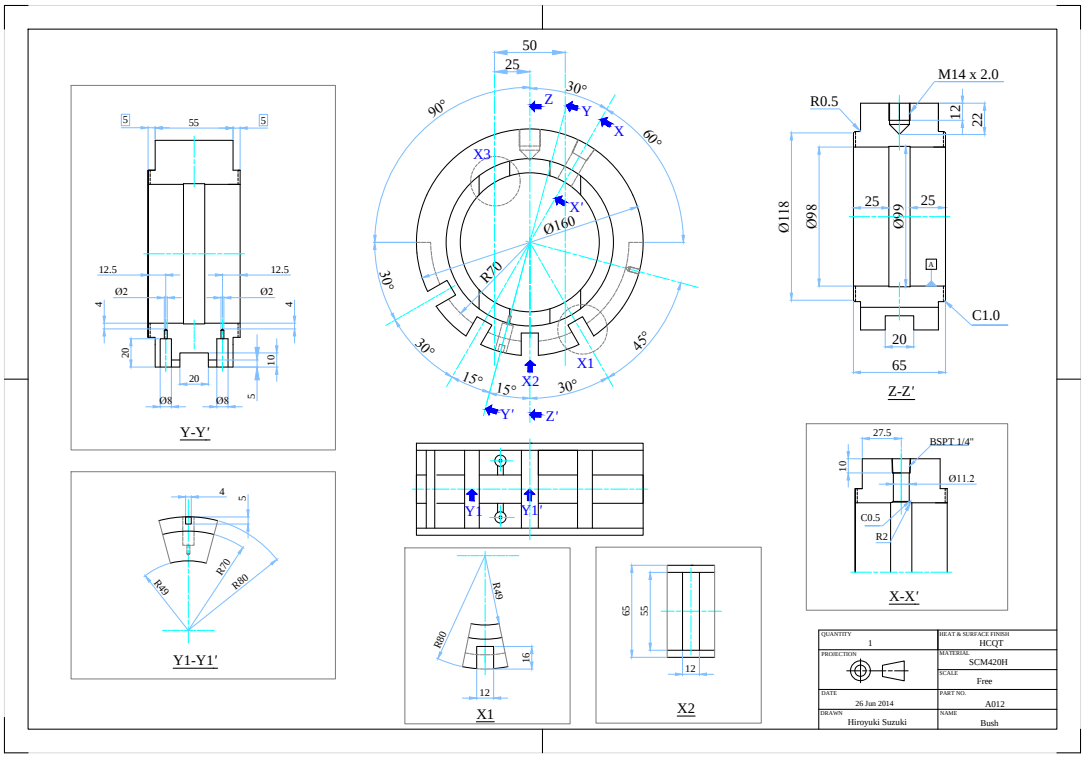

Figure A.12: A012 - Bush.

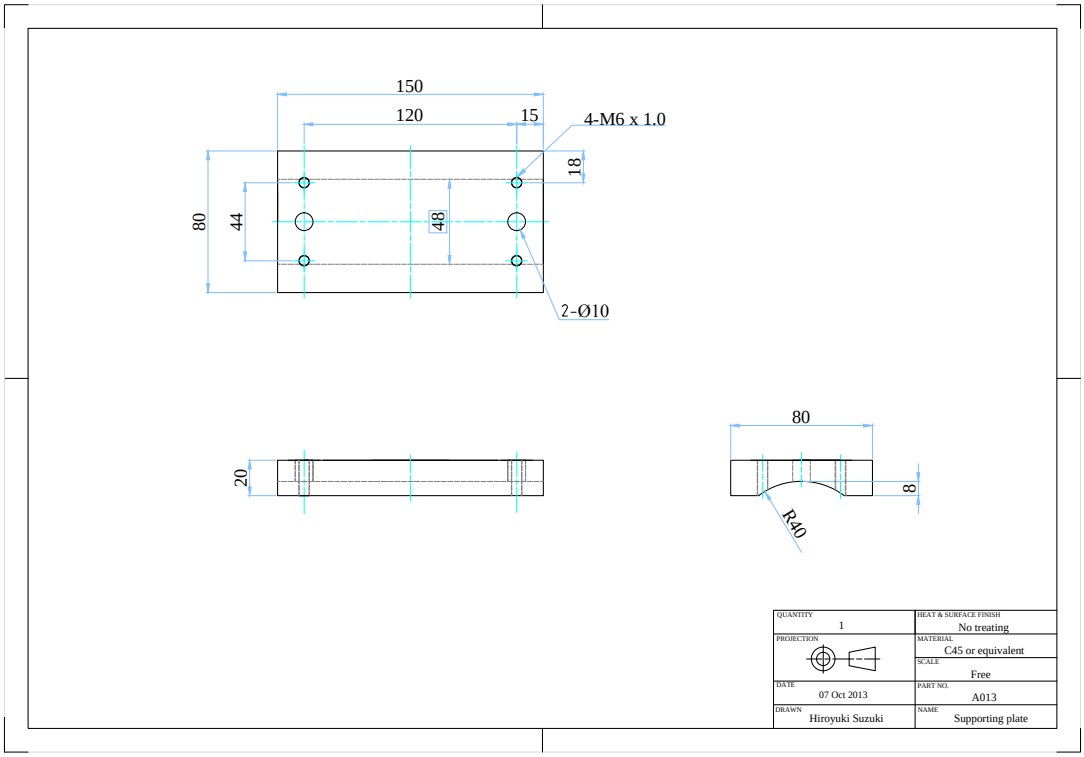

Figure A.13: A013 - Supporting plate.

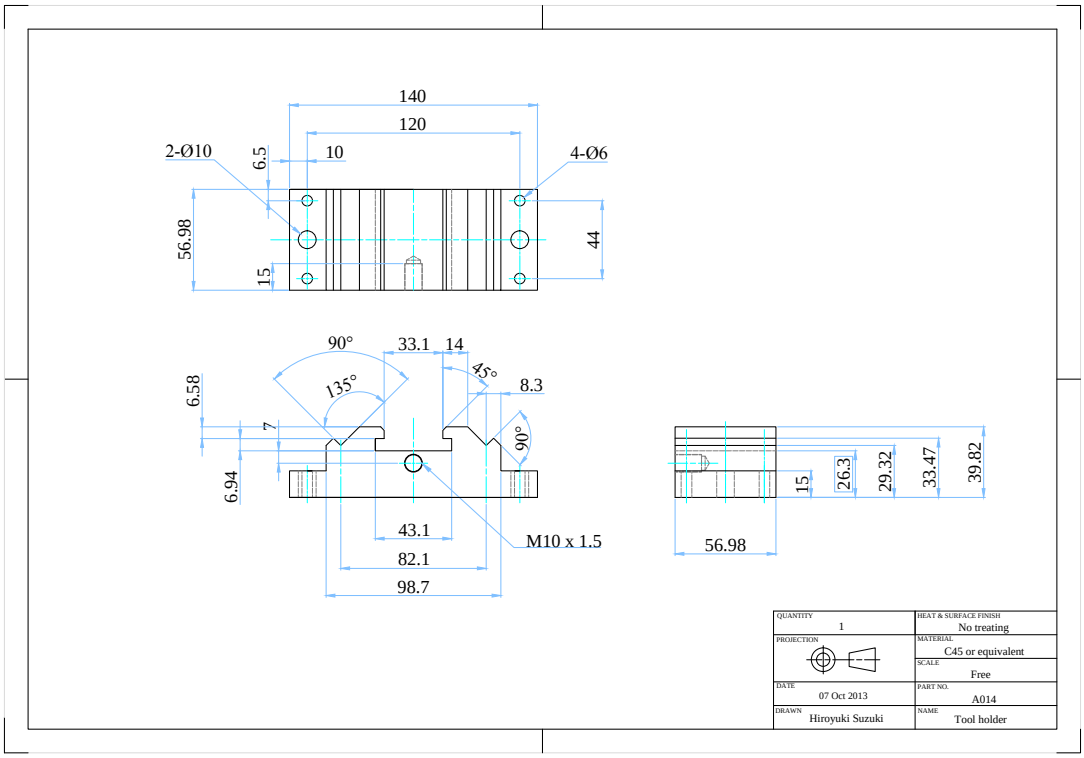

Figure A.14: A014 - Tool holder.

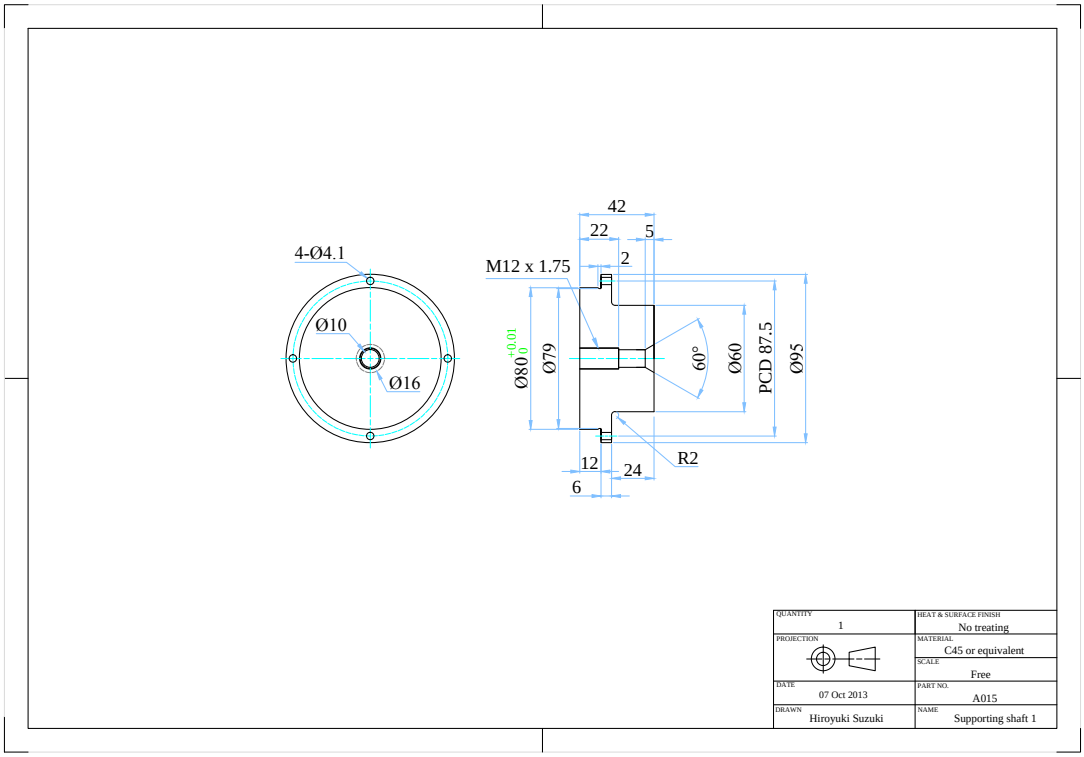

Figure A.15: A015 - Supporting shaft 1.

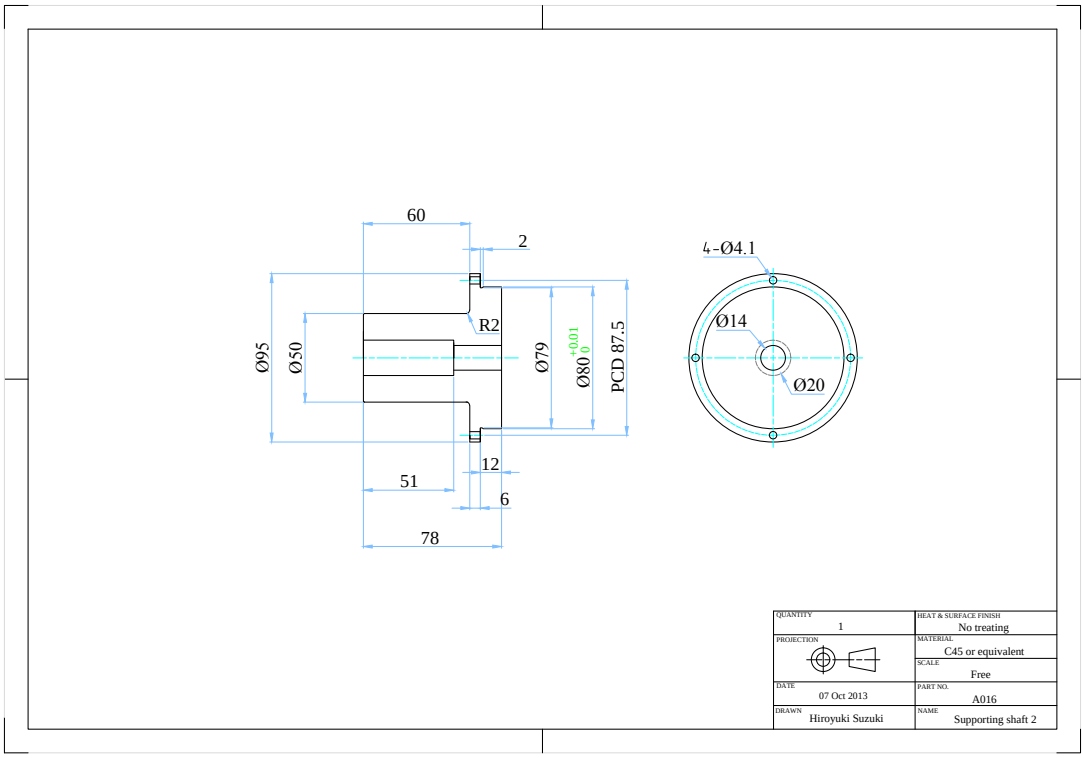

Figure A.16: A016 - Supporting shaft 2.

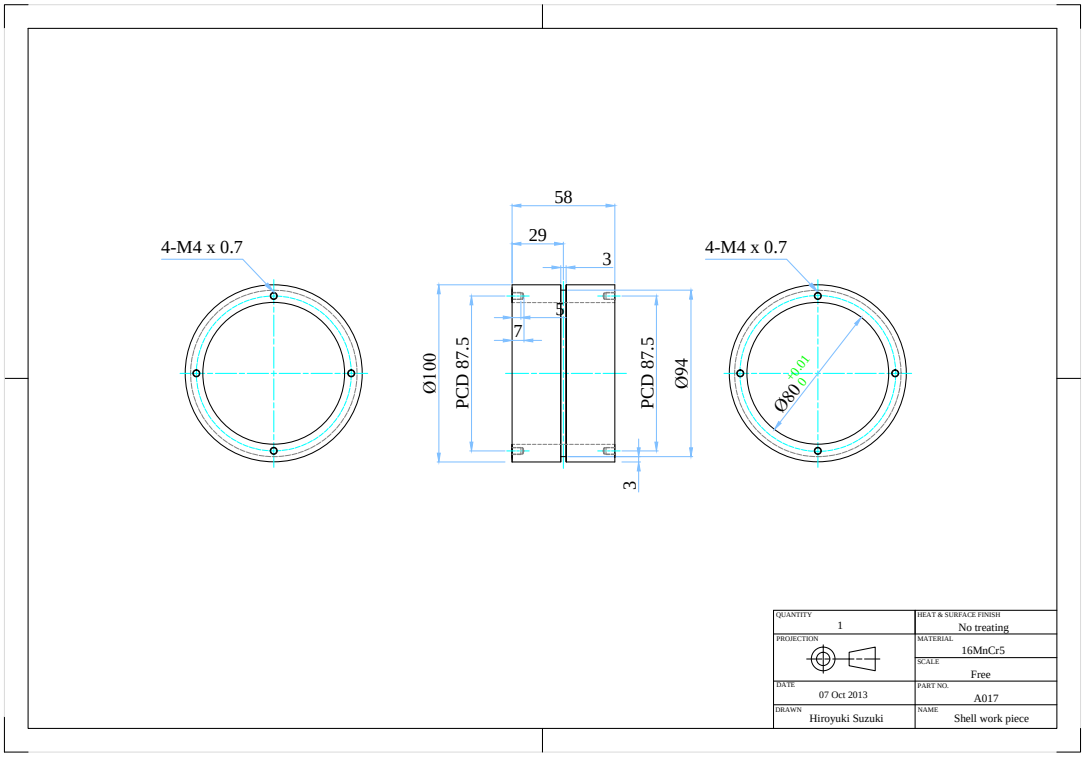

Figure A.17: A017 - Shell work piece.

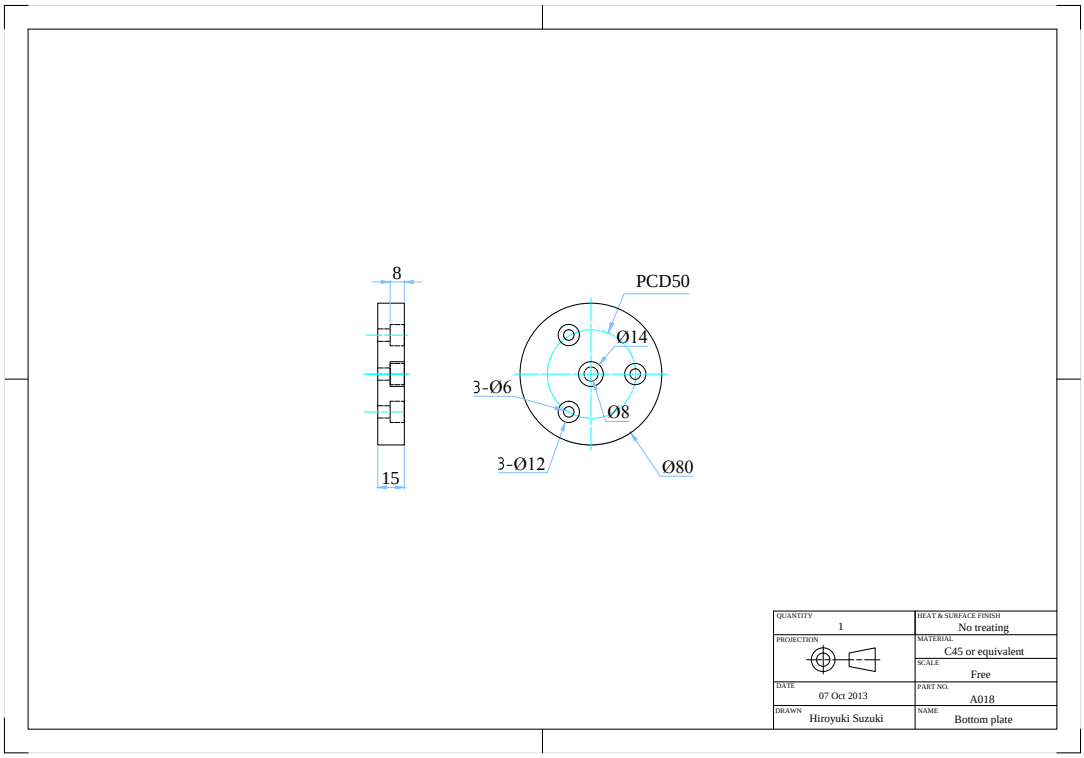

Figure A.18: A018 - Bottom plate.

Appendix B

Publications

- Suzuki H, Marshall M, Sims N and Dwyer-Joyce R (2016), Design and Implementation of a Non-Resonant Vibration-Assisted Machining to Create Bespoke Surface Textures, *Proceeding of the Institute of Mechanical Engineers, Part C: Journal of Mechanical Engineering Science* (accepted).
- Suzuki H and Dwyer-Joyce R (2015), Ultrasonic Determination of Lubricant Film Thickness in an Automotive Transmission Journal Bearing, Proceedings of the 42nd Leeds-Lyon Symposium on Tribology.
- Suzuki H, Marshall M, Sims N and Dwyer-Joyce R (2014), Surface Texturing by Vibration Assisted Machining with Piezoelectric Actuator, Proceedings of the Society of Tribologists and Lubrication Engineers Annual Meeting and Exhibition 2014, Vol. 2 (pp 778-780).
- Suzuki H, Marshall M and Dwyer-Joyce R (2013), Measurement of lubricant film thickness in a gearbox journal bearing with ultrasonic reflection, Proceedings of the 5th World Tribology Congress, WTC 2013, Vol. 3 (pp 2367-2370).